DESIGN, FABRICATION AND OPTICAL CHARACTERIZATION OF ONE-DIMENSIONAL TWO- AND MULTI-COMPONENT PHOTONIC CRYSTALS BASED ON SILICON

By

Anna Baldycheva

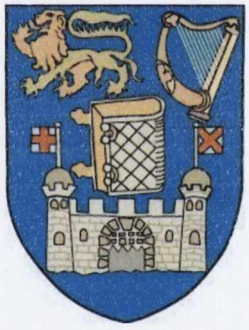

A thesis submitted to the
University of Dublin
for the degree of
Doctor of Philosophy

Department of Electrical and Electronic Engineering
University of Dublin, Trinity College
Dublin

September, 2012

Declaration

I, the undersigned, declare that this thesis has not been submitted as an exercise for a degree in this or any other university or institution. The work described in this thesis is entirely my own, with exception of assistance recognized in the acknowledgments and the collaborative work noted in the publications. I furthermore agree that the Trinity College library may lend or copy this thesis on request.

Abstract

The objective of this thesis was the design, fabrication and optical investigation of a novel type of one-dimensional photonic crystal structures for application in integrated Silicon microphotonics. This thesis reports on new and unique optical properties of the developed ultra-wide pass-band filters based on multi-component photonic crystal model and thermo-, electro-tunable filters based on micro-cavity photonic crystal resonator model.

For the first time, the formation of the flat-top regions of transparency, pass-bands, was experimentally demonstrated for the grooved Silicon photonic crystal reflectors using the multi-component model. Using this method for the decrease of the optical contrast in photonic crystals allows omni-directional photonic band gaps to be obtained in high-contrast photonic crystal structures. The multi-component model enables easy and precise engineering of the optical contrast of the grooved-Silicon photonic crystal. This achieved, not by filling the air grooves with refractive index matching liquid, but via appropriate selection of the thickness or refractive index of the additional materials.

The proposed novel design of the electro-controllable band-pass integrated filters is based on the defect-free one-dimensional Silicon photonic crystal model and liquid crystal opto-fluidic technique, which allows the realization of the individual optical defects, microcavities, with tuning capabilities. By either varying the temperature or by application of electric field individually to each microcavity of the device the continuous precise tuning was demonstrated, which possess: i) the widest tunability of the resonance peaks known to date and ii) a unique fine electro-controllable tuneability of individual resonances in the system. Most importantly, only small change of the refractive index of liquid crystal is sufficient for realization of this tuning.

Finally, a model for investigation of the photonic band gap deviations caused by structural fluctuations in fabricated one-dimensional photonic crystals has been elaborated. It was established that the deviations of the photonic band gaps strongly depend on the magnitude of the structural fluctuations and increases with an increase in the order of the photonic band gaps. The approach has been proposed for the

determination of the fabrication tolerances and optimization of the photonic band gap properties of the fabricated photonics crystal structures.

The optical effects demonstrated have practical applications in integrated Silicon microphotonics. The models developed in this work can be applied to the design of one-dimensional photonic crystal devices of any micro- and nano-structured semiconductor or dielectric materials for application in optical-interconnects, biochemical sensing, medicine, defence and security across the entire electromagnetic spectrum.

Acknowledgements

As my thesis writing days draw to a close I would like to take this opportunity to thank those who made it all possible.

The research undertaken for this thesis was guided and encouraged throughout by Prof. Tatiana S. Perova, to whom I would like to express my gratitude and sincere appreciation for giving me the opportunity to embark on this exciting journey. I would like to deeply thank Prof. Perova for her time, encouragement and helpful discussions during all four years.

Prof. Vladimir Tolmachev for supplying guidance, help with writing of publications and many englighting conversations during all these years and most of all for sharing his enthusiasm for research.

I would also like to thank all the past and present members of the Microelectronic Technology Group for all their help and interests, particularly, Elena Krutkova, Joanna Wasyluk, Sergey Dyakov, David Adley, Victor Ermakov, and Franz Schmied.

All collaborators, for their help with the sample fabrication and for many fruitful conversations along the way, particularly, Prof. Ekaterina Astrova, Dr. Yulia Zharova, Galina Li (Fedulova), Dr. Kevin Berwick and Dr. Mike Bain.

Prof. John Donegan's and Prof. Louise Bradley's group and especially Robert Lennox and Michael Lynch for help in building of experimental set-up and valuable discussions.

Part of the fabrication work was funded by Science Foundation Ireland through the National Access Programme (NAP) at Tyndall National Institute.

I would like to acknowledge all the engineers from Tyndall National Institute for the great fabrication job of the samples during NAP 94 and NAP 368, particularly people who did the really critical parts were Alan Blake, Brendan McCarthy (e-beam lithography), Jim Scully and Alan Hydes (Silicon-etch for the nano-structures).

I would like to acknowledge the full financial support from the ICGEE GREP (Internation School for Graduate Education in Nano- and Micro-Engineering), without which this work would not be possible. It was a great honor to get this award and to be a part of this great organization.

The Trinity Trust Travel Award for supporting financially travelling to the two major European Photonics conferences: SPIE Optical Metrology 2009 as a part of World of Photonics Congress 2009 in Munich and SPIE Photonics Europe 2012 in Brussels.

The SPIE Travel Award for supporting financially travelling to the SPIE Photonics Europe 2010 in Brussles.

To my mother for her love, support and patience and for always looking at the bright side of life. I love you mommy!

Finally, I would like to express my deepest appreciation to family and friends for all the laughs, good times and support through the PhD studies. Special thanks to aunty Nina, uncle Vova, aunty Anna, aunty Larisa, baba Ada, Mashulya, Ira, Masha, Anastasia, Elena, Julie, Camille, Misha, Marina, Pasha, Nina Sergeevna, Anya, Nadezhda Mikhailovna, Krolik, Milena. I am forever greatful for your friendship and understanding.

For my mother and
in memory of my grandparents.

Table of Contents

List of Figures

Acronyms and Abbreviations

BD	Band diagram
BOX	Buried Oxide
CMOS	Complementary metal oxide semiconductor
DRIE	Deep reactive ion etching
FP	Fabry-Perot
FPR	Fabry-Perot resonator
FSR	Free spectral range
FTIR	Fourier transform infrared
FWHM	Full width at half maximum
GM	Gap Maps
IB	Interference bands
LC	Liquid crystal
MEMS	Microelectromechanical systems
MIR	Middle infrared
NF	Normalized frequency
NIR	Near infrared
NW	Normalized wavelength
ODB	Omni-directional band
PB	Pass band
PBG	Photonic band gap
PhC	Photonic crystal
RIE	Reactive ion etching
SB	Stop band
TB	Transmission band
TE	Transverse electircal
TM	Transverse magnetic
TMM	Transfer matrix method
a	Lattice constant
d_{air}	Thickness of air component
d_{cav}	Thickness of cavity
d_H	Thickness of high-refractive index component

$(d_H)_i$	Thickness of the *i*-th high-refractive index component
d_L	Thickness of low-refractive index component
$(d_L)_i$	Thickness of the *i*-th low-refractive index component
d_{Si}	Thickness of Si component (Si wall)
d_{SiO2}	Thickness of SiO_2 component
d_t	Thickness of additional *t*-layer
f_H	Filling fraction of high-refractive index component
$(f_H)_{min}$	Minimum level of high-refractive index component filling fraction
f_L	Filling fraction of low-refractive index component
f_{Si}	Filling fraction of Silicon
h_{Si}	Etching depth of Silicon walls
I	Intensity
i	Number of the high-refractive index component
N	Number of periods
n_{air}	Refractive index of air component
n_e	Extraordinary refractive index of LC
n_{E7}	Refractive index of nematic liquid crystal E7
n_H	Refractive index of high-refractive index component
n_L	Refractive index of low-refractive index component
n_o	Ordinary refractive index of LC
n_{rand}	Refractive index value for a random orientation of the LC molecules
n_{Si}	Refractive index of Silicon layer
n_{SiO2}	Refractive index of SiO_2 layer
n_t	Refractive index of *t*- layer
m	Order of reflection band/transmission band
$maxf_{Si}$	Maximum value of filling fraction of Si component
porSi	Porous Silicon
Q	Quality factor
R_{PBG}	Minimum reflection level of photonic band gap
R_{cutoff}	Reflection cutoff level
T_{PBG}	Maximum transmission level of photonic band gap
T_{cutoff}	Transmission cutoff level
V	Voltage

Δd_H	Thickness deviation range of high-refractive index component
Δf	Range of filling fraction
ΔNF_{ODB}	Width of omni-directional reflection band in normalized frequency
Δn	Refractive index change
Δn_{E7}	Refractive index change of nematic liquid crystal E7
Δn_{LC}	Birefringence of LC
ΔR	Reflection signal modulation
δ	Standard deviation
δ_i	Relative deviation of the *i*-th high-refractive index component
δd	Thickness deviation
δd_{Hi}	Thickness fluctuation of the *i*-th high-refractive index component
δf_{Si}	Step size of Silicon filling fraction range
θ	Angle of incidence of light
λ_c	Band-pass filter wavelength of operation
λ_m	Stop band/ pass band operational wavelength
λ_s	Channel spacing

Author's Publications

Peer-Reviewed Publications

1. **A. Baldycheva**, V.A. Tolmachev, K. Berwick and T.S. Perova, Multi-channel Si-Liquid Crystal Filter with Fine Tuning Capability of Individual Channels for Compensation of Fabrication Tolerances, *Nanoscale Research Letters*, Vol. 7, pp. 387/1-387/8 (2012).
2. Sergey A. Dyakov, **Anna Baldycheva**, Ekaterina V. Astrova, Tatiana S. Perova, Vladimir A. Tolmachev, Galina V. Fedulova, Viktor Yu. Timoshenko, Sergei G. Tikhodeev, Nikolay A. Gippius, Surface states in the optical spectra of two-dimensional photonic crystals with various surface terminations, *Physical Review B*, Vol. 86, pp. 115126/1-8 (2012).
3. V.A. Tolmachev, **A.V. Baldycheva,** K.Berwick and T.S. Perova, Influence of fluctuations of the geometrical parameters on the photonic band gaps in one-dimensional photonic crystals, *Progress in Electromagnetic Research*, Vol.126, pp. 285-302 (2012).
4. V. A. Tolmachev, V. A. Melnikov, **A. Baldycheva**, T. S. Perova, Fabry-Pérot resonator based on microstructured Si and liquid crystal tunable by electric field, *Progress In Electromagnetics Research*, Vol. 122, pp. 293-309 (2012)
5. **A. Baldycheva**, V. Tolmachev, T. Perova, Y. Zharova, E. Astrova and K. Berwick, Silicon photonic crystal filter with ultrawide passband characteristics, *Optics Letters,* Vol. 36, No. 10 (2011).
6. **A. Baldycheva**, V. Tolmachev, T. Perova and K. Berwick, Formation of infrared regions of transparency in one-dimensional silicon photonic crystals, *IEEE Photonics Technology Letters*, Vol. 23 (4), pp. 200-202 (2011).
7. T. S. Perova, V. A. Tolmachev and A. Baldycheva, Design of three-component one-dimensional photonic crystals with tuning of optical contrast and regions of transparency, *Phys. Stat. Sol. (c)*, Vol. 8(6), pp. 4961-1965 (2011).
8. Yu.A. Zharova, G.V. Fedulova, E. V. Astrova, **A.V. Baldycheva**, V.A. Tolmachev and T.S. Perova, Fabrication technology of heterojunctions in the lattice of a 2D photonic crystal based on macroporous silicon, *Semiconductors,* Vol. 45, Number 8, pp 1103-1110 (2011).

9. V. Tolmachev, **A. Baldycheva**, S. Dyakov, K. Berwick and T. Perova, Optical contrast tuning in three-component 1D Photonic Crystals, *IEEE Journal of Lightwave Technology*, vol. 28, no. 10, pp. 1521-1529 (2010).

10. E.V. Astrova, V.A. Tolmachev, Yu.A. Zharova, G.V. Fedulova, **A. V. Baldycheva** and T.S. Perova, Silicon periodic structures and their liquid crystal composites, *Solid State Phenomena*, Vol. 156-158, pp 547-554 (2010).

Conference Proceedings

1. A. Baldycheva and T. Perova, Si photonic crystal pass-band filters with individual tuning capability, Microscopy Society of Ireland Symposium 2012, *Proceedings of the Microscopy Society of Ireland Annual Symposium 2012*, p. 33, 29-31 August 2012, UCC, Cork, Ireland. (Oral)

2. **A. Baldycheva**, V.A. Tolmachev, T.S. Perova, Fine tunable multi-cavity Si photonic crystal filter, *Photonics Europe 2012, Silicon Photonics VI, SPIE Proceedings*, vol. 84310H/1-13, Brussels, Belgium, 2012. (Oral)

3. V.A. Tolmachev, **A.V. Baldycheva**, T.S. Perova, Electrotunable optical filters based on microstructured silicon infiltrated with liquid crystal for mid-infrared range, *Book of Extended Abstracts of the 8th International Conference on Porous Semiconductors-Science and Technology*, ISBN 978-84-370-7693-5, March 2012, Malaga, Spain.

4. S.D. Dyakov, T.S. Perova, **A.V. Baldycheva**, E.V. Astrova, G.V. Li, S.G. Tikhodeev, N.A. Gippius, Optical properties of two-dimensional photonic crystal bars fabricated by photoelectro-chemical etching of silicon, *Book of Extended Abstracts of the 7th International Conference on Porous Semiconductors- Science and Technology*, ISBN 978-84-370-7693-5, March 2012, Malaga, Spain.

5. **A. Baldycheva**, V.A. Tolmachev, K. Berwick and T.S. Perova, Widely Tunable Photonic Crystal Filters for optical interconnects on Si chip, *SPIE Photonics West*, January 2012, San Francisco, USA. (Oral).

6. **A. Baldycheva**, V. Tolmachev, Yu. Zharova, E. Astrova, K. Berwick and T. Perova, Multi-component band-gap devices for integrated Silicon microphotonics, *Photonics Ireland 2011*, September 7-9, 2011. (*The best poster presentation award*).

7. **A. V. Baldycheva**, V. A. Tolmachev and T. S. Perova, Influence of geometrical dimensions fluctuations on photonic band gap regions for one-dimensional silicon

photonic crystals, *Photonics Ireland 2011*, September 7-9, 2011, Dublin, Ireland. (Poster)

8. S. A. Dyakov, E. V. Astrova, T. S. Perova, V. A. Tolmachev, G. V. Fedulova, **A. Baldycheva**, V. Yu. Timoshenko, S. G. Tikhodeev, N. A. Gippius, Two-dimensional hexagonal photonic crystals for microphotonics application, *Photonics Ireland 2011*, September 7-9, 2011, Dublin, Ireland.
9. S. Dyakov, **A. Baldycheva**, T. Perova, G. Fedulova, E. Astrova, S. Tikhodeev , N. Gippius, Two-dimensional hexagonal photonic crystals for silicon microphotonics, *Proceedings of Intel European Research and Innovation Conference 2011*, 12-14th of October, Intel-Lexlip, Ireland.
10. T. S. Perova, V. A. Tolmachev, and **A. V. Baldycheva**, Electrically tunable Fabry-Perot resonators based on microstructured silicon and liquid crystal, *Photonics Ireland 2011*, September 7-9, 2011, Dublin, Ireland.
11. **A. Baldycheva**, T. Perova, E. V. Astrova, V. A. Tolmachev, S. A. Dyakov, Yu. A. Zharova, G. V. Fedulova, V. Yu. Timoshenko, S. G. Tikhodeev, N. A. Gippius, FT-IR Microspectroscopy for Development and Optimization of in-plane Silicon Microresonators based on 1D and 2D Photonic Crystals, *Proceedings of the Microscopy Society of Ireland Annual Symposium*, p. 33, 24-26 August 2011, CRANN, Trinity College Dublin, Ireland. (Oral)
12. **A. Baldycheva**, V.A. Tolmachev, Yu. A. Zharova, G. V. Fedulova, E. V. Astrova and T.S. Perova, Si micro-resonators realized in 1D and 2D photonic crystal structures, *2011 SPIE Europe Conference "Optical Metrology"*, Munich, Germany, 23-26 May 2011, EOM 8083-52. (Oral presentation only).
13. **A. Baldycheva**, V. Tolmachev, T. Perova, K. Berwick, Yu. Zharova and E. Astrova, Design, fabrication and Optical Characterization of Multi-Component Photonic Crystals for Integrated Si Microphotonics, *Silicon Photonics VI SPIE Proceedings*, vol. 7943, 79430F, San Francisco, USA, 2011. (Oral)
14. V. Tolmachev, T. Perova and **A. Baldycheva**, Transformation of one-dimensional silicon photonic crystal into Fabry-Pérot resonator, *Silicon Photonics VI SPIE Proc.*, vol.7943, 79430E, San Francisco, USA, 2011.
15. S. Dyakov, E. Astrova, V. Tolmachev, G. Fedulova, T. Perova, **A. Baldycheva**, V. Timoshenko, S. Tikhodeev and N. Gippius, Optical spectra of two-dimensional

photonic crystal bars based on macroporous Si, *Silicon Photonics VI SPIE Proc.*, vol. 7943, 79431I, San Francisco, USA, 2011.

16. **A. Baldycheva**, T. Perova, V. Tolmachev, Y. Zharova, Fabrication and Optical Properties of Three-Component Silicon Photonic-Crystal Filters, *Book of abstract: Intel European Research and Innovation Conference 2010*, 12-14^{h} of October 2010, Intel-Lexlip, Ireland, p. 82, B7, 2010 (Poster).
17. **A. Baldycheva,** T. Perova**,** Wide-band filter based on three-component silicon photonic crystals, Book of abstracts: *INSPIRE-ICGEE School "Fabrication to Application"*, Tyndall National Institute, October 5 – 7th 2010, Cork, Ireland, p.82, 2010. (Best poster presentation)
18. **A. Baldycheva**, T. Perova, and V. Tolmachev, Three-component one-dimensional silicon photonic crystals with regions of transparency, *Abstract Book of The X International Conference on "Nanostructured Materials" (NANO 2010),* September 13-17, Rome, Italy, p.80, Poster-Tu-28, 2010. (Poster)
19. **A. Baldycheva**, Design, fabrication and investigation of 1D and 2D photonic crystals based on Si, *ICGEE Workshop,* 31 August 2010, Galway, Ireland. (Oral)
20. **A. Baldycheva**, T. Perova, V. Tolmachev, IR Microspectroscopy for Investigation of Silicon-Liquid Crystal Photonic Crystals, Proceedings of the *Microscopical Society of Ireland and the Northern Ireland Biomedical Engineering Society Joint Annual Symposium*, 25th-27th August 2010, University of Ulster, Northern Ireland, United Kingdom. (Oral)
21. S. Dyakov, **A. Baldycheva**, T. Perova, E. Astrova and S. Tikhodeev, Optical properties of two-dimensional photonic crystal bars obtained by photoelectrochemical etching of silicon, Proceedings of the *Microscopical Society of Ireland and the Northern Ireland Biomedical Engineering Society Joint Annual Symposium*, 25th -27th August 2010, University of Ulster, Northern Ireland, United Kingdom.
22. V.A. Tolmachev, T.S. Perova, V.A. Melnikov and **A.V. Baldycheva**, Fabry-Pérot microresonators on silicon chip for infrared range 1-10 um, *14th International Conference "Laser Optics 2010"*, June 2010, St. Petersburg, Russia.
23. **A. V. Baldycheva**, V. A. Tolmachev, T.S. Perova and K. Berwick, Design of three-component one-dimensional photonic crystals for alteration of optical contrast and omni-directional reflection, *Photonics Europe 2010, Photonic Crystals Materials and Devices IX, Proceedings of SPIE*, Vol. 7713, 771321, 2010.

24. V. A. Tolmachev, V. A. Melnikov, **A. V. Baldycheva**, T.S. Perova and G. I. Fedulova, Design, fabrication and optical characterization of Fabry-Pérot tunable resonator based on microstructured Si and liquid crystal, *Photonics Europe 2010, Photonic Crystals Materials and Devices IX, Proceedings of SPIE,* Vol. 7713, 771320, Brussels, Belgium, 2010.

25. S.A. Dyakov, S.G. Tikhodeev, E.V. Astrova, V.A. Tolmachev, G.V.Fedulova, T.S. Perova, **A. Baldycheva** and V.Yu. Timoshenko, Investigation of optical properties of two-dimensional photonic crystals by means of the scattering matrix method, *Photonic Crystals Materials and Devices IX, SPIE Europe*, May 2010, Brussels, Belgium.

26. T. S. Perova, V. A. Tolmachev and **A. V. Baldycheva**, Design of three-component one-dimensional photonic crystals with tuning of optical contrast and regions of transparency, *Book of Extended Abstracts of the 7th International Conference on Porous Semiconductors- Science and Technology*, ISBN 978-84-370-7693-5, March 2010, Valencia, Spain.

27. Yu.A. Zharova, G.V. Fedulova, **A.V. Baldycheva**, V.A. Ermakov, Influence of Si wall roughness on optical characteristics of 1d PC, *Proceedings of the International conference "Optics-2009"*, Saint-Petersburg, 19-23 October 2009, p.152.

28. T.S. Perova, **A.V. Baldycheva**, V.A. Melnikov, E.V. Astrova, V.A. Tolmachev, G.V. Fedylova and Yu.A. Zharova, Optical Characterisation of one-dimensional photonic crystals manufactured by electrochemical and dry etching, *Book of abstracts: Photonics Ireland – 2009*, 14-16 September, Kinsale, Ireland, p. A41.

29. **A.V. Baldycheva**, V.A. Tolmachev, S.A. Dyakov, T.S. Perova, and K. Berwick, Tuning of the optical contrast in three-component one-dimensional photonic crystals, *Book of abstracts: Photonics Ireland – 2009*, 14-16 September, Kinsale, Ireland, p. B57.(Best Student Poster Presentation Award)

30. **A. Baldycheva**, T. Perova, V. Tolmachev, E. Astrova, G. Fedulova and Y. Zharova, Characterization of One-dimensional Photonic Crystals Fabricated by Wet and Dry Etching, *Book of Conference Abstracts: Intel European Research and Innovation Conference 2009*, 8-10th of September, Intel-Lexlip, Ireland, p. 79. (Poster)

31. V. Ermakov, **A. Baldycheva,** T. Perova, V. Tolmachev, E. Astrova, G. Fedulova, and Yu. Zharova, AFM and FTIR micro-spectroscopy analysis of two-dimensional silicon photonic crystals, *Proceeding of the 33rd Annual Symposium of Microscopical Society of Ireland*, 26-28 August, 2009, Dublin, p.44.

32. V.A. Tolmachev, **A.V. Baldycheva**, E.Yu. Krutkova, T.S. Perova and K. Berwick, Optical characteristics of a one-dimensional photonic crystal with an additional regular layer, *Proceedings of SPIE,* Vol. 7390 739017-1, Munich, Germany, 2009. (Poster)

33. E.V. Astrova, V.A. Tolmachev, G.V. Fedylova, V. A. Melnikov, **A. Baldycheva** and T.S. Perova, Optical Properties of One-dimensional Photonic Crystals Fabricated by Electrochemical Etching of Silicon, *Proceedings of the 5th Kurt Schwabe Symposium May 24 - 28, 2009*, Erlangen, Germany, p. 49.

Chapter 1.

Introduction

It is now one-half century since the advent of the solid state electronics with the invention of the transistor. The semiconductor revolution, which is still continuing, enabled profound and unanticipated improvements in our standard of living. Advances in semiconductor physics have had a profound impact on all aspects of society transforming the way people work, live, learn and communicate [1]. The resultant explosion in information technology is based on the ability to control the flow of electrons in a semiconductor in the most intricate ways.

What is known today as a technology shrink has increased computational speed due to a shorter gate width, increased functionaltity through higher levels of integration and decreased costs by processing more transistors/chip and more chips/wafer. The key driving forces for the Silicon electronics technology roadmap is a high speed and functionality at low cost. In the last three decades, this performance level has increased exponentially with rates of more than 100/decade. This has led to increasingly difficult problems in communication between computer boards, chips and even individual chip components as well as the integration of optics and microelectronics. These problems create an interconnect bottleneck which is a 'grand challenge' to be overcome by the semiconductor industry according to the ITRS (International Technology Roadmap for Semiconductors).

The invention of the laser in the nineteen sixties inspired the photonics industry, thus enhancing the transmission of information by replacing electronic signals in wires with laser pulses in optical fibres. The alternative interconnect technology can be Silicon based optical interconnects, which can efficiently deal with large bandwidths of information and is not limited by resistance, capacitance and reliability constraints of metal lines. In particular, the incorporation of optical components on a Silicon chip

would provide a new platform for the monolithic integration of optics and microelectronics and open doors to new technologies. However, the difficulty in controlling light and diverting its path on Silicon need to be addressed before this technology can be successfully used to resolve current microelectronics interconnect bottlenecks [2]. Investigation of solutions to the interconnect bottleneck has stimulated much research into actively controlling and manipulating the propagation of light through materials. Along this course of technological progress there has been much interest in the development of a photonic analogue to the electronic semiconductor. This requires the design and fabrication of photonic materials that can control and manipulate light on a microscopic scale [3]. This research has led to the development of photonic crystals (PhCs) or Photonic Band Gap (PBG) materials, structures which prohibit the propagation of certain wavelength ranges of light in certain directions depending on their physical properties.

1.1 Photonic Crystals

Since the invention of the laser, progress in Photonics has been intimately related to the development of optical materials which allows one to control the flow of electromagnetic radiation or to modify light matter interaction. Photonic Crystals are a novel class of the optical materials which elevates this principle to a new level of sophistication [1]. The PhCs are materials with a periodic modulation (translational symmetry) of the dielectric constant. This modulation gives rise to what is known as a Stop Band (SB), or a Photonic Band Gap within the crystal [4, 5]. The easiest way to understand the PBG effect is to rely on an analogy with natural crystals, which is a periodic repeated arrangement of atoms and molecules in space. A crystal therefore presents a periodic potential to electron propagation through it, and the geometry of the crystal dictates the energy band structure of the crystal, so that (due to Bragg-like diffraction from the atoms) electrons are forbidden to propagate with certain energies in the certain directions. For example, a semiconductor has a band gap between the valence and the conduction energy bands.

The PhCs are the artificial optical analogy of the natural crystals, in which the periodic "potential" is due to a lattice of microscopic dielectric media instead of atoms. If the dielectric constants of the materials in the crystal are different enough, and the absorption of light by the material is minimal, then scattering at the interfaces can

produce many of the same phenomena for the photons (light modes) as the atomic potential does for electrons [3].

The benefits of such a photonic band gap for direct-gap semiconductors are illustrated in Figure 1-1. On the right-hand side is a plot of the photon dispersion (frequency versus wavevector). On the left-hand side, sharing the same frequency axis is a plot of the electron dispersion, showing conduction and valence bands appropriate to a direct-gap semiconductor. Since atomic spacings are 100 times shorter than optical wavelengths, the electron wavevector must be devided by 1000 in order to fit on the same graph with the photon wavevector. The dots in the conduction and valence bands are meant to represent electrons and holes respectively.

If an electron were to recombine with a hole, they would produce a photon at the electronic band-edge energy. As illustrated in Figure 1-1, if a photonic band gap overlaps the electronic band edge, then the photon produced by electron-hole recombination would have no place to go [6].

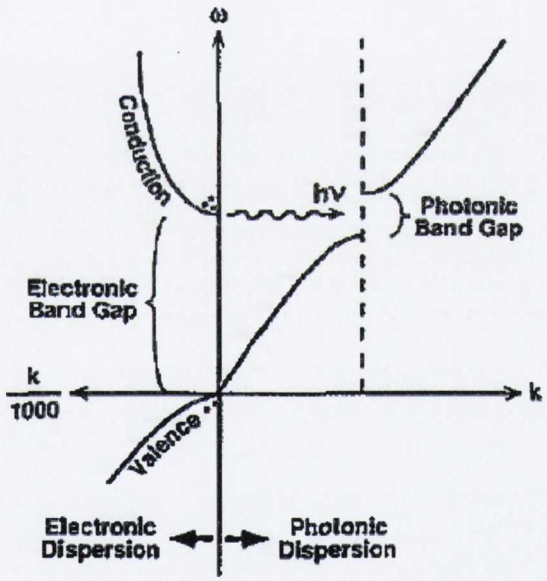

***Figure 1-1**: On the right is the electromagnetic dispersion, with a forbidden gap at the wavevector of the periodicity. On the left is the electron wave dispersion typical of a direct-gap semiconductor, the dots representing electrons and holes. Since the photonic band gap straddles the electronic band edge, electron-hole recombination into photons is inhibited. The photons propagation is prohibited [6].*

Depending on the number of directions that the SB (or PBG) exists in, there are one-dimensional, two-dimensional and three-dimensional photonic crystals (Figure 1-

2). If, for some wavelength range, a photonic crystal reflects light of any polarization incident at any angle, then the crystal has a complete photonic band gap (or omni-directional band gap). Only a 3D periodicity, with a more complex topology than is shown here, can support a complete photonic band gap. However, over the last decade, the focus of research groups has returned to 1D PhCs, due to their unique property to possess an omni-directional reflection, i.e. the presence of highly reflective bands over a wide range of angles of incidence and for both polarizations of light [7-9].

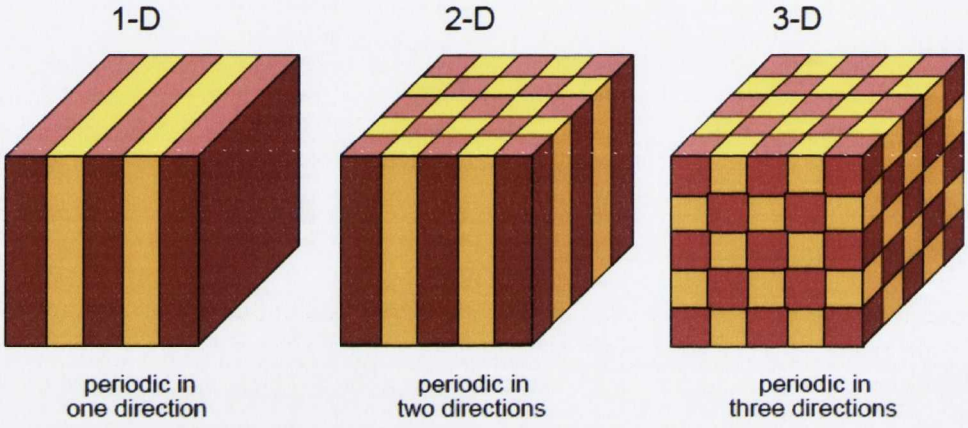

***Figure 1-2**: Simple examples of one-, two-, and three-dimensional photonic crystals. The different colors represent materials with different dielectric constants. The defining feature of a photonic rystal is the periodicity of material along one or more axes [3].*

1.2 Si based Photonic Crystal devices

Recent advances in nano-, micro- and submicron-structuring technology provide an enormous flexibility in the choice of material composition, lattice periodicity and symmetry of the period arrangements allowing one to fabricate multi-dimensional PhCs operating in a wider range of electro-magnetic waves. For example, a PhC of a given geometry with millimeter dimensions can be constructed for control of microwave radiation, while with micron dimensions for control of infrared radiation. In this regard Silicon is the most attractive optical material from the variety of other different suitable materials mainly due to its transparency in the Near Infrared (NIR) range for both 1.3 and 1.55 μm telecommunication wavelengths as well as in the middle-infrared (MIR) and long-wave infrared ranges up to 100 μm. The success in the development of the in-plane light emitters and other microphotonics elements based on

monocrystalline Si, made the realization of all-Silicon optoelectronic circuits to be possible [10]. The term of "*Silicon microphotonics*" was first introduced by Lionel C. Kimerling in Ref. [11]. Briefly, the Si microphotonics is the optical equivalent of micro-electronics for integrated circuits. It enables interconnection bandwidth that is not limited by the resistance, capacitance and reliability constraints of metal lines.

Modern Si fabrication technology allows fabrication of the PhC structures on nano-, micro-scale and of all dimensions on a single integrated platform. Examples of in-plane PhC realized on Si substrate are demonstrated in Figure 1-3.

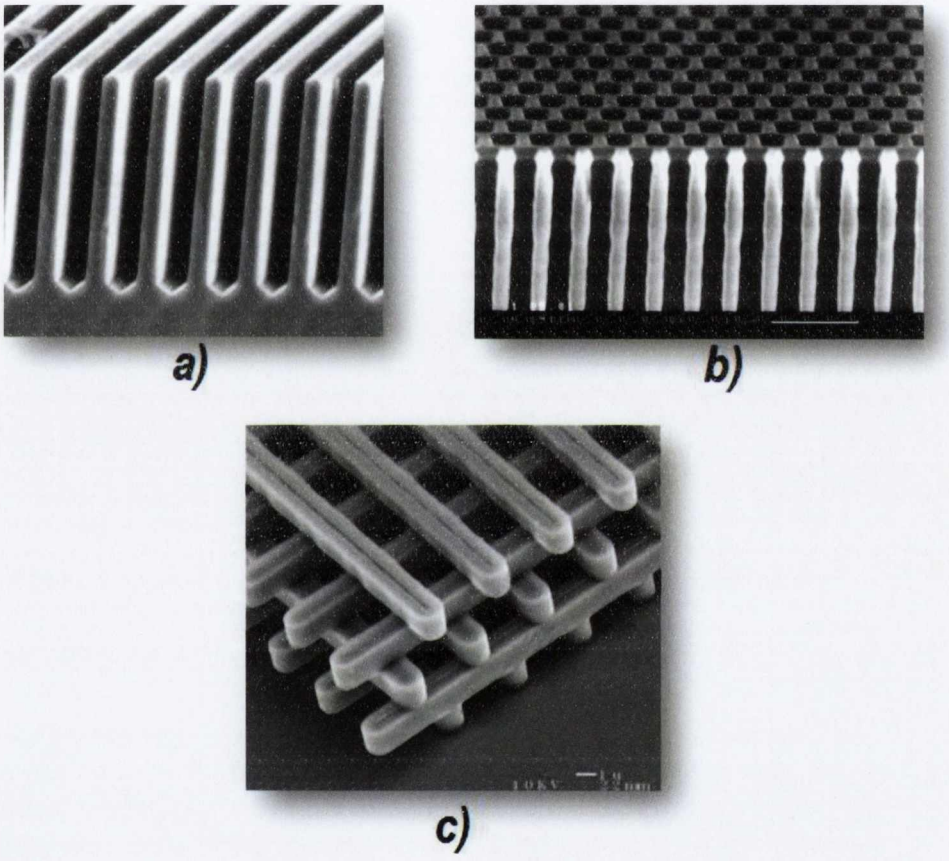

Figure 1-3: *SEM images of PhCs on Si platform: a) one-dimensional periodicity porous Silicon Bragg mirrors fabricated by vertical anisotropic etching of Silicon [12]; (b) two-dimensional hexagonal porous Si structure fabricated by anodization of p-type Silicon [12]; (c) three-dimensional Silicon photonic crystal woodpile structure fabricated by successive multiple masking-etching-alignment steps [13].*

The Si-based photonic crystal structures have provided a good platform for numerous opto-electronic devices with applications in optical interconnects, chemical- and bio-sensing and etc. Below are some examples of utilization of 1D and 2D photonic crystals based on Silicon:

- ***Photonic crystal waveguides***, obtained by realization of line defect within perfect periodical PhC structure [13]:
    - 2D-in-1D hybrid photonic crystal waveguide device fabricated by dry etching of Silicon (Figure 1-4) [18];

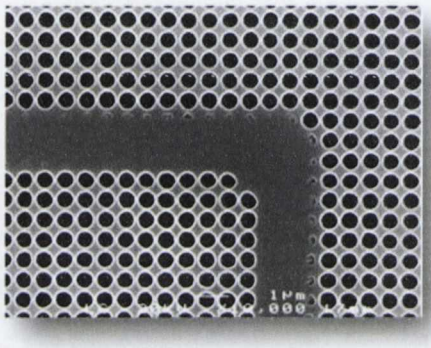

Figure 1-4: *2D-in-1D PhC waveguide for the measurements at 90° [18].*

- Hollow waveguide with multilayer pairs of Si/SiO_2 coated on Si substrate (Figure 1-5) [19];

Figure 1-5: *a) Schematic structure of hollow waveguide; b) SEM image of cross-section of hollow waveguide [19].*

- ***Photonic crystal fibres.*** The total internal reflection phenomenon in photonic crystal fibres achieved by forming a two-dimensional photonic crystal around a hollow or Silica core [14, 15];
- ***Photonic Crystal Microresonators,*** realized by introduction of the defects/cavities within regular periodical structure [16, 17];
    - Microresonators based on nano-, meso-porous Si 1D photonic crystal with defects [20] (Figure 1-6);

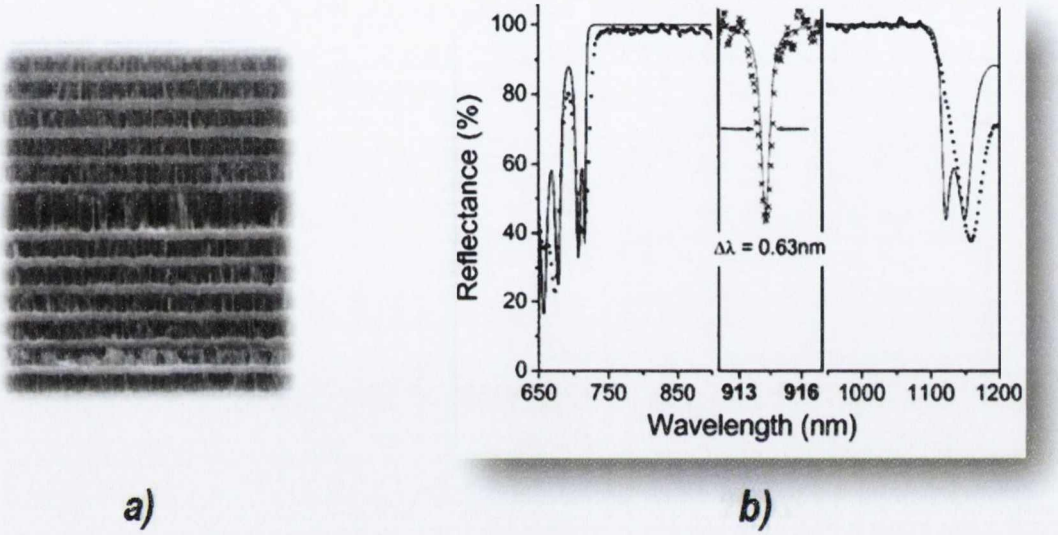

Figure 1-6: *(a) SEM image of a Porous Silicon microcavity. (b) Resonance peak realized within the PBG at 0.63 nm [20].*

- Microresonators based on macro-porous Silicon 2D photonic crystal with point defect [16] (Figure 1-7(a)) ;
- Microresonators based on photonic crystal waveguides with defect/cavities [21] (Figure 1-7 (b));

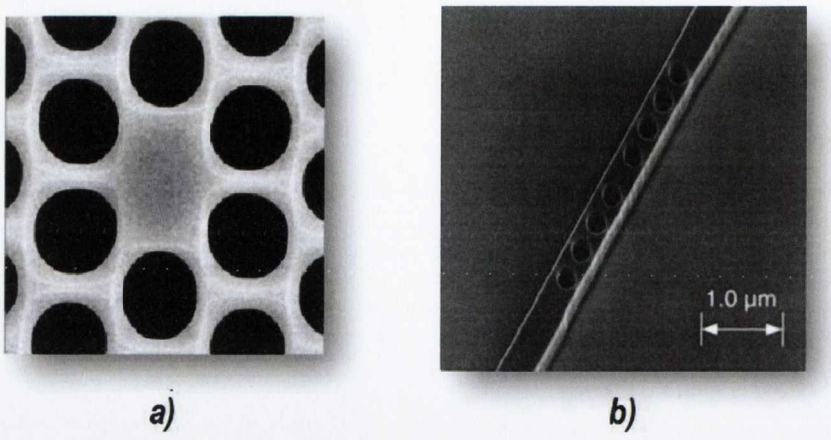

Figure 1-7 : *A point defect (cavity) realized in (a) macro-porouse Silicon photonic crystal [16] and (b) in photonic crystal waveguide fabricated by X-ray lithography [21].*

- Microresonators based on grooved-Silicon 1D PhC, fabricated by means of e-beam lithography and dry etching of Silicon [22] (Figure 1-8);

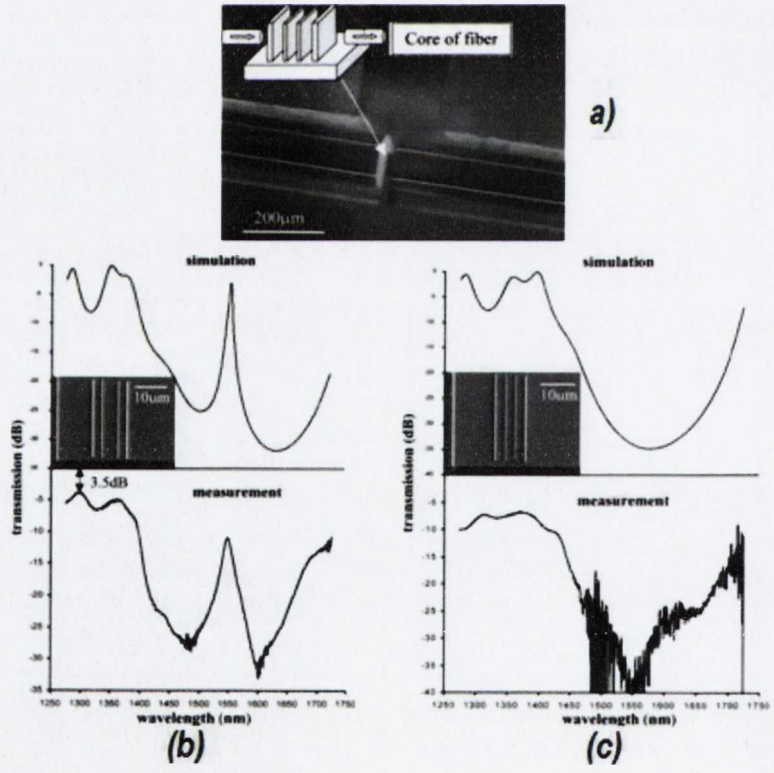

Figure 1-8: *(a) Optical image of the "fiber-photonic crystal-fiber" system; (b) Microresonators based on 1D PhC with defect; (c) Mirror based on 1D PhC [22].*

1.3 *Tunable Photonic Crystal Devices*

One of the most important functions of the integrated Si-based photonic devices is the tuning capability of the optical characteristics by application of the electric field or by changing the temperature. The ability to modify the parameters of PBGs and resonances in a controllable way after PhC fabrication is a desirable property. The PBG parameters, e.g. bandwidth and wavelength of operation, depend on the structure of the crystal and on its constituent materials. The large variety of promising applications of photonic crystals depends on many adjustable parameters [1]. For the Si based PhCs the tuning of the optical properties can be achieved by either varying the optical thickness of Si/filler materials or by changing the geometrical parameters of the structure. If we can externally alter the materials and/or the structure during the device operation, we have an actively tunable PhC device (Figure 1-9). For example, in Si-based 1D and 2D PhCs the refractive index of Si can be altered by varying the temperature and the donor concentration, through the variations of the free carrier concentration [23].

In paper [24] the tuning of Silicon refractive index was experimentally demonstrated by injection of free carriers with 800 nm, 300 fs pulses, which allows ultra-fast band-edge tuning of 2D Si PhC. Also, the injection of free-carriers at any point of the p-i-n/cavity region can be used for the ultra-fast modulation of light in the waveguide [2]. Although, this method provides ultra-fast operation of the device (~ 1nsec), the associated relative spectral shift is very small, as the refractive index changes $|\Delta n|$ are below 10^{-3}.

Alternatively, the refractive index of Silicon can be tuned by changing the temperature. In work [25] this effect was utilized in the optical filter based on 1D Si PhC fabricated by deep reactive ion etching. However, as for the previous tuning examples, the relative spectral shift is limited to the maximum variation of Si refractive index.

Microelectromechanical systems (MEMS) technology provides an attractive approach to provide the mechanical tuning mechanism, thus enabling a low-cost highly integrated tunable PhC filter. By varying the geometrical parameters of the PhC devices, e.g. filling fraction and size of the cavities, the precise position of the PBGs, band edges and/or resonances can be tuned or switched ON/OFF [1, 26-28]. The mechanical movement is controlled by either simple digital electronics or by means of the electrostatic deflection. However, current MEMS technology is capable of

producing mechanical devices that are on the scale of 10 to 500 μm [29], which limits the maximum tunability of the device.

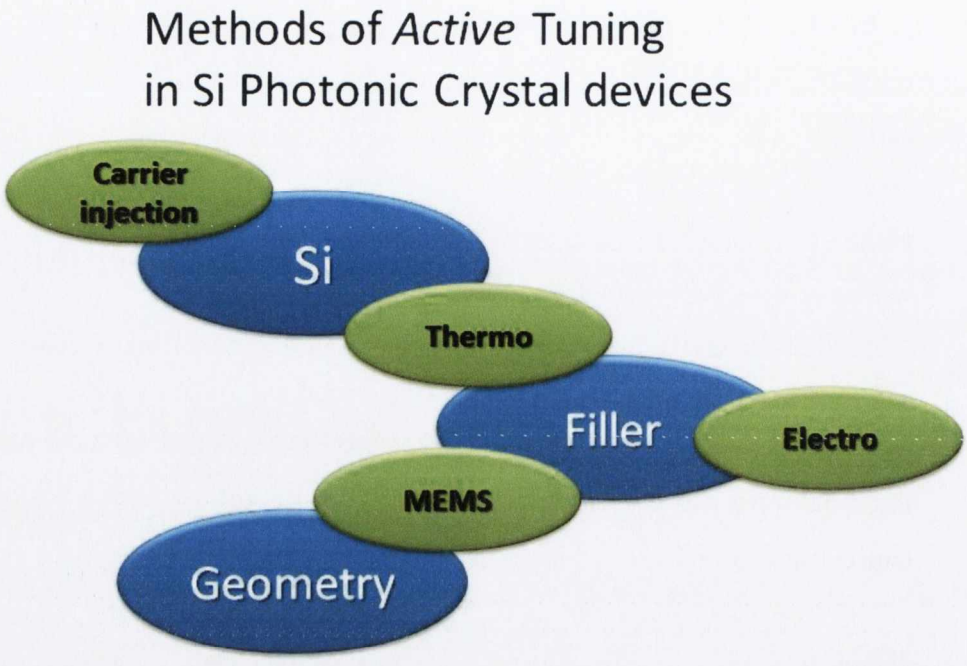

Figure 1-9: *Methods of active tuning (green) and correspondent parameters of tuning (blue) that can be realized in Si based Photonic Crystal devices.*

Significantly wider tunability can be achieved for the non-mechanical design of composite PhC devices, based on Silicon and various filler-materials that can change their optical characteristics by changing temperature or applying the electric field. In this regard, the most promising filler-material is considered to be liquid crystal (LC) with its extraordinary optical properties. Firstly, LCs show large optical birefringence in which molecular reorientations can be induced by low power electric fields. Secondly, the LCs possesses high transparency, low absorption and scattering losses in a wide wavelength range span from visible to middle infrared. One of the disadvantages of the exisiting up to date commercial nematic LC, suitable for this purpose, is a slow response time. However, recently the MEMS-driven tuning of the liquid crystal fillers was demonstrated providing much shorter response time than using temperature and electric field [30]. A brief introduction and background of tunable LC-infiltrated photonic crystals are reviewed in the following Section.

1.4 Photonic Crystals and their liquid crystal composites

Liquid crystals combine fluid behaviour and anisotropic properties in a unique way. Anisotropy, i.e. the dependence of bulk material properties on the crystallographic direction, indicates non-spherical symmetry of the corresponding material. This phenomenon is traditionally attributed to solid crystals. However, organic compounds that consist of molecules with anisotropy of shape (for example rod-like or disk-like) can show an orientational order of these molecules even in a fluid state. If so, this fluid state is referred to as being the liquid crystalline state. Thermotropic, calamatic LCs consist of rod-like organic molecules which form mesophases. These mesophases exist between the conventional crystalline phase and the isotropic liquid phase (Figure 1-10).

The most common LC mesophase is the *nematic* which is characterized by uniaxial orientational order, i.e. one preferred axis is sufficient to describe its local anisotropy. The director $\boldsymbol{N}$ (a pseudo vector) can be used to indicate the local molecular alignment and a scalar order parameter S is sufficient to describe the degree of orientational order [1, 31].

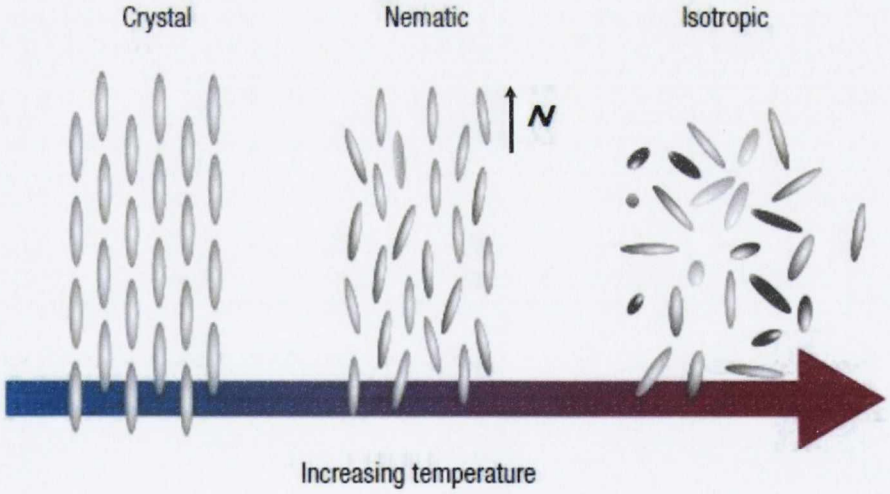

Figure 1-10: *The nematic liquid crystal mesophase has an orientational order, but lacks of a long-range positional order, and exists between the crystalline and isotropic phases.* $\boldsymbol{N}$ *is the nematic director [32].*

The most important anisotropic property from the optical point of view is *birefringence*. The effective refractive index for linear polarized light with the direction of the electric field vector perpendicular to the director (ordinary refractive index n_o) is

different from the effective value for polarized light with the direction of electric field vector parallel to the director (extraordinary refractive index n_e). The difference between these two effective refractive indexes is called birefringence of LC, $\Delta n_{LC} = n_e - n_o$, and can be as large as 0.3. The birefringence of thermotropic LC $\Delta n_{LC} = n_e - n_o$ decreases with increasing temperature (decreasing orientational order) and vanishes above the nematic-isotropic transition temperature (clearing temperature for nematic LC).

There are numerous publications devoted to experimental investigations of the electro-tuning effect in LC photonic structures such as LC-opal composite structures [33-35], micro-porous "*Si-LC*" structures [36, 37] and multilayered 1D PhC with liquid crystal cavity [38] which manipulate with light propagating perpendicular to the substrate. The number of papers dealing with the molding of in-plane light propagation is relatively small and these mainly present the results on the thermo-tuning effect in 1D and 2D PhCs. One of the main reasons for that is the difficulty with the application of an electric field to the matrices based on electro-conductive materials. Also, the response time for the nematic LC is in the range of milliseconds, which makes the LC material not very suitable for optical interconnect applications.

However, today, "*Si-LC*" based photonic research is undergoing a modern-day renaissance. For example, bio-sensors fabricated with LC and Si materials can allow label-free observations of biological phenomena. Moreover, as it will be demonstrated in Chapter 4, the continuous electro-tunability of LC filler in the optical devices based on PhC may be used for compensation of the post-fabrication tolerances and, thus, adjustment of the optical device to its nominal operational mode.

1.5 Thesis Overview

Chapter 1: An introduction to Photonic Crystals and their application in integrated Silicon photonics is presented. The contexts in which this body of work was performed and the motivation behind the studies contained therein are outlined.

Chapter 2: The basic concepts of theoretical and experimental background are introduced. A classic model of 1D PhC is described for the grooved Silicon case. The methods used for fabrication of the grooved Silicon structures in this work are

discussed. The optical experimental techniques applied to the investigation of the fabricated structures are described.

Chapter 3: In this Chapter, the design of a new type of 1D Si PhC based on multi-component model is described. The fabrication techniques for realization of multi-component PhCs by introduction of additional regular layers into a grooved Silicon structure are discussed. The novel optical effects such as omni-directional PBGs and ultra-wide regions of transparency have been obtained for the suggested model. Based on the obtained results the band-pass filter based on three-component PhC structure was fabricated and successfully examined experimentally in Mid-IR.

Chapter 4: The model of transformation of defect-free photonic crystal structures into tunable Fabry-Perot resonators on Si chip is theoretically described and experimentally demonstrated. The transformation is achieved by introduction of the optical defects into certain periods of grooved Silicon structures. The ultra-wide and electro-controllable tunability is experimentally demonstrated for the Fabry-Perot filters based on Si and nematic liquid crystal. Furthermore, a technique for precise position control of individual transmission resonances/channels in a triple Fabry-Perot filter is also proposed.

Chapter 5: An approach for investigation of the photonic band gap deviations caused by structural fluctuations in fabricated one-dimensional photonic crystals is demonstrated. The deviations of the photonic band gaps are strongly dependant on the magnitude of the structural fluctuations and demonstrate an increase with the order of the photonic band gaps. The approach is proposed for the determination of the fabrication tolerances and optimization of the photonic band gap properties of the fabricated photonics crystal structures.

Chapter 6: Finally conclusions and future work are drawn.

1.6 References

[1] K. Busch, [Photonic Crystals: Advances in Design, Fabrication, and Characterization] Wiley-VCH, (2004).

[2] M. Lipson, "Switching light on a silicon chip," Optical Materials, 27(5), 731-739 (2005).

[3] J. D. Joannopoulos, [Photonic Crystals: Molding The Flow Of Light] Princeton University Press, (2008).

[4] E. Yablonovitch, "Inhibited Spontaneous Emission in Solid-State Physics and Electronics," Physical Review Letters, 58(20), 2059-2062 (1987).

[5] S. John, "Strong localization of photons in certain disordered dielectric superlattices," Physical Review Letters, 58(23), 2486-2489 (1987).

[6] E. Yablonovitch, "Photonic band-gap crystals," Journal of Physics: Condensed Matter, 5(16), 2443 (1993).

[7] D. N. Chigrin, A. V. Lavrinenko, D. A. Yarotsky *et al.*, "Observation of total omnidirectional reflection from a one-dimensional dielectric lattice," Applied Physics A: Materials Science & Processing, 68(1), 25-28 (1999).

[8] P. S. J. Russell, S. Tredwell, and P. J. Roberts, "Full photonic bandgaps and spontaneous emission control in 1D multilayer dielectric structures," Optics Communications, 160(1–3), 66-71 (1999).

[9] Y. Fink, J. N. Winn, S. Fan *et al.*, "A Dielectric Omnidirectional Reflector," Science, 282(5394), 1679-1682 (1998).

[10] T. Trupke, J. Zhao, A. Wang *et al.*, "Very efficient light emission from bulk crystalline silicon," Applied Physics Letters, 82(18), 2996-2998 (2003).

[11] L. C. Kimerling, "Silicon microphotonics," Applied Surface Science, 159–160, 8-13 (2000).

[12] V. Tolmachev, L. Granitsyna, E. Vlasova *et al.*, "One-dimensional photonic crystal obtained by vertical anisotropic etching of silicon," Semiconductors, 36(8), 932-935 (2002).

[13] J. T. Londergan, J. P. Carini, and D. P. Murdock, [Binding and Scattering in Two-dimensional Systems: Applications to Quantum Wires, Waveguides, and Photonic Crystals] Springer, (1999).

[14] J. C. Knight, T. A. Birks, P. S. J. Russell *et al.*, "All-silica single-mode optical fiber with photonic crystal cladding," Optics Letters, 21(19), 1547-1549 (1996).

[15] P. S. J. Russell, "Photonic-Crystal Fibers," J. Lightwave Technol., 24(12), 4729-4749 (2006).

[16] F. Müller, A. Birner, U. Gösele *et al.*, "Structuring of Macroporous Silicon for Applications as Photonic Crystals," J. of Porous Materials, 7(1), 201-204 (2000).

[17] A. Birner, A. P. Li, F. Müller *et al.*, "Transmission of a microcavity structure in a two-dimensional photonic crystal based on macroporous silicon," Materials Science in Semiconductor Processing, 3(5–6), 487-491 (2000).

[18] C.-O. Cho, Y.-G. Roh, Y. Park *et al.*, "Towards nano-waveguides," Current Applied Physics, 4(2–4), 245-249 (2004).

[19] S.-S. Lo, M.-S. Wang, and C.-C. Chen, "Semiconductor hollow optical waveguides formed by omni-directional reflectors," Opt. Express, 12(26), 6589-6593 (2004).

[20] P. J. Reece, G. Lerondel, W. H. Zheng *et al.*, "Optical microcavities with subnanometer linewidths based on porous silicon," Applied Physics Letters, 81(26), 4895-4897 (2002).

[21] J. S. Foresi, P. R. Villeneuve, J. Ferrera *et al.*, "Photonic-bandgap microcavities in optical waveguides," Nature, 390(6656), 143-145 (1997).

[22] L. Chen, Y. Suzuki, and G. E. Kohnke, "Integrated platform for silicon photonic crystal devices at near-infrared wavelengths," Applied Physics Letters, 80(9), 1514-1516 (2002).

[23] A. S. Sanchez, and P. Halevi, "Simulation of tuning of one-dimensional photonic crystals in the presence of free electrons and holes," Journal of Applied Physics, 94(1), 797-799 (2003).

[24] S. W. Leonard, H. M. van Driel, J. Schilling *et al.*, "Ultrafast band-edge tuning of a two-dimensional silicon photonic crystal via free-carrier injection," Physical Review B, 66(16), 161102 (2002).

[25] Y. Sung-Sik, and L. Jong-Hyun, "A micromachined in-plane tunable optical filter using the thermo-optic effect of crystalline silicon," Journal of Micromechanics and Microengineering, 13(5), 721 (2003).

[26] A. Lipson, and E. M. Yeatman, "Low Loss Tunable Optical Filter using Silicon Photonic Band Gap Mirrors," Solid-State Sensors, Actuators and Microsystems Conference Proceedings, 1445-1448 (2007).

[27] W. Zhou, D. M. Mackie, M. Taysing-Lara *et al.*, "Novel reconfigurable semiconductor photonic crystal-MEMS device," Solid-State Electronics, 50(6), 908-913 (2006).

[28] S. Rajic, J. L. Corbeil, and P. G. Datskos, "Feasibility of tunable MEMS photonic crystal devices," Ultramicroscopy, 97(1–4), 473-479 (2003).

[29] W. R. Jamroz, R. V. Kruzelecky, and E. I. Haddad, [Applied Microphotonics] CRC Taylor & Francis, (2006).

[30] D. Erickson, D. Sinton, and D. Psaltis, "Optofluidics for energy applications," Nature Photonics, 5(10), 583-590 (2011).

[31] R. B. Wehrspohn, H. S. Kitzerow, and K. Busch, [Nanophotonic Materials: Photonic Crystals, Plasmonics, and Metamaterials] John Wiley & Sons, (2008).

[32] S. J. Woltman, G. D. Jay, and G. P. Crawford, "Liquid-crystal materials find a new order in biomedical applications," Nat Mater, 6(12), 929-938 (2007).

[33] D. Kang, J. E. Maclennan, N. A. Clark *et al.*, "Electro-optic Behavior of Liquid-Crystal-Filled Silica Opal Photonic Crystals: Effect of Liquid-Crystal Alignment," Physical Review Letters, 86(18), 4052-4055 (2001).

[34] Q. B. Meng, C. H. Fu, S. Hayami *et al.*, "Effects of external electric field upon the photonic band structure in synthetic opal infiltrated with liquid crystal," Journal of Applied Physics, 89(10), 5794-5796 (2001).

[35] E. Graugnard, J. King, S. Jain *et al.*, "Electric-field tuning of the Bragg peak in large-pore TiO_2 inverse shell opals," Physical Review B, 72(23), 233105 (2005).

[36] S. M. Weiss, and P. M. Fauchet, "Electrically tunable porous silicon active mirrors," physica status solidi (a), 197(2), 556-560 (2003).

[37] G. Pucker, A. Mezzetti, M. Crivellari *et al.*, "Silicon-based near-infrared tunable filters filled with positive or negative dielectric anisotropic liquid crystals," Journal of Applied Physics, 95(2), 767-769 (2004).

[38] R. Ozaki, H. Moritake, K. Yoshino *et al.*, "Analysis of defect mode switching response in one-dimensional photonic crystal with a nematic liquid crystal defect layer," Journal of Applied Physics, 101(3), 033503-6 (2007).

Chapter 2.
Theoretical and Experimental Background

2.1 Introduction

In this Chapter, the basic concepts of the simulation, and experimental fabrication and characterization techniques employed to study the optical properties of the in-plane grooved Silicon photonic crystal structures are discussed. The design of one-dimensional photonic crystals and the analysis of their optical properties have been performed using transfer matrix [1] and forbidden gap map (GM) methods [2]. The GM method is one of the most powerful design methods since it can be applied to modelling of PhCs with any possible geometrical configurations, e.g. PhCs with defects [3], disordered PhCs [4], multi-component PhCs [5] and others, providing the optimal design parameters using a single graphical representation. For the fabrication of grooved Silicon structures two etching techniques were employed: Wet Anisotropic Etching (WAE) of (110)Si in an aqueous solution of potassium hydroxide (KOH) and Deep Reactive Ion Etching (DRIE) of (100)Si. WAE produces good quality smooth mirror like side-walls which is important for obtaining PBGs with high reflection. However, WAE can only be performed on (110)Si. DRIE can be performed on (100)Si and hence it is compatible with current processing technology. The optical characterization of the photonic properties of fabricated structures was mainly performed using the Fourier Transform Infrared (FTIR) microspectroscopy in mid-IR range and using optical-fiber-coupling set-up based on an optical spectrum analyzer (OSA) in near-IR range.

2.2 Calculation methods

2.2.1 The Transfer Matrix Method

The transfer matrix method is a 2x2 linear matrix describing light propagation in a stratified medium. A stratified medium is a medium whose properties are constant throughout each plane perpendicular to a fixed direction. The TMM is based on the fact that the equations that govern the propagation of light are linear and the continuity of the tangential fields across an interface between two isotropic media can be regarded as a 2x2 linear-matrix transformation [1, 6]. One of the most attractive features of the TMM method is the ease of introducing any number of different additional layers (strata) and defects at any point in the TMM's matrix equation, which enables the engineering of various complicated 1D PhC devices for different applications [7, 8].

Consider a stratified structure that consists of a stack of 1, 2, 3,...j,...N parallel layers (strata) placed in (0) media (Figure 2-1). Let all media be linear homogeneous and isotropic, and let the complex index of refraction of the j-th layer be n_j and its thickness d_j. The complex index of refraction of (0) media is n_0.

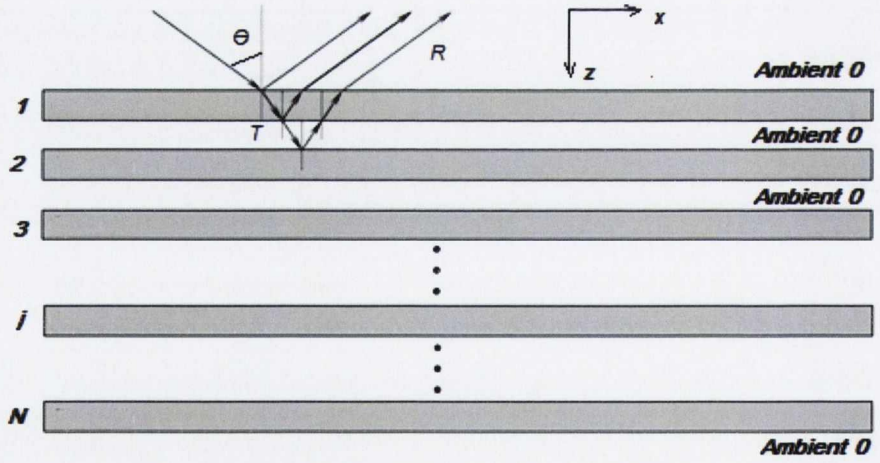

Figure 2-1: *Reflection, R, and transmission, T, of a plane wave by a multi-layer structure with high and low refractive indexes of layers. Θ is the angle of incidence.*

An incident monochromatic plane wave in medium (0) generates a resultant reflected plane wave, R, and a resultant transmitted plane wave, T. The total field inside the j-th layer, which is excited by the incident plane wave, consists of two plane waves: a forward-travelling plane wave denoted by (+), and a backward travelling plane wave denoted by (-).

The wave-vectors of all plane waves lie in the same plane (the plane of incidence), and the wave-vectors of the two plane waves in the *j*-th layer make equal angles with the *z*-axis which is perpendicular to the plane boundaries. When the incident wave in the ambient is linearly polarized with its electric vector vibrating parallel (TE or E) or perpendicular (TM or H) to the plane of incidence, all plane waves excited by that incident wave in the various layers of the stratified structure will be similarly polarized, parallel or perpendicular to the plane of incidence, respectively. In the following, it will be assumed that all waves are either TE(E)- polarized or TM(H)-polarized.

Let $E^{+}(z)$ and $E^{-}(z)$ denote the complex amplitudes of the forward- and backward-travelling plane waves at an arbitrary plane z. The total field at z can be described by a 2x1-column vector.

$$E(z)=\begin{bmatrix} E^{+}(z) \\ E^{-}(z) \end{bmatrix} \qquad (2.1).$$

If we consider the fields at two different planes z' and z'' parallel to the layer boundaries then, by virtue of system linearity, $E\ (z'')$ and E (z') must be related by a 2x2 matrix transformation

$$\begin{bmatrix} E^{+}(z') \\ E^{-}(z') \end{bmatrix}=\begin{bmatrix} S_{11} & S_{12} \\ S_{21} & S_{22} \end{bmatrix}\begin{bmatrix} E^{+}(z'') \\ E^{-}(z'') \end{bmatrix} \qquad (2.2).$$

More concisely, Eq. (2) can be written as

$$E(z') = SE(z'') \qquad (2.3),$$

where

$$S=\begin{bmatrix} S_{11} & S_{12} \\ S_{21} & S_{22} \end{bmatrix} \qquad (2.4).$$

Note that S must characterize that part of the stratified structure confined between the two parallel planes at z' and z''. By choosing z' and z'' to be immediately adjacent to the *0-1* and *N-0*, interfaces respectively, Eq. (2.3) will read

$$E(z_1 - 0) = SE(z_0 + 0) \qquad (2.5),$$

where z_1 and z_0 are adjacent media to the 01 interface.

Equation (2.5) defines a *scattering matrix, S,* which represents the overall reflection and transmission properties of the stratified structure. *S* can be expressed as a product of the interface and layer matrices, *I* and *M,* that describe the effect of the individual interfaces and layers of the entire stratified structure, taken in proper order, as follows:

$$S = I_{01}M_1I_{12}M_2...I_{(j-1)j}M_j...M_NI_{N0} \qquad (2.6).$$

The matrix I_j of an interface between two adjacent layers *j-1* and *j* (7), and the matrix M_j of the layer *j* (2.8):

$$I_j = \left(\frac{1}{t_j}\right)\begin{bmatrix} 1 & r_j \\ r_j & 1 \end{bmatrix} \qquad (2.7)$$

$$M_j = \begin{bmatrix} e^{i\beta_j} & 0 \\ 0 & e^{-i\beta_j} \end{bmatrix} \qquad (2.8),$$

where r_j and t_j are the interface Fresnel coefficients of reflection and transmission, respectively, and the phase shift (phase thickness of the layer), β, is given by (2.9):

$$\beta_j = 2\pi\left(\frac{d_j}{\lambda}\right)n_j\cos\theta \qquad (2.9),$$

where λ - wavelength; n_j – refractive index of *j*-th layer , d_j – thickness of *j*-layer and θ-angle of incidence.

From the matrices of interface, *I,* and layer, *M,* the overall scattering matrix *S* of the stratified structure can be found by straightforward matrix multiplication:

$$\begin{bmatrix} E_0^+ \\ E_0^- \end{bmatrix} = \begin{bmatrix} S_{11} & S_{12} \\ S_{21} & S_{22} \end{bmatrix}\begin{bmatrix} E_{0_S}^+ \\ 0 \end{bmatrix} \qquad (2.10),$$

where, for simplicity, the subscripts *0* and 0_S refer to the semi-infinite air input and output media, respectively, and $E_{0_S}^- = 0$. Further expansion yields the total reflection, *R,* and transmission, *T,* coefficients of the stratified structures as

$$R = \frac{E_0^-}{E_0^+} = \frac{S_{21}}{S_{11}} \qquad (2.11),$$

$$T = \frac{E_{0_S}^+}{E_0^+} = \frac{1}{S_{11}} \qquad (2.12),$$

respectively.

2.2.2 Modelling of grooved Si structures

In this work, a One-Dimensional Photonic Crystal structure was investigated by modeling it as a free-space microstructured grooved Silicon structure with linear grooves, as shown in Figure 2-2. The refractive index of Si for the high-refractive index layer, *H*, $n_H=n_{Si}=3.42$, in the mid- and near-IR range, is considered in accordance with Reference [9]. Since the modelling was performed for normalized frequency (wavelength) range, which allows to design of PhC structure for operation in a wide IR range, the dispersion of Si was not taken into account. The structure is operating in the free space; therefore the refractive index of the incoming and outgoing medium is 1. A considerable advantage of these 1D PhCs is that the air grooves (the low-refractive index layer, *L*) with refractive index $n_L=n_{air}=1$, can be easily infiltrated with filler whose refractive index is different from air. In the case of the original "*Si-air*" structure, the optical contrast is $n_H/n_L= n_{Si}/n_{air}=3.42/1$ and the structure can be considered as a high-contrast PhC. Therefore, only a small number of periods is needed in order to obtain a PBG with a reflectance, *R*, of over 99% and a substantial edge sharpness. The optical spectra of this structure can be calculated using the TMM.

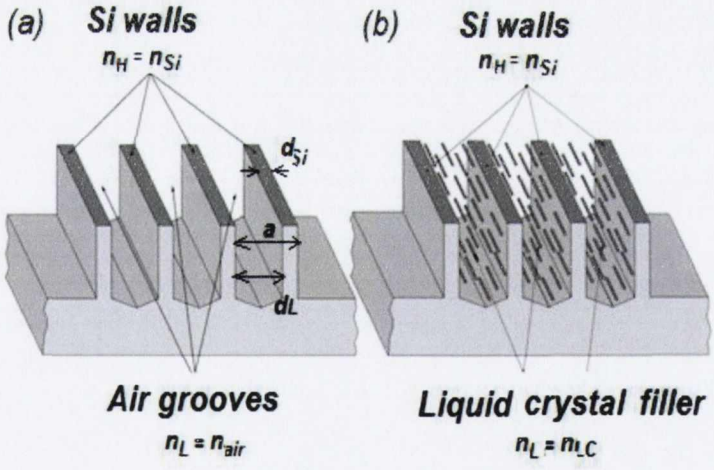

Figure 2-2: *Schematic fragment of grooved-Si structure with (a) air grooves and (b) grooves infiltrated with LC.*

As all thicknesses of periods are the same for this type of grooved Silicon structure, the equation (2.6) can be written in more compact form:

$$S = [(I \cdot M)_{Si} \cdot (I \cdot M)_{air}]^N \cdot (I \cdot M)_{Si} \quad (2.13),$$

where $(I \cdot M)_{Si}$ and $(I \cdot M)_{air}$ are the optical matrixes of the Si and air layers, N is the number of periods in the structure, I is the matrix of the interface between the layers and M is the matrix of the layer transmission.

The value I depends on the refractive indexes of the components of the periodic structure, while the value of M depends on their thickness, d, and on the wavelength, λ. In accordance to the Eq. (2.11-12), the reflection coefficient, $R(\lambda)$, and the transmission coefficient, $T(\lambda)$, can be calculated from the following equations

$$R(\lambda) = \left[\frac{S(\lambda)_{21}}{S(\lambda)_{11}}\right]^2 \quad (2.14),$$

$$T(\lambda) = \left[\frac{1}{S(\lambda)_{11}}\right]^2 \quad (2.15),$$

respectively.

2.2.3 Design of the Photonic Band Gap characteristics

The design of grooved Si structure with desired photonic band gap characteristics normally starts with the selection of the wavelength λ of its operation. Then, the materials with corresponding refractive indexes, n_L and $n_H=n_{Si}$, for suitable periodic structure fabrication are chosen. Based on the above selection, the geometrical thickness of both components, d_L and d_{Si}, are determined in accordance with the Bragg condition

$$\frac{\lambda}{2} = n_{Si} \cdot d_{Si} + n_L \cdot d_L \qquad (2.15),$$

where $n \cdot d$ is the optical thickness of the corresponding high-(H) and low (L)-refractive index components. For equal optical thicknesses of each component $n \cdot d = \lambda/4$, the maximum width of the PBG (or stop-band (SB)) is achieved for the required wavelength λ.

The PBG properties of the grooved Silicon structure are strongly dependent from the following design parameters:

- Optical contrast of layers, $(n_{Si}/ n_L)_j$
- Lattice constant, $a=d_{Si}+d_L$ (Figure 2-2)
- Filling fraction of Si, $f_{Si}= d_{Si}/a$

- Number of periods, N.

A precise control of these parameters over the design and fabrication process is obviously necessary for the proper operation of the PhC device. The value of lattice constant, a, is normally very well controlled during the fabrication process and, so, by varying only thickness of Si, $f_{Si}=d_{Si}/a$ and/or the refractive index of the L-layer, n_L, the following general PBG parameters can be altered:

- order of PBGs;
- wavelength of operation of PBGs;
- width of the PBGs;
- vanishing and splitting of the PBGs.

2.2.4 Gap Map Approach

The design procedure requires the investigation of the influence of all nominal parameters listed above on optical characteristics of PhC devies, this makes the design part very complex involving calculation and analyses of the vast number of spectra. Several approaches can be used in order to determine the optical properties of a 1D PhC. One of these is to calculate the band diagrams (BD) [10] for the selected filling fractions $f_{Si}=d_{Si}/a$. The second design approach is based on the Gap Map (GM) presentation, which was first suggested by John D. Joannopoulos et al. in Ref. [2]. For drawing the GM, in principle, both the BD [11] and the reflection spectra calculation method [1] can be used. The calculation of the reflection spectra of 1D PhC with the certain number of lattice periods is normally performed using the TMM [12]. The GM approach is one of the most attractive design tools for the band-gap structures [11, 13] as well as tunable [12] and composite [14] photonic structures, since it allows quick and easy analysis of structures for a large set of spectra (normally over 100) to be done practically on one plot.

Using the transfer matrix method, the set of reflection spectra, R, for sequential values of filling factor, f_{Si}, in the range from 0 and 1 is calculated. For each of the calculated spectra, the values of λ (or wavenumber, ν) for which R>99% (PBG regions), are plotted against f_{Si} as shown in Figure 2-3(a). For the structures with smaller number of periods, e.g. elementary Fabry-Perot unit with N=1.5, this level was lowered to R>85% for more clear representation, as in this case the map represents the

regions of high reflectivity (SBs). The PBG GM allows an effective comparison of PhC structures with various number of periods, N, lattice constant, a, refractive index contrast, $\Delta n=n_{Si}/n_L$, angle of incidence, θ, and polarization of the incident light.

An example of the reflection spectrum which constitutes the Gap Map is shown in Figure 2-3 (b). As lattice constant, a, is kept constant, prediction of the wavelength range in which a PhC with a particular d_{Si} will operate is possible. Alternatively, the d_{Si} which is necessary to obtain a PhC over a certain wavelength range can be determined. For example, it can be determined from Figure 2-3(a) that the wavelength range of the main PBG of a PhC with the parameters f_{Si}=0.226 and a=4 μm is between λ=10 μm and λ=15.5 μm. Alternatively, if required criteria is to design a PhC with a PBG with a maximum width between λ = 14 μm and λ = 20 μm, the optimal design parameter would be f_{Si} = 0.6 for the main PBG.

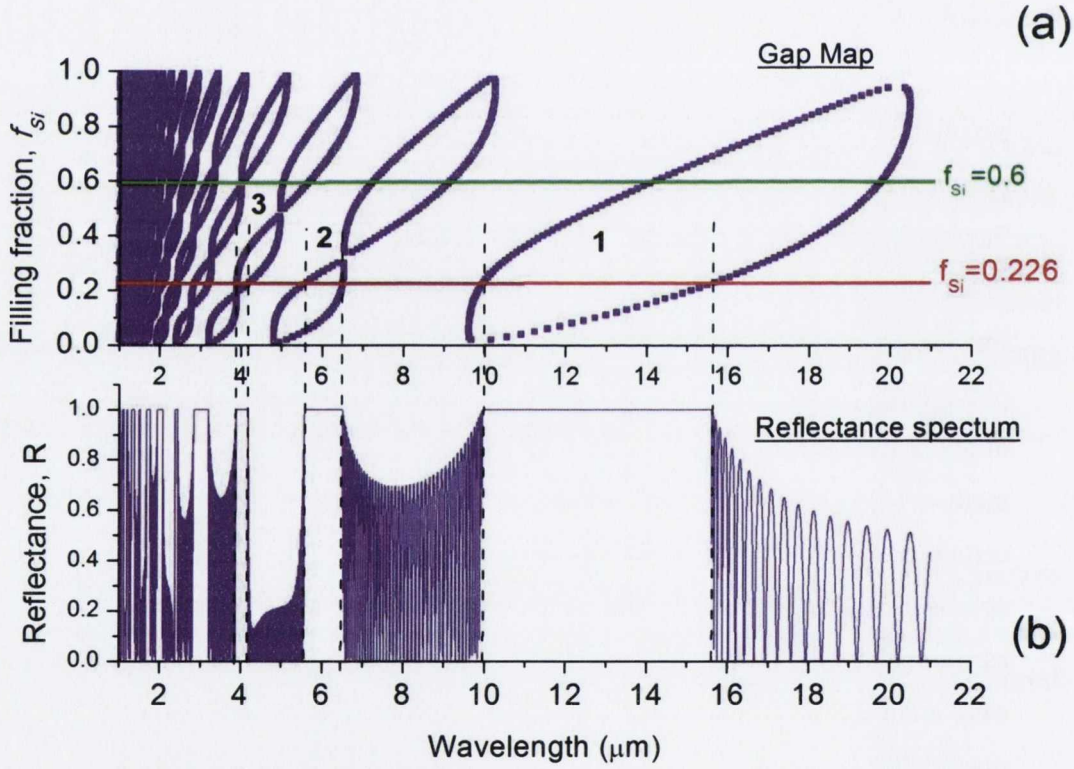

Figure 2-3: *(a) Calculations of the main PBG (1) and secondary PBGs (2, 3 etc.) for a 1D PhC based on the grooved Si with number of periods N=50, a=4μm at normal incidence of light. (b) Calculated reflectance spectrum of the structure with f_{Si}=0.226.*

Using Figure 2-3(a) it is also possible to determine the maximum fabrication tolerances of the designed structure. The range of filling fraction Δf_{Si} for which the main

PBG characteristics, such as bandwidth, operational wavelength and flat-top 100% reflection, remain the same, can represent the maximum lithography error for the fabrication of the grooved Si structure. Obviously, as it can be seen in Figure 2-3, the high order PBGs demonstrate the highest lithography tolerances (the PBG regions are located almost parallel the filling fraction axis) comparing to the lowest PBGs. For example, the PhC mirror with f_{Si} =0.6 and operating at the 3rd PBG and reflecting light from 5.00μm to 5.75μm has the fabrication tolerance Δf_{Si}=0.05, which is 200 nm for the considered example with a=4 μm.

By using the normalized ranges of frequencies, $NF=a/\lambda$, or normalized wavelengths $NW=\lambda/a$, the Gap Map becomes universal and therefore can be applied to a wide range of structure sizes including micro- and nano-structures.

2.3 Fabrication methods

Modern micromachining of semiconductors allows the construction of PhCs with high optical contrast and high dimensional tolerances. A preliminary templating of a Si wafer with subsequent electrochemical or chemical etching through the template is used for the initial patterning. A template is usually produced by means of lithography. The classical optical lithography offers the possibility of fabrication of patterns with the minimum size of ~1 μm.

In general, there are two classes of etching processes:

1. Wet etching, where the material is dissolved when immersed in a chemical solution

2. Dry etching where the material is sputtered or dissolved using reactive ions or a vapour phase etchant

In the following Sections, we will briefly discuss Wet Anisotropic Etching and Deep Reactive Ion Etching techniques that were used in this work.

2.3.1 Crystallographic Orientation of Silicon

A crystal is a solid in which the constituent atoms, molecules, or ions are packed in a regularly ordered repeating pattern extending in all three spatial dimensions. Atoms in a crystal arrange themselves at specific points in a structure known as a unit cell. The unit cell structure is repeated everywhere in the crystal [15]. In single crystal

materials the unit cells are all neatly and regularly arranged to each other while in polycrystalline crystals they are not. Silicon wafers are single crystalline materials.

Crystalline materials have two main features which affect most of their properties, namely anisotropy and symmetry. Crystal anisotropy arises from the fact that interatomic distances and forces vary in different directions and are regular at the same time. Hence, the properties of the crystal vary in different directions but are the same in parallel directions. The symmetry of crystals is due to the symmetry of the crystal lattice. The symmetry of a single crystal arises from the repeating symmetry of its lattice.

Crystal planes in single crystal are identified by a series of three numbers known as the Miller indexes. This theory can be conceptualised as slicing a single crystalline block at different angle to expose different planes with different properties. The (100), (110) and (111) planes defined by the Miller indexes are shown in Figure 2-4. Miller indexes characterise all planes parallel to the plane concerned. The two most common orientations used for Silicon wafers are (100) and (111) planes [15].

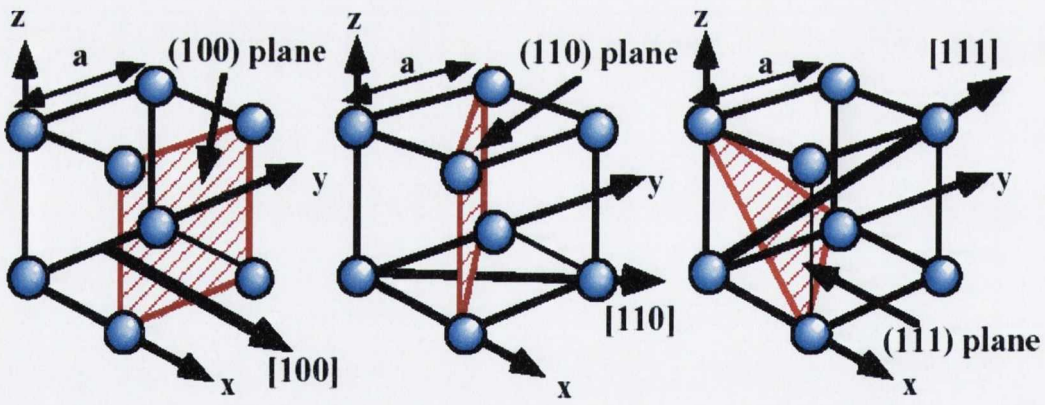

Figure 2-4: *Planes defined by the Miller indexes.*

2.3.2 The Wet Anisotropic Etching Technique of (110) Si

This wet etching is the simplest etching technology. There are actually two types of wet etching: isotropic and anisotropic etching (Figure 2-5). Wet isotropic etching is a uniform etching process that decays in the Si material at the same rate in both vertical and horizontal directions while anisotropic etching decays in the material in a more selective direction (Figure 2-5). For wet anisotropic etching of Silicon the

aqueous solution of KOH with addition of alcohols and a number of other anisotropic etchant is typically used [16]. In 1979, Kendall reported the fabrication of extremely narrow grooves in Silicon due to this technique and forecast that this would probably spawn a number of technological revolutions [17]. However, the technique is not widely used in the fabrication of optical elements, despite the possibility of fabricating periodic structures with high refractive index contrast and smooth mirror-like side-walls in Silicon transparency range [18].

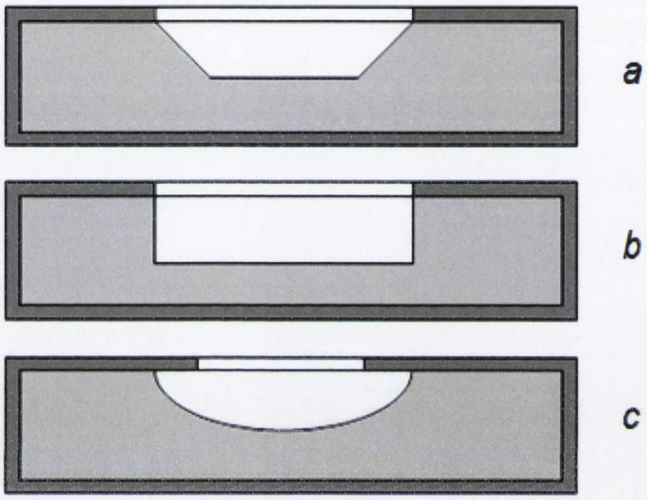

Figure 2-5: *Difference between (a, b) anisotropic and (c) isotropic wet etching [19].*

Fabrication of grooved Si by the wet anisotropic etching of (110) Silicon in KOH is based on the difference in the etching rate for the (110) and (111) crystallographic planes [20]. The main etching rules of mono-crystalline Si of different crystallographic orientations were established in seventies of the last century [21] and can be summarized as:

i) The ratio of the etching rates is highly dependent on the crystallographic orientation. The ratios of the etch rate for the (111), (110) and (100) planes in 44% KOH at 70°C are related as $V_{111}:V_{110}:V_{100}=1:600:300$ [17]. Therefore, this technique is only compatible with (110) Silicon.

ii) The etch rates of SiO_2 or Si_3N_4 in KOH solution are hundreds of times smaller than the etch rate of Silicon. This enables their use as a protective mask for forming patterns using relevant methods of lithography and to etch through these patterns the air holes of different shape.

For this work, (110)-oriented Si is of a principal interest. If long, narrow windows, precisely oriented along the (111) plane trace, are patterned in the masking film via lithography, the trench walls obtained in the Silicon after anisotropic etch are oriented perpendicular to the substrate plane. The method permits the fabrication of deep trenches of various widths with smooth side-walls of optical quality without under-etch of the sidewalls (Figure 2-6). As it was demonstrated in the past [20], this technology could be used for the fabrication of 1D PhCs for in-plane infrared light propagation.

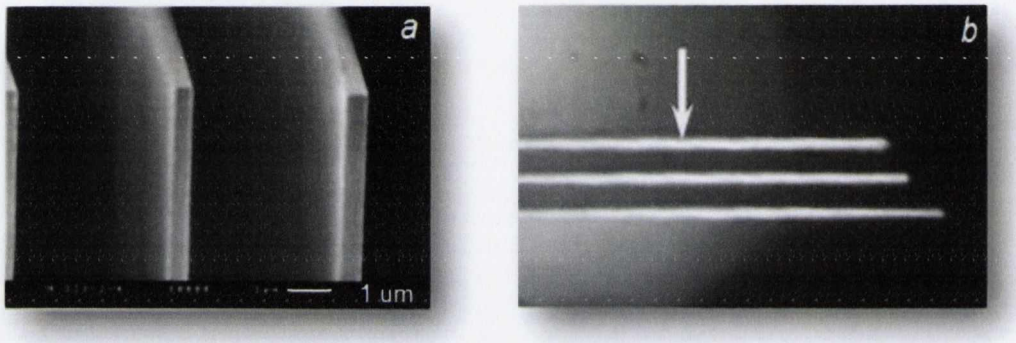

Figure 2-6: *(a) SEM image of Si walls for periodic photonic structure, obtained by deep anisotropic etching of (110) Si. (b) The optical microscopy image of 1D PhC, fabricated by WAE method: the top view of structure with lattice period a=7μm.*

The WAE method is also suitable for fabrication of defects in the periodic structure, which can be used as micro-cavities. Using the WAE method allows PBG structures to be fabricated on an SOI substrate. This offers advantages in receiving the total internal reflection in planar waveguides and provides electrical isolation from the substrate. The latter is crucial in the fabrication of electro-tunable PBG devices, as will be shown in Chapter 4. However, WAE methods have also some disadvantages. (110)-oriented Si substrates are expensive and not in use in mass-production. In addition, it is imperative to precisely align the lithographic mask with the Silicon crystallographic axes, increasing the difficulty of the technique. Cross cut walls of the trenches are tilted and this results in an ineffective use of the substrate area. The long side of the grooves can be only oriented along two directions in the (110) plane which form the angle of 70.50°. This places substantial restrictions on the structure design, and may result in

undercutting where elements cross. DRIE etching of Si does not suffer from these disadvantages.

2.3.3 The Deep Reactive Ion Etching Technique of (100) Si

Dry etching is a generic term that refers to the etching techniques in which gases are the primary etch medium, and the wafers are etched without wet chemicals and rinsing. The wafers enter and exit the system in a dry state. The dry etching technology can split in three separate classes called reactive ion etching (RIE), plasma, and ion beam milling (etching) [15].

In RIE, the Silicon wafer is placed inside a reactor in which several gases are introduced. Plasma is struck in the gas mixture using a radiofrequency (RF) power source, breaking the gas molecules into ions. The ions are accelerated towards, and react at, the surface of the Si material being etched, forming another gaseous material. This is known as the chemical part of reactive ion etching. There is also a physical part which is similar in nature to the sputtering deposition process. If the ions have high enough energy, they can knock atoms out of the material to be etched without a chemical reaction. It is a very complex task to develop dry etch processes that balance chemical and physical etching, since there are many parameters to adjust. By changing the balance it is possible to influence the anisotropy of the etching, since the chemical part is isotropic and the physical part highly anisotropic the combination can form sidewalls that have shapes from rounded to vertical. A schematic of a typical reactive ion etching system is shown in Figure 2-7.

A special subclass of RIE which was used for fabrication of the PhC structures in this work is deep RIE (DRIE). DRIE systems combine plasma etching and ion etching principles [22]. DRIE is a combination of three primary processes, etching, passivation and ion bombardment. A highly reactive gas is used to perform an isotropic etch of the substrate. After a brief period the etching is stopped and a passivation layer is deposited over the whole surface of the substrate. This protects the substrate from chemical attack and prevents further etching. The process then returns to etching and a collimated stream of directional ions bombard the substrate. These ions remove the passivation layer from the bottom of the previous etch step, but not from the sides, in a process called sputtering. The etchant chemicals can then erode only the bottom of the channels. The process is repeated many times over resulting in a large number of very

small isotropic etch steps taking place only at the bottom of the etched pits. It is this selectivity that leads to the overall anisotropy of the process and the creation of high aspect ratio channels with vertical sidewalls. As a result, etching aspect ratios of 50 to 1 can be achieved. The process can easily be used to etch completely through a Silicon substrate, and etch rates are 3-4 times higher than wet etching.

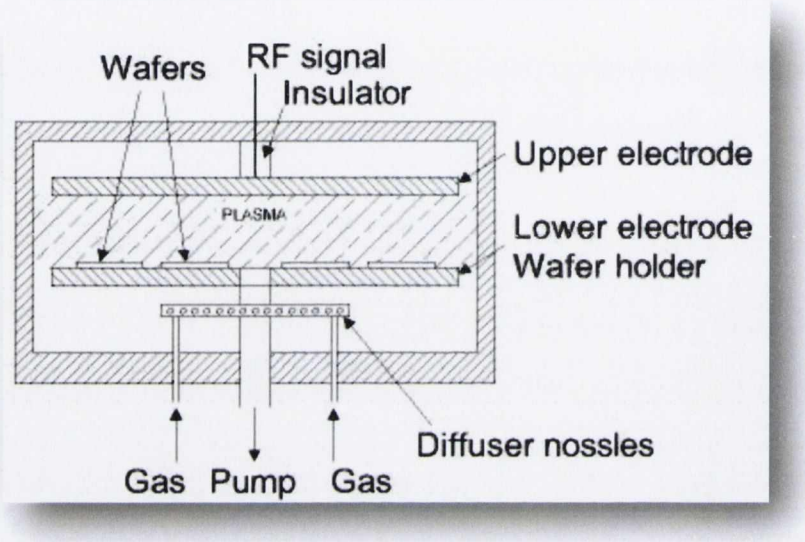

Figure 2-7: *Typical parallel-plate reactive ion etching system.*

In Silicon micromachining a profile control of high-aspect ratio trenches (HARTs) is increasingly important. The aspect ratio is defined as the maximum depth divided by the maximum width. The HARTs give rise to the following specific problems:

- The aspect ratio dependent etching (ARDE) effects (Figure 2-8(a)):
    - RIE lag is associated to the effect that smaller trenches are etched at a different speed than wider trenches. It is explained in considering the depletion of reactive particles during their trajectory in the trench.
    - Bowing is the observation of a parabolic curvature of etched sidewalls as found for the wider opening.
    - Trench area dependent tapering of profiles is the effect that wider trenches have different sloes/tapering with respect to the smaller trenches.

- Bottling shows up as bottle-shaped trenches and is caused by ion shadowing and sharpening of the collimated ion beam incoming from the glow zone. Generally it is pronounced only at a high pressure (Figure 2-8(b)).
- Micrograss is the existence of long-tailed spikes at the trench bottom. Generally, the appearance of such rough surface is grey or even black (Figure 2-8(c)).
- Tilting is observed near geometrical obstacles and is due to boundary distortion or local differences in radical density. In the demonstrated Figure 2-8(d), the wafer edge is responsible for the tilting [23].

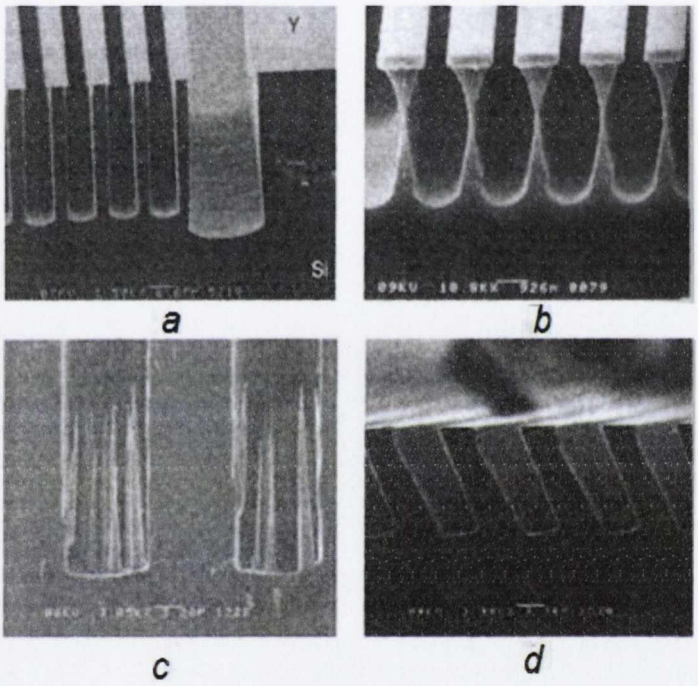

***Figure 2-8**: SEM images of the grooved-Si structures fabricated by DRIE: (a) The ARDE effect, (b) Bottling of the grooves, (c) Micrograss in the grooves, (d) Tilting of grooves [21].*

Another disadvantage of DRIE method is the high interface roughness of the structures etched on the great depth (>10-15 μm), which results in the scattering losses of the light during the optical operation. In order to overcome these problems the DRIE etching technological process should be carefully controlled during the etching process. The DRIE process settings, the equipment parameters, the plasma characteristics, and the trench-forming mechanisms are responsible for the final HART profile and, therefore, should be carefully monitored during the etching process. Dry etching is one

of the most enabling technologies, which comes at a sometimes high cost. However, it remains the most preferable etching technique for fabrication of deep patterns with vertical side-walls, since it can be performed on all crystallographic orientations of wafer. Therefore, it is highly compatible with current CMOS processing.

Grooved Si samples were fabricated by this technique in Tyndall Institute Ireland, Cork, thanks to NAP94 (Prof. Tatiana Perova) and NAP368 (Anna Baldycheva, Prof. Tatiana Perova).

2.4 Methods of characterization

2.4.1 FTIR Microspectroscopy Technique

Fourier Transform Infrared Spectroscopy is a workhorse of the industrial materials testing division. The combination of a microscope with an infrared spectrometer results in a powerful instrument that allows analysis of very small photonic samples in a wide IR range. Indeed, infrared microspectroscopy has become the technique of choice for samples smaller than 100 μm, or where spectra of small areas within a large sample, like layers in a laminate or defects in a matrix, are required. Also, information about the chemical makeup, heterogeneity, and layers within the sample can be derived with infrared microspectroscopy.

The basic process in FTIR spectroscopy is light wave interference. The main component of a Fourier Transform Infrared spectrometer is the Michelson interferometer. The Michelson interferometer contains a fixed mirror, a movable mirror and a beamsplitter. The beamsplitter transmits half of the incident radiation to the moving mirror and reflects the other half to the fixed mirror. The two beams are reflected by these mirrors back to the beamsplitter, where they recombine. When the fixed mirror and the moving mirror are equidistant from the beamsplitter, the amplitudes of all frequencies are in phase and interfere constructively. As the moving mirror is moved away from the beamsplitter, an optical path difference is generated. A pattern of constructive and destructive interferences (interferogram) is generated depending on the position of the moving mirror and on the frequency of the radiation. This beam is then directed through the sample compartment to the broadband detector and a digital signal processor sorts out the signal corresponding to each frequency using a fast Fourier Transform (Figure 2-9) [24].

The Bio-Rad Digilab FTS 6000 spectrometer was used to measure reflection and transmission spectra in the wide range of 700-7000 cm^{-1} of photonic crystals structures. It consists of a step scan interferometer bench (FTS 6000) coupled to a MCT (*HgCdTe*) detector equipped with a microscope, UMA-500, for delivering a focused incident beam on the sample. One of the advantages of this particular system for reflection and transmission measurements on grooved Silicon is the possibility to form a rectangular shape of the incident beam on the sample using microscope aperture for increasing the signal-to-noise ratio. This setup allows the measurement of Si structure with a minimal incident beam aperture 10x10 μm^2.

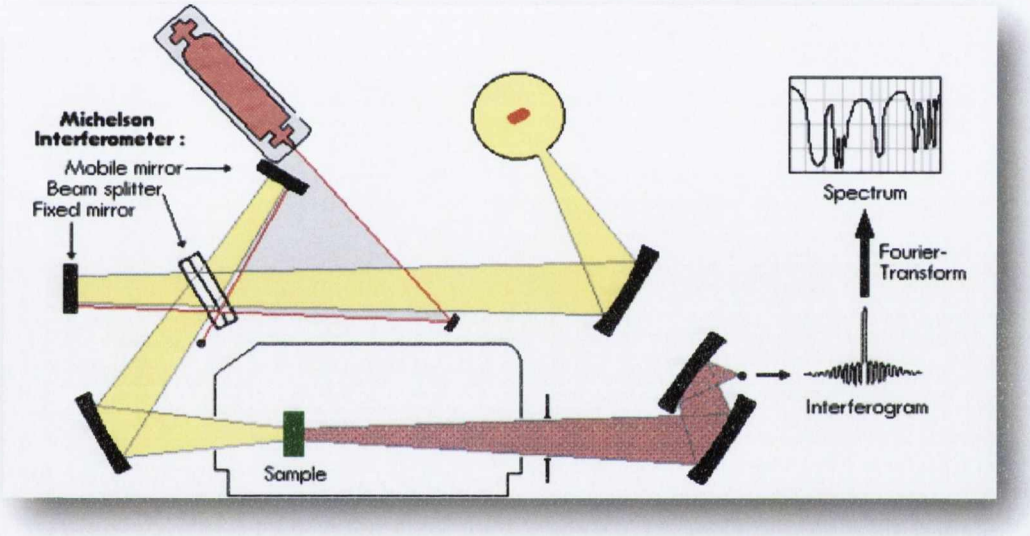

Figure 2-9: *Layout of a simple FTIR spectrometer.*

IR measurements of grooved Si are very critical to the direction of the light propagation through the whole structure. The IR beam should be exactly perpendicular to the Si walls along the entire path. For this reason a special sample holder, shown in Figure 2-10, has been used for the measurements. This allows adjusting the sample in the *X-Y-Z* direction.

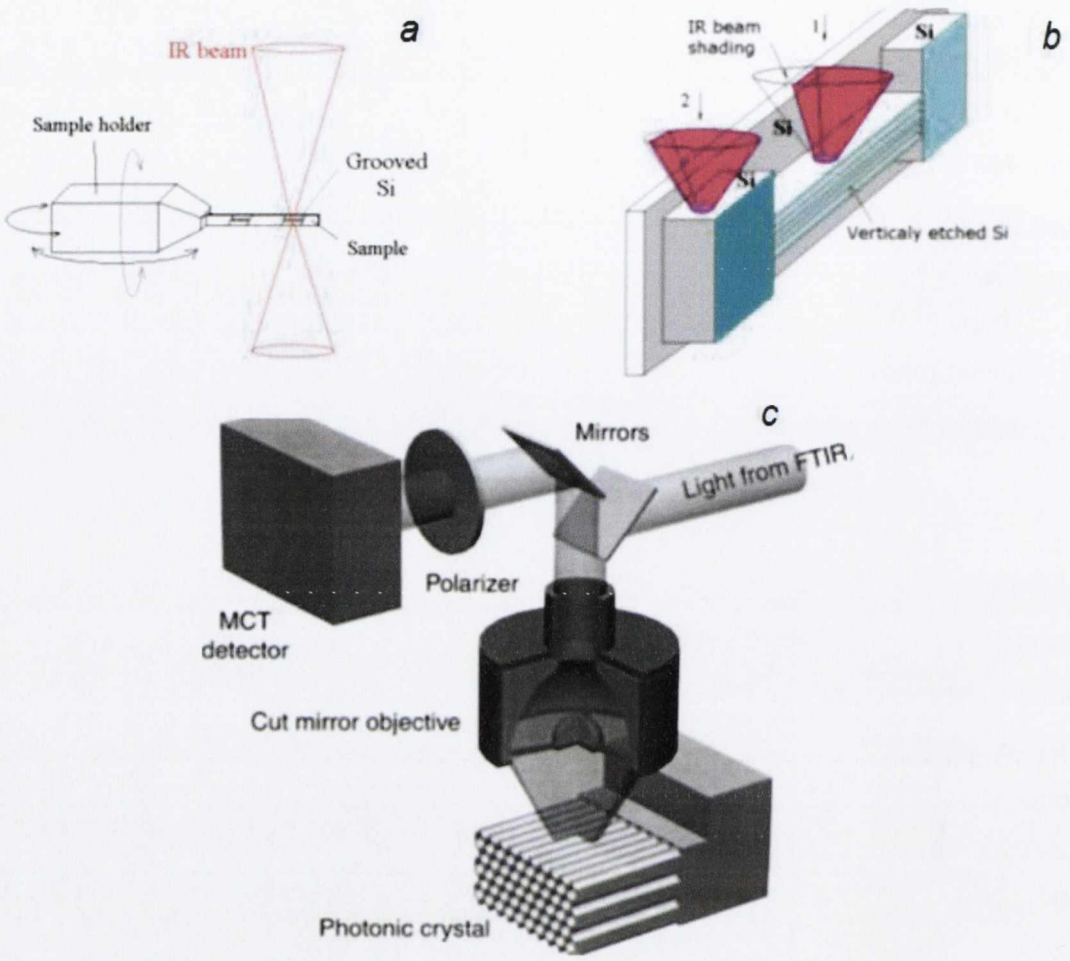

Figure 2-10: *(a, b) Schematic of the experimental set-up with IR beam focused by microscope on the grooved Si (position 1) and on bare Silicon (position 2). (c) Reflection characterization setup using a Fourier-transform infrared spectrometer coupled to an achromatic infrared microscope [25].*

Certain difficulties arose during the measurements due to complicated structure of the samples. In particular, the part of the unetched Si walls at the bottom of the grooves masked both the incident and reflected IR beams, which reduced the intensity of the signal reaching the microscope objective. In order to avoid this "shading effect" from the Si substrate, which interfere with the cone of incident light, the photonic crystal structures were fabricated close to the edge of the substrate (Figure 2-10(b)). An infrared spectrum is generally displayed as a plot of the energy of the infrared radiation (expressed either in microns or wavenumbers) versus the percent of light reflected/transmitted by the sample. The reflection/transmission coefficients are obtained by dividing the spectra obtained with the PhC structure by the background

spectra. The Single Beam reflection signal from the gold-coated glass (R=0.99) has been used as a reflection background, while Single Beam transmission signal without sample (T=0.99) has been used as a transmission background. Reflection of the bare crystalline Si was used for the comparison. For polarized FTIR measurements, the polarizer was placed before the microscope detector (Figure 2-10(c)).

2.4.2 End-fire Technique

For analysis of the structures in the near-infrared range (1200-1700 nm) an optical fibre-coupling set-up based on Optical Spectrum Analyser has been used. The free-space end-fire setup was mainly developed for the purpose of polarized transmission measurements of LC PhC resonators around the telecommunication wavelength range.

The coupling of light into guided modes by transverse excitation is known as the end-fire coupling method. End-coupling experiments involve the coupling of light into waveguide samples or free-space photonic samples that are end-polished with an optically smooth finish. End-fire coupling can be achieved by means of microscope objective lens focused on the sample or butt-coupling an optical fiber to the sample ends. In this work the free-space coupling was used to couple the light source into PhC structures. The schematic of the experimental setup is shown in Figure 2-11.

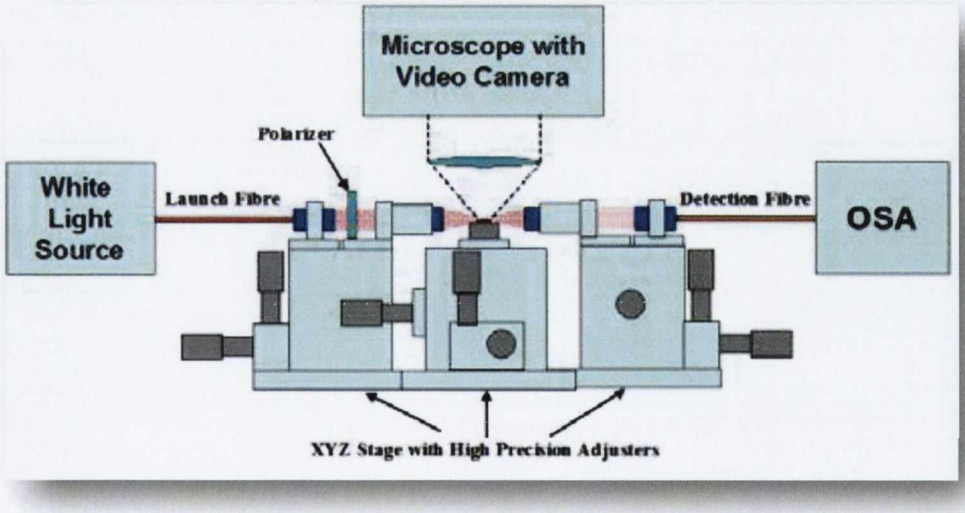

***Figure 2-11**: Schematic of the setup for end-fire light coupling using microscope objectives (also known as free-space coupling).*

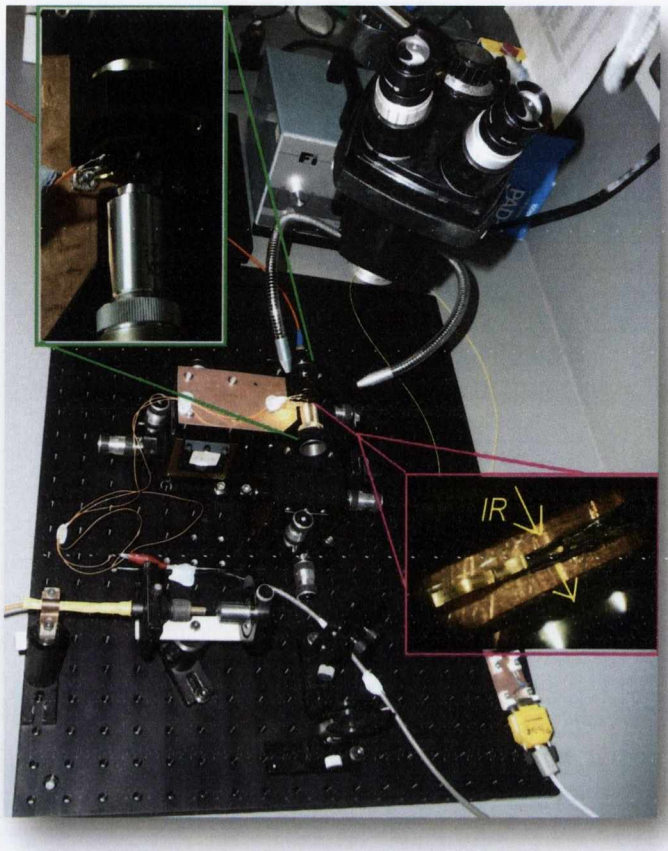

Figure 2-12: *A free-space fiber coupling set-up. The insets demonstrate the light coupling using microscope objectives and in-plane alignment of the PhC sample during the optical measurements.*

A broadband light source Oriel® Arc 75W Xenon Lamp that provides light with a broad wavelength range in the near infrared region from 1200 to 1700 nm was used. A light beam from a source was transmitted from the end of a single-mode fiber, through the polarizer and then focused on the sample using the microscope objective. The experimental setup typically comprises of trio of optical stages. The input and output components (i.e. microscope objectives) and the sample are separately mounted on high precision micro-positioners and micro-manipulators to achieve accurate and stable alignment. Transmitted light is then collected by the microscope objective and coupled to the single mode fiber which is connected to the optical spectrum analyzer Agilent 861408B, allowing the monitoring of the PBGs and resonance peaks. The measured transmittance is normalized by the light intensity measured without sample. Finally, the

results of these measurements are compared with theoretical calculations and FTIR measurements.

The TMM calculation method described in Section 2.2 considered for the parallel incident light beam for simulations of the optical spectra of photonic crystals. However, in both experimental techniques the incident light beam was focused with the maximal angle of the light cone up to 30°. The cone-shape of the light beam causes the degradation of the main PBG characteristics, e.g. smoothing of "Π"-shape, narrowing, shift and even disappearance of high-order PBGs [26].

2.5 *Summary*

The basic concepts of theoretical and experimental background have been introduced. A one-dimensional photonic crystal structure was investigated by modeling it as a free-space microstructured grooved Silicon structure with linear grooves. The utilization of the transfer matrix and forbidden gap map methods allows easier modelling of the optical properties of the grooved Silicon photonic crystals with additional components for realization of multicomponent photonic crystals (Chapter 3) cavities/defects for realization of the micro-cavity photonic crystals (Chapter 4) and disorder in geometrical parameters (Chapter 5). The introduction to the methods of Silicon microstructuring used for the fabrication of the grooved Silicon structures in this work has been discussed. The optical experimental techniques applied to the investigation of the fabricated multi-component photonic crystal and microcavity photonic crystal structures in a wide infrared range have been described.

2.6 *References*

[1] R. M. A. Azzam, and N. M. Bashara, [Ellipsometry and polarized light] North-Holland, (1987).

[2] J. D. Joannopoulos, [Photonic Crystals: Molding The Flow Of Light] Princeton University Press, (2008).

[3] N. Ansari, and M. M. Tehranchi, "Influence of filling fraction on the defect mode and gap closing of a one-dimensional photonic crystal: An analytical approach," Physica B: Condensed Matter, 405(13), 2900-2906 (2010).

[4] V. A. Tolmachev, A. V. Baldycheva, K. Berwick *et al.*, "Influence of fluctuations of the geometrical parameters on the photonic band gaps in one-dimensional photonic crystal " Progress In Electromagnetics Research, Vol.126, 285-302, (2012).

[5] H. Shen, H. Tian, and Y. Ji, "Photonic bands, gap maps, and intrinsic losses in three-component 2D photonic crystal slabs," Chin. Opt. Lett., 7(3), 231-234 (2009).

[6] P. Markoš, and C. M. Soukoulis, [Wave Propagation: From Electrons to Photonic Crystals and Left-Handed Materials] Princeton University Press, (2008).

[7] A. Baldycheva, V. A. Tolmachev, T. S. Perova *et al.*, "Design, fabrication, and optical characterization of multicomponent photonic crystals for integrated silicon microphotonics," Proceedings of SPIE, 7943, 79430F-11.

[8] A. Baldycheva, V. A. Tolmachev, and T. S. Perova, "Fine tunable multi-cavity Si photonic crystal filter," Proceedings of SPIE, 8431-16, 1-13 (2012).

[9] E. D. Palik, "Handbook of Optical Constants of Solids," 1, (1998).

[10] P. Yeh, [Optical waves in layered media] Wiley, (2005).

[11] D. N. Chigrin, A. V. Lavrinenko, D. A. Yarotsky *et al.*, "Observation of total omnidirectional reflection from a one-dimensional dielectric lattice," Applied Physics A: Materials Science & Processing, 68(1), 25-28 (1999).

[12] V. Tolmachev, T. Perova, and K. Berwick, "Design Criteria and Optical Characteristics of One-Dimensional Photonic Crystals Based on Periodically Grooved Silicon," Appl. Opt., 42(28), 5679-5683 (2003).

[13] V. Tolmachev, T. Perova, and R. Moore, "Method of construction of composite one-dimensional photonic crystal with extended photonic band gaps," Opt. Express, 13(21), 8433-8441 (2005).

[14] V. A. Tolmachev, T. S. Perova, and K. Berwick, "Design of one-dimensional composite photonic crystals with an extended photonic band gap," Journal of Applied Physics, 99(3), 033507-5 (2006).

[15] P. Van Zant, [Microchip Fabrication, 5th Ed] McGraw-Hill, (2004).

[16] E. Istrate, and E. H. Sargent, "Photonic crystal heterostructures and interfaces," Reviews of Modern Physics, 78(2), 455-481 (2006).

[17] D. L. Kendall, "Vertical Etching of Silicon at very High Aspect Ratios," Annual Review of Materials Science, 9(1), 373-403 (1979).

[18] V. Tolmachev, L. Granitsyna, E. Vlasova *et al.*, "One-dimensional photonic crystal obtained by vertical anisotropic etching of silicon," Semiconductors, 36(8), 932-935 (2002).

[19] H. Martin, and V. Edgar, "Bulk silicon micromachining for MEMS in optical communication systems," Journal of Micromechanics and Microengineering, 12(4), 349 (2002).

[20] V. A. Tolmachev, T. S. Perova, E. V. Astrova *et al.*, "Vertically etched silicon as 1D photonic crystal," Physica Status Solidi (a), 197(2), 544-548 (2003).

[21] M. Elwenspoek, and H. V. Jansen, [Silicon Micromachining] Cambridge University Press, (2004).

[22] S. M. Sze, [Semiconductor devices, physics and technology] Wiley, (1985).

[23] R. A. Gottscho, C. W. Jurgensen, and D. J. Vitkavage, "Microscopic uniformity in plasma etching," Journal of Vacuum Science & Technology B: Microelectronics and Nanometer Structures, 10(5), 2133-2147 (1992).

[24] S. Perkowitz, [Optical characterization of semiconductors: infrared, raman, and photoluminescence spectroscopy] Academic Press, (1993).

[25] S. Rowson, A. Chelnokov, and J. M. Lourtioz, "Two-Dimensional Photonic Crystals in Macroporous Silicon: From Mid-Infrared (10 m) to Telecommunication Wavelengths (1.3-1.5μ m)," J. Lightwave Technol., 17(11), 1989 (1999).

[26] S. A. Dyakov, V.A. Tolmachev, E. V. Astrova, S.G. Tikhodeev, V.Yu. Timoshenko, T.S Perova, "Numerical methods for calculation of optical properties of layered structures," SPIE Proceedings, 7521 (2009).

Chapter 3.

Multi-Component Photonic Crystals

3.1 Introduction

The precise and technologically controllable engineering of the photonic crystal structures with optimal parameters is still remaining an art, requiring intuition as well as analytical knowledge to create a structure with unique properties. Indeed, these structures operate by the Photonic Band Gap effect and, therefore, possess high sensitivity to the refractive index, n, (or optical thickness) of their components. The PhCs are normally composed of two-components, with high (n_H) and low (n_L) refractive indexes. By changing the value of n_H or n_L, tuning of the PBG position can be achieved. As discussed in Chapter 1, the precise control of the PBGs width and wavelength positions can be achieved by thermal, electrical or mechanical approaches. Although these techniques are technologically well developed, there is an alternative approach to engineering the PBG. This approach requires the introduction of an additional component to the PhC, forming a multi-component PhC.

Multi-component PhCs have already been investigated in a number of recent papers, among which it is worthwhile to refer to the investigation of multi-component 1D PhC [1, 2]. The authors of paper [1] have theoretically analyzed the variations of the PBG's width and position with an increase of the number of components with variouse refractive indexes. However the same geometrical thickness was used for all the components in a multi-component structure despite the fact that it is well known that the thickness of each component significantly influences the optical properties of PhC. The authors of Ref. [2] have investigated theoretically and experimentally how the additional layer, introduced between H- and L-component, can

influence the reflectance spectrum position and leads to the narrowing of high-order PBG. As a result the analysis, performed in Refs. [1, 2], is related to specific structural types only and does not reflect the general behavior of multi-component PhCs.

In paper [3] more detailed investigations of 2D PhCs, containing intermediate layers on the surface of cylindrical pores, have been carried out. The authors have obtained the dependences of the PBG width and position from the additional interlayer thickness and its dielectric constant. They have considered a possibility to vary the lowest PBG position and width in 2D PhCs. It was shown that an interlayer with a thickness of only 1% of the lattice constant influences the band gap position quite significantly. In addition the insertion of the third component into the photonic structure decreases the PhC's contrast and, consequently, the PBG width.

The authors of paper [4] succeeded in studying multi-component 3D PhC and have shown how to selectively manipulate with PBGs in multi-component PhC based on opal structure. For the description of optical characteristics with respect to the structural features more complicated model approaches, than that for 1D and 2D structures, were used. They have shown the possibility to control the stop-bands appearance, their width, and shift and ON/OFF switching by variation of additional layer's thickness, permittivity and other factors in multi-component PhC.

In this Chapter, a three-component 1D PhC based on grooved Silicon was selected as the simplest example for calculations, as well as for demonstrating PBG modifications in both position and width, due to the introduction of an additional regular *t*-layer (Figure 3-1(d,e)). The optical properties of a three-component PhC structures have been analyzed using the GM approach and the TMM method. The introduction of a third component to a 1D PhC allows manipulation of the optical contrast to a high degree of precision by varying the thickness and refractive index of the additional layer. The approach can also be useful for finding the solution of the inverse problem, that is, for the interpretation of experimental reflection/transmission spectra for the photonic structures discussed here. Using the approach to decrease optical contrast in "*Si-air*" PhCs, omni-directional PBGs (ODBs) can be obtained. For some wavelengths, the limited number of PBGs vanish and are replaced by ultra-wide transmission bands (TBs) in the entire range of filling fraction. The fabrication of both band-pass and band-stop filters on a single PhC device enables optical manipulation at a variety of wavelengths. The suggested multi-component PhC model can be applied to

the design of any micro- and nano- structured semiconductor or dielectric materials for application across wide electromagnetic spectrum.

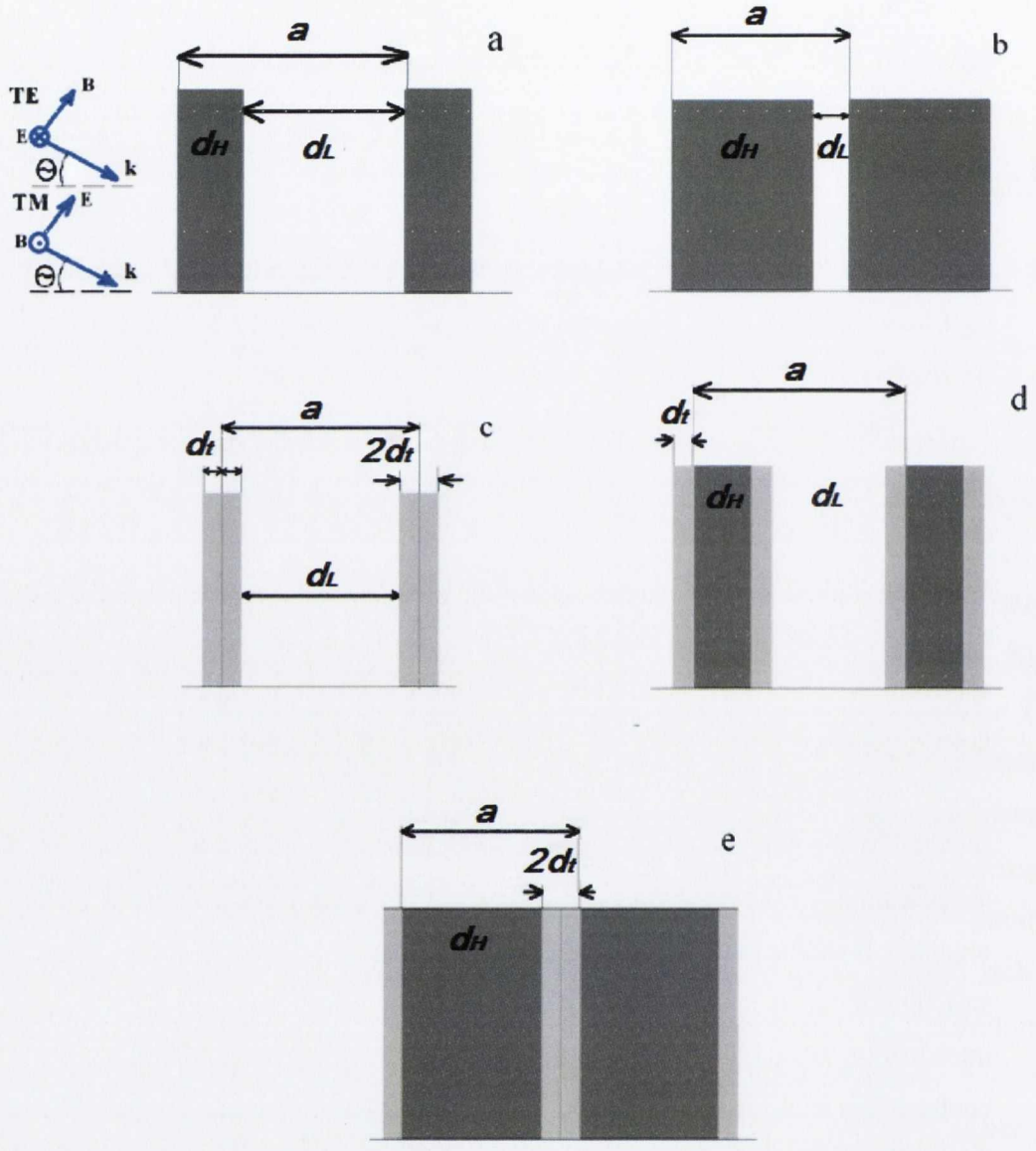

***Figure 3-1**: Schematic fragments of (a, b, c, e) two-component 1D PhC and (d) three-component 1D PhC with fixed value of lattice constant, a, and an additional t-layer. The thicknesses of H, L and t-layers are d_H, d_L, dt, accordingly.*

3.2 *Fabrication methods*

The possible multi-component Si-based photonic crystal structures suitable for practical applications can be realized by, for example:

1. Fabrication of additional layers on the Si based structures using different deposition techniques

   or

2. Alteration of the existing layers formed on the Si side-walls, by either wet etching or reactive ion etching.

Several illustrative examples are discussed below.

Example 1a. Using a 1D PhC based on a *"Si-air"* structure, that is, grooved Si [5], and following the introduction of an additional SiO_2 layer, tuning of the PBG edge, either the main one or the high order PBGs [2], can be performed with a high degree of precision. This is because manipulation of the SiO_2 thickness for either 1D or 2D PhCs [3] can be performed very accurately by either thermal oxidation or by partial removal by wet etching using chemical reagents (Figure 3-2(a)).

In addition, SiO_2 is a solid material which is strongly attached to Si walls without an associated transition layer at the Si-SiO_2 interface. Lowering the optical contrast in a high contrast *"Si-air"* PhC enables the formation of a new PhC with a quasi-complete PBG. For this case, the sequence of layers can be $n_{Si}/n_{SiO2}/n_{air}$= 3.42/1.5/1.

Example 1b. Using a 1D PhC based on a multilayered "*Si-Si0*$_2$" structure, and introducing an additional layer of Si_3N_4, one can obtain a similar tuning of optical contrast, since in modern, thin-film technology, deposition of layers with tight thickness control ranging from nanometer (monolayer) to several micrometers and the optical characteristics required is possible to a high degree of precision. The sequence of layers in this case can be $n_{Si}/n_{Si3N4}/n_{SiO2}$ =3.42/2.2/1.5.

Example 1c. Using stain-etching for the fabrication of an additional porous layer on the Si side-walls, one can obtain a new photonic system with the desired optical properties and/or use the micro-porous layer as a matrix for sensing [6] (Figure 3-2(b)). Since the micro-porosity can be controlled, this ultimately can be used for tuning of the original 1D or 2D PhC. The sequence of layers in this case can be $n_{Si}/n_{porSi}/n_{air}$ =3.42/1.2-3/1.

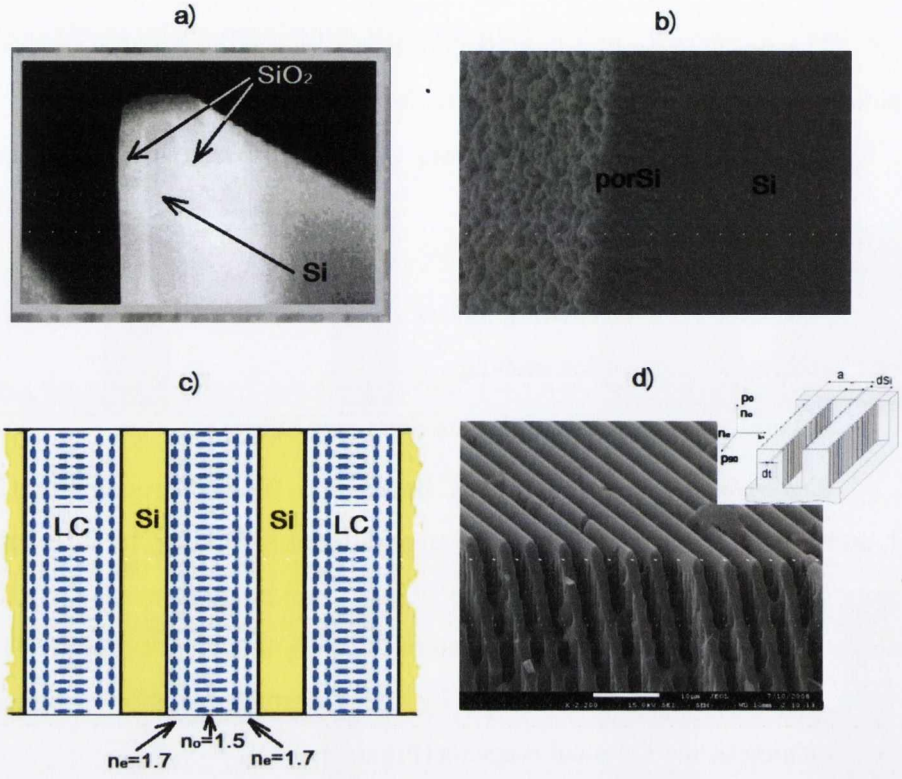

Figure 3-2: *Fabrication examples of the multi-component PhCs based on Si. Additional component obtained by a) thermal oxidation; b) stain etching; (c) infiltration with LC, and d) fabrication imperfection (here the corrugation of Si surface) as an additional t-layer.*

Example 1d. Fabrication of an additional component in 1D and 2D PhCs, based on a "*Si-LC*" structure. In this case, the additional layer can be formed at certain orientations of nematic LC (e.g. commercially available LC E7 by Merck [7]) at the Si-LC interface [8], which is different from the orientation of the LC in the bulk. For example, at the interface, the orientation of the LC could be planar with an extraordinary refractive index n_e=1.7, while in the bulk, the LC could be in a homeotropic orientation with respect to the Si walls, which exhibits the ordinary refractive index n_o=1.5 (Figure 3-2(c)). For this case, the sequence of layers can be $n_{Si}/n_e/n_o$=3.42/1.7/1.5.

Example 2. The additional *t*-layers can be formed by residual roughness with characteristic traces of the ribs left by the incompletely merged pores during electrochemical etching of Si [9] or the rough layer left after reactive ion etching. As the height of these residual ribs are comparable with the wavelength, they can be

considered as anisotropic layers with the direction of the ribs along the etch depth. This rib system can be considered as an effective medium formed by a stack of parallel Si planes with air gaps between them with refractive indexes n_{Si} and n_{air} correspondingly (Figure 3-2(d)). The effective refractive indexes, n_o and n_e, of the anisotropic layer can be described by formula for anisotropy of form [10]:

$$n_e^2 - n_o^2 = \frac{p(1-p)(n_{Si}^2 - n_{air}^2)^2}{(2-p)n_{air}^2 + pn_{Si}^2}, \quad (3.1)$$

where p is the rib system filling fraction. The values of n_o vary from 2.8 to 3.0, while those of n_e vary from 1.3 to 1.5 [11]. The following layer sequence can be considered in this case $n_{Si}/n_{rib}/n_{air}$ =3.42/1.3-3/1.

3.3 *Model of Multi-Component Photonic Crystal Structure*

3.3.1 Modelling of the additional regular layers

A micro-structured Si structure with linear grooves [12] is considered here as a model for a basic 1D PhC structure, (see Figure 3-1(a, b)). The refractive index of Si for the high-refractive index, *H*, component in the mid-IR range is chosen as $n_{Si}=n_H=3.42$. For the groove area, the refractive index of the low-refractive index, *L*, component, is considered to be $n_{air}=n_L=1$. In this case, the refractive index contrast is $n_H/n_L=3.42/1$ and the structure can be considered a high-contrast PhC. As a result, only a small number of periods N are needed to obtain a PBG with a reflectance of greater than 0.99. For comparison, the PhCs with other different contrasts, namely 3.42/1.5, 3.42/2.21, 2.21/1 and 1.5/1 are also considered here. We are looking for the common tendencies in PBGs caused by insertion of an additional regular *t*-layer with different refractive indexes, n_t, and thickness, d_t (Figure 3-1(d)). During selection of n_t values a particular attention is paid to two very common cases in practical applications i.e. when n_t is varied between 3.42 and 1. In particular, in the case of n_t = 1.5 we are dealing with an interlayer such as, for example, SiO_2 which can be deposited on Si walls with tunable thickness, while value n_t =2.21 we can use to take into account the roughness of Si walls (see Section 3.2).

In the latter case the optical characteristics of the roughness layer, n_{rib}, are equivalent to the effective homogeneous layer constructed from the combined parts of n_{Si} and n_{air}. This assumption holds if the parameters of roughness (rout-mean-square height and autocorrelation length) are much smaller than the wavelength of the incident

light. The value of n_t=2.21 for the porosity p=0.4 [9] is taken as the average value of the refractive indexes of Si, n_{Si} and air, n_{air}. The refractive index of the incoming and outgoing medium is 1.

Calculation of the reflection spectra of 1D PhCs with N periods and a filling fraction of Si, $f_{Si}=d_H/a$, where a is the lattice constant, can be performed using the TMM [13]. An attractive feature of the method is the ease of introducing any number of additional layers at any point in the TMM's equation (see Chapter 2).

The Transfer Matrix S_2 used in calculations for a two-component 1D PhC structure, is given schematically by:

$$S_2=((I\cdot M)_H\cdot(I\cdot M)_L)^N\cdot(I\cdot M)_H \qquad (3.2)$$

for a three-component PhC matrix S_3, as shown in Figure 3-1(b), is:

$$S_3=((I\cdot M)_t\cdot(I\cdot M)_H\cdot(I\cdot M)_t\cdot(I\cdot M)_L)^N\cdot(I\cdot M)_t\cdot(I\cdot M)_H\cdot(I\cdot M)_t, \qquad (3.3)$$

where $(I\cdot M)_H$, $(I\cdot M)_L$ and $(I\cdot M)_t$ are the matrices of the H, L and t-layers respectively.

3.3.2 Gap Map presentation

For each reflection spectrum calculated, the region of Normalized Frequency ($NF=a/\lambda$) where the reflection is greater than 0.99 was recorded on the plot. The PBG ranges obtained were then plotted, over a range of filling fractions, to give a plot known as a Gap Map (see Chapter 2 for more details). The result is displayed in Figure 3-3. For both GM and spectral calculations, the optical characteristics are presented in unitless dimensions of NF and, therefore, can be applied to a wide range of structure sizes, including micro- and nano-structures.

The lattice constant, a, and the t-layer thickness, d_t, do not change, since t-layers with refractive index n_t were introduced on both sides of the H-layer in the PhC structure, as shown in Figure 3-1(b). When generating f_{Si}, the value of d_H for both the two-component and the three-component PhCs was kept the same. Thus, we can compare the two different PhC structures using the same f_{Si} scale. As shown in Figure 3-1(c, e), d_L decreases by $2\cdot d_t$. When plotting the GM for this structure, not all filling fraction values f_{Si} from 0.01 to 0.99 can be realized. The larger the value of d_t, the lower the maximum value of the filling fraction f_{Si} that can be realized in the three-component PhC.

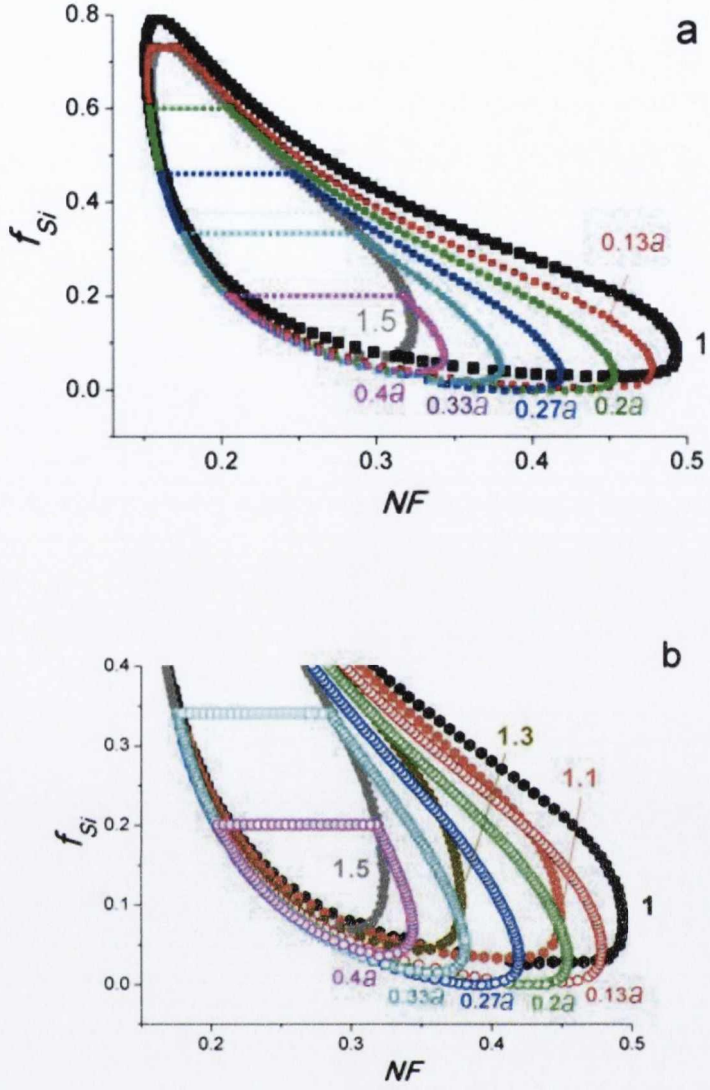

***Figure 3-3**: a) The lowest stop-band regions for GMs of three-component 1D PhCs, obtained from a two-component PhC with optical contrast 3.42/1 (curve 1) with an additional regular t-layer with various thicknesses d_t, shown, in units of a, by numbers beside the PBG areas. The value of n_t=1.5, number of periods N=10 and a normal incidence of light. For comparison, a two-component PhC with contrast 3.42/1.5, marked as 1.5, is also shown. The cutoff lines of the PBG regions correspond to $maxf_{Si}$=0.74 for d_t=0.13a, $maxf_{Si}$=0.6 for d_t=0.2a, $maxf_{Si}$=0.46 for d_t=0.27a, $maxf_{Si}$=0.34 for d_t = 0.33a and $maxf_{Si}$=0.2 for d_t=0.4a; b) Comparison of the lowest PBG areas for three-component and two-component PhCs with different optical contrasts (3.42/1, 3.42/1.1, 3.42/1.3 and 3.42/1.5), shown by numbers beside the curves.*

In order to clarify this, consider an illustrative example with a=3 μm. This modifies the Si wall thickness $d_H=a \cdot f_{Si}$ from 0.03 to 2.97 μm. A t-layer thickness was taken, in this example, as d_t=0.4 μm, corresponding to the parameter d_t =0.13a. From Table 3-1, the GM for the three-component PhC can be calculated only up to the maximum value of the filling fraction, $maxf_{Si}$, depending on d_t. In units of a, this covers the range from 0.03a to 0.47a.

***Table 3-1**: The maximum value of the filling fraction, $maxf_{Si}$, for various values of t-layer thicknesses, d_t, required for GM calculations of a three-component PhC with a lattice constant a=3 μm.*

d_t, μm	0.1	0.2	0.3	0.4	0.6	0.8	1.0	1.2	1.4
d_t/a	0.03	0.07	0.10	0.13	0.20	0.27	0.33	0.40	0.47
$maxf_{Si}$	**0.94**	**0.86**	**0.80**	**0.74**	**0.60**	**0.46**	**0.34**	**0.20**	**0.06**

3.4 Engineering of the optical contrast

3.4.1 Normal Incidence of Light

i) Influence of t-layer thickness on Gap Map formation

It is assumed that light is incident normal to the PhC structure and the angle θ=0° (Figure 3-1(a)). We select an n_t value between 3.42 and 1, for example, n_t =1.5. Note we are dealing with an interlayer such as SiO_2, which can be deposited on Si walls with tunable thickness.

Let us calculate the GM of the lowest PBG for the PhC (N=10) with d_t=0.13a (Figure 3-3(a), curve 0.13a) and compare that with the GM for the original two-component PhC with d_t=0 (Figure 3-3(a), curve 1). As can be seen in Figure 3-3(a), $maxf_{Si}$ restricts the formation of the PBG according to the data presented in Table 3-1. Hence, the GM was drawn for PBGs calculated over a range of filling fractions, f_{Si}, from 0 to 0.74. For other d_t values, different GMs with corresponding cutoff lines at $maxf_{Si}$, as shown in Figure 3-3(a), will be obtained. In Figure 3-3(a), the first PBG was considered for PhC structures with different t-layer thicknesses. A red shift of the PBG's blue edge as d_t increases is apparent from this figure. In the limiting case, as the t-layer thickness d_t increases to the maximum value, the L component tends to disappear

and is totally replaced by the *t*-layer (Figure 3-2(e)). In this case, we obtain a two-component PhC again but with a different optical contrast of 3.42/1.5. Indeed, the cutoff line at f_{Si}=0.74 intersects two SB areas for the first three-component PhC (d_t=0.13a) and for the second two-component PhC, but with a different contrast n=3.42/1.5. Similar trends are observed for other d_t values as shown more clearly in Figure 3-3(b) (d_t/a=0.33 and 0.4a).

ii) Influence of t-layer refractive index on Gap Map formation

Figure 3-3(b) enables the determination of the thickness of the additional layer with n_t=1.5 (at a value of f_{Si}=0.2) which forms a similar PBG to that in a two-component PhC with a specific value of n_L. It can be seen that the PBG edges for n_L=1.1 and 1.3 for the two-component PhC intersect the PBG edges for the three-component PhC at f=0.2 with d_t=0.13a and 0.27a. As a result, we observe an impact on the PBG areas of the three-component PhC, demonstrating the possibility of manipulating the optical contrast by changing the *thickness* of the additional regular layer in the PhC structure. In other words, the d_t value provides an equivalent value of n_L^{equ} for a two-component PhC with the same n_H value. However, in our case, the range of possible f_{Si} values for PhC fabrication decreases significantly. This in turn leads to a reduction of the regions of PBGs on the GM. For example at d_t=0.33a, the values of f_{Si} range from 0 to only 0.34 (Figure 3-3(a)). It is worth mentioning that the remaining portion of the PBG's on the GM is still comparable to that for the original two-component PhC and, indeed, they remain the widest PBGs inside this range of f_{Si}.

In order to prove the equivalency concept demonstrated in Figure 3-3(b), the three-component "*Si-SiO$_2$-air*" PhC structure was fabricated using optical lithography and Deep Reactive Ion etching of (100)Si (see Chapter 2 for details) followed by thermal oxidation at 1000°C in order to grow a smooth oxide layer of thickness d_{Si}=580nm on top of Si side walls. The reflection spectrum of the obtained structure was measured in mid-infrared range from 2000 to 7000 cm^{-1} using FTS 6000 FTIR spectrometer in conjunction with a UMA IR microscope. Note, the reduction of the maximum R intensity as well as a smoothinig of the "Π"-shape of PBGs in the experimental spectra (Figure 3-4) is due to the "shading" effect from the substrate of the structure and cone-like shape of the light beam (see Section 2.4). The simulations of the obtained experimental spectrum have demonstrated that the positions and width of the PBGs of the fabricated three-component structures are *the same* as for the same

structure without the third component but instead infiltrated with some unknown filler with refractive index n_L=1.185 (Figure 3-4). Obviously, manipulation of the PBG parameters by changing the thickness of the additional layer is the preferred route. Apart from the thickness, one can also vary the n_t value of the additional layer and, by doing so, obtain the dependence of $n_L^{equ} = f(n_t)$. An example of this for values of n_t = 2.2 and 3 is shown in Figure 3-5, along with results obtained earlier for n_t =1.5. As can be seen from this figure, for the parameters of n_t selected, the range of n_L^{equ} can be varied from 1.1 to 2.2.

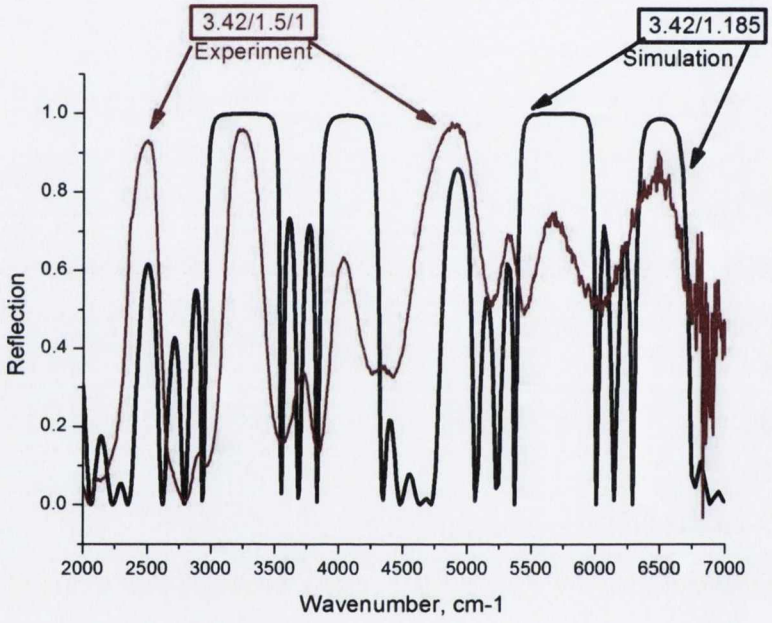

Figure 3-4: *Equivalency of the experimental PBGs of three-component PhCs with N=4, a=4μm and f_{Si}=0.157 with additional layer thicknesses of the SiO_2, d_{Si02}=580nm and simulated PBGs of the same PhC without SiO_2 component, but infiltrated with some unknown filler with refractive index n_L=1.185.*

The examples illustrate the influence of n_t and d_t on PBG formation, since both of these parameters can be altered technologically. For example, the refractive index of the additional layer can be changed keeping the thickness constant, or the additional layer with a constant value of n_t can be fabricated with different thicknesses using various deposition techniques from the gas or liquid phase, or by thermal oxidation. We conclude that using a multi-component PhC is a viable alternative technique for the

alteration of the optical contrast of PhCs and, therefore, for tuning the position and width of PBGs in the reflection/transmission spectra of these structures.

Let us analyse what happens to PBGs of high order following the introduction of an additional layer using the GM of PBGs in the range of NF = 0-2.5. As can be seen from Figure 3-6, the introduction of the t-layer with different d_t =0.13a and n_t =1.5 results in:

- a decrease in the area of every PBG region,
- a red shift of the PBG regions with respect to the original two-component PhC.

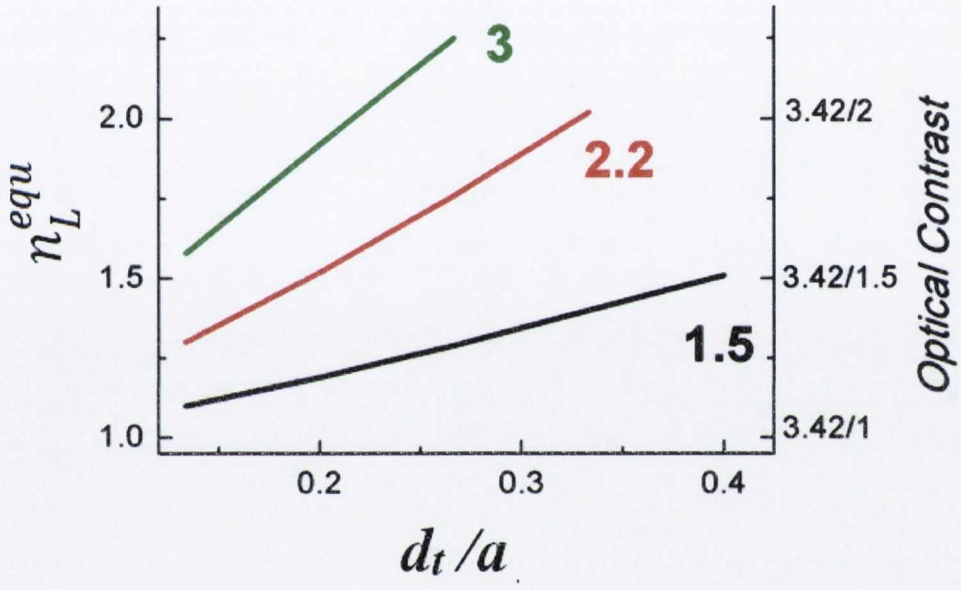

***Figure 3-5**: The dependence of n_L^{equ} (which is equivalent value for a two-component PhC) versus d_t/a for three-component PhC with a t-layer of thickness, d_t, and refractive index, n_t, (the numbers beside the lines) and f_{Si}=0.2.*

A decrease of the PBG width with an increase in the t-layer thickness can also be seen in Figure 3-3(a) for the lowest PBG in more detail. Similar behavior was observed earlier in the GM of PBGs in a two-component PhC as n_L increased [12, 14]. Thus, the introduction of the t-layer has a similar effect to the substitution of n_L, i.e. it serves to decrease the optical contrast or, in accordance with Ref. [3], to decrease the effective dielectric constant. As can be seen from Figure 3-6, the size of the high-order SBs regions for three-component PhCs differs from that in ordinary PhCs. In the range of NF values from 1 to 1.5, a suppression of high order PBGs takes place. The

suppression of stop-bands and their replacement with transparent regions was investigated earlier for multi-layer films in Refs. [15-17]. A similar narrowing effect was also observed in our case for the high-order PBG realized for Si-based PhC, as shown in Figure 3-6. One possible explanation of this effect is that the third component is acting as an antireflection coating, suppressing the high order PBGs. This interesting effect will be a subject for investigation in the next Section 3.5.

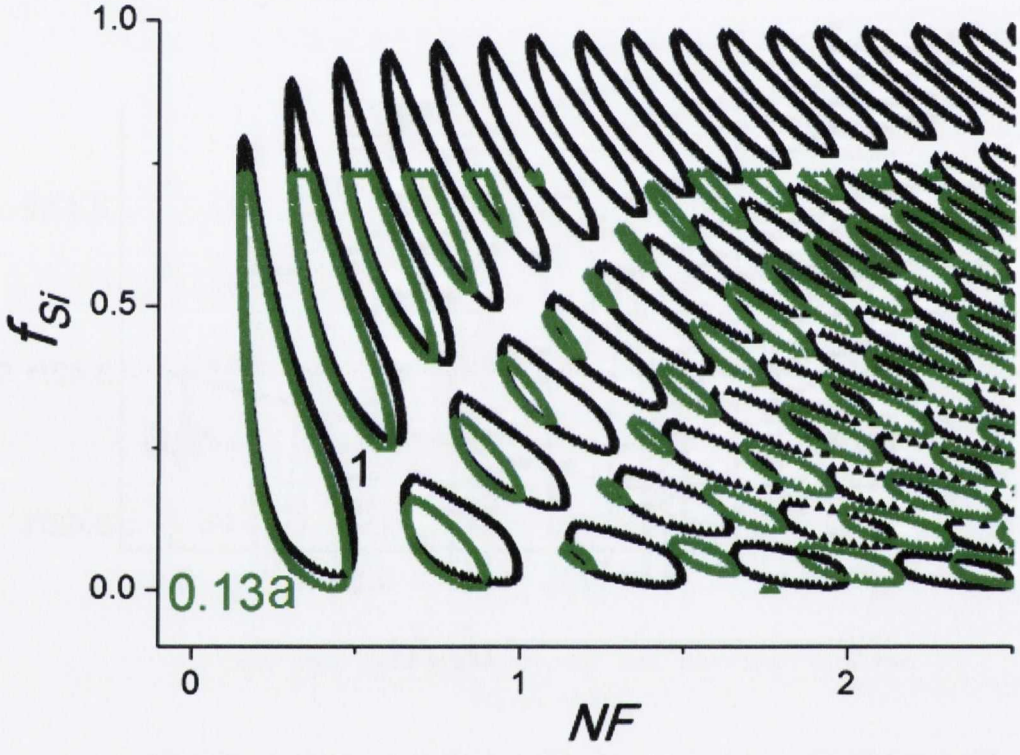

***Figure 3-6**: Influence of the t-layer (d_t/a=0.13a) on the shift and decrease of PBG regions of high order in the region NF=0-2.5.*

Furthermore, we have developed a series of maps with the lowest PBGs for the consequent two-component PhC by changing the optical contrast of the original two-component PhC from 3.42/1 to 3.42/1.5 and letting n_t =2.2 (see Figure 3-7(a)). As shown earlier, we obtain tuning of the optical contrast by introduction of the additional *t*-layer. Using a smaller value of n_t =1.7, we have obtained a much smaller shift of the blue edge of the PBG as seen in Figure 3-7(b). In summary, we demonstrate, once again, the possibility of tuning the optical contrast of a three-component PhC by varying either the thickness or the refractive index of the *t*-layer.

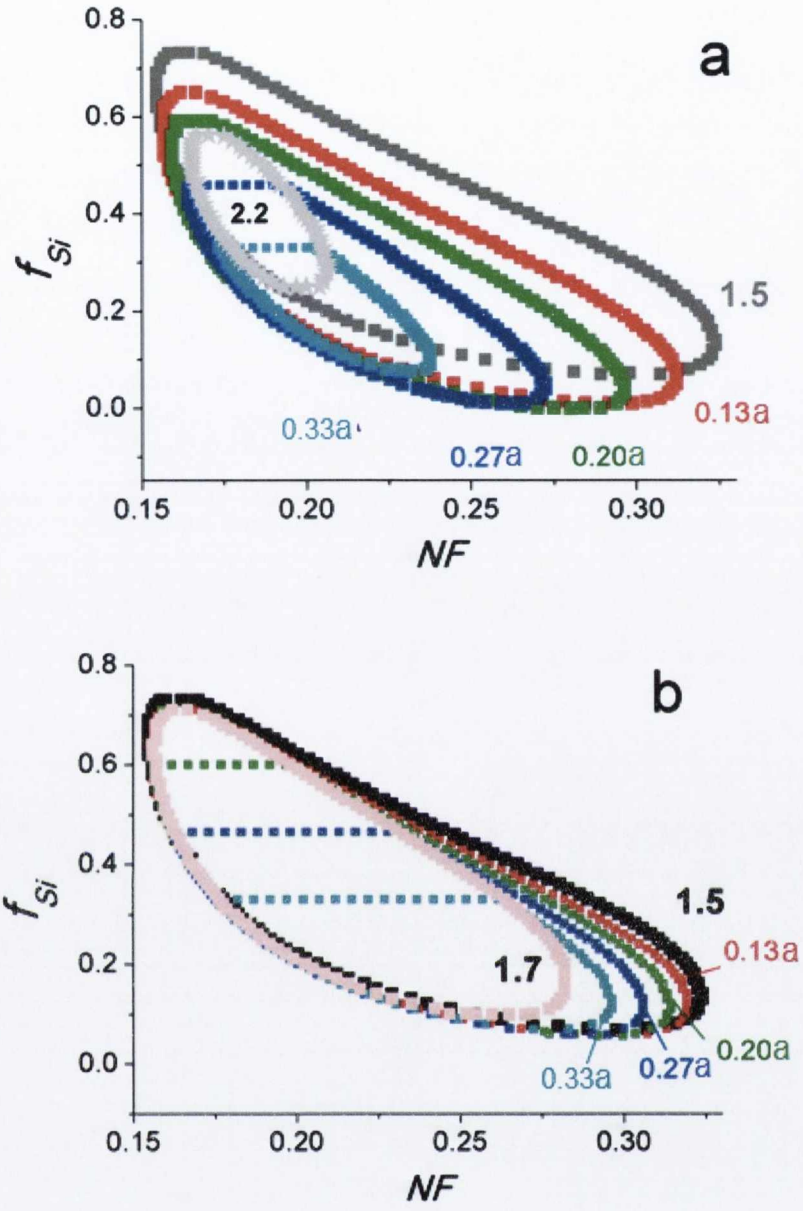

Figure 3-7 *:a) Gap maps of a two-component 1D PhC with contrast n=3.42/1.5 (curve 1.5) with added t-layers of different thicknesses d_t, shown beside the curves in units of a, and with refractive index n_t=2.2. The GM with contrast n=3.42/2.2, the SB region marked as 2.2, is also presented for comparison. (b) Gap maps of a two-component 1D PhC with contrast n=3.42/1.5 (curve 1.5) with added t-layers of different thicknesses with a refractive index n_t=1.7. The GM with contrast n=3.42/1.7, marked as 1.7, is presented for comparison. The calculation is performed at a normal incidence of light with the number of periods N=10. The cutoff lines are the same as in Figure 3-3. Note that only the lowest stop-band areas are shown for simplicity.*

It is worth noting that the additional layer, with a definite optical thickness, $n_t \cdot d_t$, introduces a contribution to the overall interference of the reflected wave, but it does not have a damaging effect on the R value in the PBGs. As can be seen from Figure 3-3 and Figure 3-7, the reflection coefficient is still equal to 0.99, since this value is still the criterion for PBG formation. However, this is a rough estimate. We will consider further how under these conditions the quality of the reflection bands is changed within the PBGs, because different perturbation factors often result in a decrease in the absolute value of the reflection coefficient in the PBG to R=0.9 or even less. In addition, changing the shape of the PBG can increase the noise level and other types of band degradation can also occur. Typically, these effects are better seen in transmission mode of the lowest PBG. The spectrum for a contrast of 3.42/1 and a filling fraction of f_{Si}=0.23, corresponding to the quarter wavelength thickness of the layers, is shown in Figure 3-8 with the smallest transmission value of T=10^{-11}. The introduction of a t-layer

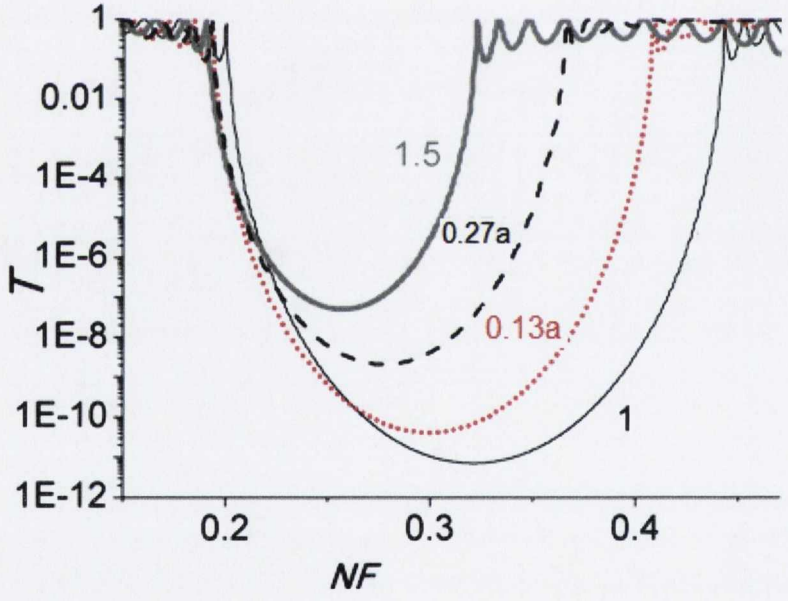

***Figure 3-8**: Transmission spectra shown for the lowest SB areas for a two-component PhC with an optical contrast of 3.42/1 (curve 1) and 3.42/1.5 (curve 1.5) and for three-component PhCs with an additional t-layer of n_t=1.5 and thicknesses of d_t=0.13a and 0.27a. Calculations were performed at a normal incidence of light with f_{Si}=0.23 and N=10.*

with d_t =0.13a increases T to 10^{-10}, while this increases to T=10^{-7} at a lower PhC optical contrast of 3.42/1.5. Therefore, the introduction of the t-layer affects the properties of

the lowest PBG, not as a degradation factor, but as a characteristic tendency to decrease the optical contrast of the PhC.

3.4.2 Oblique incidence of light: Omni-directional properties

It is known [18] that the omni-directional band in the gap map is determined by the overlapping regions of the stop-bands obtained for different angles of incidence and various polarizations of light. Using the TMM, reflection spectra can be obtained for different deviation angles, θ, of the wave-vector from the normal (see Figure 3-1(a)), over a range of θ from 0° to 90° for TM- and TE-polarizations, where TM and TE are the Transverse Magnetic and Transverse Electric polarizations, respectively.

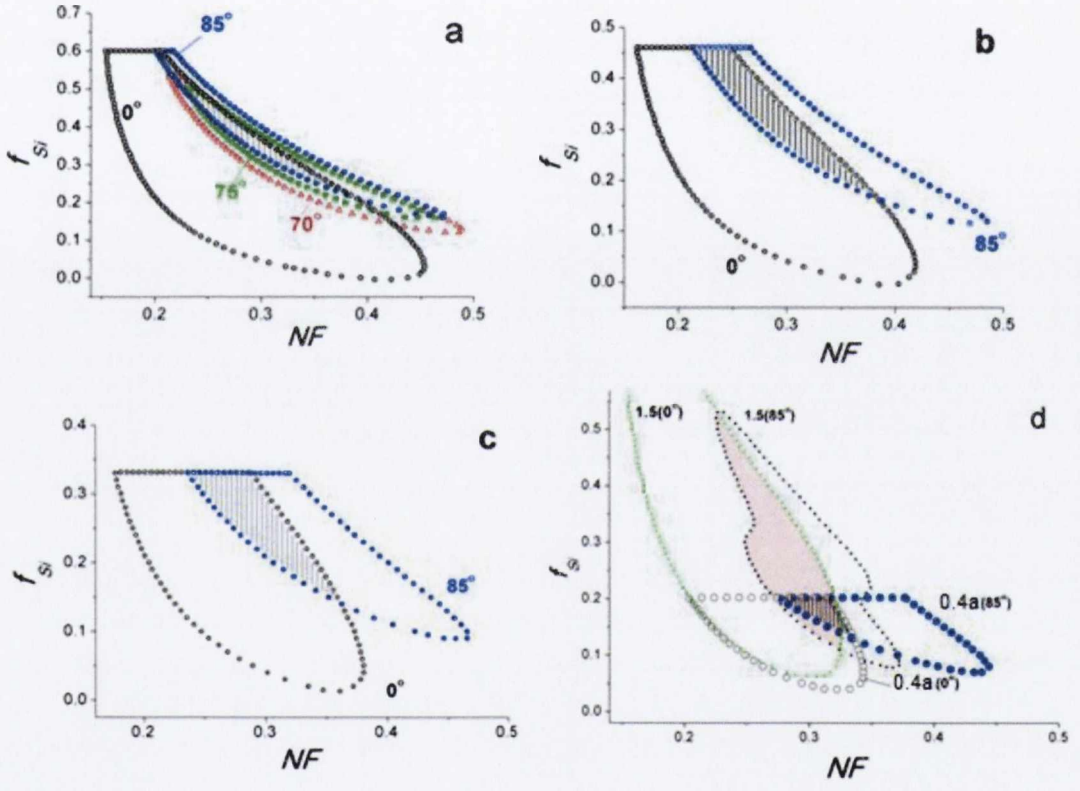

***Figure 3-9**: Gap maps, demonstrating the formation of an ODB region (the striped area), as a common area formed by the overlapping of PBG regions at different angles of incidence. Angles of incidence are indicated by the number beside the curves. The contrast was 3.42/1 and the additional layer had n_t=1.5 and a) d_t=0.2a, b) d_t=0.27a, c) d_t=0.33a and d) d_t=0.4a. ODB regions for a two-component PhC with contrast of 3.42/1.5 (grey region) and for three-component PhC (striped region) are shown for comparison in (d).*

The width of the PBGs for TE-polarization increases with an increase in θ, while for TM-polarization it decreases. As a rule, it is necessary first to be sure that the PBGs for TM-polarization have a common area for different θ and then to identify this area as the ODB. Let us perform the GM calculation for an optical contrast of 3.42/1 and number of periods N=10. The ODB region does not form for this optical contrast [19]. The additional introduced layer is of thickness d_t=0.2a and refractive index n_t =1.5 with angle of incidence change from θ = 0° to a maximum value of 85° with a step size of 5°. Figure 3-9(a) shows that the photonic band gaps obtained for TM-polarization overlap at different angles θ. Note that, for clarity, only a few angles viz. θ =0°, 70°, 75°, 85° are shown on Figure 3-9(a). They form a common ODB area, shown by the striped area.

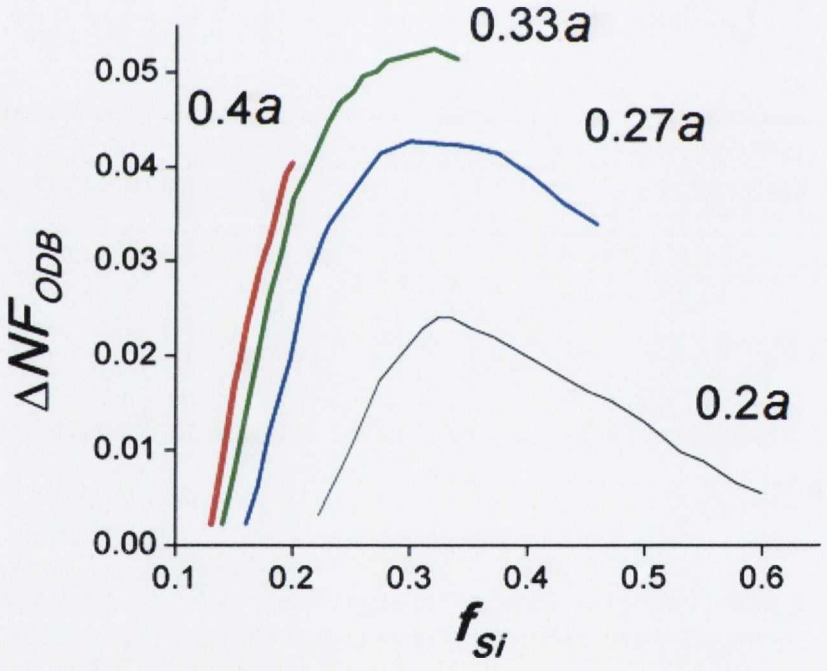

***Figure 3-10**: The width of ODBs versus filling fraction (calculation from Figure 3-9).*

This region is formed in the three-component PhC under consideration over a range of filling fractions, f_{Si}, from 0.25 to 0.6, causing the position of the ODB region to vary from 0.22 to 0.39 in units of NF. Note that the cutoff line of the PBG is located at higher values of f_{Si} than are necessary for formation of the ODB (see Figure 3-9(a)), therefore the parameter $maxf_{Si}$=0.6 does not limit the f_{Si} values for a PhC with an ODB. Figure 3-10 demonstrates the dependence of the ODB width (ΔNF_{ODB}) on f_{Si}, from which the region of formation of the ODB can be deduced for f_{Si} values from 0.22 to 0.6

with a maximum ΔNF_{ODB}=0.024 at f_{Si}=0.31. As pointed out in Ref. [20], this value does not correspond to $\lambda/4$ layers, corresponding to f_{Si} = 0.23 for the PhC with contrast 3.42/1, and shifts to higher values of f_{Si} due to the necessity of taking into account overlapping of the PBG at different angles of incidence and different light polarizations.

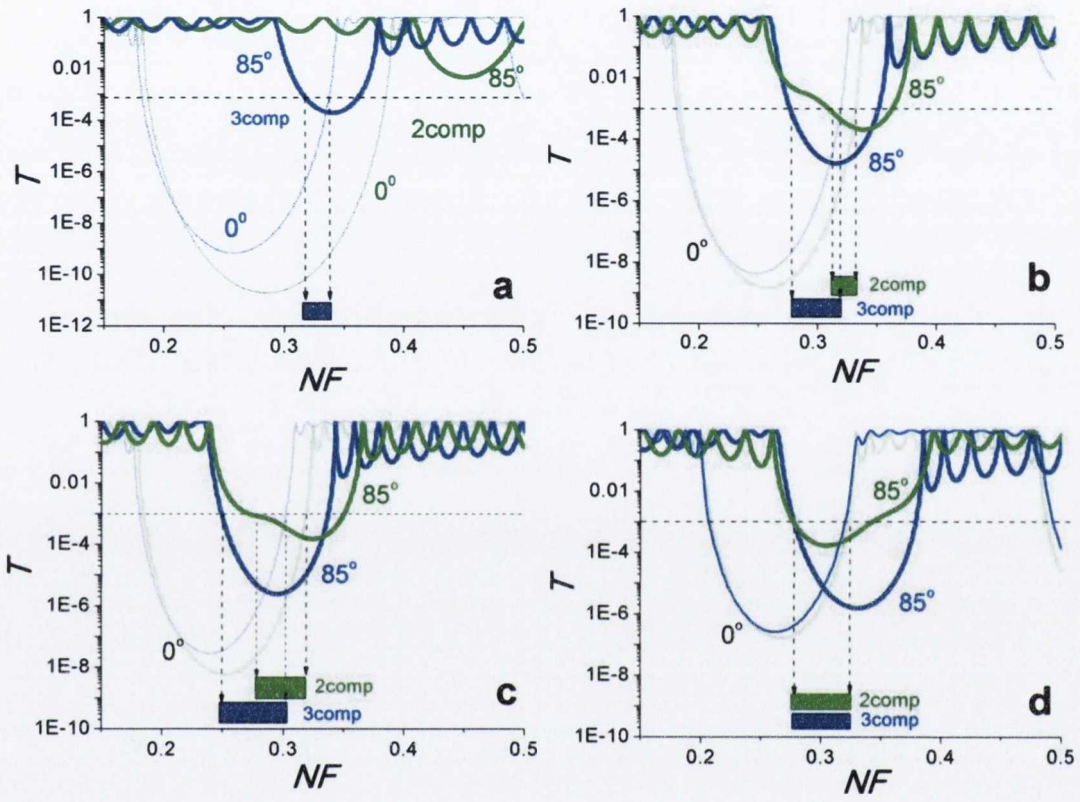

***Figure 3-11**: Transmission spectra T and ODB width (filled rectangles) shown for the first PBG at incident angles of 0° and 85° for: a) three-component PhC (denoted as 3comp) with an additional layer n_t=1.5 and d_t=0.2a and two-component PhC (denoted as 2comp) with optical contrast 3.42/1 without ODB region (filling fraction f_{Si}=0.3); b) three-component PhC with an additional layer n_t=1.5 and d_t=0.27a and two-component PhC with contrast 3.42/1.2 (f_{Si}=0.3).; c) three-component PhC with n_t=1.5 and d_t=0.33a, f_{Si}=0.3 and two-component PhC with contrast 3.42/1.4 (f_{Si}=0.3); d) three-component PhC with additional layer n_t=1.5 and d_t=0.4a and two-component PhC with contrast 3.42/1.5 (f_{Si}=0.2).The dashed line corresponds to the level of Tpbg=0.001(or Rpbg=0.999).*

As mentioned above, introduction of the t-layer with d_t=0.2a is in fact equivalent to an increase of the n_L value to ~1.2. This is higher than the minimum value of n_L=1.1, which allows the appearance of ODBs in high optical contrast PhCs [18]. However, in practice it is problematic to find a suitable filler with a refractive index n_L=1.1-1.2 for impregnation into a PhC. Therefore, introduction of a t-layer is the preferred approach in this case.

Let us now use another value of d_t =0.27a for calculating the GM (see Figure 3-9(b)) and plot two stop-bands only, which determine the ODB areas for TM-polarization and incident angles in the range 0° to 85°. As shown in Figure 3-9(b), and in accordance with Table ***3-1***, the cutoff line is drawn at a value of f_{Si}=0.46 and actually truncates the ODB. At the same time, the maximum ΔNF_{ODB} increases to 0.043. The increase of d_t to a value of 0.33a leads to a lowering of the cutoff line (see Figure 3-9(c)), as expected, and to a simultaneous increase in ΔNF_{ODB} (Figure 3-10, line 0.33a). A further increase of d_t to 0.4a significantly decreases ΔNF_{ODB} (Figure 3-10, line 0.4a). Since the introduction of layer d_t is equivalent to a reduction in the optical contrast of the PhC, at the limit of this case we should obtain a PhC with contrast 3.42/1.5. Indeed, as can be seen in Figure 3-9(d), the ODB area for the three-component PhC, shown by the striped area, practically overlaps the ODB area for the two-component PhC, the grey area, within the limit of the permitted range of f_{Si}.

In order to demonstrate the qualities of PBGs in transmission T spectra, T-spectra were calculated using a filling fraction f_{Si} = 0.3 from Figure 3-10, for which maximum ODB width can be achieved. Calculated transmission spectra are presented in Figure 3-11. For a sample with d_t =0.4a, we can select a value of f_{Si} =0.19 due to the cutoff line. The spectra obtained demonstrate overlapped regions of stop-bands for TM-polarization and two incident angles of 0° and 85°. In producing this plot, transmission spectra were calculated over the total range of possible angles of incidence with a step size of 5°, but these were omitted from the plot for clarity.

Figure 3-11(a) shows spectra for comparison from a two-component PhC with a contrast of 3.42/1. The structure does not form an ODB, since there is no overlapping of the PBGs for angles of incidence of 0 and 85°, see the curves corresponding to 0° and 85° for the two-component case on the plot. At the same time, introduction of a t-layer with d_t =0.2a results in overlapping of the PBGs and leads to the formation of an ODB area. A similar effect is observed for other ODB areas with different t-layers (see Figure

3-11(b-d)). As can be seen from all the plots presented in Figure 3-11, the introduction of the *t*-layer into ordinary two-component PhC does not decrease the width of the ODB area.

3.5 Formation of Infrared Regions of Transparency

An analysis of the GMs of the PBGs for the three-component PhC revealed a red shift, as well as a decrease of the PBG area, with respect to the original ordinary two-component PhC, with an increase of the *t*-layer thickness, d_t (see Figure 3-6). Further investigation has revealed that for the small number of period $N<10$ the high order PBGs are not only suppressed but can be vanished in a wide frequency and entire filling fraction range.

3.5.1 Suppression of Photonic Band Gaps

In Figure 3-12 we compare the GMs over a wide range of *NF* for an ordinary two-component "*Si-air*" PhC (grooved Si) with the number of periods $N=5$ and for multi-component PhC based on the same "*Si-air*" structure after introduction of the regular *t*-layer with thickness of $d_t = 0.10a$. It is apparent that the lower PBGs are least affected by the addition of the *t*-layer, retaining a similar area and experiencing a negligible red shift in frequency. At the same time, inspection of the high-order PBGs over the entire range of *NF*, reveals regions of frequency, or equivalently wavelength, for which PBGs are suppressed, with $R<0.99$. Note that the SBs determined for the original "*Si-air*" PhC structure are not suppressed over the entire *NF* range (Figure 3-12). A detailed examination of the suppressed high-order PBGs in these frequency regions reveals that PBGs are not only significantly suppressed, but can actually disappear, with $R=0$. It is obvious that the regions of transmission could appear in these regions of frequency instead. Let us calculate a set of transmission spectra for a multi-component 1D PhC with a *t*-layer thickness of $d_t=0.1a$ over a range of f_{Si} values from 0.08 to 0.1 with a step size of $\delta f_{Si}=0.001$ (Figure 3-13(a)). Indeed, the transmission bands are formed between the suppressed PBGs, with *R* less than 0.99. It is clear from Figure 3-13(a) that the TB's range is constant for filling factors, f_{Si}, in the range 0.083 to 0.093, that is, with a change in the filling factor of $\Delta f=0.093-0.083=0.01$. Additional detail can be seen in Figure 3-13(b), where the transmission range is expanded across the range of transmissions from 0.97 to 1 in order to increase the clarity of the diagram. As shown in Figure 3-13(b), the width of the TBs is also dependent on the selection of

the cutoff transmission value. For example, if a cutoff transmission was chosen as 0.995, then the TBs within a narrow range of *NF* will appear narrower and less uniform than those for a cutoff level of 0.99. The choice of an appropriate cutoff level is an important design criterion when engineering practical device structures. Let us consider an example of the design of a real band-pass filter based on the three-component PhC model from Figure 3-13. Suppose the lattice period, a, is 3000 nm and the Si-wall thickness, $d_H = f_{Si} \cdot a$, is 260 nm, corresponding to a filling factor f_{Si}=0.087. According to Figure 3-13(b), such an optical filter has a wide pass-band with bandwidth of 0.36 *NF* (350 nm) centered at *NF*=1.7 or a wavelength $\lambda = a/NF$=1760 nm for a cutoff level T=0.99. From Figure 3-13(a) the filling factor deviation Δf_{Si} is up to 0.03, which corresponds to the possible Si wall thickness deviation Δd_H=30 nm for this particular example filter.

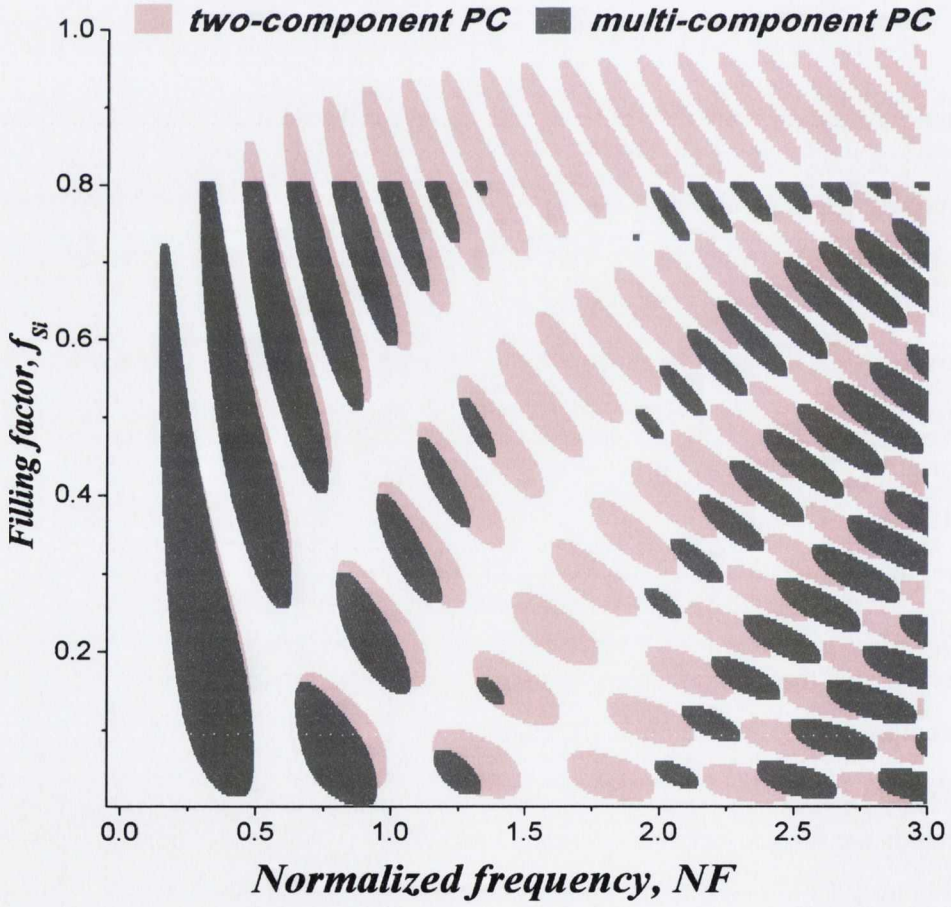

Figure 3-12: *GMs for a two-component "Si-air" PhC (light regions) and for a multi-component PhC with n_t=1.5 and d_t=0.10a (dark regions) over a wide range of NF; maxf_{Si}=0.80. The calculations are performed at normal incidence of light with number of periods N=5.*

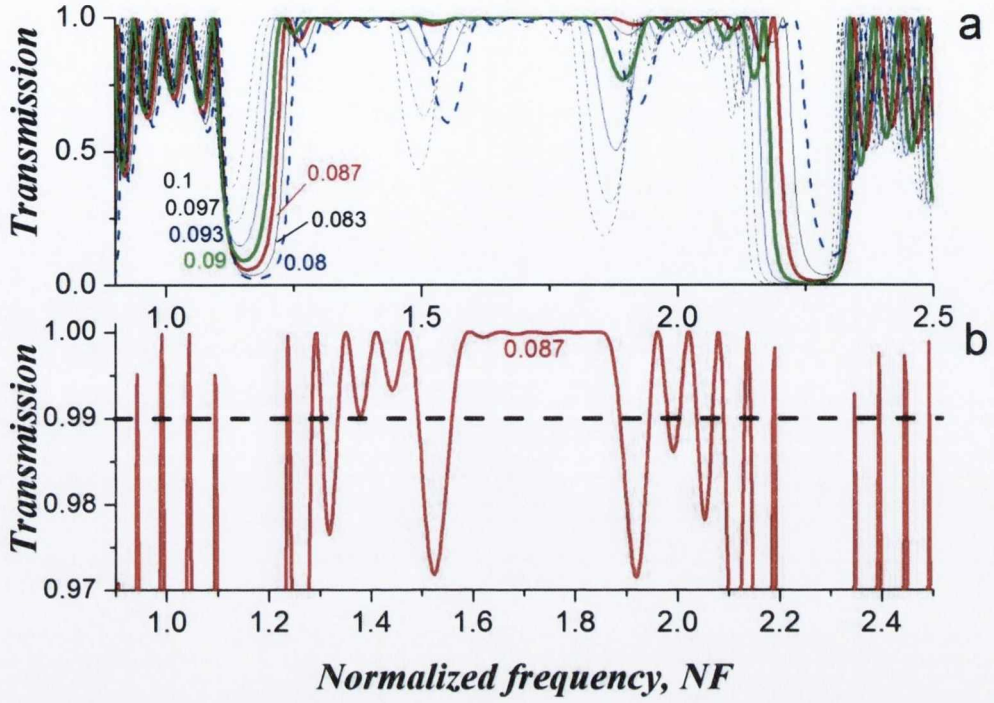

***Figure 3-13**: The transmission spectra T for multi-component PhC with t-layer refractive index n_t=1.5 and thickness d_t=0.10a for (a) f_{si}=0.08...0.1. (b) The same as in figure (a) shown for clarity in expanded transmission scale for f_{si}=0.087. The calculations are performed at normal incidence of light with number of periods N=5.*

3.5.2 Influence of the additional component thickness

Now that we have established the general criteria for TB formation, we can plot a map of the regions of transparency (RTs) for the multi-component PhC by analogy with the GM for PBGs [14, 19]. In order to avoid plotting very narrow peaks with high transmission, T>0.99, from the spectrum in Figure 3-13(b) (see, for example, peaks at NF=1, 2.2, 2.4) we need to define a minimum range of ΔNF>0.01, which provides transmission values T>0.99. Removal of the narrow regions, by defining ΔNF<0.01 greatly improves the clarity of the TBs. In Figure 3-14(a) the map of TBs is demonstrated with the GM, simulated for the "*Si-air*" PhC structure with additional component with refractive index n_t=1.5 and thickness d_t =0.13a. It is apparent, that the TB regions are located between the SBs areas of the corresponding PhC structure. Note the total suppression of high order SBs over a range of NF from ~1.1 to ~1.5. This NF range also contains the widest TBs. This is also confirmed by the transmission

spectrum, shown below in Figure 3-14(b). Therefore, we conclude that the third layer in 1D PhC structure can be treated as an antireflection layer by analogy with multilayer dielectric coatings.

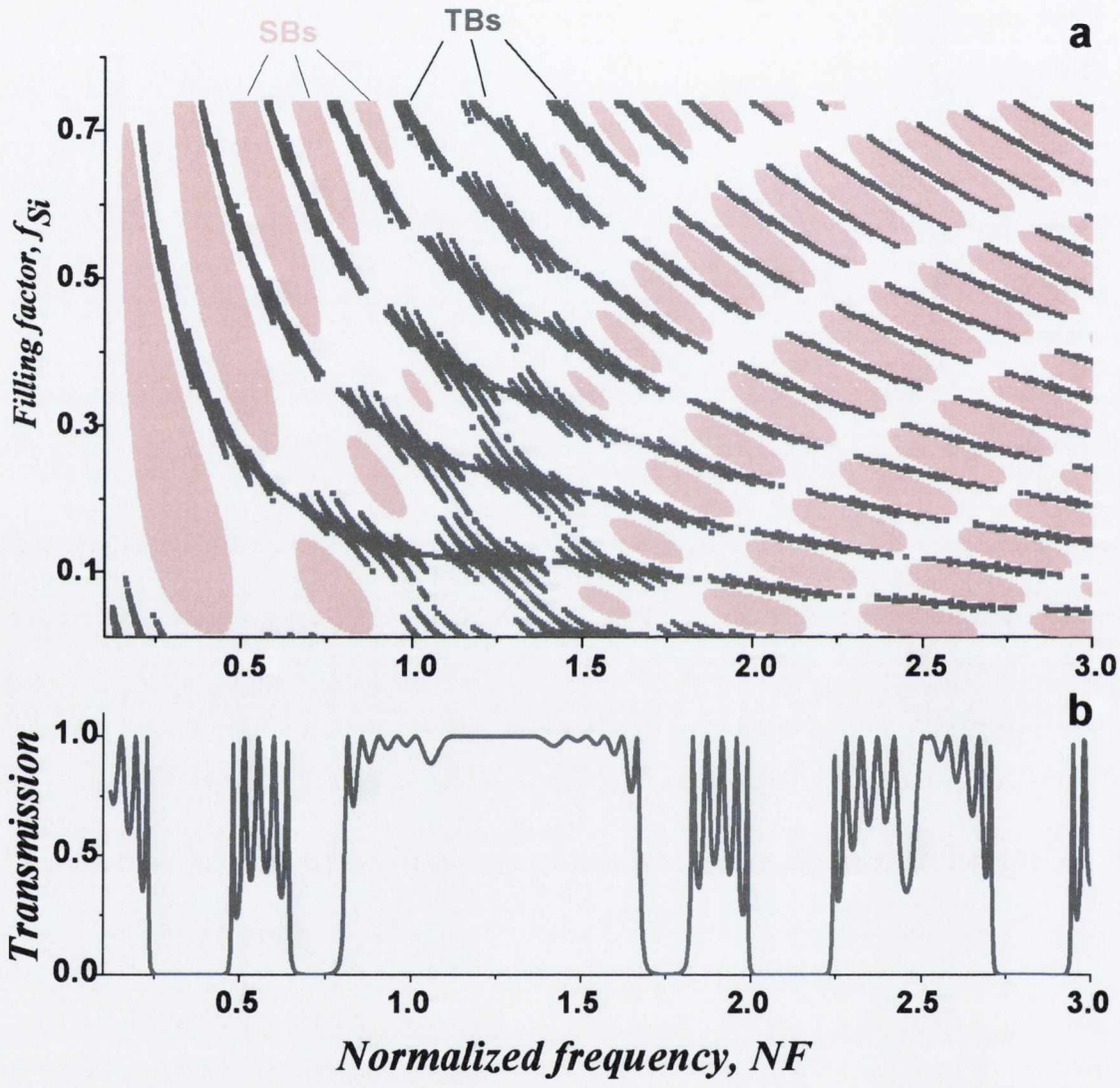

Figure 3-14: *a) The GM of stop-bands (R>0.99), denoted as SBs, and map of transmission bands (T>0.99), denoted as TBs, for the multi-component PhC with n_t=1.5and d_t=0.13a. b) The transmission spectrum T for the same multi-component PhC for f_{si}=0.117. The calculation is performed at normal incidence of light with number of periods N=5.*

It should be noted that the PBGs, also referred here as SBs, determined for the ordinary PhC structure, shown in Figure 3-12, are not suppressed over the whole *NF* range and, therefore, originally have no wide TBs in this range.

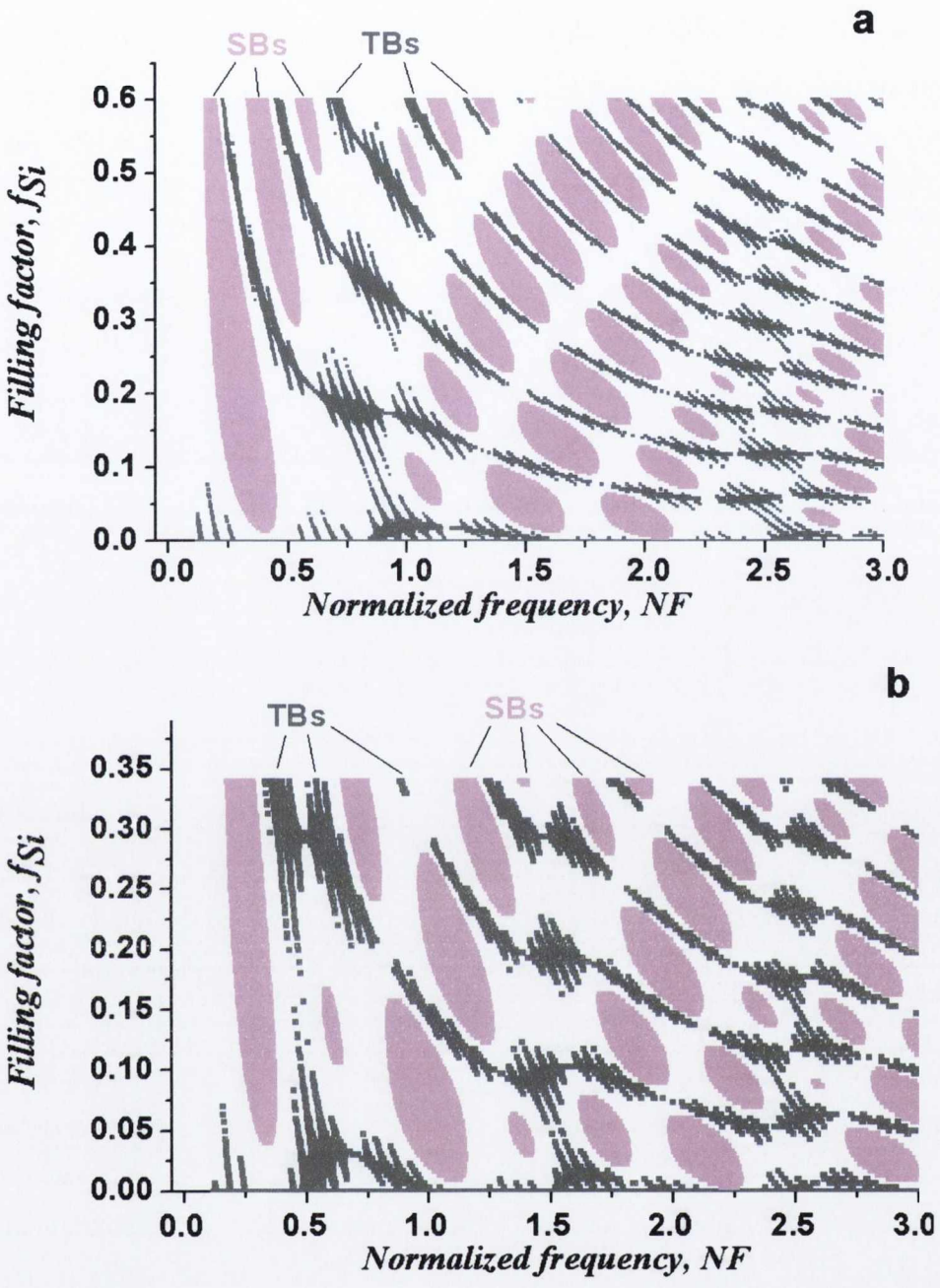

Figure 3-15: *a) The GMs of PBGs (denoted as SBs) and maps of TBs (denoted as TBs) for the multi-component PhC with additional t-layer of refractive index of n_t=1.5 and thicknesses (a) d_t=0.20a and (b) d_t=0.33a. The calculation is performed at normal incidence of light with number of periods N=5.*

Let us now analyze the changes that occur in these wide TBs, when the thickness of the additional *t*-layer is varied, using maps of the transparency regions. For this purpose, maps of TBs for the three-component PhC with *t*-layer thicknesses d_t =0.20a and d_t =0.33a were calculated (Figure 3-15). The calculation procedure, used to

determine the TBs and the form of their graphical representation are the same as that described earlier.

It is worth noting that, for the PhC with d_t=0.20a, the TBs exhibit a different behaviour than for the case of d_t=0.13a. The widest TBs disappear between 1.1 and 1.4, reappearing again in two *NF* regions, viz. from 0.5 to 1.1 and from 2.3 to 2.6. As shown before, these features were not observed for the ordinary two-component PhC with optical contrast 3.42/1 (see Figure 3-12(a), light grey curves). Moreover, as expected, for an additional layer thickness of d_t=0.33a, we can already see the formation of three regions with wide TBs over the same *NF* range. Thus, an increase in the *t*-layer thickness results in an increase in the number of TBs. Therefore, by changing the thickness values of *t*-layer we can manipulate with width and number of TBs in Si PhC device.

3.5.3 Influence of the oblique incidence of light

Based on the preliminary calculations performed in Section 3.5.2, we have successfully demonstrated how the thickness of the *t*-layer is affecting the formation of the regions of transparency in multi-component Si photonic crystal. The next important issue, which needs further investigation, is the impact of oblique incidence of light on TBs. As it was demonstrated earlier, the PBGs cannot be obtained at certain angles of incidence of light for 1D "*Si-air*" PhC structures, regardless of the filling factor f_{Si}. In Section 3.4 we have shown, that by lowering the effective optical contrast (e.g. from high to medium) due to introduction of the additional components, one can obtain the omni-directional PBGs in initially high-contrast structures. The calculated omni-directional PBGs for multi-component PhC structure have even larger width, than those for the equivalent two-component structures with medium optical contrasts, for both TM- and TE-polarizations of light.

Let us consider now the multi-component "*Si-air*" PhC system with the additional *t*-layer of the thickness d_t=0.2a. A detailed analysis have shown that an increase of the angle of incidence of light, θ, does not affect significantly the formation of TBs, which are experiencing only a blue shift in an entire range of f_{Si}. At the same time, a large increase of the angle of incidence (θ >50°) leads to the widening of TBs for TM-polarization and their narrowing for TE-polarization. On the contrary, as was demonstrated in the past, the width of the SBs for TE-polarization increases with an

increase in θ, while for TM-polarization it decreases [19]. Therefore, we can expect that at certain conditions the wide SBs for TE-polarization may overlap with the wide TBs for TM-polarization. The overlapping regions determine the regions of frequency for

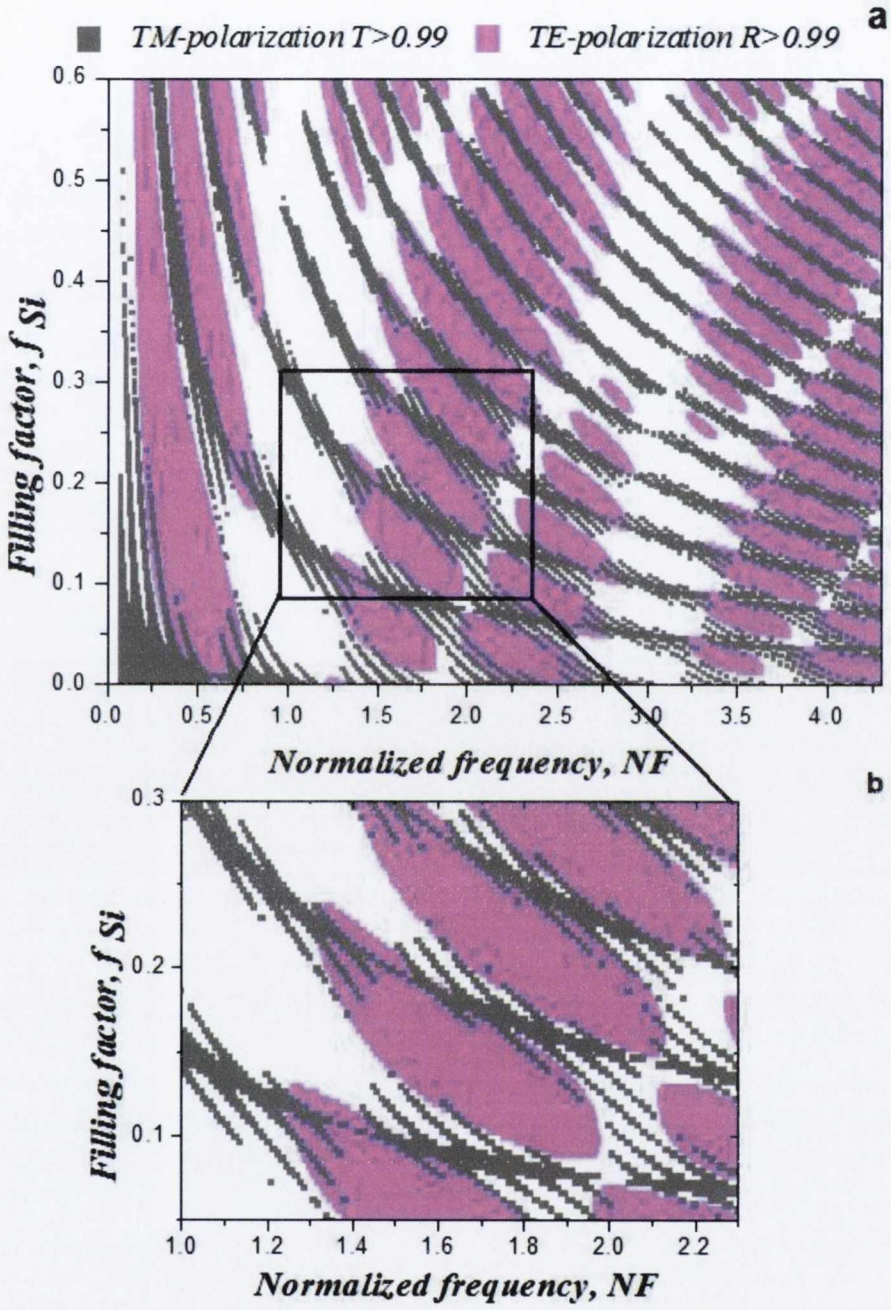

Figure 3-16: *The GM of SBs (R>0.99) for TE-polarization (light regions) and map of TBs (T>0.99) for TM-polarization (dark regions) for the multi-component PhC with* d_t *=0.2a in a wide* f_{Si} *range (a) and in limited* f_{Si} *range (b). The calculation is performed at angle of incidence* $\theta = 60^o$.

which a multi-component PhC structure is totally transmitting the TM-polarized light and totally reflecting the TE-polarized light, and, therefore, this structure is acting as a highly efficient polarizer. In Figure 3-16(a), we demonstrate the GM, calculated for θ=60° for TE-polarization, which is compared to the map of TBs, calculated for the same angle θ but for TM-polarization of the incident light. It is apparent from Figure 3-16(a) that the TBs have partially overlapped with SBs in a whole range of f_{Si}. For clarity, the same maps are demonstrated in the limiting range of f_{Si} and *NF* in Figure 3-16(b). It is clearly seen, that the overlapped regions can reach the width up to 0.05 *NF* for certain values of f_{Si}. For the example considered here, a=3 μm, this width value is equivalent to approximately 60 nm. In order to demonstrate the overlapped regions in details, as well as to show the qualities of the obtained TBs in transmission spectra, the *T*-spectra for both polarizations were calculated using a filling factor f_{Si}=0.18 (Figure 3-17). The overlapped regions for both polarizations correspond to the maximum value of *T* for TM-polarization and the minimum value of *T* for TE-polarization. It is also apparent, that the overlapped regions (with *T*>99%) demonstrate a negligible number of ripples on the top.

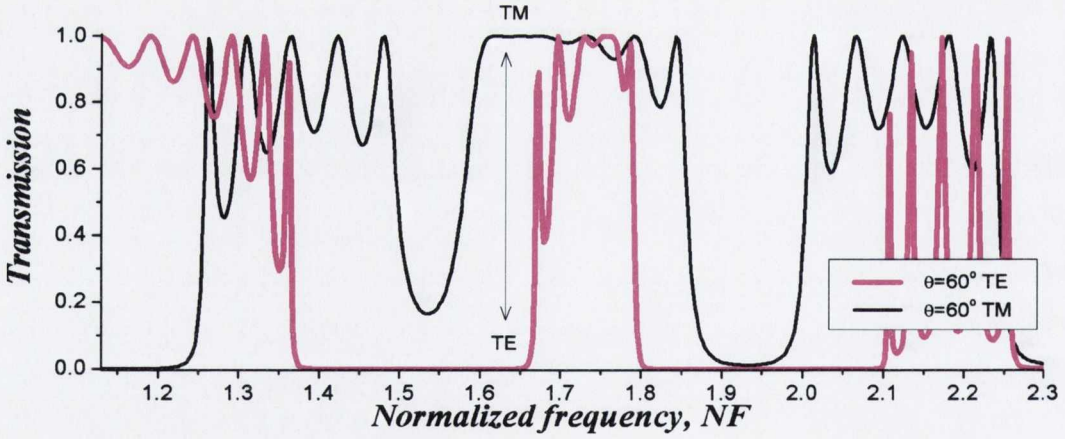

***Figure 3-17**: The T spectra for f_{Si}=0.18 calculated for the multi-component PhC with d_t =0.2a at angle of incidence θ= 60°. The formation of TB for TM-polarization and SB for TE-polarization at NF=1.62 demonstrates the transformation of the PhC into TM-polarizer in transmission mode and TE-polarizer in reflection mode.*

We conclude that the introduction of the additional, regular layer into a high optical contrast 1D PhC, like for example grooved Si, results in the appearance of wide

regions of transparency for TM-polarization for an oblique incidence of light. Using an appropriate design a photonic crystal polarizer, based on grooved Si, can be fabricated for efficient operation with T>99% for TM-polarization and R>99% for TE-polarization in a specific wavelength regions.

The proposed model of in-plane Si-based multi-component PhC allows realization of the highly compact integratable broadband polarizer on Si chip. Comparing to the other typical commercial non-integratable polarizer solutions the multi-component PhC polarizer demonstrate an outstanding wide angular field of 30° and high extinction ratio of about 30dB. However, further theoretical and experimental investigation required in order to understand how the dispersion of Si and insertion losses may influence the polarizing characteristics.

3.6 Photonic Crystal ultra-wide pass-band filter

Let us use the suggested in the previous Section GMs of TBs for the fabrication of the real band-pass optical filter with wide bandwidth operating in a mid-infrared (MIR) wavelength range. In order to introduce the third component into original two-component structure, we exploited thermal oxidation of the grooved Si structures. While other complex and more expensive deposition techniques, such as chemical vapour deposition or sputtering, can be used to deposit dielectric layers, thermal oxidation of Si has the advantage of having a better growth isotropy, especially for narrow, deep trenches and precise control of the grown thickness. Also the fundamental limitations of fabricated Si based devices, such as high roughness and corrugation of the etched Si surfaces, can be overcome by oxidation smoothing (see Section 3.2). In the course of the model calculations we have to pay attention to the following important issues. Firstly, owing to the strong absorption band of $Si0_2$ around 9 μm in MIR range of spectra, the imaginary part of $Si0_2$ refractive index, n_{SiO2}, has been taken into account [21]. It was found that this absorption band does not coincide with total transmission regions in multi-component PhC with lattice constant, a, less than 5 μm. Secondly, during thermal oxidation the 44% of oxide thickness is formed at the expense of Si wall while the remaining 56% of the oxide grows outside in the air [2]. Therefore, the maximum f_{Si} of resulting three-component device will be reduced by the value $\Delta f_{Si} = (2 \cdot 0.44 \cdot d_{SiO2})/a$. For fabrication convenience let us use the original grooved Si structure with a lattice period a= 4 μm and the thickness of the additional component

$d_t=d_{SiO2}=0.18a$. Only three *"Si-air"* paired layers with $N=3$ are needed in order to demonstrate the SBs formation and their further replacement with TBs, making the device extremely compact and potentially low loss. An in-plane design, in which the SBs structure is etched into the Si substrate, allowing the incorporation of optical fibre in-plane, eases the integration process and facilitates the construction of a high-quality filter. The reflection, R, spectra for the original (two-component) structure in the range of filling fractions from 0.25 to 0.33 are demonstrated in Figure 3-18(a). The device calculated can operate as a reflecting filter, with a wide SB centred at $\lambda c= 0.85\ NF$.

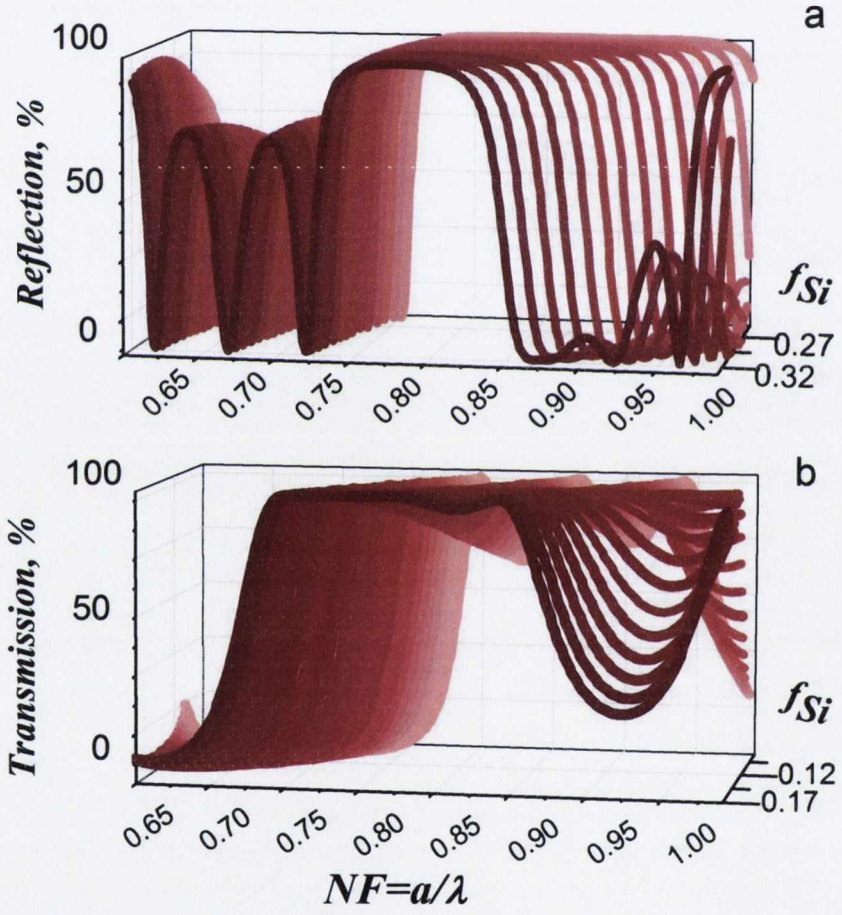

Figure 3-18: *3D representation of (a) flat-top SB centred at 0.8NF in the range of filling fractions f_{Si}=0.25-0.33 before oxidation and (b) flat-top pass-band centred at the same frequency calculated for the same device after oxidation in the range f_{Si}=0.10-0.17. The thickness of SiO_2 is $d_{SiO2}= 0.18a$.*

In Figure 3-18(b), the transmission spectra, T, are demonstrated for the structure after thermal oxidation over the new range of filling fractions $f^*_{Si}= f_{Si}-\Delta f_{Si}$, varying from 0.10 to 0.17. It is apparent from the T spectra that the regions of high transmission

(T>99%) have widened and totally replaced the SB. The obtained structure can now operate as a band-pass filter centred on the wavelength, λc.

Figure 3-19(a) shows the maps for the discussed structure calculated in a wide range of $f^*_{Si}=f_{Si}-\Delta f_{Si}$ from near-infrared to mid-IR spectral ranges. As can be seen for this figure, the introduction of the regular SiO_2 layers in the device has affected the formation of SBs significantly. The limited number of high-order SBs have vanished in a full range of f^*_{Si} over two wavelength regions (around 4 μm and 1.5 μm). At the same time the regions of high transparency with T>99 % (black regions) have become significantly wider in the same wavelength regions. It is also clear that the widest TBs are observed for the filling factor values less than 0.5, which actually corresponds to more realistic structures. According to TB's map the final device should have a filling factor f^*_{Si}=0.145 and, therefore, the final Si-wall thickness, $d_H=f^*_{Si}\cdot a=0.58$ μm. In the Figure 3-19(b) the same map is presented in the limited range of f^*_{Si} from 0.075 to 0.2 in order to study the TBs and SBs for the proposed structure in details. It is obvious that the filling factor deviation, which corresponds to the pass-bands of the same bandwidth and centered at the same wavelength λc, is up to 0.03. Thus, the fabrication tolerance (photolithography error) can be easily estimated from the proposed TB's map, which constitutes 120 nm for the particular demonstrated example filter.

For the fabrication of the original grooved structure we used a fabrication process that was described in details in Chapter 2. The anisotropic chemical etching of (110)Si by KOH was used for the initial step. The depth of etching was 15 μm. Following this, grooved structure was thermally oxidized at the temperature T=900 °C for 120 min in order to grow an oxide layer of the thickness d_{SiO2}= 0.18a=720 nm on the top of Si side-walls (Figure 3-20). The spectroscopic ellipsometer Ellipse 1891 developed in the Institute of Semiconductor Physics of the Siberian branch of the Russian Academy of Sciences was used for thickness control of the SiO_2 layers on witness samples. Measurements were performed at an angle of light incidence ϕ_0=70° over the photon energy range 1.5-5.0 eV. The thickness of thermally grown oxide layer and information about the refractive index were obtained by fitting the measured data to multi-layer model calculations. The R and T spectra measurements have been performed using an FTS 6000 FTIR spectrometer in conjunction with a UMA IR microscope (see Chapter 2 for details). The aperture of the focused IR beam was 15×15 μm^2 and the spectral resolution was 8 cm^{-1}. A golden mirror was used as a 100% reference for

measurements of reflection spectra. All measurements have been performed for normal incidence of light.

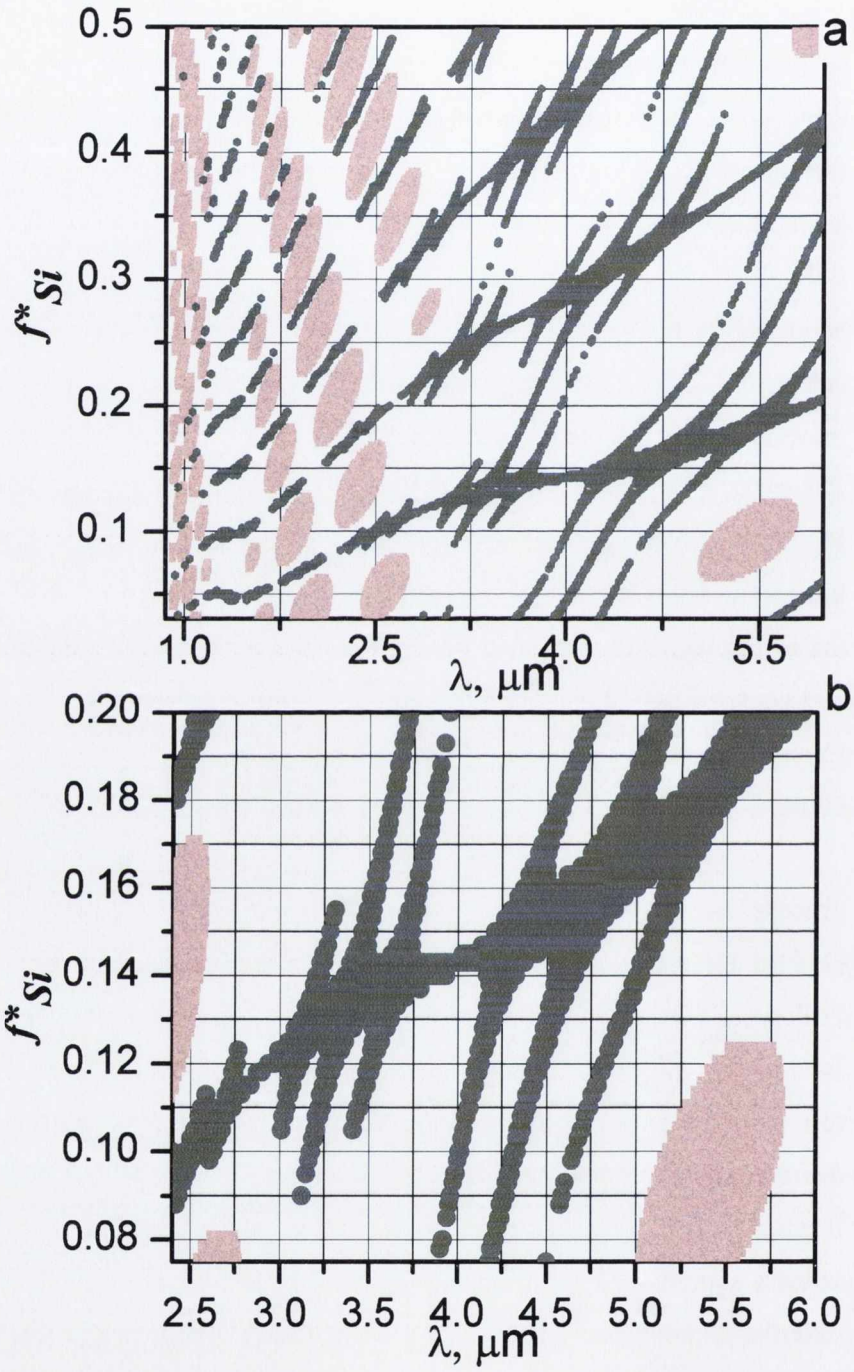

Figure 3-19: *(a) The GM of SBs with R>0.99 (light regions) and map of TBs with T>0.99 (dark regions) calculated for fabricated filter based on PhC structure (air-SiO_2-Si-SiO_2-air)^N with N=3 for mid-IR. (b) The same maps, demonstrated in the limited range of λ and f^*_{Si} for clarity. The dispersion of SiO_2 in MIR range and normal incidence of light θ=0° are taken into account during calculations.*

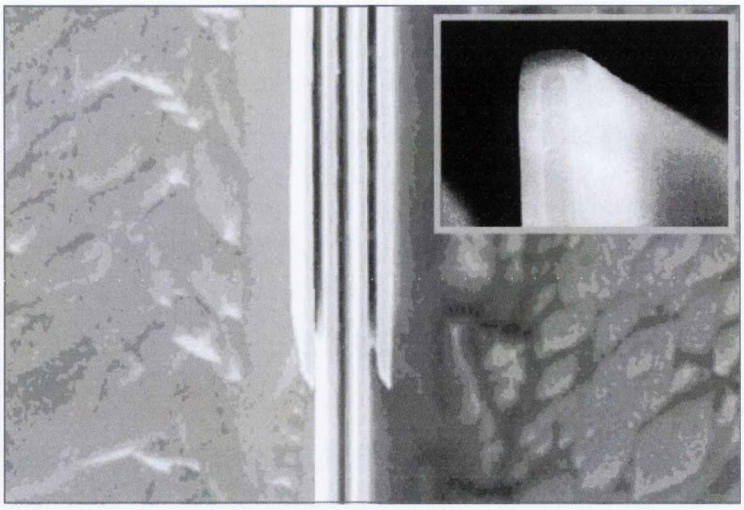

Figure 3-20: *SEM image of photonic crystal filter based on grooved Si with thermally grown SiO_2 of thickness d_{SiO2}=0.72μm. The lattice period a=4μm.*

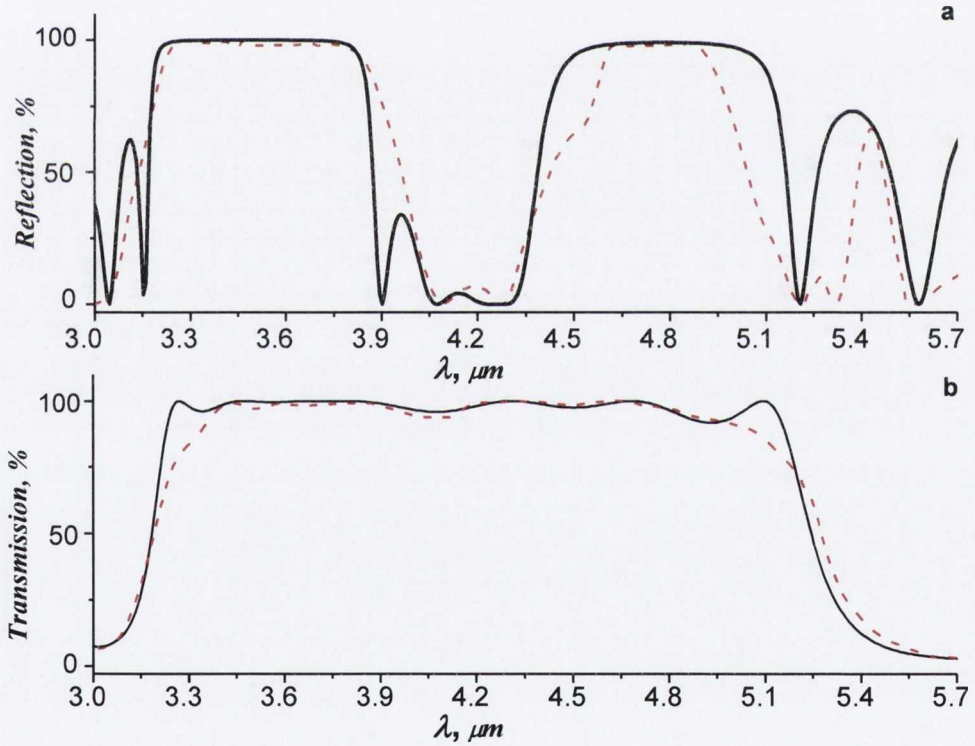

Figure 3-21: *Experimental (dashed line) and calculated (solid line) (a) R and (b) T spectra of the band-pass filter based on PhC structure $(air\text{-}SiO_2\text{-}Si\text{-}SiO_2\text{-}air)^N$ with N=3 demonstrate the transformation of the SBs at 3.5 μm and at 4.8μm into the TB at the wavelength λ_c= 4.2 μm.*

Figure 3-21 shows the experimental R and T spectra in comparison with the simulated ones. Apart from some excess losses, which may be due to optical scattering, there is good agreement between experiment and calculation. We note that the original grooved Si structure has the SBs centred at 3.5 μm and 4.8 μm. Thus, the original device is acting as a stop-band filter (Figure 3-21(a)), while after thermal oxidation these SBs have been replaced with ultra-wide TB with bandwidth of 1400 nm in the range of wavelength from 3.4 μm to 4.8 μm. The obtained device can now operate as band-pass filter (Figure 3-21(b)). To our knowledge this is the first report of the broadband band-pass filter with flat-top characteristics which can be integrated on Si chip. The utilization of the thermally grown SiO_2 for the fabrication of the multi-component PhC device has resulted in the appearance of the negligible number of ripples (with depth up to 4-5%) on the otherwise flat-top transmission. Therefore, the fabricated band-pass filter can provide an ultra-wide transmission of 95-96% centred at 4.2 μm.

3.7 Summary

Utilisation of a three-component photonic crystal by the introduction of an additional layer to a two component structure, while leaving the lattice constant unchanged, provides a suitable model for designing a new type of photonic crystal. Use of a GM allows visualization of the transformation of the PBG areas caused by converting a two-component PhC to a three-component PhC by the addition of the new layer. The introduction of the third component to the 1D PhC allows variation of the PBGs areas of the three-component PhC and, therefore, engineering of the optical contrast of the original two-component PhC. This is achieved, not by filling its air channels, but by selecting either the thickness or refractive index of the third layer. However, in this case, we sacrifice the range of possible f_{Si} values for the formation of stop-bands and SB's area. The widest SBs are observed for this restricted range of possible f_{Si} values. Using the approach suggested for decreasing the optical contrast in photonic crystals, omni-directional bands can be obtained in a high-contrast Si-air periodic structure. A number of simulated models of three-component 1D photonic crystals are described, some of which may have practical applications.

The principle of suppression of the PBGs and replacing them with TBs is demonstrated for a high contrast 1D PhC with the introduction of an additional *t*-layer. By varying the thickness of the *t*-layer, the width and the number of the TBs can be altered. The TBs obtained numerically show a high transmission value (>99%) and a substantial band width in the infrared spectral range. The GM approach was used to generate the map of transmission bands in order to observe the effect in the entire range of Si filling factor and in a wide wavelength range. The generated maps of TBs have demonstrated the formation of the ultra-wide transmission bands over the suppressed PBGs in a whole range of possible filling factors. The TBs obtained demonstrate a substantial bandwidth (> 200 nm) and a negligible number of ripples within the bands.

In order to fine tune the wavelength position, number and width of the output transmitting or reflecting bands, thermal oxidation of the grooved Si structures was exploited. Based on the generated map of TBs the PhC filter with ultra-wide TB characteristics have been successfully fabricated and characterized. The TB obtained exhibit a high transmission of 92-96% and a substantional bandwidth 1800nm with negligible number of ripples on the top.

The effects demonstrated have practical applications in integrated Silicon microphotonics. It suggests that fabricating interference filters with almost 100% transmission over a selected wide range of the infrared spectrum is practical. Also, we note that the approach suggested can be applied to the design of any micro- and nanostructured semiconductor or dielectric material for application across the entire electromagnetic range.

3.8 References

[1] Y. Zhang, and Q. Wang, "Properties of photonic bandgap in one-dimensional mutlicomponent photonic crystal," Optoelectronics Letters, 2(1), 44-47 (2006).

[2] G. Barillaro, S. Merlo, and L. M. Strambini, "Bandgap Tuning of Silicon Micromachined 1-D Photonic Crystals by Thermal Oxidation," IEEE Journal of Selected Topics in Quantum Electronics, 14(4), 1074-1081 (2008).

[3] A. Glushko, and L. Karachevtseva, "PBG properties of three-component 2D photonic crystals," Photonics and Nanostructures - Fundamentals and Applications, 4(3), 141-145 (2006).

[4] M. V. Rybin, A. V. Baryshev, A. B. Khanikaev *et al.*, "Selective manipulation of stop-bands in multi-component photonic crystals: Opals as an example," Physical Review B, 77(20), 205106 (2008).

[5] V. A. Tolmachev, E. V. Astrova, J. A. Pilyugina *et al.*, "1D photonic crystal fabricated by wet etching of silicon," Optical Materials, 27(5), 831-835 (2005).

[6] H. Ouyang, M. Lee, B. L. Miller *et al.*, "Silicon photonic bandgap biosensors." Proceedings of SPIE, 5926, 59260J-11 (2005).

[7] M. KGaA, [Data Sheet Licristal® E7], Germany(2001).

[8] K. Busch, [Photonic Crystals: Advances in Design, Fabrication, and Characterization] Wiley-VCH, (2004).

[9] E. Astrova, V. Tolmachev, G. Fedulova *et al.*, "Optical properties of one-dimensional photonic crystals fabricated by photo-electrochemical etching of silicon," Applied Physics A: Materials Science & Processing, 98(3), 571-581 (2010).

[10] M. Born, E. Wolf, and A. B. Bhatia, [Principles of Optics: Electromagnetic Theory of Propagation, Interference and Diffraction of Light] Cambridge University Press, (1999).

[11] E. Astrova, T. Perova, V. Tolmachev *et al.*, "IR birefringence in artificial crystal fabricated by anisotropic etching of silicon," Semiconductors, 37(4), 399-403 (2003).

[12] T. S. Perova, V. A. Tolmachev, and E. V. Astrova, "Tunable photonic structures based on silicon and liquid crystals." 6801, 68010W-15.

[13] R. M. A. Azzam, and N. M. Bashara, [Ellipsometry and polarized light] North-Holland, (1987).

[14] V. Tolmachev, T. Perova, and K. Berwick, "Design Criteria and Optical Characteristics of One-Dimensional Photonic Crystals Based on Periodically Grooved Silicon," Appl. Opt., 42(28), 5679-5683 (2003).

[15] L. I. Epstein, "Improvements in Heat-Reflecting Filters," Journal of the Optical Society of America, 45(5), 360-362 (1955).

[16] A. Thelen, "Multilayer Filters with Wide Transmittance Bands II," Journal of the Optical Society of America, 63(1), 65-68 (1973).

[17] V. Y. Pervak, and Y. A. Pervak, "Suppression of background transmission of interference filters," Optics and Spectroscopy, 88(3), 455-458 (2000).

[18] J. D. Joannopoulos, [Photonic Crystals: Molding The Flow Of Light] Princeton University Press, (2008).

[19] V. Tolmachev, T. Perova, E. Krutkova *et al.*, "Elaboration of the gap-map method for the design and analysis of one-dimensional photonic crystal structures," Physica E: Low-dimensional Systems and Nanostructures, 41(6), 1122-1126 (2009).

[20] D. N. Chigrin, A. V. Lavrinenko, D. A. Yarotsky *et al.*, "Observation of total omnidirectional reflection from a one-dimensional dielectric lattice," Applied Physics a-Materials Science & Processing, 68(1), 25-28 (1999).

[21] E. D. Palik, "Handbook of Optical Constants of Solids," Volume 1, (1998).

[22] E. L. Gurevich, S. Kittel, R. Hergenröder *et al.*, "Modification of GaAs surface by low-current Townsend discharge," Journal of Physics D: Applied Physics, 43(27), 275302 (2010).

Chapter 4.
Micro-cavity Photonic Crystals

4.1 Introduction

Modern Si fabrication technology has advanced remarkably over the last decade demonstrating an unprecedented level of photonics integration [1]. The development of the integrated compact multi-channel filters for different applications, such as, communication systems [2-4], multifunctional sensing [5, 6] and microwave antennas [7] has been important and active area of research in this field. The required characteristics are the high quality factor (Q), high selectivity (the ability to separate two adjacent channels), high out-of-band rejection in order to guarantee a low cross talk between channels, low power and possibly low insertion. Moreover, the filter capability of low-power and low-loss tuning of channel properties significantly advances device functionalities for the applications where the reconfiguration is required. In this regard, resonance based devices, such as microring resonators [8, 9], travelling-wave resonators [10] and photonic crystal micro-cavity resonators [11], are the most promising solutions. In this Chapter, we will focus on micro-cavity PhC systems due to their significant advantages over other types of resonators, in terms of device simplicity, ease of integration on Si chip, and power consumption. The main objective of this project was the technological realization and experimental demonstration of an integratable solution for the Si-based band-pass filters with ultra-wide continuous tuning capability. The design of a fine-tunable passband filter proposed in this Chapter is based on a one-dimensional Si photonic crystal technology. It requires realization and tuning of the optical defects within the periodical structure by infiltrating it with liquid crystal, thus transforming PhC mirror into a high efficiency passband filter. An LC is one of the most attractive tuning materials for Si based integrated

devices; enabling tuning of the resonance modes using low applied voltages (from 1.5 V) with negligible absorption during device operation (see Chapter 2).

Section 4.3 presents theoretical and experimental demonstration of integrated optical narrow-band filters based on ***single-cavity*** 1D Silicon PhC. Using an example of the nematic LC E7, with $\Delta n \approx 0.2$, a significant shift of the resonance peak up to 10% at high modulation of reflection/transmission coefficient (ΔR (or (ΔT))≈95%) was demonstrated. The precise tuning of the obtained resonance bands was experimentally achieved by either varying the temperature from 10° to 65°C or by application of electric field from 0 V to 15 V. Using the gap map approach as a core engineering tool allows prediction of the formation of transmission bands within the Stop Bands, i.e. photonic band gaps, and, thus, effectively determine the exact optimal design parameters of the filter device.

In Section 4.4 the continuous fine-tuning capability of a LC single micro-cavity is extended to a system of individually tunable, coupled multi-cavities. Application of an electric field to each cavity individually, and its continuous selective variation across all cavities allows problems due to the strong coupling between channels to be overcome. Using an example of a coupled, triple-cavity, PhC filter, operated using the first SBs, we have developed a simple model for easier manipulation of the LC within individual cavities, enabling independent fine tuning of each channel in the overall system. We note that the model suggested can be extended to a higher number of coupled cavities (defects) and, therefore, to a higher number of resonances, with an improved Q value. To the best of our knowledge, there have been no reports in the literature on addressing this problem using electro-tuning for the individual channels in a multi-channel system that is compatible with CMOS (Complementary Metal Oxide Semiconductor) technology.

4.2 Basic Concept: Modelling of 1D micro-cavity Photonic Crystals

A free-space, microstructured grooved Si structure, with quarter-wavelength "*Si-air*" layers of optical thicknesses

$$d_{Si} \cdot n_{Si} = d_{Si} \cdot n_{air} = m \cdot \frac{\lambda_m}{4} \qquad (4.1)$$

is considered here as a model for an ordinary 1D PhC mirror, where d_{Si}, n_{Si} and d_{air}, n_{air} are the geometrical thickness and refractive index of Si and air layers, accordingly and m is the order of the SBs. The refractive indexes of Si and air in NIR and MIR are taken from Ref.[12]. As the optical contrast of the PhC, n_{Si}/n_{air}, is sufficiently high, only a small number of periods is required to obtain a SB with a reflection, R, of greater than 0.99. Let us consider an example of 1D PhC with the number of periods N=7.5 and the lattice period $a=d_{Si}+d_{air}$ (Figure 4-1(a)). The optical spectra of this simple structure can be calculated using the Transfer Matrix Method [13]. For all spectral simulations in this Chapter, the optical characteristics are presented in unitless dimensions of normalized frequency ($NF=a/\lambda$) and/or normalized wavelength ($NW=\lambda/a$) and, therefore, can be applied to a wide range of filter sizes and range of operation. For the considered example structure with filling fraction value $f_{Si}=d_{Si}/a$=0.243, the 6th order, m=6, SB is centred at the normalized wavelength NW=0.29 or normalized frequency NF=3.45 (Figure 4-1(b)).

The single/coupled resonators induced transparency around the operational wavelength λ_m, occurs when optical or geometrical defects (micro-cavities) are introduced into a perfect periodical structure [14, 15] (Figure 4-1(c, e)). Formation of a microcavity resonator requires a doubling of the optical thickness of certain periods in 1D PhC

$$n_{cav}^{(i)} \cdot d_{cav}^{(i)} = m \cdot \frac{\lambda_m}{2}, \qquad (4.2)$$

where $n_{cav}^{(i)}$ and $d_{cav}^{(i)}$ are the refractive index and the geometrical thickness of the introduced defect (cavity), accordingly, and i is the number of the cavity, thus transforming the broadband mirror into the narrow passband filter. This type of micro-cavity 1D Photonic Crystals feature Fabry-Perot-style resonators (an optical resonator in which feedback is accomplished using two mirrors, e.g. "*Si-cavity-Si*") with ultra-high reflectance mirror technology [16]. This can be achieved, for example, by infiltration of the groove with a filler of a suitable refractive index. TMM calculations, performed for the single-cavity PhC structure with 7.5 period, after infiltration of its central groove with an example fillers of refractive indexes n_{cav}=2 and n_{cav}= 1.5 are shown in Figure 4-1(d). The realized resonance peak is centered at NW= 0.289 (NF=3.46) for the n_{cav}=2 (black line) and blue shifted to NW=0.286 (NF=3.50) for n_{cav}= 1.5 (green line). The reflection spectra of "*Si-cavity-Si*" Fabry-Perot resonators (FPRs) are plotted in Figure

4-1(d) for n value of cavity being 1.5 (dashed green line) and 2 (dashed black line) along with R spectra for single-cavity PhC with 7.5 periods. The Q of a single-cavity PhC of 7.5 periods is significantly higher, Q=15000, in comparison to the elementary single 1.5- period (N=1.5) FPR for which Q is only 334.

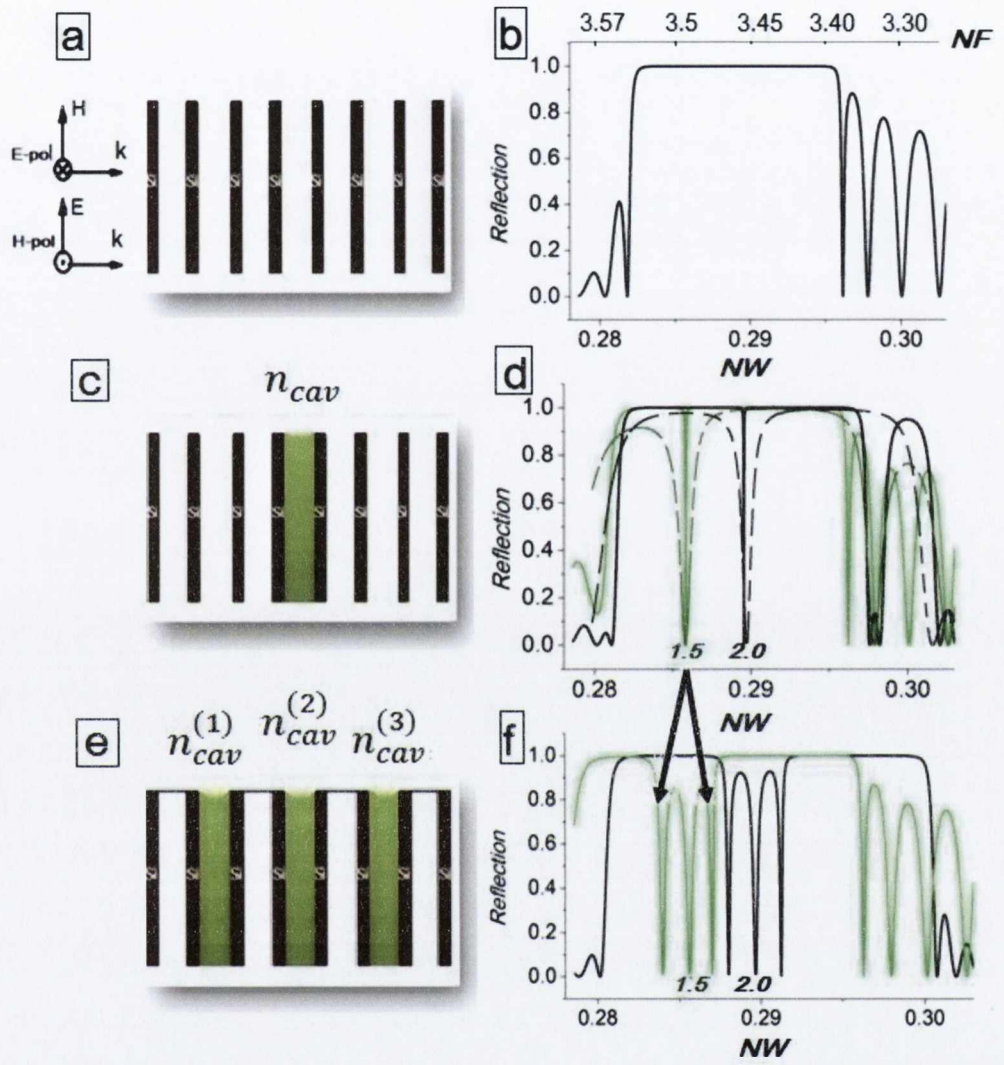

Figure 4-1: *Schematic fragments of (a) defect-free 1D PhC and 1D PhCs with (c) single and (e) triple optical defects. (b, d, f) The TMM simulated reflection spectra for the sixth order SB are demonstrated in normalized wavelength units NW=λ/a ((b) lower scale) and normalized frequency NF=a/ λ ((b) upper scale). The value of filling fraction is 0.243 and the refractive index of defect is* $\mathbf{n_{cav}^{1,2,3}}$*=1.5 (light green line) or* $\mathbf{n_{cav}^{1,2,3}}$*=2 (black line). R spectra of the single 1.5 periods FPRs are also shown for comparison (dashed lines).*

Similar technique is used for the realization of the multiple-coupled defects (cavities) within the defect-free PhC. From an optical point of view, increasing of the number of coupled cavities results in a mode-splitting effect, i.e. in increase of the number of resonance peaks realized within the SBs and the proportional increase of the Q comparing to the single FPR. In Figure 4-1(e) we demonstrate an example of the triple-optical defect structure with refractive indexes $n_{cav}^{(1)}=n_{cav}^{(2)}=n_{cav}^{(3)}$, realized in a defect-free PhC. The resonance peaks of PhCs with a single cavity have split into three-coupled resonances. The central resonance has retained its wavelength of operation, while the other resonances are separated from the central peak by a fixed resonance-spacing, λ_s, or by a free spectral range (FSR). For the considered example of a triple-cavity the Q was increased in 3 times, comparing to the Q of a single 1.5-period FPR.

4.3 *Single cavity Photonic Crystal: a Fabry-Perot resonator*

4.3.1 Gap Map design of Fabry-Perot resonators

4.3.1.1 "Si-air-Si" Fabry-Perot Resonator

In order to draw the map of SBs for 1.5-period PhC (FPR), a set of R spectra (~ 100 in total) are calculated for filling fraction, f_{Si}, varied from 0 to 1 with step of 0.01, assuming that the parameter $a=d_{air}+d_{Si}$ is constant. The obtained values of the reflection coefficient, R, are cutt off using the criterion [17, 18] $R_{cutoff}>0.85$, while the rest of the values are plotted on the graph versus normalized frequency, NF, as shown in Figure 4-2. The lower than usual value of cut off criterion for SBs ($R_{cutoff}=0.85$) for selection of data for gap map formation is chosen for clearer presentation (see Chapter 2 for details).

As shown in Figure 4-2(a), the obtained SBs are relatively wide, that is due to the high optical contrast and the low value of R_{cutoff}. Then the set of calculated T (or R) spectra is filtered using another cut off criterion, namely $T_{cutoff}>0.99$. From the obtained data the map of transmission bands (or pass-bands) is plotted on the obtained above map of SBs (see Chapter 3). This is used for more clear demonstration of the location of transmission bands with respect to the SBs depending on f_{Si}. Figure 4-2(a) shows the SBs surrounded by the transmission bands. In TB regions the resonance modes with large signal modulation ($\Delta R\approx 0.95$) as well as low signal modulation are included. The second y-axis, from the right side of the plot shown in Figure 4-2(a), presents the filling fraction for air, f_{air}, as a part occupied by air relatively to a value, i.e. $f_{air}=d_{air}/(d_{air}+d_{Si})$.

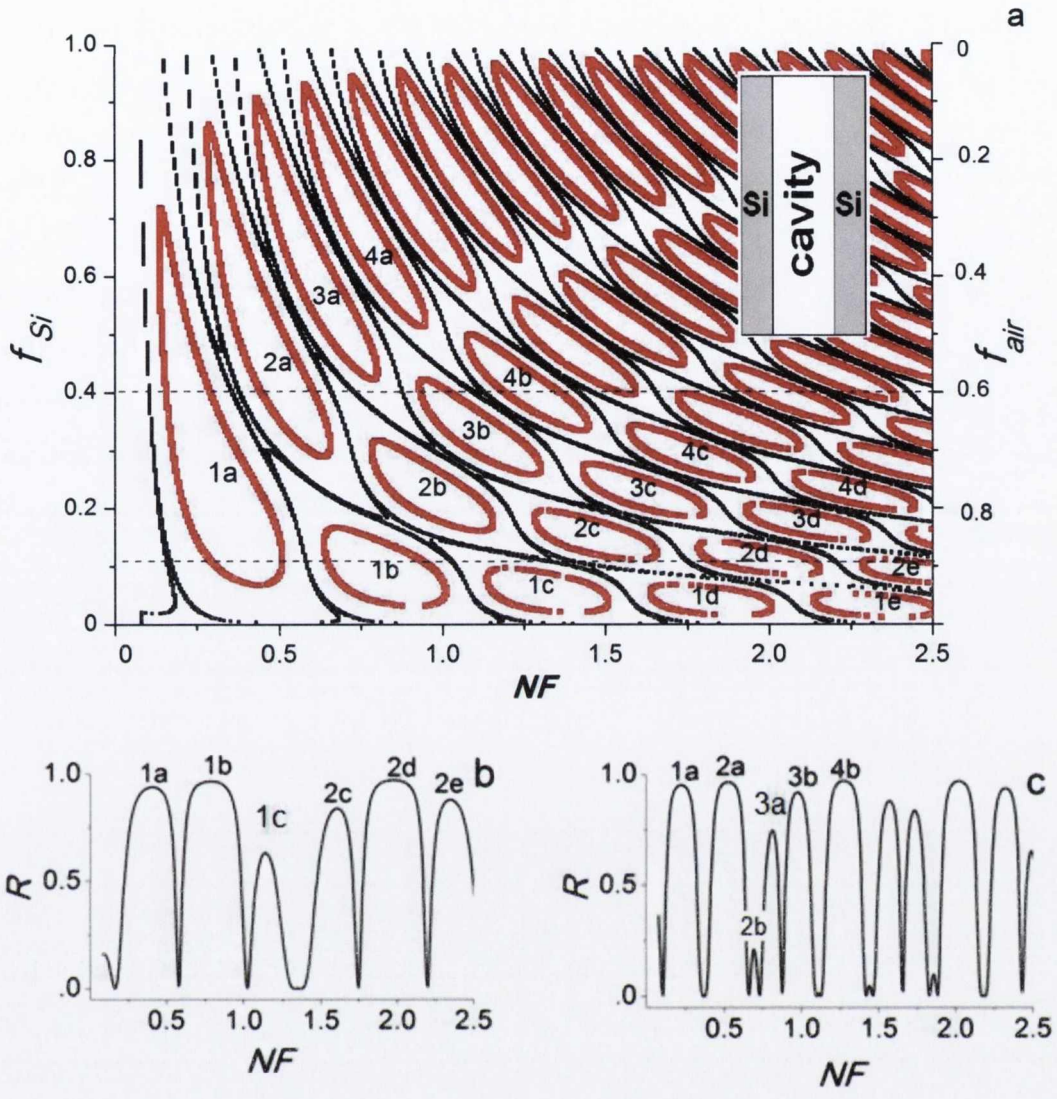

Figure 4-2 : *(a) Map of stop-bands (shown by red contour with symbolic numeration) with R>0.85 and regions of transparency (black contour) with T>0.99 for 1.5-period PhC or FPR (shown in insertion). The incoming and outgoing media are air, n_{Si}=3.42, and the incidence of light is normal. (b) The R spectrum for f_{Si}=0.11 with few largely-modulated resonance peaks between SBs 1a-1b, 2c-2d and 2d-2e. (c) Spectrum R for f_{Si}=0.4 demonstrated the absence of narrow resonance peak between SBs 1a-2a, 3b-4b.*

Since the resonance peaks in 1D PhC are characterised by a sharp change in transmission (from ~0 to ~1) in vicinity of the resonance peak, as a consequence the TB region must be surrounded by two SBs on the GM. Let us consider the structure with the filling fraction f_{Si} = 0.11, for example. For this value we draw the horizontal line, which intersects the SB regions as well as TBs. For convenience we numerate the SBs

in order as shown in Figure 4-2(a). It is seen in Figure 4-2(a), that in the region of NF=0.6 there is a TB region, which is surrounded by SBs **1a** and **1b**, while in spectrum R, depicted in Figure 4-2(b), the resonance peak is observed at NF=0.6. We can also see the presence of resonance peaks with large modulation in the regions NF =1.7 and NF =2.2, which are predicted from the map between SBs **1b-1c**, 2**c**-2**d** and 2**d**-2**e** for the corresponding values of f_{Si}.

Let us now concentrate more precisely on what is observed between SBs **1a** and **2a**, for example, for f_{Si}=0.4 (Figure 4-2(c)). We can see that the transmission peaks observed between these stop-bands are considerably wide. Similar result is obtained for the other values of filling fractions, f_{Si}, for transmission bands located between SBs 2a - **3a**, **1a-2b**, **2b-3c** and others. Therefore, for considered type of FPR the formation of resonance peaks with large signal modulation can occur in the region of $f_{Si} \sim 0.2$ and below. This rule is related to the fact that for obtaining the total constructive interference for transmission a substantial part of low-refractive index component in a structure is necessary.

4.3.1.2 "Si-LC-Si" Fabry-Perot Resonator

Taking into account the analysis and conclusions made in the previous Section, let us now investigate a 1.5-period FPR, in which the compound with refractive index birefringence (that can be changed by the external forces) will replace the air in the cavity (Figure 4-1(b)). For this purpose we can use the nematic LC E7 with extreme values of the refractive indexes, n_{LC}=n_{cav} equal to 1.49 and 1.69 (see Chapter 2 for details). We calculate the set of R and T spectra and draw the GMs of SBs and TBs for two values of n_{LC} in the resonator cavity (Figure 4-3(a)).

Two types of SBs with defect cavity modes corresponding to n_{LC}=1.49 and 1.69 can be seen in Figure 4-3. These SBs are narrower than SBs demonstrated above in Figure 4-2(a) due to the lower optical contrast (in ~1.4 times). From Figure 4-3(a) in the region of f_{Si}=0.06 one can observe the intersection of SBs with transmission bands, in vicinity of values NF=1, 1.2 and 1.6, for example. More clearly this can be seen on spectra shown in Figure 4-3(b).

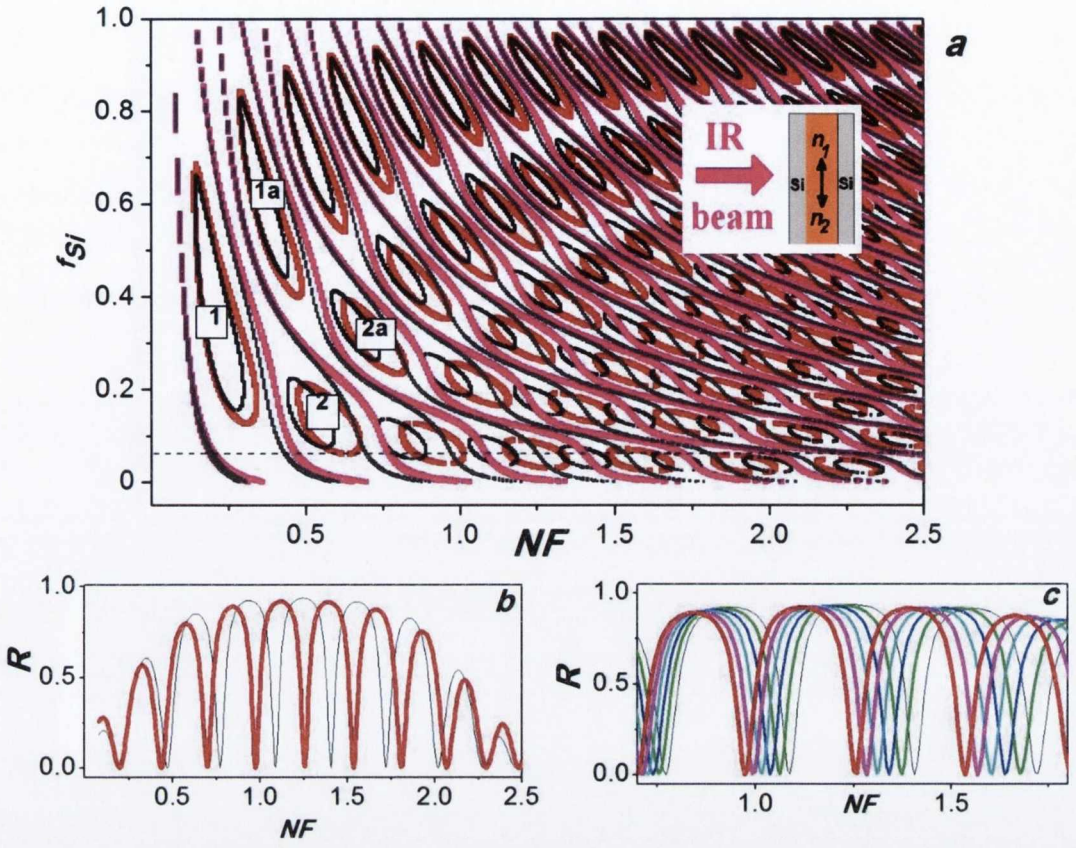

Figure 4-3 : *(a) The map of stop-bands(oval-like figures) and transmission bands(lines) for 1.5-period PhC (FPR) based on 3-layers model "Si-LC-Si" with two values of* $n_{LC}=n_1=1.49$ *(red contours for SBs and pink lines for TBs) and* $n_{LC}=n_2=1.69$ *(black contours for SBs and grey lines for TBs).* $R_{cutoff}=0.85$, $T_{cutoff}=0.99$. *(b) Spectrum R calculated for* $f_{Si}=0.06$ *and demonstrating the cut off line of R values, used for drawing of SBs map. (c) Fine tuning of peak positions and stop-bands with variation of* n_{LC} *from 1.49 to 1.69. Relative peak shift* $\Delta NF/NF=0.14/1.33=10.5\%$.

The presented spectra demonstrate that the variation of n by 0.2 in resonator cavity leads to the shift of the resonance peak from 1.40 to 1.26 *NF* resulting in a relative shift value, $\Delta NF/NF = 0.14/1.33 = 10.5\%$. The width of the SB in this diapason is ~ $0.2NF$, as well as SB shifts by approximately the half of its width during the tuning. The LC molecules can be oriented in such way, that their refractive index possesses not only the extreme values (n_o and n_e), but also some intermediate values. Figure 4-3(c) is depicted the spectra for these intermediate values of n_{LC} that demonstrate the possibility of fine tuning of resonance peaks and stop-bands position.

Thus, using TMM, the reflection spectra of FPR (or 1.5-period PhC) based on structures "*Si-air*" and "*Si-LC*" can be calculated. The filtering of these spectra using two criteria for maximum and minimum values of the reflection coefficient provides the set of data for drawing the maps of stop-bands and transmission bands. The resonance bands with large modulation of R values ($\Delta R \approx 0.95$) are located between the certain stop-bands regions. By means of this approach, the range of optimal filing fractions of FPR can be established in the range of f values from 0.05 to 0.4 for achieving a significant shift of SBs and the resonance peaks up to 10% using LC birefringence of Δn=0.2 with R modulation up to 0.95.

4.3.1.3 Photonic Crystal with "optical" defect

To obtain a well pronounced resonance peak, it is necessary to increase at least twice the optical thickness of one of the component in the centre of PhC structure (Figure 4-1(a)). This can be achieved by increasing the geometrical width of the structure (Figure 4-1(c)) or by replacing the air gap (n=1) in the centre of structure by a compound with refractive index n = 2 (Figure 4-1(d)). If it is not possible to use a compound with n = 2, but with smaller refractive index, for example with n = 1.49, the resonance peak still appears, but not in the centre of SB. Although, the peak width (quality factor) and the amplitude of signal modulation for this resonance peak are nearly the same as the calculated values for an ideal resonator (at n = 2). For the formation of the corresponding defect typically the first stop-band is used. In this Section the investigation of the possibility of using the resonance peaks, formed in SBs of high order, is performed with GM approach.

Let us consider the FPR based on 3-period PhC with "optical" defect. We calculate the gap map for PhC with three periods and draw the map for PhC with central air gap infiltrated by LC, i.e. with refractive index of defect n_{cav}=1.49 (Figure 4-4). The gap map demonstrates, as expected [18], that the infiltration of LC into one central groove changes n value from 1 to 1.49, increasing the optical width of this groove and, therefore, results in the formation of the defect mode region by splitting of SBs of any order. For example, the horizontal line on the map, corresponding to f_{Si}=0.15, intersects the SBs and defect bands in the regions of NF=0.41, 0.72 and 1.54. For these NF values, very pronounced resonance peaks are observed in spectrum R shown in Figure 4-5(a). Similar appearance of the defect modes is also depicted for f_{Si}=0.4 and 0.6, for

example, as demonstrated in Figure 4-5(b) and Figure 4-5(c) for f_{Si}=0.4 and 0.6 as an example.

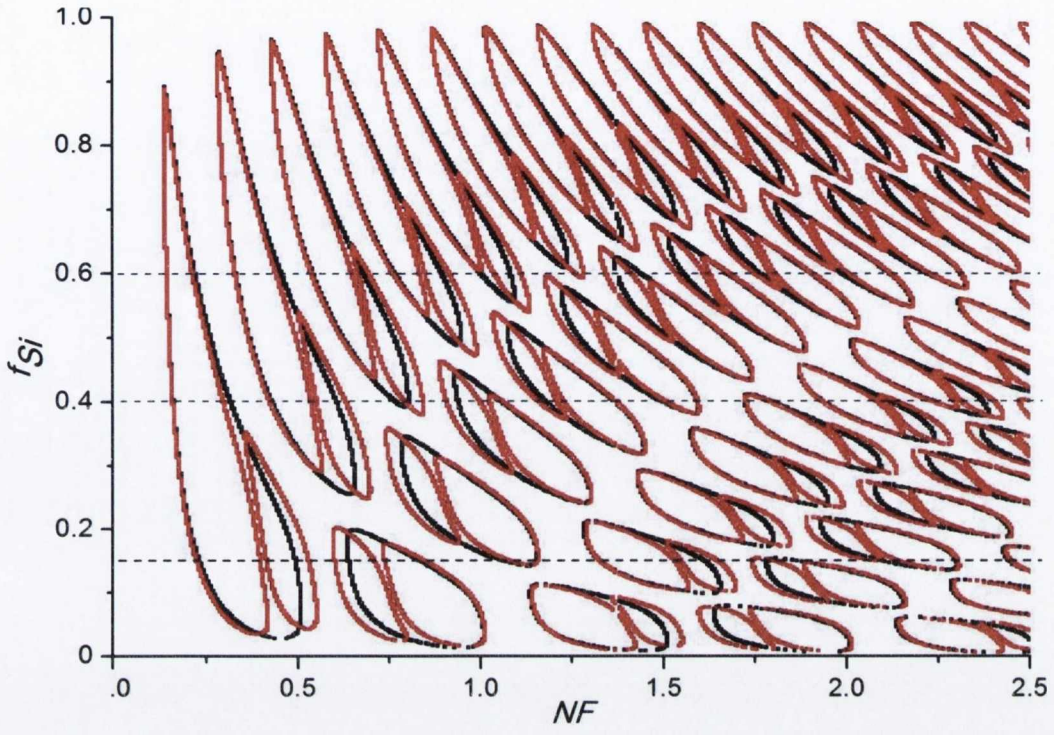

Figure 4-4: *(a) The map of SBs for 3-period PhC "Si-air"(black contour) and 3-period PhC "Si-air" with LC "optical" defect (red contour) with* n_{LC}*=1.49*

These examples demonstrate a possibility to cover with resonance peaks the entire range of *NF* values for PhC resonator of the above mentioned type with using the first stop-band as well as the SBs of high order. During the fabrication of such FPR (or PhCs with optical defect), there can be certain advantage in retaining the same thickness of Si walls and air gap. At the same time in case of PhC with a resonator where a geometrical defect is used, it is necessary to control additionally the size of the resonator cavity.

The map of the transmission bands which are located between the stop-bands is depicted in Figure 4-6. Careful examination of the TBs for this type of resonator shows that it is impossible to generate the resonance peaks with high signal modulation between the stop-bands for any values of f_{Si} (Figure 4-6).

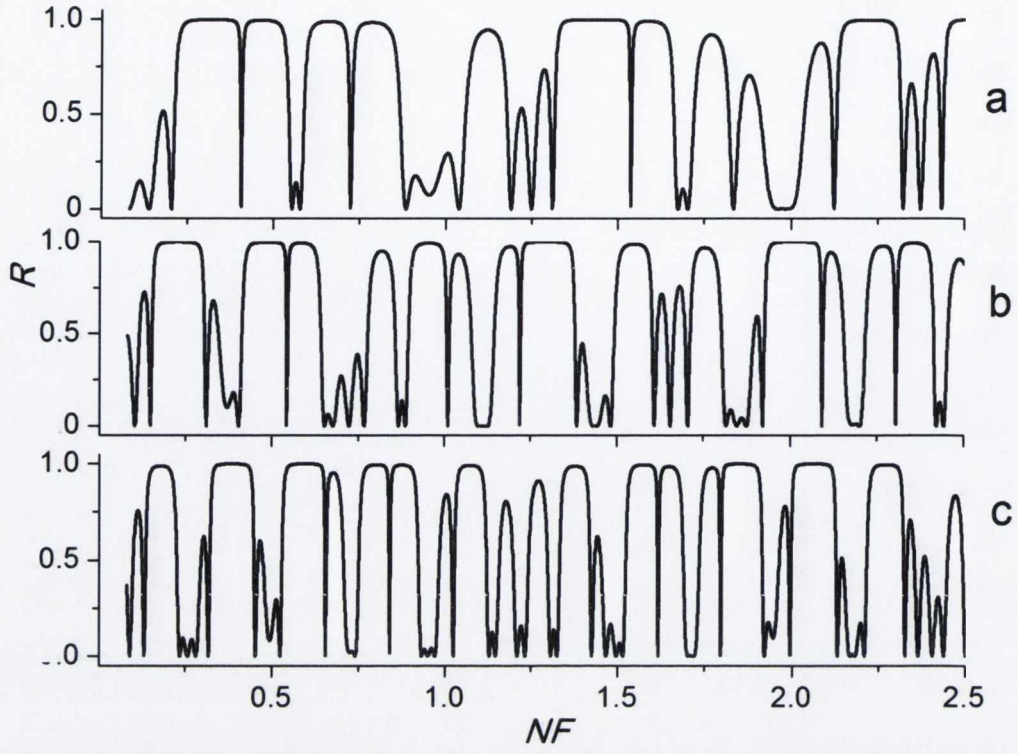

Figure 4-5: *R spectra for f_{Si}=0.15 (b), 0.4 (c) and 0.6 (d) (see GM in Figure 4-4).*

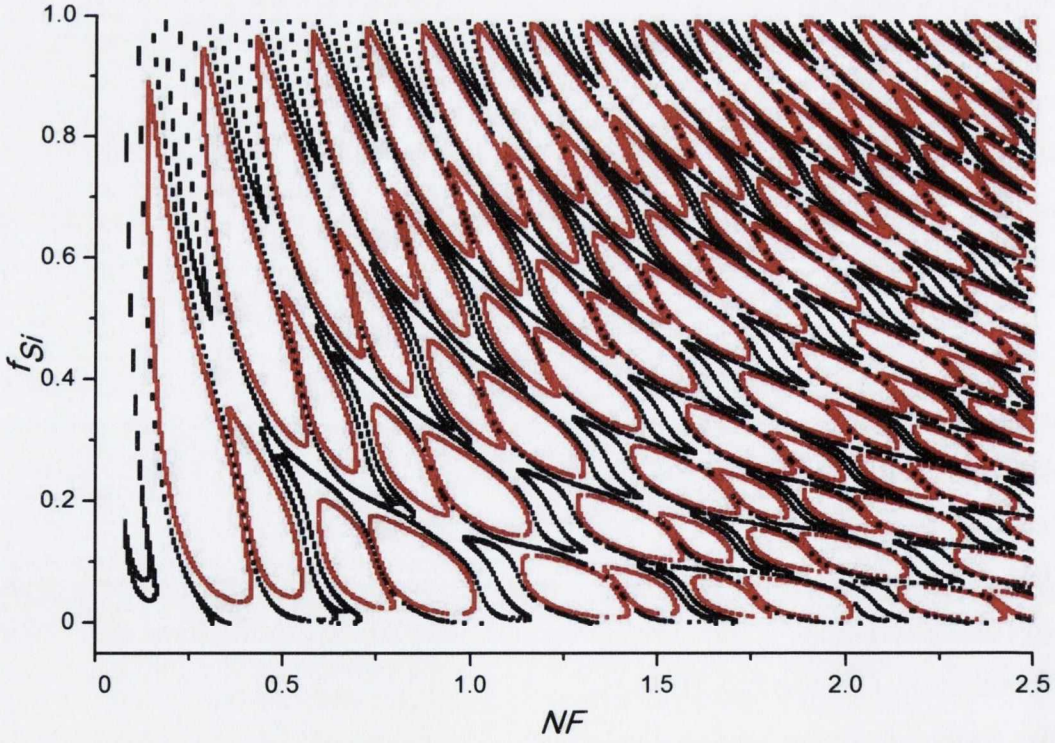

Figure 4-6: *The map of SBs for 3-period PhC "Si-LC" with n_{LC}=1.49 (red contour) and map of TBs (black lines).*

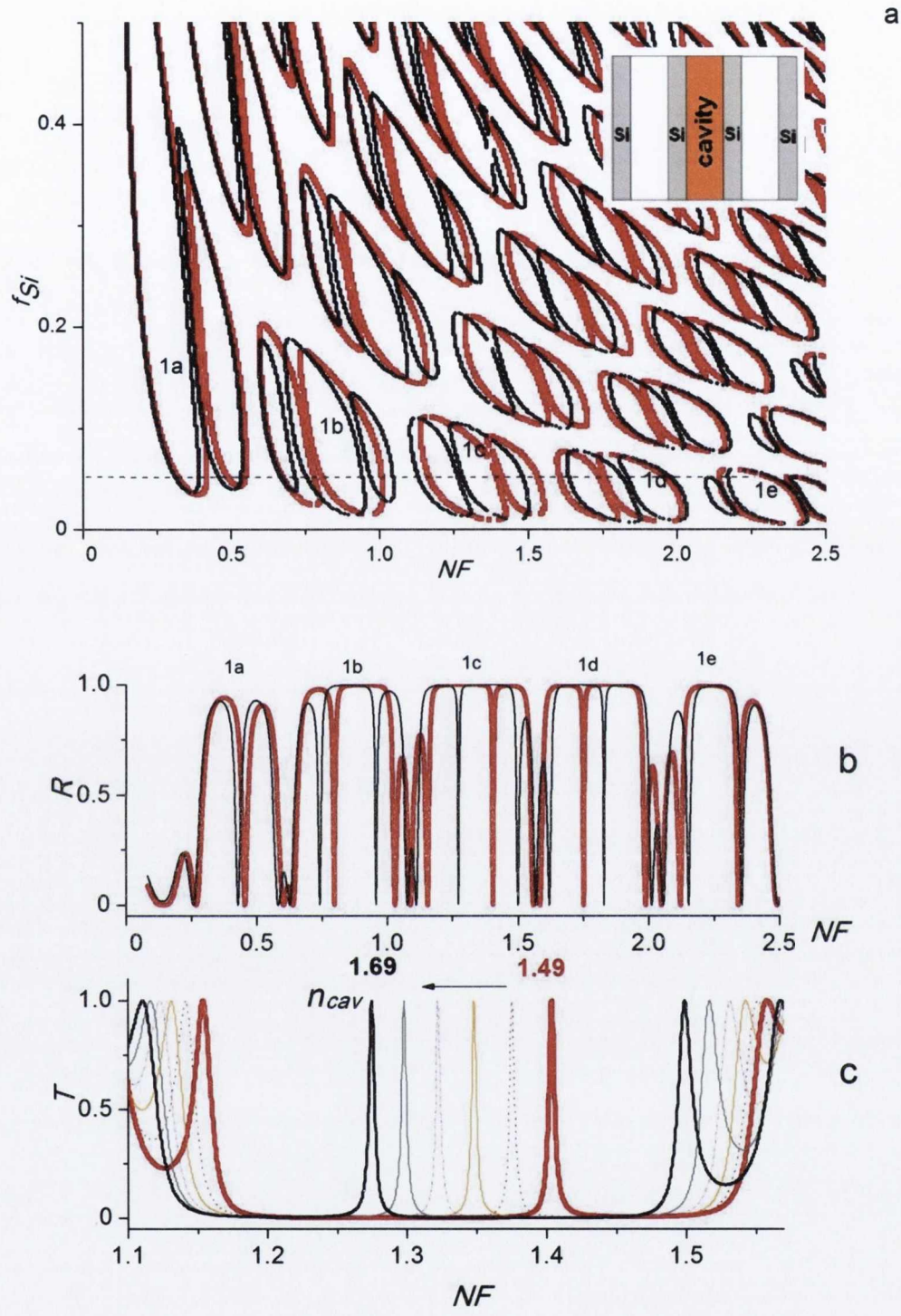

***Figure 4-7**: (a) The map of stop-bands (R_{cutoff}=0.85) for 3-period PhC "Si-LC" (see insertion) with tunable LC optical defect at n_{LC}=1.49 (red contours) and 1.69 (black contours). (b) Reflection spectra, R for f_{Si}=0.05 with n_{LC}=1.49 (red line) and 1.69 (black line); (c) the extended transmission spectra, T, with relative peak shift of ΔNF/NF = 9.7% for SB 1c.*

Next, we investigate how the PBG map will look like when the refractive index of LC defect is replaced by the value of n_{LC} =1.69 (instead of n_{LC} =1.49 used in the previous case). As can be seen from Figure 4-7(a), the first stop-band as well as SBs of high order have changed insignificantly by this replacement of n, as expected, since the optical contrast of PhC was not significantly changed. The major changes are observed in the regions of the defect modes, namely, the smaller the f_{Si} values, the larger variations are. For example, in SB obtained at $f_{Si} \sim 0.1$ and NF=0.6-1.0 for the modelled transformation at given value of Δn=0.2, two defect modes with a consequent band shift may appear instead of one mode. This can be explained by an increase of the optical width of the cavity. As the purpose of this Section is to consider how the maximal shift of the resonance peaks can be achieved, we have to analyse the following points. What values of f_{Si} must be selected to obtain the resonance peaks in the limited range of SB width? To make the solution easier, the f_{Si} values must be in the range where SB is the widest. In Figure 4-7(a) this region of SB corresponds to f_{Si}<0.5. We note that this range of f_{Si} is larger than in case of "*Si-air*" structure (see Figure 4-2(a)) where f_{Si}<0.2.

The regions of defect modes must also demonstrate the maximal shift and at the same time the resonance peak with minimal n=1.49 located near the blue edge of SB, since when the value of n increases to 1.69, the resonance peak should not leave a selected stop-band. As can be seen from Figure 4-7 (a), the width of SBs **1a**, **1b**, **1c**, and **1d**, for example for f_{Si}=0.05, is large enough to accommodate both resonance peaks. Based on these conditions, it is more preferable to select PhC with f_{Si}=0.05, for which the spectrum R is depicted in Figure 4-7(b). Figure 4-7(b) shows that the maximal shift of the resonance peak is provided by SBs **1c**. Figure 4-7(c) demonstrates the extended transmission spectra, T, for SB **1c**. The resonance peak is shifted from 1.27 to 1.4 NF correspondent to $\Delta NF/NF$ = 9.7 %.

The obtained dependencies enable us to design the tunable filters for selection of the required transmission band. For this design it is necessary to select the operational range of frequencies (or wavelengths), to determine the lattice constant, a, a refractive index of a filler and the filling fraction of Si, f_{Si}.

4.3.2 Experimental: Fabrication and Optical Characterization

The FBRs with optimal design parameters were fabricated using optical lithography and anisotropic chemical etching of (110)Si [19] as well as DRIE process of (100)Si [20]. For fabrication of the passive FPRs the conventional Si wafers were used while tunable LC-FPR devices were formed on (110) Si-on-insulator (SOI) wafers. The thickness of the Si device layer and the Buried Oxide (BOX) layer were 20 μm and 2 μm, respectively. Thermally grown Silicon dioxide was used as a mask when etching the wafers. The choice of 20 μm for the depth, in particular, was dictated by the minimum size of the IR microscope aperture used for optical characterization, in conjunction with an FTIR, FTS 6000 spectrometer [21] (Chapter 2). The example of Silicon resonator, fabricated on (110)Si is depicted in Figure 4-8. The SEM investigation has demonstrated quite smooth (practically mirror-like) Si sidewalls of the structure fabricated by anisotropic chemical etching (Figure 4-8(b)). At the same time, the roughness of Si sidewalls, obtained after DRIE, is quite substantial (see Section 4.3.2, Figure 4-13(f)). The cavity was infiltrated with commercial LC E7 (Merck) [22] using a specially designed reservoir and the channels shown in Figure 4-8(a).

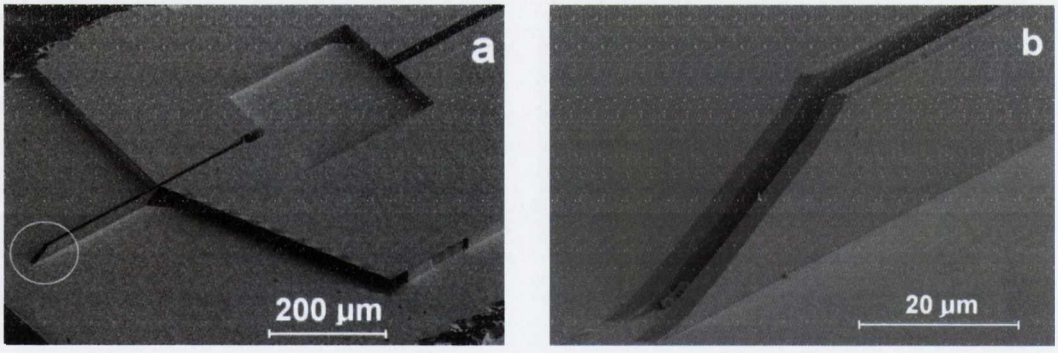

Figure 4-8: *SEM images of air-resonator, fabricated on SOI platform, using (110)Si, with (a) reservoir for LC infiltration and b) the cross-section of the resonator edge. Depth of Si-walls is* $h_{Si}=20\mu m$.

Optical characterisation was performed with a polarized FTIR microspectrometer in reflection, *R*, and transmition, *T*, modes in the wavenumbers range of ν = 650-6500cm^{-1} (λ=1.5-15μm). For polarized infrared measurements, the electric vector of the incident light is aligned with the Si grooves for *E*-polarized light, while for *H*-polarized light the electric vector is aligned along the depth direction of the grooves,

as shown in Figure 4-9. For characterization of the structure in the Near Infrared (NIR) range λ= 0.9-1.7 μm the optical fiber-coupling set-up based on an OSA was used. The setup was developed for the purpose of polarized transmission measurements in the NIR range.The characteristic vibrational bands of the liquid crystal were also analysed, together with the interference bands of high reflection, the Stop Bands, and the resonant transmission peaks. Note that all the experimental spectra (*R* and *T*) are presented in this Section in arbitrary, or normalized, units in order to clearly compare the results. Normalization of the data was necessary due, in particular, to a shading effect [21] of the focused light beam onto the Si wall of the resonator, integrated onto the chip, during infrared measurements (see Chapter 2 for details).

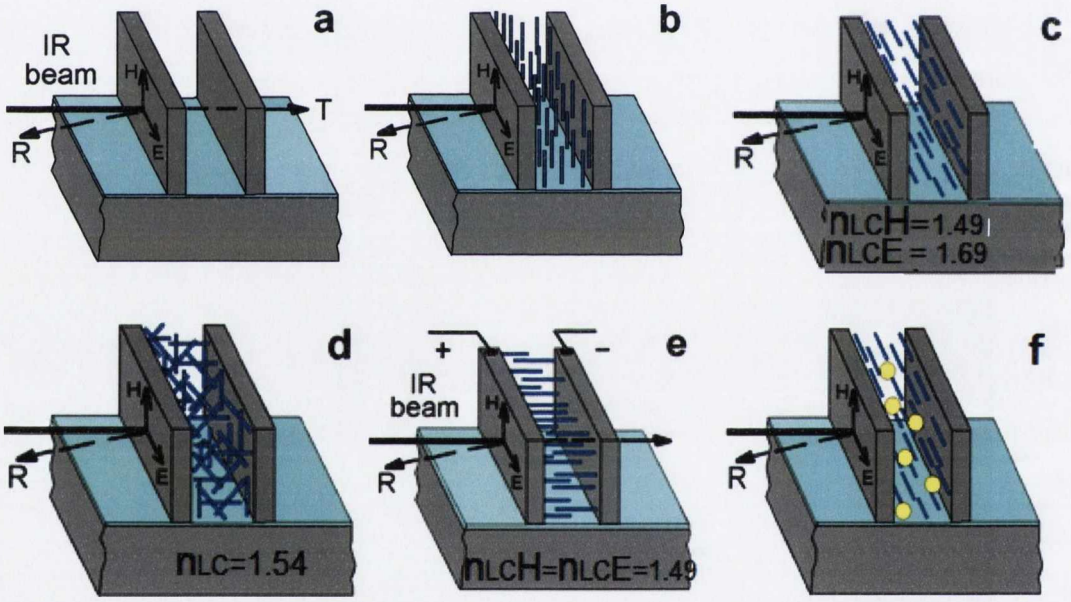

Figure 4-9: *Schematic presentation of Fabry-Pérot resonator, consisting of two Si walls separated by (a) a gap and infiltrated with liquid crystal molecules with different alignment: (b) vertical planar, (c) horizontal planar, (d) isotropic, (e) homeotropic and (f) horizontal planar with air voids.*

The obtained experimental spectra were fitted using the chosen model for the three-layer system ("*Si-air-Si*" or "*Si-LC-Si*"), which allows us to obtain the precise values of the thicknesses d_{Si} and d_{cav} as well as n_{LC}, served as fitting parameters. Both thickness values, obtained from the fitting coincide well with the results estimated from SEM images. The used nematic LC E7 is a dispersive material demonstrating three absorbtion bands in MIR at 1497 cm^{-1}, 1606 cm^{-1} and 2226 cm^{-1}. The dispersion formula for the ordinary and extraordinary refractive indexes can be described as:

$$n_o = 1.4990 + 0.0072\lambda^{-2} + 0.0003\lambda^{-4}$$

$$n_e = 1.6933 + 0.0078\lambda^{-2} + 0.00028\lambda^{-4}$$

The variations of n_{LC} values with wavelength are not significant and, hence, were not considered in the spectra simulations.

4.3.2.1 Fabry-Perot resonator fabricated by anisotropic etching of (110)Si

The polarized reflection spectra R of the resonator, fabricated by anisotropic etching of (110)Si, are discussed in this Section. The experimental, E-polarized reflection spectra of the air and LC resonators are shown in Figure 4-10(a). This figure depicts the characteristic interference bands spread uniformly throughout the entire range of spectra from 650 to 6500 cm^{-1} (15-1.5 μm). The fitting of the registered spectra was performed until the best fitting was achieved at certain fitting parameters d_{Si} and d_{cav}. The spectrum calculated with the best fitting parameters (d_{Si}=1.2 μm and d_{cav}=3.4 μm) is shown in Figure 4-10(b) for n_{cav}=1. As can be seen from Figure 4-10(b) the calculated spectrum shows four characteristic resonance peaks, which are also observed in the experimental spectrum with some degradation of peak quality.

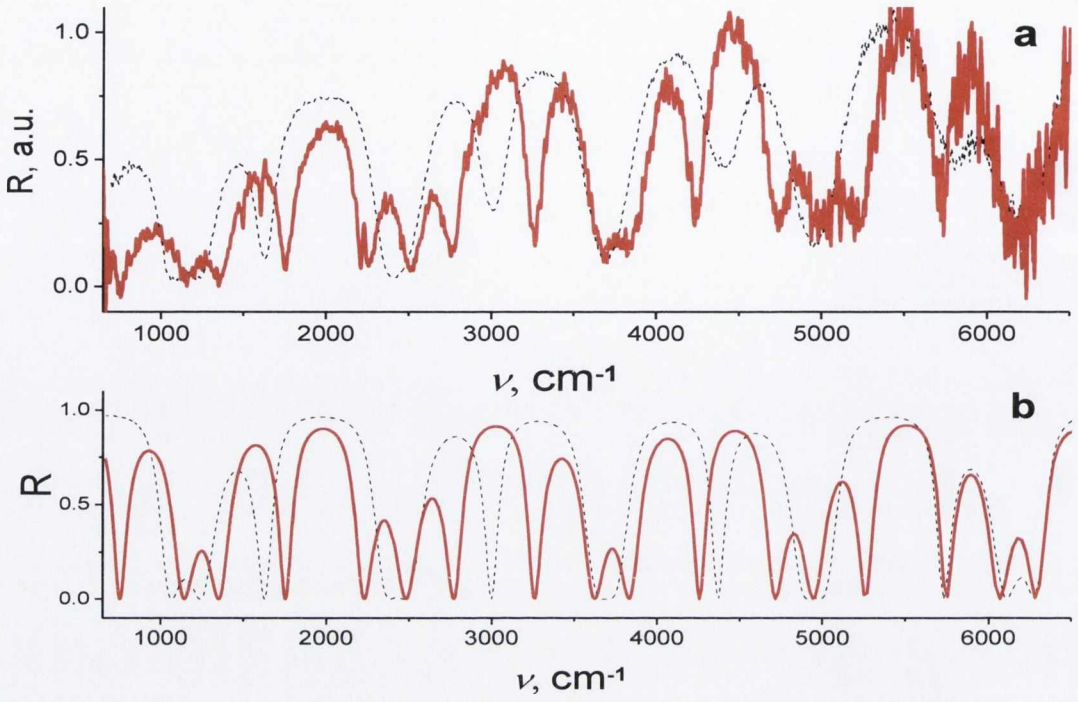

Figure 4-10: *The (a) experimental and (b) calculated reflection spectra for air (dashed line) and LC (solid line) resonators. For spectrum, shown in (b),* $n_{cav}=1$ *(dashed line) and* $n_{LC}=1.72$ *(solid line) for* $d_{Si}=1.2$ *μm and* $d_{cav}=3.4$*μm. The height of Si wall is* $h_{Si}=50$*μm.*

The latter is demonstrated as a broadening of the resonance peaks as well as decrease of the peak's amplitude. This degradation could be caused by few factors such as the focused light beam of the FTIR microscope, shading effect, unevenness of the Si walls and others. Nevertheless, the position of all experimental SB peaks is in a good agreement with calculated spectrum, which confirmed a good quality of the Si sidewalls and their correspondence to the desired geometrical parameters. The infiltration of LC into the cavity results in substantial blue-shift of nearly all of the interference bands (IBs), which reflects the increase in the refractive index of the resonator cavity. Moreover, the shape of the resonance peaks becomes more distinct.

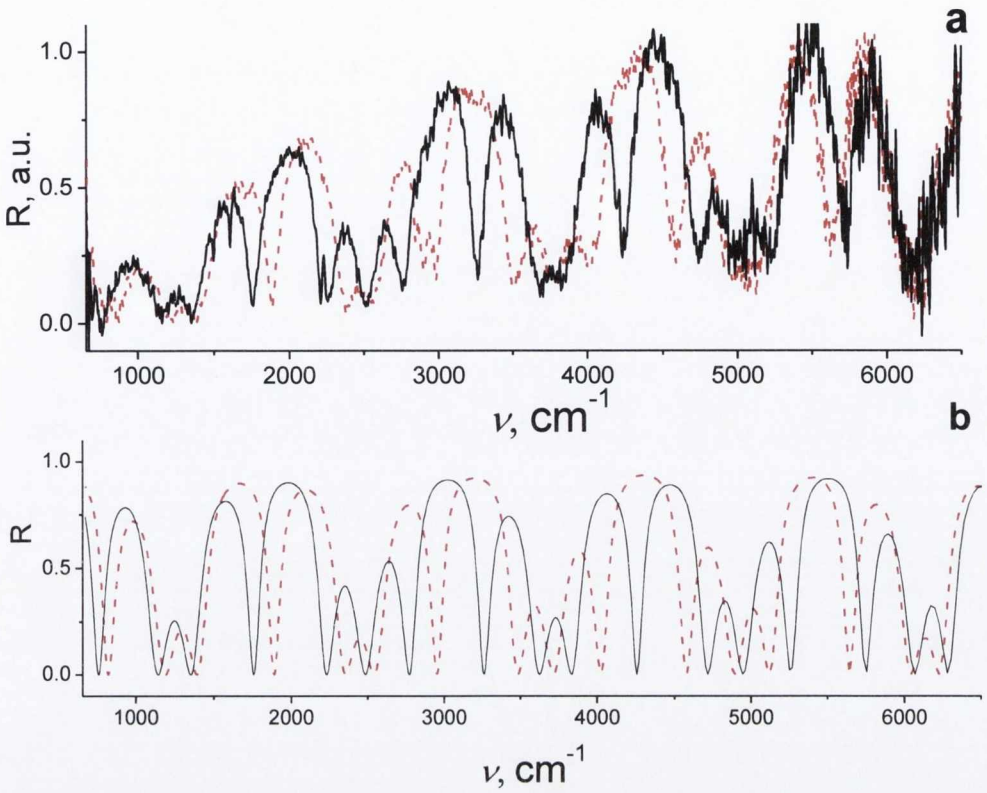

Figure 4-11: *The (a) experimental and (b) calculated reflection spectra for LC-resonator for E-(solid line) and H-polarization (dashed line). Calculated spectra with* n_{LC}*=1.72 (solid line) and* n_{LC} *=1.53 (dashed line),* d_{Si}*=1.2μm and* d_{cav}*=3.4μm.*

As is well known a decrease in the optical contrast at the interface of two phases diminishes the effect of light scattering, which can influence the peak quality and thereby explains some improvement in the resonance peaks quality. The fitting of the reflection spectra R for LC-resonator with the same parameters d_{Si} and d_{cav}, but at variation of n_{cav}=n_{LC} in the range from 1.3 to 1.8, leads to a reflection spectrum R for E-polarization, shown in Figure 4-10(b) (solid line) at n_{LC} =1.53. Quite good agreement is observed again between calculated and experimental spectra in Figure 4-10.A similar approach was used for fitting the R spectra of the LC-resonator for H-polarization, and both spectra (for E- and H- polarizations) are shown in Figure 4-11. Figure 4-11 reveals that the R spectrum for E-polarization for three lowest SBs is blue-shifted with respect to that for H-polarization. Apart from this, the resonance peaks are observed on Figure 4-11 in maxima of IBs at ~3300 cm^{-1} and at ~4200 cm^{-1} as was predicted by GMs in Section 4.3.1.

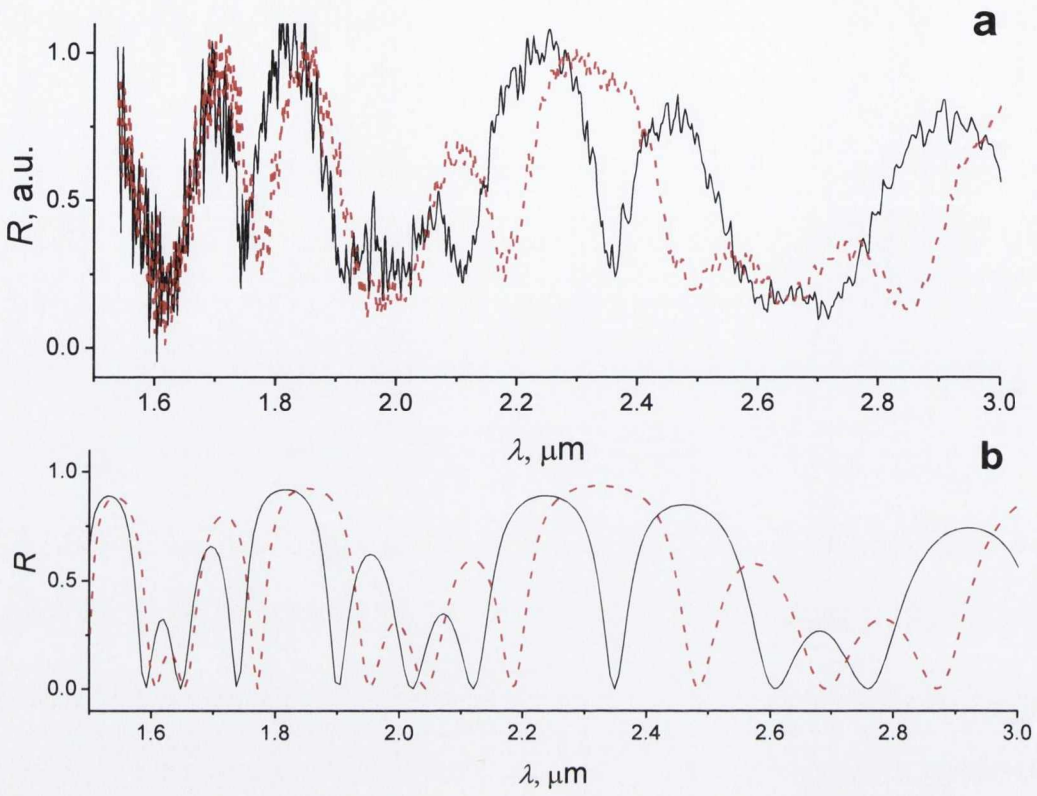

Figure 4-12: *The (a) experimental and (b) calculated reflection spectra in NIR range vs. wavelengths (from Figure 4-10).*

As was already shown for the *E*-spectrum, the fitting of *H*-spectrum demonstrates a very good convergence between experimental and calculated spectra at n_{LC}=1.53. From the fitting we receive practically the same value of birefringence of LC E7 which is Δn=0.19 comparing to the literature [23], but slightly different values for the ordinary amd extraordinary refractive indexes: n_o=1.53 and n_e =1.72. At the same time, the high value of Δn is also confirmed by the appearance of the characteristic vibrational bands of LC E7 [24] at 1497, 1602 and 2222 cm^{-1}, which are observed in the *E*-spectrum and almost absent in the *H*-spectrum. Therefore, one can conclude that the spontaneous planar orientation of the LC director along the channel has occurred, which corresponds to the schematic, presented in Figure 4-9(c). The experimental *R* spectra versus wavelengths (the same ones as presented in Figure 4-11(a) vs. wavenumbers) are presented in Figure 4-12(a) with extension to the NIR range 1.5–3 μm. A good correspondence between the positions of *R* bands and the resonance peaks is observed

in the regions of 1.7-1.8 and 2.2-2.35 μm, which is in agreement with the calculated data shown in Figure 4-12(b).

Thus, the resonator with d_{cav}=3.4 μm demonstrates quite promising characteristics as follows from simulations. If it is an LC-resonator, then, $\lambda_0=(2\cdot 1.6)\cdot d_{cav}$=11μm and d_{Si}=11/(3.42·4)=0.8μm. During fabrication we have received a resonator with d_{Si}=1.2 μm, which is quite close to the calculated value. We can, therefore, conclude that the LC-resonator with a working wavelength of 11 μm (or ~910 cm^{-1}) is fabricated. The resonance peak of this FPR is seen in experimental and in calculated reflection spectra (Figure 4-11). In addition to that, the corresponding resonance peaks of 2nd, 3rd, 4th and 5th SBs are perfectly depicted in the calculated as well as in experimental spectra of air and LC resonators (see Figure 4-10…Figure 4-12).

4.3.2.2 Fabry-Perot resonator fabricated on (100)Si by deep reactive ion etching

Let us now investigate a non-ideal resonator with non-optimal calculated parameters. In contrast to the previously described FPR, this resonator is fabricated on (100)Si by DRIE process. In this case, if the depth of the etching is relatively large, quite significant roughness of the Si sidewalls is observed (see Figure 4-13(e, f)), which may strongly influence the quality of the experimentally registered spectra. Another distinct feature of this resonator is the smaller depth (or height, h) of its Si walls (h_{Si} = 20 μm). The decrease in the height of the Si walls results in a decrease of the aperture of the incident light beam, which in turn leads to reduction of the signal-to-noise ratio during FTIR measurements.

The experimental and calculated reflection spectra for air and LC resonators are presented in Figure 4-13(a-d). The interference bands in spectrum R are deformed and demonstrate the reduced amplitude modulation and so only the part of the spectral range below 4000 cm^{-1} is shown. The fitting of this reduced range of spectra (650 – 4000 cm^{-1}) for the air resonator (see Figure 4-13(a)) yields the following parameters of the resonator: d_{Si}=2.6 μm and d_{cav}=5.4 μm. Therefore, if we use this resonator as a resonator calculated for utilisation with LC, then it's working wavelength (the position of the first resonance peak) will correspond to $\lambda_0=2\cdot 1.6\cdot d_{cav}$=17.3 μm and the thickness of the Si walls to d_{Si}= 17.3/(3.42·4)=1.26 μm.

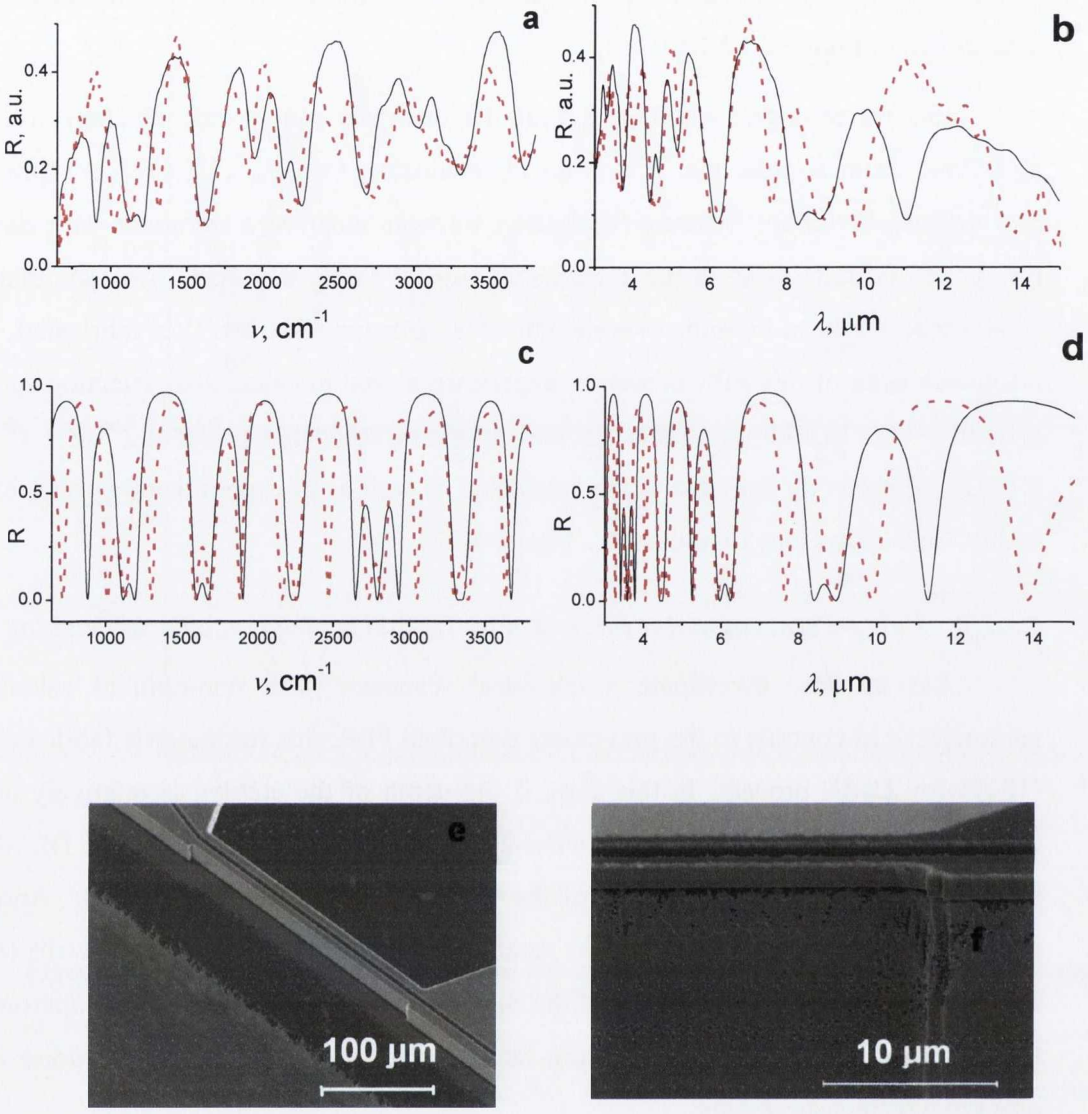

Figure 4-13: *The (a, b) experimental reflection H-spectra of empty (dashed line) and LC (solid line) resonator vs. (a, c) wavenumber and (b, d) wavelength. (c, d) Calculated spectra with n=1 (dashed line) and n_{LC} =1.53 (solid line). SEM images of the resonator: (e) the top view and (g) a sidewall roughness, obtained after DRIE of (100)Si, h_{Si}= 20μm.*

Thus, according to the calculations, the obtained resonator does not have optimal parameters and, as a result, the position and the quality of the resonance peaks will be different. Nonetheless, the characteristic peaks (dashed lines in wavenumber (Figure 4-13(a, c)) and in wavelength (Figure 4-13(b, d)) presentations) at ~1300 cm^{-1} (7.7 μm) and at ~2500 cm^{-1} (4 μm) are well identified during the fitting as resonance peaks in

the reflection spectrum of the air resonator. After the infiltration of the air cavity with LC, the n_{cav} changes and this leads to change in the experimental and calculated spectra R, denoted by solid lines in Figure 4-13(a, b) and Figure 4-13(c, d), respectively. Performing the fitting with known parameters d_{Si} =2.6 μm and d_{cav}=5.4 μm, we find the value of n_{cav}=1.53. This value of n_{LC} provides the shift of spectral patterns in such a way that at the frequency of ~900 cm^{-1} (11 μm) the empty resonator R has high values, while for LC-cavity the values of R are low. A reverse situation is observed at frequency of ~2500 cm^{-1} (4 μm) where for the empty resonator the low R values are obtained, while for the LC-cavity the R values are high. Therefore, it was shown that an LC resonator can be designed even with non-optimal parameters and despite this it can possesses relatively good optical characteristics close enough to the calculated values of an ideal resonator. It was also shown that the roughness of Si sidewalls impairs the quality of the resonator fabricated on Si using the DRIE technique.

4.3.3 Ultra-wide tuning of resonance modes

4.3.3.1 Thermo-tunable single channel devices

The tunable LC resonator was fabricated on (110)Si by anisotropic etching, in which the tuning of optical properties was obtained due to the reorientation of LC molecules (or LC director) as was predicted by GM in Section 4.3.1. Initially, the reflection spectrum, R of an air resonator was measured and its parameters were determined, using a fitting procedure as described in previous Sections. The air resonator parameters were chosen close to the ideal ones, as described in Section 4.3.2; the parameters obtained during the fitting of the reflection spectra are: d_{Si} =1.2 μm and d_{cav}=3.6 μm.

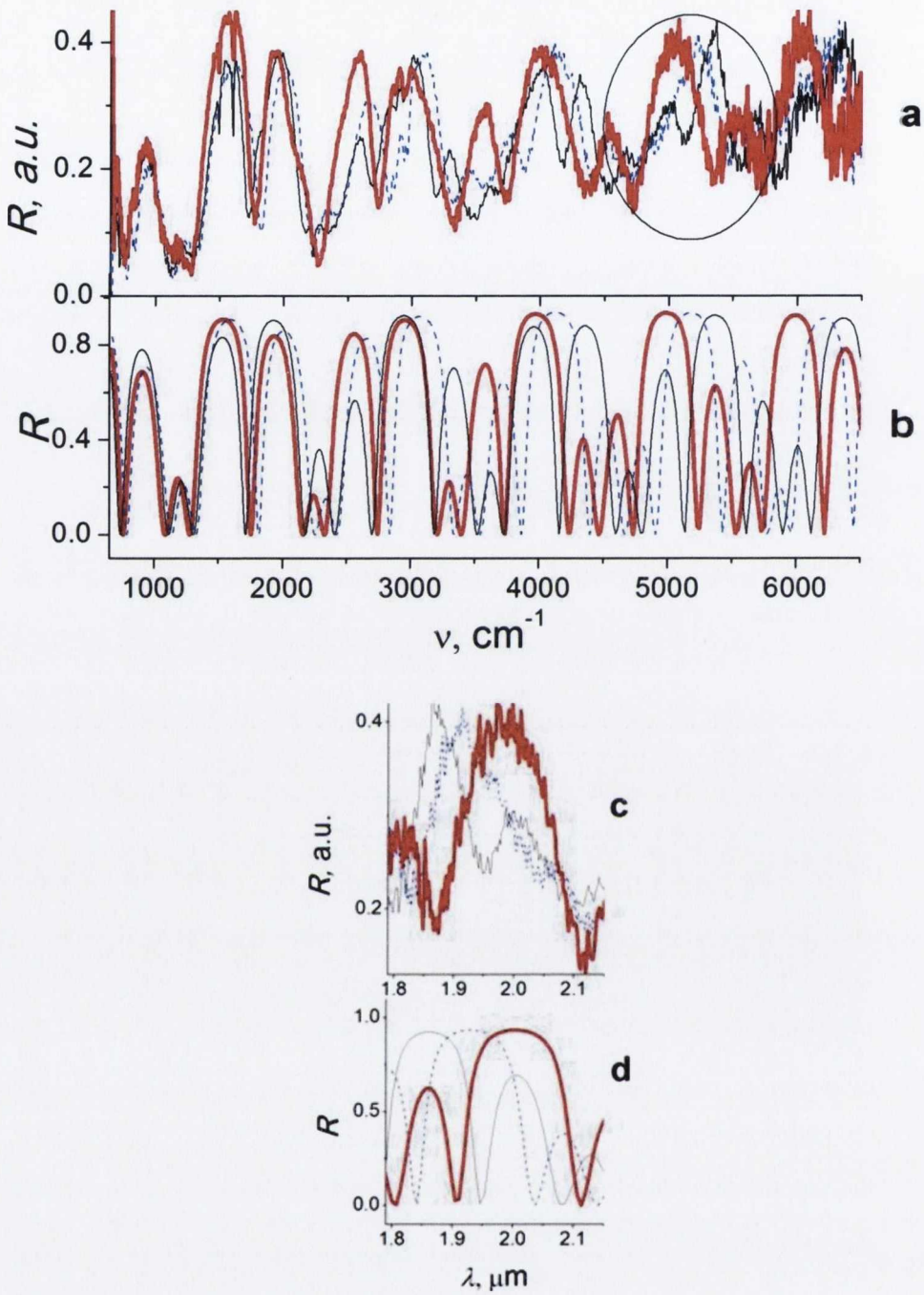

Figure 4-14: *(a, c) The experimental reflection spectra of LC resonator, demonstrated the effect of thermo-tuning, namely the transition from LC mesophase at 20 °C (dashed line for H- and thin line for E-polarization) to the isotropic phase at 65 °C (thick line). (b, d) Calculated spectra with* n_{LC}*=1.67 (thin line),* n_{LC} *=1.54 (thick line) and* n_{LC} *=1.5 (dashed line).* d_{cav} *=3.6 μm,* d_{Si}*=1.2 μm and* h_{Si}*=50 μm.*

Then, the cavity was infiltrated with LC E7 and the reflection spectra were measured at room temperature for *E*- and *H*-polarization of the incident light (see Figure

4-14(a)). As can be seen from Figure 4-14(a), the spectra R are shifted at different polarizations. The fitting, performed for R spectra (Figure 4-14(b)), enables the value of n_{LC} to be determined from each of these spectra. The n_{LC} value, obtained for E-polarization is 1.67, while for H-polarization n_{LC}=1.5. Moreover, as can be seen from Figure 4-14(a), the characteristic vibrational bands of LC E7 at 1497, 1603 and 2222 cm^{-1} are also present in the spectrum R only for E-polarization, which confirmed that LC has a pronounced spontaneous orientation of rod-like molecules along the channel. This type of LC orientation is shown schematically in Figure 4-9(c) and is one of the most common types of alignment, obtained in this work during LC-infiltration into 1D PhCs air channels by capillary effect.

The resonator was heated up to 65°C using a calibrated thermocouple micro-heater and the reflection spectrum was registered again at this temperature (Figure 4-14(a)). The variation of n_{Si} at heating to 65°C is not larger than 0.001 and, therefore, can be neglected in this case. Using the fitting of the registered reflection spectrum, the value of n_{LC} was estimated to be around n_{LC}=1.54. Two spectral effects were revealed for R spectrum at E-polarization (see the stop-band in Figure 4-14 shown by circle). In particular, the resonance peak, observed at frequency ~ 5100 cm^{-1} (at wavelength of 1.94 μm on Figure 4-14(c)), is situated quite close to the maximum of reflection from the heated resonator (thick line). The value of R=0.25 a.u. is observed at this resonance peak at room temperature, while at 65°C the maximum of reflection increases up to R=0.4 a.u. At the same time, at frequency of ~5300 cm^{-1} (wavelength 1.94 μm) the reflection is R=0.41 a.u. at room temperature, while at heating of LC to 65°C and its transition to isotropic phase (see Figure 4-9(d)) the resonance peak at λ=1.9 μm with R=0.19 a.u. is appeared. Thus, the thermo-optical effect of LC can be used at two wavelengths. With improved fabrication technology of this type of FPRs, the much higher ratio of the reflection values (up to 0.01/0.89) for these two cases can be achieved (Figure 4-14(d)). Unfortunately in this type of experiment it is difficult to return to the original LC orientation after cooling the structure down to room temperature. However, this example demonstrates the principle of tuning the resonator for controlling the relative intensity of the reflected light of certain polarizations. It is also demonstrates the possibility of utilizing the observed optical effects in SB and in resonance peaks of high order.

4.3.3.2 Electrically tunable Fabry-Perot resonator

The electro-tunable LC-FPR was fabricated using optical lithography and anisotropic etching of (110) SOI wafer. A view of the resonator, fabricated on (110) Si, is depicted in Figure 4-15. Si wall-electrodes were connected to the outer pads by attaching thin metal wires to the chip contact areas with conductive silver paste. An AC rectangular pulse train, with various amplitudes between 0.5 V and 15 V, with a pulse duration of $\tau_p = 1$ ms and a frequency of $f_p = 100$ Hz was used to drive the device [25].

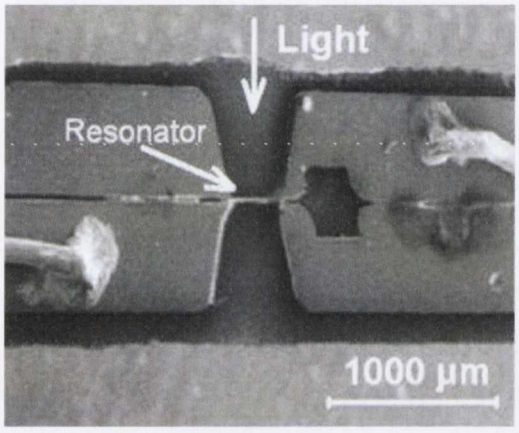

Figure 4-15: *SEM image of the top view of the FPR fabricated on an SOI wafer.*

A best fit to the experimentally measured spectra was performed using using the Transfer Matrix Method [12] was performed. For the empty resonator (n_{cav}=1) the fit was performed with a Si wall width of $d_{Si} \approx 1 \pm 0.3$ μm and a cavity width of $d_{cav} \approx 4.0 \pm 0.3$ μm as fitting parameters, while for the LC FPR, n_{cav} was used as a fitting parameter.

Reflection spectra in *E*- and *H*-polarization, registered from a 20x20 μm^2 area of an LC FPR prior to the application of the electric field are shown in Figure 4-16(a). A pronounced shift of the interference bands in the reflection spectra as a result of the change in the polarization of the probe beam from *E*- to *H*-polarization is observed, confirming the anisotropy of the LC molecules infiltrated into the resonator. In other words, this shift is caused by the alignment of the LC director along some preferred orientation within a Si groove and, therefore, due to the influence of the ordinary, n_o, and extraordinary, n_e, refractive indexes for the appropriate polarization. Similar results are obtained from the same spot when measuring the transmission, *T*, spectra (Figure 4-16(b)). We note that the transmission spectra are noisier than those taken in reflection,

due to the reduction in the total intensity of the light transmitted through the resonator. Also, the 20% reduction of the *R/T* signal comparing to the predicted in theory is due to the "shading effect" from the substrate of the fabricated FPR as well as the non-parallel light source used for the measuremtns (see Section 2.4). Nevertheless, general trends in the behavior of reflection and transmission spectra are clearly seen from a comparison of Figure 4-16(a) and Figure 4-16(b). For both polarizations, the position of the minima in the transmission spectra corresponds to the maxima of the reflection spectra and *vice versa.*

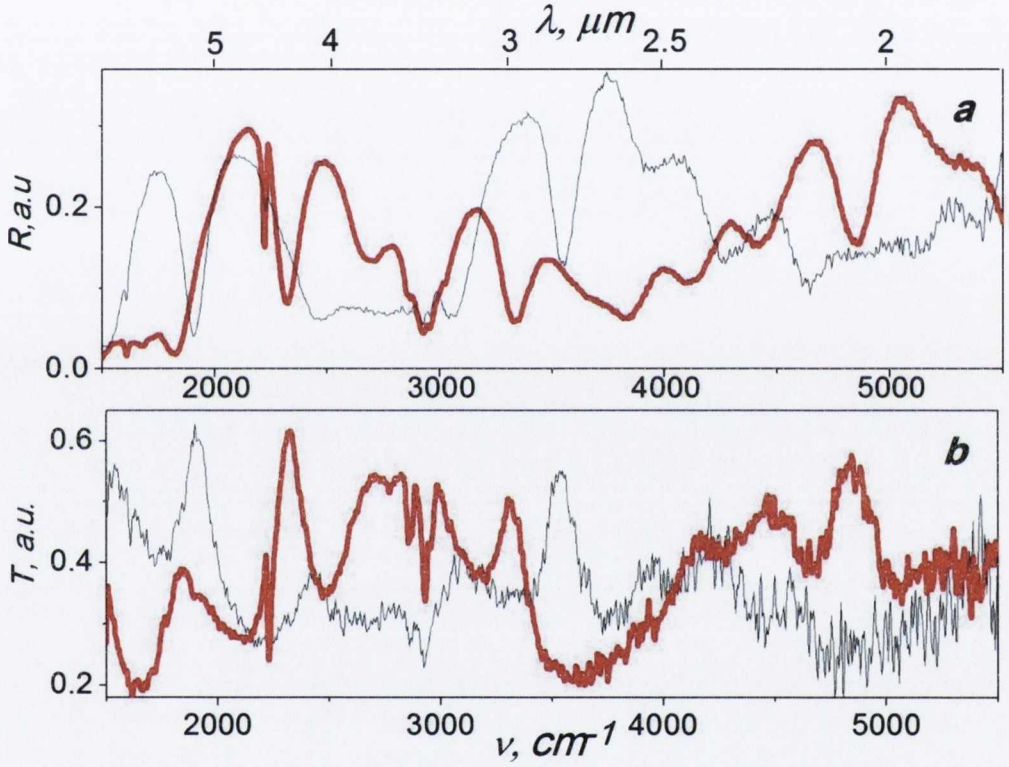

***Figure 4-16**: FTIR (a) reflection and (b) transmission spectra of the FP resonator with LC filler for E-(thick line) and H-(thin line) polarizations in the absence of an applied electric field. The resonator parameters are: width of Si walls, d_{Si}=1 μm, cavity width, d_{cav}=4 μm.*

A fit to the *R* spectra from the LC FPR results in a value of n_{cav} =1.57 for *E*-polarization, and n_{cav} =1.45 for *H*-polarization, using known values of d_{Si} = 1 μm and d_{cav} = 4 μm. The value of n_{cav} =1.45 for *H*-polarization obtained appears to be smaller than the value of n_o = 1.49 from the literature for LC E7 [23]. This discrepancy will be discussed in the following Section. The presence of the LC in the cavity is confirmed by

observation of the absorption band of LC E7 molecules at 2222 cm^{-1} [24] in the *R* (Figure 4-16(a)) as well as in the *T* (Figure 4-16(b)) spectra for *E*-polarization. We note that for the *H*-spectrum, this band is suppressed significantly in comparison to the *E*-spectrum. This behavior is typical due to the dichroism of LC molecules. The dominant behavior of the band at 2222 cm^{-1} for *E*-polarized spectra indicates a preferred orientation of the LC director in the *X*-direction, along the groove, as shown in Figure 4-9(c).

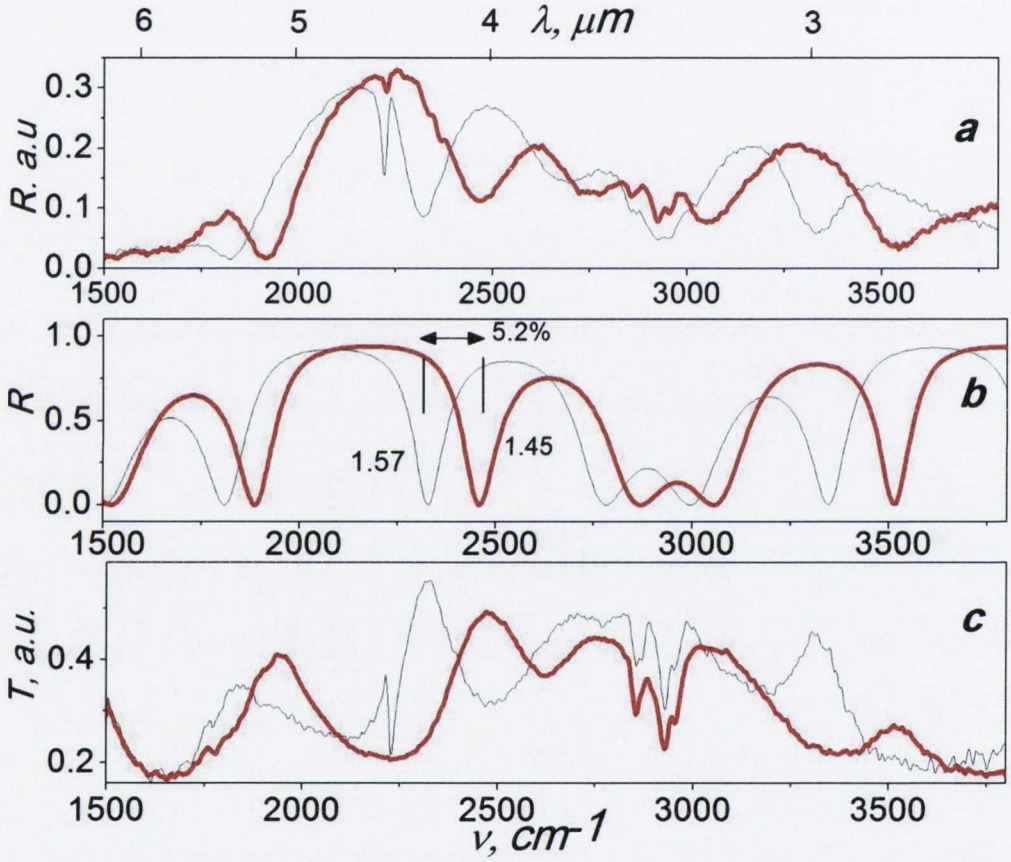

***Figure 4-17**: Experimental (a) reflection and (c) transmission spectra in E-polarization in the absence (0V – thin line) and presence (10V thick line) of an applied electric field. The spectral shift observed demonstrates the reorientation of LC molecules in the FP-cavity from planar to homeotropic alignment, b) Calculated reflection spectra, obtained from the best fit, for two values of n_{cav} shown beside the curves. Resonance peaks are seen at 1800, 2320 and 3400cm^{-1}, corresponding to 5.6, 4.2 and 2.9μm.*

Under an applied voltage of 10V, the *E*-spectra are blue-shifted, as seen in Figure 4-17(a, c), indicating that the value of n_{LC} is reduced in the resonator by the

electric field. The *H*-spectra are practically unchanged by the electric field (not shown). The intensity of the vibrational band of the LC at 2222 cm^{-1} is decreased in the *E*-spectrum at 10V (Figure 4-17(a, c), indicating that a reorientation of molecules from the initial, planar, alignment to homeotropic alignment has occurred, in accordance with the model presented in Figure 4-9(c, e). The obtained value of n_{cav} = 1.45 (at 10V) appears to be lower in this case than the n_{cav} =1.57 previously observed at 0V in the *E*-polarized spectrum. In the former case, the orientation of the LC is driven by the electric field and is strongly expected to be homeotropic. In accordance with the schematic shown in Figure 4-9(b), for homeotropic alignment of LC molecules, n_{cav} must correspond to the refractive index, n_o, of LC E7, i.e. to be equal to 1.49. The value of 1.45 obtained from the fitting routine is smaller than 1.49 by 0.04. This deviation is larger than any inaccuracies that one would expect from determining the value of n from the fitting routine with typical deviation of $\delta n = \pm 0.02$.

As was already noted above, after infiltration of the LC into FPR, the determined value of n_{cav} was 1.57 for the *E*-spectrum (significantly lower than in the previous Section). This value is close to the expected value of refractive index for a random orientation of the LC molecules n_{rand}=1.56 [23]. However, dichroism, clearly observed for the 2222 cm^{-1} absorption band, indicated that the initial orientation of LC molecules was planar. In this case, in accordance to literature, n_e must be equal to 1.69 [23], while from the fit of the spectra a significantly smaller value of n_{LC} =1.57 was obtained. Therefore we conclude from the spectral fitting process that both of the calculated n values (n_o and n_e) are smaller than those predicted by the model.

One possible reason for the lower values of n_{LC} here could be the presence of air voids inside the groove with LC. Indeed, air voids are visible in some SEM images of the LC infiltrated devices. In order to avoid the appearance of air voids, it is better to perform the infiltration of the LC at higher temperatures, typically at the temperature of the isotropic phase. However, in comparison to the previous experiment, the infiltration of the LC was intentionally carried out at room temperature, when the LC E7 is in the nematic phase. An infiltration under these conditions results in a spontaneous planar orientation of the LC director, either along the depth or along the length of the grooves [26]. In the experiment, the degree of infiltration of LC in the groove is normally observed using an optical microscope, allowing the propagation of the LC molecules

along the groove, the *X* direction in Figure 4-9(c), and the infiltration quality to be assessed.

The results obtained using the Effective Medium Approach (EMA) [27] indicate the possibility of the existence of a volume fraction of air voids in the cavity of V_{air} = 0.08, i.e. 8 % (Figure 4-9 (f)). This could explain the lower values of *n* obtained from fitting the experimental spectra for both *E*- and *H*- polarizations.

The spectrum registered across the whole infrared range, as well as the spectrum in the region of the vibrational mode at 2222 cm^{-1}, reverts to that originally seen at 0 V after the electric field is switched off. Therefore, in this work, we have demonstrated, for the first time, a spontaneous planar orientation of nematic LC molecules on an untreated Si surface, which can be reversed by the removal of the electric field, using voltages up to 10 V. As a result of electrotuning, the FP peaks are shifted reversibly by 128, 168 and 206 cm^{-1}, corresponding to relative shifts of $\Delta\lambda/\lambda$ = 4.2, 5.2 and 4.8 %.

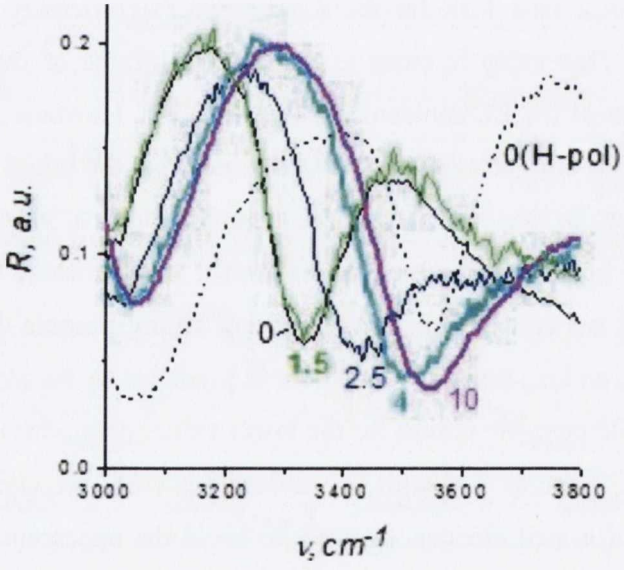

Figure 4-18: *Smooth tuning of the position of the resonance peak from 3330 cm^{-1} to 3550 cm^{-1} for E- and H-polarization (dotted line). The applied voltage is shown in Volts beside each curve.*

We also investigated the resonant peak shifts at intermediate applied voltages between 0 V and 10 V, as demonstrated in Figure 4-18 for *E*-polarization in the spectral range from 3000-3800cm^{-1}. The applied voltage of 1.5 V is not enough to cause reorientation of the LC from one state to another. At 2.5 V, which is close to the

threshold voltage of LC E7 (1.5 V), a pronounced shift of the bands is seen. The shift reaches a maximal value at a voltage of 10 V. We note that the position of the resonance peak at 10 V for *E*-polarization corresponds to the position of this peak at 0 V for *H*-polarization, as expected from the alignment models demonstrated in Figure 4-9(c, e).

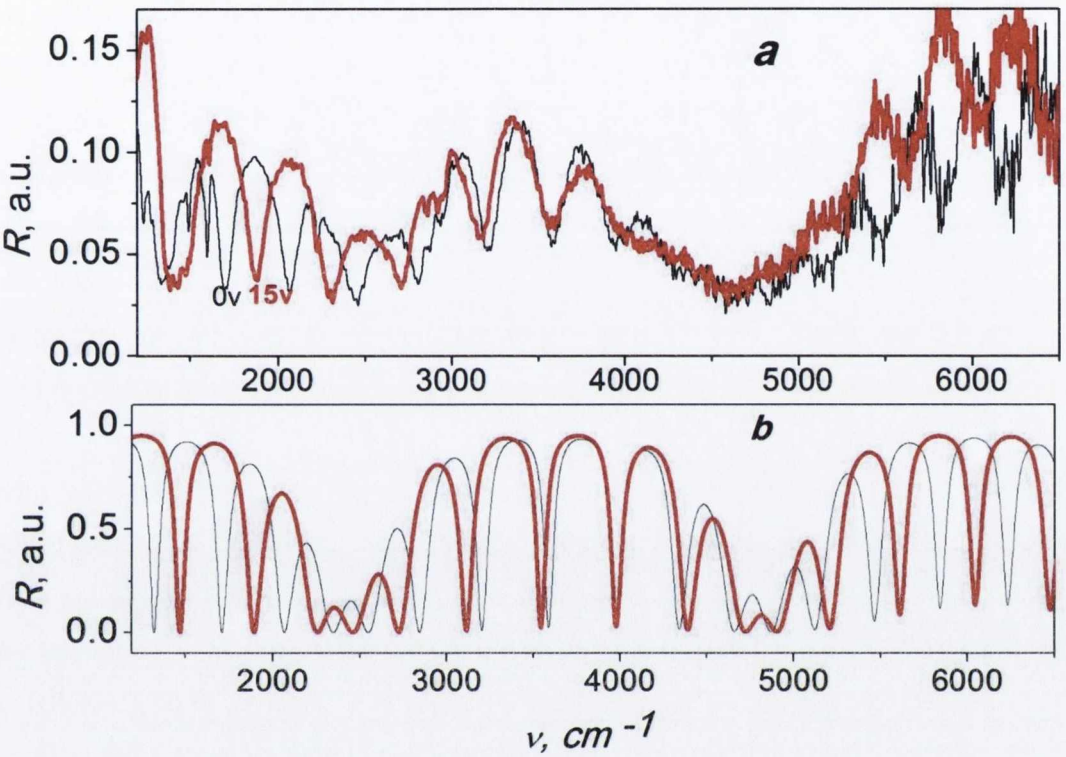

Figure 4-19: *(a) Experimental and (b) calculated E-polarized spectra of the FP resonator with d_{Si}=0.6 μm and d_{cav}=7.4 μm without electric field (thin line) and with an electric field generated by an applied voltage of 15 V (thick line). Application of a voltage of 15 V results in a shift of the resonance peaks across the spectral range. The best fit is obtained at Δn_{LC} = 0.17 (n_{LC} = 1.51, 0 V)) and (n_{LC} = 1.34, 15 V).*

A similar experiment was conducted on a different sample with a higher filling fraction of $f_{LC} \approx 0.9$ ($f_{Si} \approx 0.1$). By fitting the experimental spectrum for the empty sample, a value of d_{Si} = 0.6 μm was obtained, with a resonator cavity width, d_{cav}= 7.4 μm (f_{Si} = 0.07). The reflection spectrum, registered for this sample after LC infiltration, demonstrate the shift of the band positions, depending on the polarization of the probe beam, that is, the system exhibits anisotropy. For *E*-spectrum of *R* (Figure 4-19(a)), all three characteristic vibrational bands of the LC (at 1497, 1602 and 2222 cm^{-1}) have a higher intensity than those in the same spectrum taken using *H*-polarization (not

shown). This indicates that certain orientation of the LC molecules along the *X*-axis has occurred (Figure 4-9(c)). Reflection spectra in *E*- polarization, registered after electric field application, are shown in Figure 4-19(a). The applied voltage of 15V results in a blue-shift of the *E*-spectrum, and to a decrease in the intensity of the LC peaks, as demonstrated previously, causing a homeotropic orientation of the LC molecules (Figure 4-9(e)). The results of the best fit to the experimental spectra, using n_{LC} as a fitting parameter and values of d_{Si} = 0.6 μm and d_{cav} =7.4 μm, are presented in Figure 4-19(b). The characteristic FP peaks are seen in the calculated spectrum, which coincide well with the corresponding experimental peaks across the spectral range investigated from 650 to 6500 cm^{-1} (see Figure 4-19(a)). The shifts in the experimental spectrum, obtained after the application of an electric field, are also confirmed in the simulated spectrum. In addition, after the application of voltage of 15 V, the intensity of all three vibrational bands of the LC decreases significantly, confirming the transition of the LC to a homeotropic alignment.

The electro-optical effect observed here can be considered as a reversible, because after the electric field was switched off (0 V) the spectrum returns to its initial state, corresponding to a planar orientation of the LC molecules. The same effect was observed in the first sample, discussed earlier. Figure 4-20 shows intermediate spectra, obtained using a range of applied voltages from 0 V to 15 V, in an extended spectral region from 1480 to 2300 cm^{-1}. These spectra demonstrate the possibility of fine tuning of the resonance peaks. This tuning effect is clearly apparent, for example, in the vicinity of ~ 1750 cm^{-1} (λ=5.7 μm). The reorientation of LC molecules under an applied voltage is also clearly demonstrated by the change in intensity of the 1602 cm^{-1} vibrational band. As noted earlier, the values obtained for the parameter n_{LC}, calculated during the fitting routine, are slightly lower than the ordinary and extraordinary refractive indexes of LC E7 from the literature. Note that the values of birefringence of 0.12 and 0.17 are close to the Δn_{LC} = 0.2 obtained for LC E7 in the mid-IR range [23]. We assume that the lower n_{LC} values obtained here are related to the presence of a small number of voids in the LC, formed during the LC infiltration process.

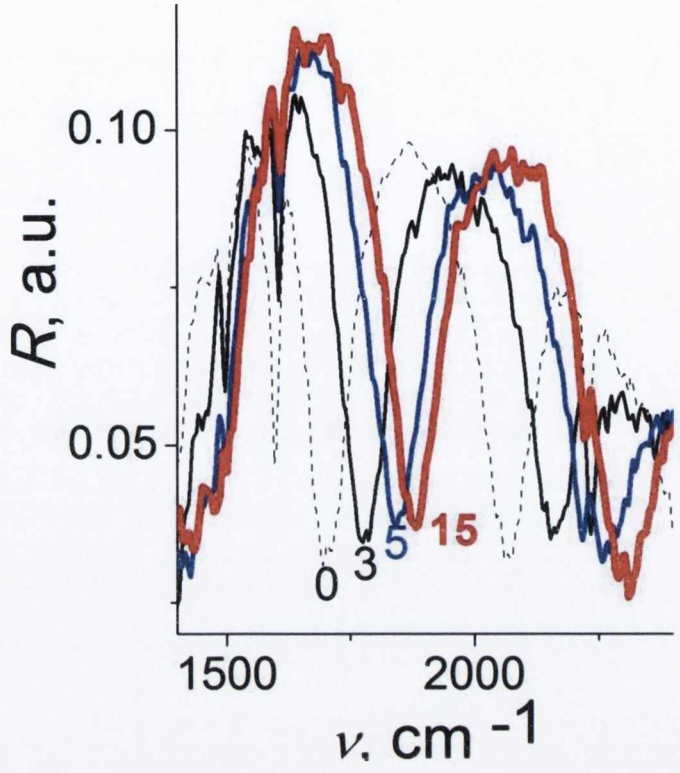

Figure 4-20: *Smooth tuning of the resonance peak from 1700 to 1880 cm^{-1} in the experimental reflection spectra of the FP resonator (from Figure 4-17) with a maximal relative shift of $\Delta\lambda/\lambda$ =10%.*

An electro-tunable LC FPR, based on the principle of changing the optical thickness of the LC resonator, using resonance peaks of high order, has been demonstrated in this investigation. This electro-optical device is based on microstructured Silicon with LC filler. The closest existing analogue to the device suggested is a hybrid photonic crystal microcavity switch, as described in Ref. [28]. In this device, a relative shift in the resonance mode of the order of $(\Delta\lambda/\lambda) = 0.5\%$ in the near infrared range was achieved as a result of the electro-optical effect obtained due to the reorientation of LC E7 in the cavity of a two-dimensional PhC. We would also like to mention Ref. [29], where a shift of the resonance peak of $(\Delta\lambda/\lambda) = 0.5\%$ was reported, due to a variation in the geometrical thickness of the FP air cavity driven by an electric field applied to the second movable mirror. Therefore, the FPR fabricated in this work, fabricated by microstructuring of Si, is significantly better than comparable devices, based on the fact that the resonance peak shift is reached up to 5- 10%.

This can be explained by the fact that

i) the resonance peaks in the stop bands of high order were utilized, where a significant shift of the consequent defect mode can be obtained as a result of the change in Δn in the electro-optical material used

ii) in comparison with the rough interface in a 2D microcavity, the application of an LC with plane-parallel reflectors provides the most effective distribution of "switchable" molecules with respect to the Si side-walls and the applied electric field.

Investigations of the optical properties of electro-optical devices in the mid-IR range are also technologically important. "*Si-LC*" composite materials, and switchable elements based on them, are being researched aggressively, due to their transparency in this spectral range and these devices may have application in biochemical sensing, medicine, defense and security [1].

4.4 *Coupled multi-cavity Photonic Crystals resonators*

In Section 4.3 the investigation of FPRs constructed from "*Si-air-Si*" and "*Si-LC-Si*" structures demonstrated its effectiveness as a fine tunable filter with a shift of the resonance peak up to $\Delta\lambda/\lambda$=10%. This result has demonstrated the largest experimental shift, achieved up to date for the microstructured resonators based on Si, and utilized for molding of light propagated parallel to the substrate. In this Section the continuous fine-tuning capability of the LC single microcavity was exploited to the situation of individually tunable coupled multi-cavities. Application of the voltage to each cavity individually and its continuous random variation in all cavities allows to overcome the problem of strong coupling between channels. Using the example of coupled triple-cavity PhC filter a simple model for easier manipulation of LC within individual cavities have been elaborated, which enables independent fine tuning of each channel in the entire system. Based on the obtained results, prototypes of integrated triple-cavity PhC filters were designed and fabricated on SOI platform. Finally, using a fabricated prototype device as an example, one of the applications of the proposed method, in particular an optimization of the filter to its initially designed operational mode after fabrication process, is demonstrated.

For clarity of presentation of the methodology in this Section, we will focus only on PhC structures with a triple-coupled defect. It should be noted that the suggested model can be extended to a higher number of the coupled cavities (defects) and, thus to a higher number of resonances with improved Q value.

4.4.1 Methodology

Although the wide and precise tuning of the resonance peaks in single cavity and double cavity systems, using optical anisotropy of the LC, have been extensively studied in the past years [30-33], only the simultaneous coupled resonances tuning or coupled FSR tuning was demonstrated so far. Indeed, the optical properties of the coupled micro-cavities are strongly dependant on each other, i.e. changing the parameters of one of the coupled cavities directly leads to the change of the optical properties of the others. This coupling effect makes the individual tuning of the resonances almost impossible. Non-trivial solutions for the refractive index variations are needed.

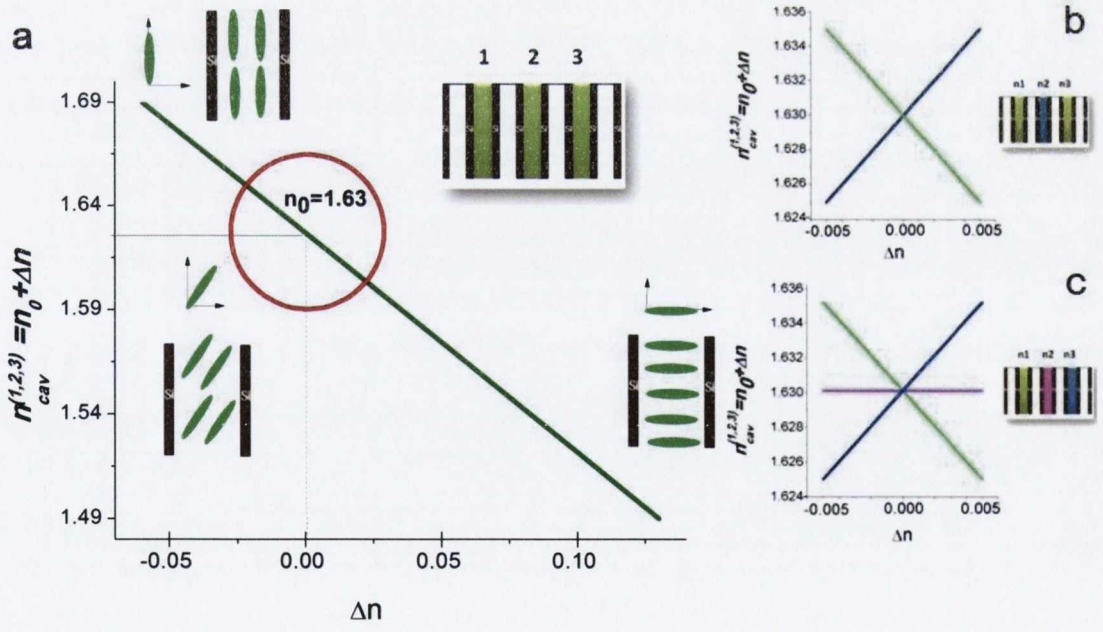

Figure 4-21: *(a) Schematic view on the variation of the refractive index of LC E7 in the cavity under an applied voltage V (see Section 4.3). (b, c) The controlled variation of the* $n_{cav}^{(1)}$, $n_{cav}^{(2)}$, $n_{cav}^{(3)}$ *that can be realized in triple-cavity system.*

In Figure 4-21(a), using the example of ne*matic* LC E7 (with n varied in the range 1.49 - 1.69) [22], the fundamental idea of the electro-tuning of the cavity mode is demonstrated schematically based on the results obtained in Section 4.3. Here, it is assumed that the original orientation of the rod-like molecules of nematic LC E7 is along the Si-walls, which ideally results in the refractive index n_e=1.69 [23]. Under an applied voltage, V=1.5...15 V, the LC molecules reorient in the cavity, which results in decrease of the effective refractive index of the LC. Obviously, this process enables to achiev a precise, continuous tuning of the cavity resonance peaks in a wide range of wavelengths [20]. By increasing the number of the coupled cavities, similar continuous tuning can be achieved for all multi-resonances simultaneously.

Let us consider the case when the electric field is applied to each micro-cavity individually. Then, by increasing or decreasing the applied voltage by ΔV in the various cavities, different variations of the LC refractive indexes can be realized, $n_{cav}^{(i)}=n_0\pm\Delta n$. For the considered example of triple-cavity PhC, the most obvious relationships between $n_{cav}^{(1)}$, $n_{cav}^{(2)}$, and $n_{cav}^{(3)}$are demonstrated in Figure 4-21(b) and Figure 4-21(c). For clarity of presentation, let us consider the initial switching position, *Position 0*, that can realize the same intermediate orientation of the LC molecules in all cavities, i.e. provide some intermediate value of the refractive index n_0 =1.63. We are interested mainly in fine tuning capabilities of the multi-channel filter and, therefore, in small variations of voltage and refractive index Δn~±5 % (red circle, Figure 4-21(a)).

4.4.2 Optimal design parameters: Gap Map Approach

Although we have chosen the simplest example of the triple-channel filter, the full investigation of the resonance modes and tuning effects in a wide wavelength range requires a long time for calculations and the data analysis can be complicated in general. The transmission spectra, obtained for different filling fractions f_{Si}, can reveal certain changes in the positioning, intensity, I, and Q-characteristics of the resonance peaks. Here, as in the case for single-cavity PhC resonator, it is proposed that the most comprehensive analysis of optical filter properties in general can only be obtained from a combination of TMM and gap map approaches [18, 34, 35]. This combination provides an easy way for graphical engineering of the SBs with multiple resonance peaks in a PhC. This is mainly due to the possibility of selection of different filling fractions, f_{si}, and an introduction of any number of cavities during spectra calculations

following by drawing of all obtained dependences in one graph. Another advantage of the GM approach is that the certain range of f_{Si}, for which the optical properties are relatively constant on the graph, provides information about maximum fabrication tolerance of the device.

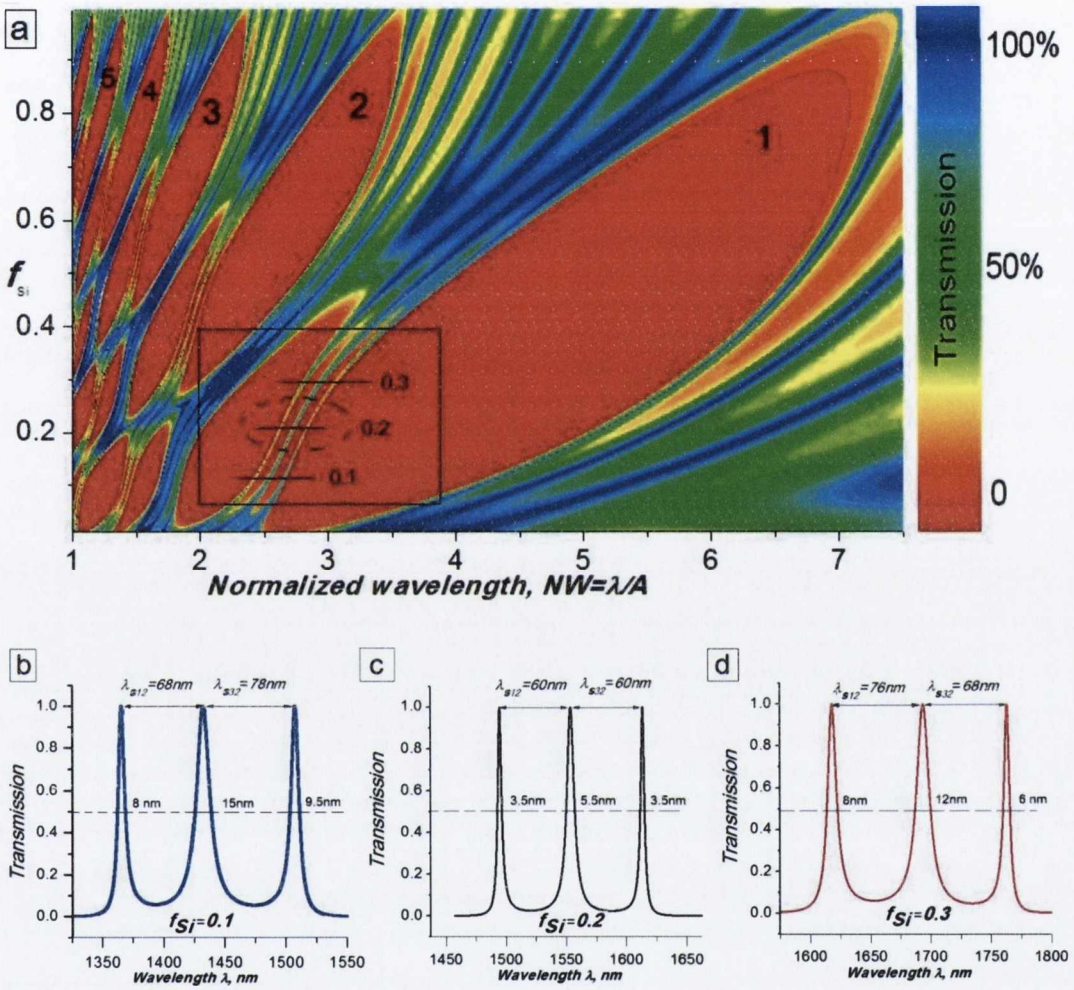

Figure 4-22: *(a) The GM of Si 1D PhC with a triple cavity with* $n_{cav}^{(i)}=n_{cav}^{(1)}=n_{cav}^{(2)}=n_{cav}^{(3)}=1.63$ *in a wide range of NW. The triple resonances within the first order SB calculated for (b)* $f_{Si}=0.1$*, (c)* $f_{Si}=0.2$*, (d)* $f_{Si}=0.3$ *and a=573 nm. The estimated channel spacing,* $\lambda s_{12,23}$*, and FWHM of each individual resonance are also demonstrated.*

In Figure 4-22(a), the GM of the PhC with induced triple defect at the *Position 0* ($n_{cav}^{(1,2,3)}=1.63$) is demonstrated. The three transmission channels are realized in a wide range of *NW*, dividing each SB along the appropriate range of f_{Si}. As for the single-

cavity case, the GM demonstrates the narrowing effect of the resonance peaks with increase of the SB's order, m. Also, the higher order micro-cavities demonstrate higher fabrication tolerances comparing to the lower order cavities, e.g. the 4th and 5th order triple-resonance lines are almost vertical as seen from Figure 4-22(a), while the 1st order triple resonances are more tilted.

In Section 4.3, devoted to investigation of the tuning capabilities of a single-cavity PhC, it was demonstrated, that the higher order SBs are normally more sensitive to the change of the cavity refractive index and demonstrate larger relative tuning shifts of the resonances. All of these properties make the higher order SBs to be the most suitable for the engineering of the tunable multi-resonance devices characterized by the high Q and narrow FSR.

However, in this Section the investigations are mainly focused on the triple-channel system operating only within the lowest SB of the PhC. This allows establishing the *minimum tunability limitations* of the suggested methodology. Utilization of the widest resonances, simplifies the presentation of the method, as well as facilitates the monitoring of the filter parameters, e.g. channels spacing, λ_s, intensity, I, and bandwidth (full width at half maximum, *FWHM,* or Q).

Let us now focus on the first order resonances in Figure 4-22(a) (the region shown by rectangle). The bandwidth of the resonances is very sensitive to the variations of f_{Si}. The most narrow resonance peaks, and, therefore, the strongest coupling between cavities, can be achieved for the range of f_{Si} that corresponds to the central part of the resonance lines within one SB on the GM (shown by the dashed ellipse in Figure 4-22(a)). In order to perform a detailed analysis, we consider an example of the triple-channel device that operates within the telecommunication wavelength 1555 nm. In accordance with the map, the most narrow first order resonances can be achieved, for example, for f_{Si}=0.2, which centred at NW=2.5=λ/a. Thus, the lattice constant of the fabricated device must be design as a=573 nm, which corresponds to the width of the air groove/cavity of 458 nm. In Figure 4-22(b) we compare the resonance peaks for the f_{Si}=0.2 (central part of the resonance lines) and f_{Si}=0.1 and 0.3 (edges of the resonance lines, outside the dashed ellipse on the GM). Obviously, the resonance peaks for f_{Si}=0.2 demonstrate the equal channel spacings, $\lambda_s = \lambda_{s12} = \lambda_{s23,}$ the highest out-of-band reflection (R=0.99) and the improved bandwidth characteristics (FWHM values are denoted by numbers on each graph).

4.4.3 Fine Tunable filtering of individual resonances

One of the main challenges of the coupled-resonator devices has remained the fixed wavelength channel spacing or free spectral range (FSR), which cannot be easily tuned due to the strong coupling effect between channels. In many applications, the individual channel position (or channel spacing) are required to be trimmed after imperfect fabrication process or to be dynamically tuned for better performance [4]. The tuning of FSR has been demonstrated previously in fiber-based devices [36]. One of the successful attempts was presented in [10], where authors demonstrated their solution for an integrated platform. This approach requires the incorporation of the metallic micro-heaters into the large 245 μm resonators, thus, requiring a precise thermo-control of the device during operation. One of the most promising solutions could be the filter device with low-power and low-loss capability of fine-tuning of individual channels in the whole filtering system in an integrated platform by application of electric field.

4.4.3.1 Precise individual tuning of the central channel in a triple-channel system

It is assumed that the refractive indexes have linear dependence, $n_{cav}^{(1,2,3)}=n_0\pm\Delta n$, demonstrated in Figure 4-21(b). Again, for the clarity of presentation of the method, we assume here, that all cavities are switched to the initial *Position 0* (see Figure 4-21), i.e. LC has refractive index n_0=1.63 and the channel spacings between edge channels and the central channel (or FSR) are equal, $\lambda_s=\lambda_{s12}=\lambda_{s23}$=60nm for the example device with a=573nm and an optimal value of f_{Si}=0.2. The transmission spectrum of this example structure is demonstrated in Figure 4-23(a) (black line, central resonance denoted by *0*). Now, let us gradually increase the refractive index of the central cavity, $n_{cav}^{(2)}=n_0+\Delta n$, by Δn=0.001, while decreasing the refractive indexes of the two edge cavities, $n_{cav}^{(1)}=n_{cav}^{(3)}=n_0-\Delta n$ by the same value of Δn (Figure 4-23(b)). In this case the central cavity has the strongest coupling, $n_{cav}^{(2)}=n_{cav}^{(1,3)}+2\cdot\Delta n$, and acts as a primary cavity in the system, while the edge cavities represent the variable mirrors from both sides of the central cavity. At the same time, the overall optical thickness of the system $n_{cav}^{(1,2,3)}\cdot d_{air}=\frac{\lambda_m^{(1,2,3)}}{2}m$ is decreased, which leads to the blue-shift of its optical characteristics [30, 35]. Let us monitor the positions of triple resonances during these refractive index variations. In Figure 4-23(a) we demonstrate the transmission spectra for the Δn=0.013 (thin blue line) and Δn= 0.026 (thick blue line). The central channel is blue-shifted,

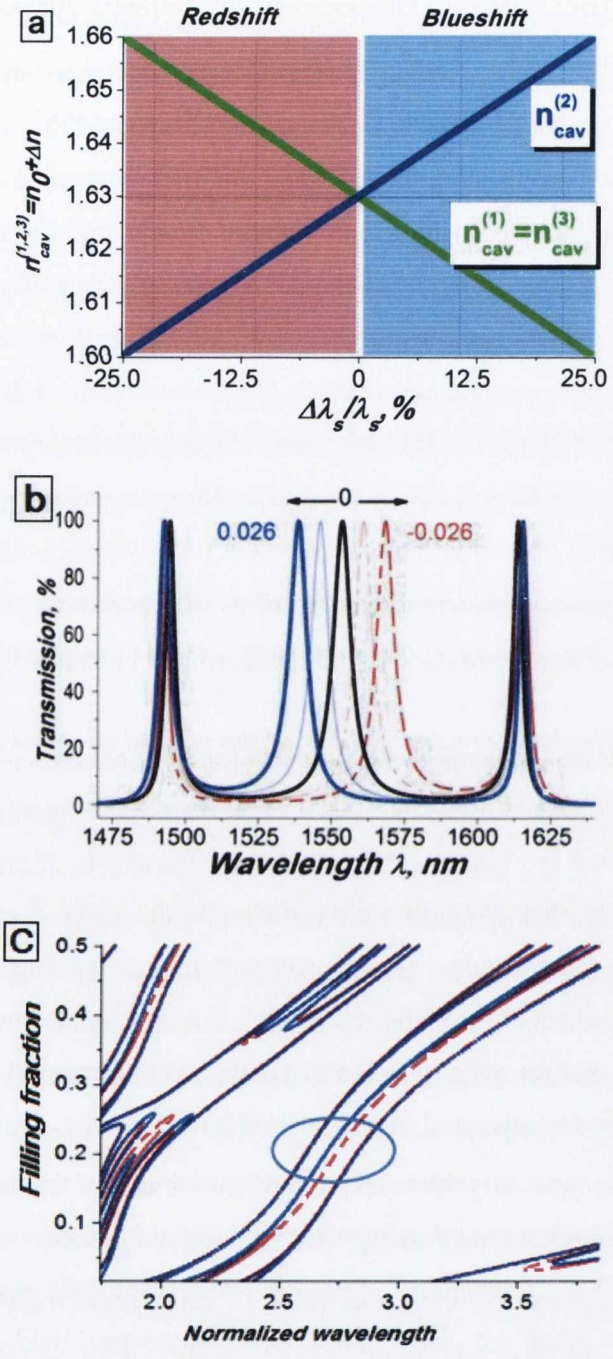

Figure 4-23: *(a) The cavity refractive indexes* $\mathbf{n}_{cav}^{(1,2,3)}$ *versus relative channel position shift normalized to the original channel spacing. (b) Continues tuning of the central channel for Δn=-0.026 (red dashed line), Δn=-0.013 (red dashed dotted line), Δn=0 (black line), Δn=0.013 (thin blue line) and Δn=0.026 (thick blue line). (c) The GM of T=100%, calculated for Δn=-0.026 (red dashed line) and Δn=+0.026 (blue line). Optimal design region is shown by ellipse.*

while the edge resonances have retained their positions. For the considered example, the maximum refractive index difference, $2 \cdot \Delta n = 0.052$ (which is only 24% of the birefringence value for the LC E7, Δn_{E7}=0.2), allows to achieve maximum relative independent shift of the central channel, $\Delta\lambda_s$, up to *25* % of the channel spacing, λ_s. However, further increase of the overall difference, $2 \cdot \Delta n$, will break the symmetry of the system and initiates the coupling effect between all cavities resulting in the shift of all resonances simultaneously. As we are interested only in fine tuning capability of the multi-cavity structures, the results obtained for the higher variations of Δn are not considered here.

The inverse manipulation with the refractive indexes, i.e. reducing the $n_{cav}^{(2)}=n_0-\Delta n$, while increasing $n_{cav}^{(1)}=n_{cav}^{(3)}= n_0+\Delta n$, results in the individual red-shift of the central channel (Figure 4-23(a), red dashed dotted and dashed lines).

In order to see the independent central resonance tuning in general, the GM is calculated in a wide range of the f_{Si} (Figure 4-23(c)). For clarity of presentation we focus only on the first order SB region and plot only regions with T=100 %. Here, the resonance lines are calculated only for two limiting cases, namely for $\Delta n = -0.026$ (blue line) and $\Delta n = +0.026$ (red dashed line). Obviously, the widest individual tunability of the central channel can be achieved for the narrowest channels, which corresponds to the optimal central part of the $f_{Si}=0.15...0.25$ (denoted by blue circle). This range of f_{Si} also demonstrates the maximum fabrication tolerance, which constitutes *54 nm* for the example optimal device. The edge resonances remain their original position within the full range of f_{Si} for the first SB. Note that the maximum intensity of T=100 % and the initial bandwidths are not affected for all switching positions of the triple-channel system.

4.4.3.2 Precise tuning of the edge channels with high-stability of the central channel

Let us now consider the variation of the refractive index of only the central cavity $n_{cav}^{(2)}=n_0-\Delta n$. The refractive indexes of the edge cavities are considered to be fixed to the initial *Position 0*, $n_{cav}^{(1)}=n_{cav}^{(3)}=n_0$=1.63 (Figure 4-24(a)). In this case the central cavity plays a role of the variable intermediate mirror between two strongly coupled edge cavities. The decrease by Δn of the overall optical thickness of the system

$n_{cav}^{(1,2,3)} \cdot d_{air} = \frac{\lambda_m^{(1,2,3)}}{2} m$ results in the blue-shift of the edge channels, while the central channel retains its wavelength position. This is clearly demonstrated in Figure 4-24(b) for the Δn=*0, 0.02, 0.052* and *0.11* for the considered optimized example structure. The increase of the channel spacing, $\Delta\lambda_s$, results in the decrease of the channel spacing between central channel and left edge channel, $\lambda_{s2,3}=\lambda_s-\Delta\lambda_s$, and, consequently, lowering the out-of-band reflection between them.

Similar to the previous model, the overall increase of the refractive index, Δn, up to 0.052, for the considered example, leads to the linearly proportional change of the channel spacings up to 25%, or $\lambda_{s12} / \lambda_{s23}$=1.5 (Figure 4-24(a, b)). Although the out-of-band reflection between central and right edge channel is decreased, it is still constitutes 95 %. Further increase of the Δn up to the limiting case, Δn =*0.11,* will result in rapidly growing difference between channel spacings, $\lambda_{s12} / \lambda_{s23,}$ up to 2.7, with decrease of the out-of-band reflection between the central and left-edge channel down to 90 % (Figure 4-24(b), red dashed dotted line).

For significantly higher values of Δn >>0.11, than considered in this Section, the central cavity acts as a single cavity independent from the edge cavities. The left edge-channel will be shifted out of the SB and the right edge channel will be merged with the central channel, thus changing the resonator mode from triple to a single mode. Obviously, the inverse manipulation with the refractive indexes, i.e. increasing the $n_{cav}^{(2)}=n_0+\Delta n$ and fixed $n_{cav}^{(1)}=n_{cav}^{(3)}=n_{0,}$ results in the individual red-shift of the edge channels on the same $\Delta\lambda_s$ value (Figure 4-24(c)).

In Figure 4-24(d), the GM of the total transmission, T=100%, for the two cases Δn=*-0.052* (blue line) and Δn=*+0.052* (red dashed line) is presented in normalized wavelength range. Again, as for the central tuning combination, the widest tunability can be achieved for the narrowest resonances from the central part of the f_{Si}=*0.15...0.25*, which corresponds to the optimal design parameters and minimum fabrication tolerances of the device. Note that the central channel remains its original position within the full range of f_{Si} for the first SB.

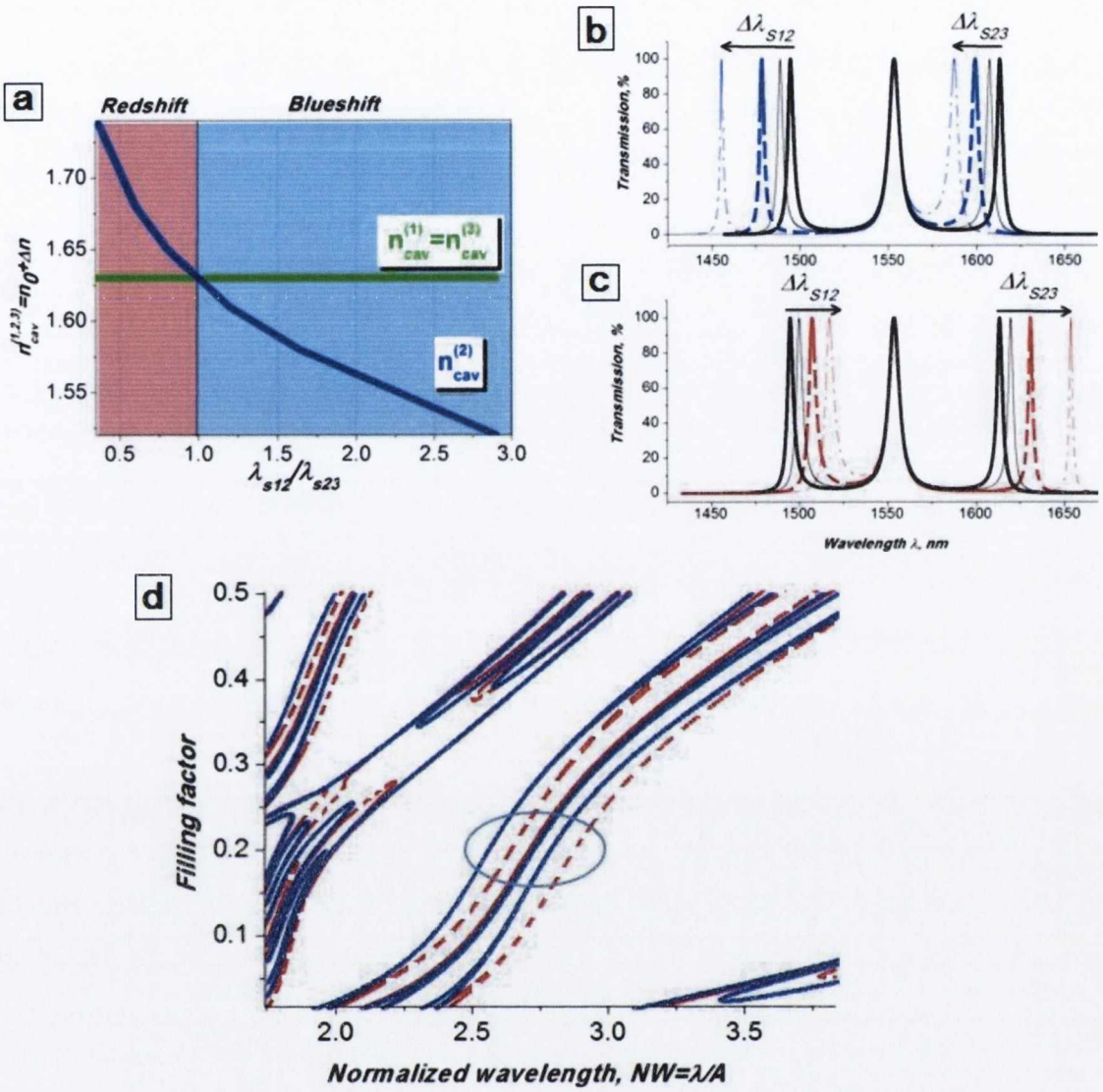

Figure 4-24: *(a) The cavity refractive indexes* $\mathbf{n}_{cav}^{(1,2,3)}$ *versus the ratio of the channel spacings,* $\lambda_{s12}/\lambda_{s23}$. *(b) Continues blue shift of the edge channels with linear decrease of the central cavity refractive index,* $\mathbf{n}_{cav}^{(2)}$, *by,* $\Delta n=0.02$ *(thin black line),* $\Delta n=0.052$ *(dashed blue line),* $\Delta n=0.11$ *(dashed dotted blue line). The triple channels, for* $\Delta n=0$, *are also demonstrated (thick black line). (c) Continues red shift of the edge transmission channels with linear increase of the central cavity refractive index,* $\mathbf{n}_{cav}^{(2)}$, *by,* $\Delta n=0.02$ *(thin black line),* $\Delta n=0.052$ *(red dashed line),* $\Delta n=0.11$ *(red dashed dotted line). (d) The GM of T=100%, calculated for* $\Delta n=-0.052$ *(blue line) and* $\Delta n=+0.052$ *(red dashed line).*

4.4.3.3 Precise control of transmission attenuation for the edge channels in triple-channel system

In two previously discussed models, devoted to the realization of fine tuning capability of the triple-defect PhC, the transmission intensities of the realized channels, $I_{1,2,3}$, were substantially stable and close to 100%. In this Section the model for precise engineering of the positions and intensities of the edge channels is demonstrated. This model requires opposite linear variation of the edge channels refractive indexes with the central channel refractive index fixed to the *Position 0* (Figure 4-21(c) and Figure 4-25(a)). The mismatch between the optical thicknesses of the edge cavities results in the attenuation of the edge channels intensities, $I_{1,3}$, which accompanied by equal increase of the channel spacing, $\lambda_{s12}+\Delta\lambda_s=\lambda_{s23}+\Delta\lambda_s$. (Figure 4-25(a, b)). By gradual increase of the refractive index difference, $2\cdot\Delta n$, the edge channel intensities can be precisely tuned from 100% down to 10%. For significantly higher values of $2\cdot\Delta n>>0.11$, than considered in this Section, the edge channels are vanished and system is operating in single channel mode.

For the case of strongly coupled cavities, when an optimal design value is chosen as f_{Si} =0.2, the difference between edge channel intensities $\Delta I_{1,2,3}$ is negligible, and equal to ~1-2 % for all switching modes. However, as it can be seen from the GM in Figure 4-25(c), this difference is significantly increases up to 25 % for all non-optimal values of f_{Si} (i.e. values outside the range f_{Si} =0.15…0.25; see Section 4.4.2). We note that the attenuation of the resonance intensity for the non- optimal f_{Si} is also not so strong in comparison to the optimal device. For example, in Figure 4-25(e), the triple-channel system, calculated for f_{Si}=0.35 and Δn=0.06, demonstrates a decrease of I_1 to 80 % and I_3 to 60 %.

One of the possible applications of the controllable transmission attenuation model can be an optimization of the edge channel intensities after fabrication process. The random fluctuation of the geometrical parameters, after the fabrication process, is affecting primarily the edge channels in terms of their intensities and, thus, the bandwidth (or FWHM). The average deviation of the fabricated device parameters up to 10 % may result in the attenuation of the edge channels intensities down to 90 %. By reducing the refractive index mismatch up to $2\cdot\Delta n_{cav}^{(1,3)}$=0.03, the edge channel intensities can be precisely tuned back to 100% with negligible decrease of the channel spacing by 1 % (Figure 4-25(e)).

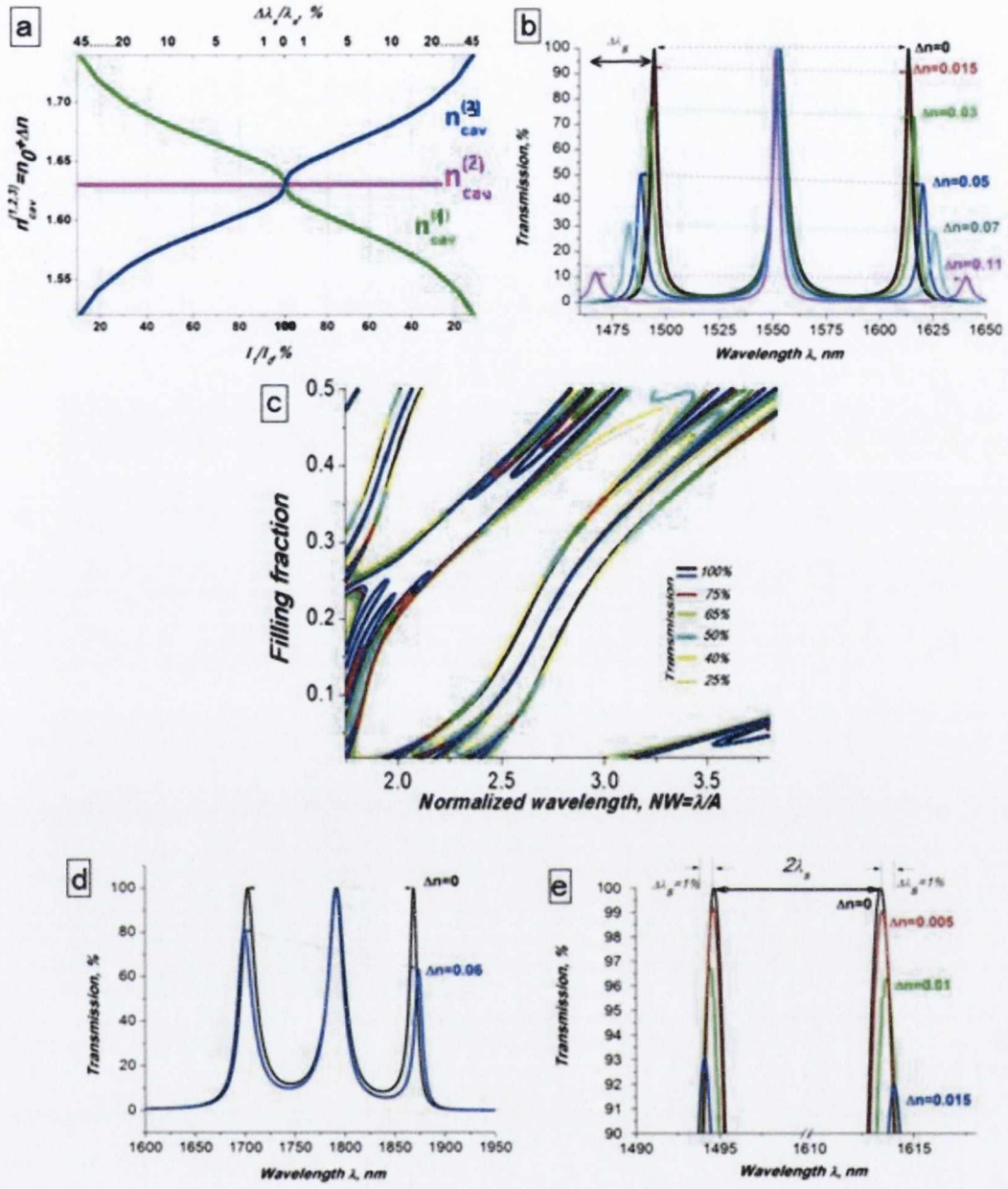

Figure 4-25: *(a) The cavity refractive indexes* $\mathbf{n}_{cav}^{(1,2,3)}$ *versus the edge channel intensity* $I_{1,3}$ *normalized to the maximum original intensity* $I_0=I_2$ *(lower scale) and versus the relative channel spacing shift normalized to the original channel spacing (upper scale). (b) The precise attenuation of the edge channel intensities,* $I_{1,3}$, *for* $\Delta n=0.015$ *(red line),* $\Delta n=0.03$ *(green line),* $\Delta n=0.05$ *(blue line),* $\Delta n=0.07$ *(cyan line) demonstrated for the* $f_{Si}=0.2$. *(c) The GM of T=25-100 %, calculated for* $\Delta n=0.06$. *(d) The attenuation of the edge channels for* $\Delta n=0.06$ *and* $f_{Si}=0.35$. *(e) Fine attenuation from 100 % to 90 % for* $\Delta n=0.005$ *(red line), 0.01 (green line), 0.015 (blue line) demonstrated for the* $f_{Si}=0.2$.

4.4.4 Design of the SOI-based device

To experimentally demonstrate the proposed idea, the triple-channel resonator device was fabricated on <100> p-type SOI wafer with Silicon device layer thickness of 4.5 μm, and a 1 μm thick buried oxide layer (Figure 4-26). The design parameters of the 1D PhC structures were selected from the GM (Figure 4-22(a)). Electron-Beam Lithography followed by the plasma etching was used to fabricate the nano-scale

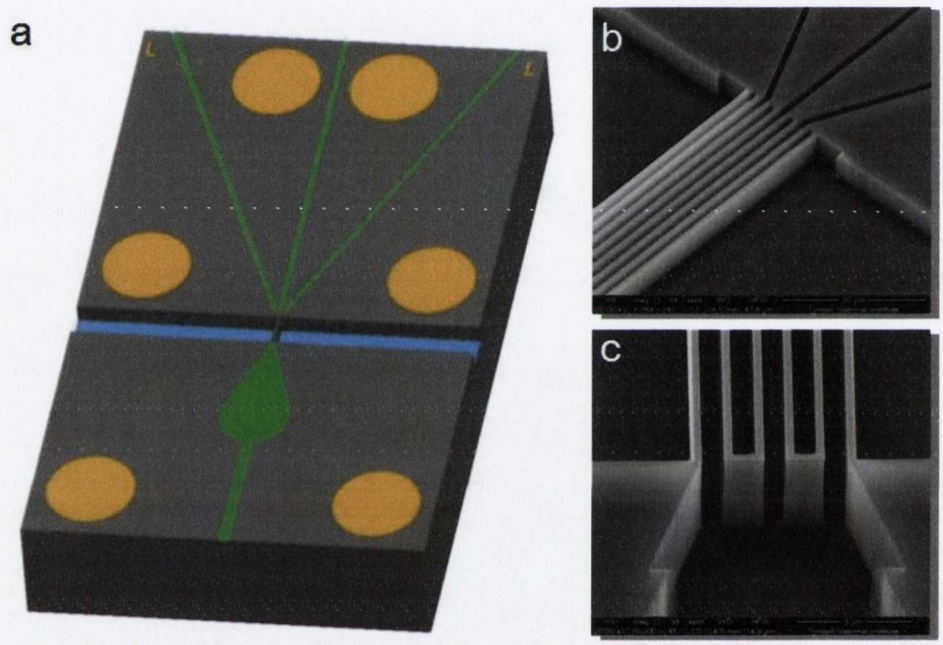

Figure 4-26: *(a) The SOI-based chip design of the triple-coupled defect photonic crystal filter filled with nematic LC (green colour) and metal contact pads (yellow circles). (b) SEM image of the fabricated defect-free 1D PhC with three-channels connected to 2nd, 4th and 6th grooves. (c) SEM image showing a view on the channels from the cone-shape cavity designed for LC infiltration.*

structures with *a* up to 1000 nm based on the first and second order SBs operating in the telecommunication wavelength range. The electrical-isolation of the 2nd, 4th and 6th grooves of 1D PhC is achieved by dry-etching of the micro-channels across the chip (Figure 4-26(a) (green lines) and Figure 4-26(b)). One cone-shape cavity is designed for the easy infiltration of these grooves with LC E7 (Figure 4-26(a) (green region) and Figure 4-26(c)). A 500 nm layer of Aluminum is deposited by sputtering. Then, by using Optical Lithography followed by wet etch process, the contact pads are defined (Figure 4-26(a), yellow circles). Finally, the U-grooves with the depth of 60 μm are

etched from both sides of the nano-structure for easier integration of the optical lensed fibers and their direct coupling to the device. By independent application of the voltage to the Aluminum contact pads different orientations of the LC molecules can be achieved in the individual grooves, allowing a variety of manipulations of the transmission channels.

4.4.5 Optimization: Compensation of the fabrication tolerances

Any structural deviations and non-uniformities affect the optical properties of the device. In particular, if the periodic structure contains coupled cavities, the thickness deviations, δd, result in deviation of the optical thicknesses of the cavities, $n \cdot d = n \cdot (d \pm \delta d)$, thus, randomly shifting and attenuating the cavity resonances.

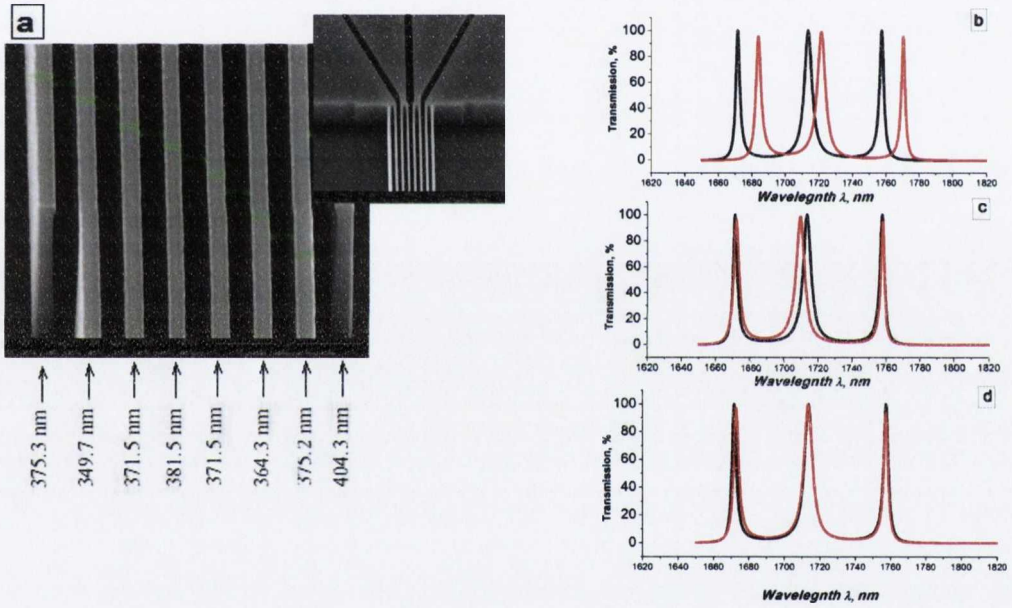

Figure 4-27: *(a) SEM image demonstrates the structural deviations obtained for the defect-free 1D PhC with a=900 nm, f_{Si}=0.4. (b) Transmission spectra of the originally designed triple-defect device (black line) and of the fabricated device with structural deviations of ±δ d_{Si}=20 nm (red line). The refractive index of all cavities $\mathbf{n}_{cav}^{(1,2,3)}$=1.63. (c) A precise adjustment of the edge channels by decreasing the refractive index to $\mathbf{n}_{cav}^{(1,2,3)}$=1.60. (d) Final adjustment of the central channel with Δn=0.01.*

In Figure 4-27(a), one of the fabricated sample PhCs with a=900 nm is demonstrated. The original value of filling fraction, f_{Si}=0.4, was chosen in accordance with the GM from Figure 4-22(a). After the infiltration of the 2nd, 4th and 6th grooves with nematic LC E7, the PhC tunable filter can be realized. By switching all of the

cavities to the *Position 0*, the three transmission channels with Q about 500 and centred at NW=1.75 (see Figure 4-22(a)), which is $\lambda=NW\cdot a$=1715 nm (Figure 4-27(a), black line), can be achieved. However, the SEM investigation of the fabricated device has demonstrated a presence of the random deviation of the geometrical parameters of the fabricated sample PhC (Figure 4-27(a)). Although, the average width of the grooves, has remained the same for all periods, an estimated average deviation of the thickness of the Si-walls is δd_{Si}=20 nm, which is about ±5.6% of the originally designed thickness. Therefore, the new optical thicknesses of the cavities can be described as $n_{cav}^{(1,2,3)}\cdot(a-d_{Si}\pm\delta d_{Si})$. The obtained transmission spectrum for the fabricated device is demonstrated in Figure 4-27(b), red line. All of the channels are unequally red-shifted which also results in the reduction of Q-factor The maximum intensity for the edge channels is also reduced by 3-5 %.

Now, let us optimize the fabricated non-ideal system by using the approach demonstrated in this Section. First, we reduce refractive index of all cavities $n_{cav}^{(1,2,3)}=n_0-\Delta n$, in order to blue shift all three channels. The edge channels are precisely adjusted to the ideal positions, when $n_{cav}^{(1,2,3)}$= 1.63-0.03=1.60 (Figure 4-27(c), red line). Now, we perform the fine tuning of the central channel by increasing the refractive index of the edge cavities $n_{cav}^{(1,3)}$= 1.61+Δn=1.6+0.01=1.61 and reducing by the same value the refractive index of the central cavity $n_{cav}^{(2)}$=1.59 (Figure 4-27(d)). The system is now fully adjusted to the originally designed operational mode.

4.5 Summary

In this Chapter, the model of transformation of one-dimensional, high-contrast Silicon photonic crystal into a tunable Fabry-Perot resonator has been investigated. This transformation is achieved by introduction of the optical defects in the ordinary photonic crystal while retaining a high modulation of the resonance peaks up to ~0.95.

The features of FP-resonator based on PhC with optical defects are:

i) possibility to avoid the specific procedure for the defects fabrication but rather use the possibility of introducing the filler in the centre of PhC;

ii) tuning of the resonance peaks within the PBG by variation of refractive index of the defect filler.

The utilisation of common GMs of PBGs (or stop-bands) and TBs allows to predict the resonance appearance or disappearance in the optical spectra and to determine the optimal design parameters, e.g. wavelength position, quality factor and free spectral range depending on the order of PBG and the value of filling fraction.

- ***Single-cavity resonator**: Wide-tuning of the resonances*

A Fabry-Pérot resonator, consisting of two Silicon walls, also acting as electrodes, and a thick cavity, filled with the nematic liquid crystal E7, was fabricated on a Si-On-Insulator platform. The experimental spectra obtained are in good agreement with the results of calculations based on GM Method. In particular, a superposition of the transmission peaks with reflection maxima, predicted from calculations, was confirmed experimentally. Altering the liquid crystal alignment, and consequently the refractive index value in the cavity, by the application of an electric field using voltages from 0 V to 15 V, results in reversible continuous tuning of the high-order resonance peaks with the ultra-wide relative shifts of up to $\Delta\lambda/\lambda \approx 10$ %.

- ***Triple-cavity resonator:** Individual tuning of resonances*

A technique for precise position control of individual transmission channels/resonances in a triple-cavity resonator device has been proposed. By controllable tuning of the refractive index in all coupled cavities, a continuous individual tuning of the central channel (or edge channels) up to 25% of the total channel spacing has been demonstrated. Additionally, an approach for precise controllable improvement of transmission up to 100% is demonstrated for the edge channels with decrease of the channel spacing on~1%. Based on the proposed design, a prototype triple-channel filter was fabricated on Silicon-On-Insulator platform and optimized to the desired operational mode.The suggested approach has been utilized for compensation of the fabrication tolerances in multi-channel Silicon devices in a wide infrared range.

This project is currently going through the final fabrication process at Tyndall Institute Ireland (NAP368 funded by SFI Ireland).

4.6 *References*

[1] R. Soref, "The Past, Present, and Future of Silicon Photonics " IEEE J. Sel.Top. Quantum Electron., 12(6), 1678-1687 (2006).

[2] S. Cao, J. Chen, J. N. Damask *et al.*, "Interleaver technology: comparisons and applications requirements," Lightwave Technology, Journal of, 22(1), 281-289 (2004).

[3] Q. Li, M. Soltani, S. Yegnanarayanan *et al.*, "Design and demonstration of compact, wide bandwidth coupled-resonator filters on a siliconon- insulator platform," Opt. Express, 17(4), 2247-2254 (2009).

[4] A. C. Turner, M. A. Foster, A. L. Gaeta *et al.*, "Ultra-Low-Power Parametric Frequency Conversion of High Data Rates On-Chip," OSA Technical Digest (CD). CThO6.

[5] X. Shu, K. Chisholm, I. Felmeri *et al.*, "Highly sensitive transverse load sensing with reversible sampled fiber Bragg gratings," Applied Physics Letters, 83(15), 3003-3005 (2003).

[6] A. M. Armani, R. P. Kulkarni, S. E. Fraser *et al.*, "Label-Free, Single-Molecule Detection with Optical Microcavities," Science, 317(5839), 783-787 (2007).

[7] D. B. Hunter, M. E. Parker, and J. L. Dexter, "Demonstration of a continuously variable true-time delay beamformer using a multichannel chirped fiber grating," Microwave Theory and Techniques, IEEE Transactions on, 54(2), 861-867 (2006).

[8] B. E. Little, S. T. Chu, J. V. Hryniewicz *et al.*, "Filter synthesis for periodically coupled microring resonators," Opt. Lett., 25(5), 344-346 (2000).

[9] M. Popovic, C. Manolatou, and M. Watts, "Coupling-induced resonance frequency shifts in coupled dielectric multi-cavity filters," Opt. Express, 14(3), 1208-1222 (2006).

[10] A. H. Atabaki, B. Momeni, A. A. Eftekhar *et al.*, "Tuning of resonance-spacing in a traveling-wave resonator device," Opt. Express, 18(9), 9447-9455 (2010).

[11] M. Ghulinyan, C. J. Oton, Z. Gaburro *et al.*, "Porous silicon free-standing coupled microcavities," Applied Physics Letters, 82(10), 1550-1552 (2003).

[12] E. D. Palik, "Handbook of Optical Constants of Solids," Volume 1, (1998).

[13] R. M. A. Azzam, and N. M. Bashara, [Ellipsometry and polarized light] North-Holland, (1987).

[14] S. V. Gaponenko, [Introduction to Nanophotonics] Cambridge University Press, (2010).

[15] L. Pavesi, S. V. Gaponenko, and L. D. Negro, [Towards the First Silicon Laser] Kluwer Academic Publishers, (2003).

[16] K. J. Vahala, "Optical microcavities," Nature, 424(6950), 839-846 (2003).

[17] V. Tolmachev, T. Perova, and K. Berwick, "Design Criteria and Optical Characteristics of One-Dimensional Photonic Crystals Based on Periodically Grooved Silicon," Appl. Opt., 42(28), 5679-5683 (2003).

[18] V. Tolmachev, T. Perova, E. Krutkova *et al.*, "Elaboration of the gap-map method for the design and analysis of one-dimensional photonic crystal structures," Physica E: Low-dimensional Systems and Nanostructures, 41(6), 1122-1126 (2009).

[19] D. L. Kendall, "Vertical Etching of Silicon at very High Aspect Ratios," Annual Review of Materials Science, 9(1), 373-403 (1979).

[20] V. A. Melnikov, E. V. Astrova, T. S. Perova *et al.*, "Stain etching of micro-machined silicon structures," Journal of Micromechanics and Microengineering, 18(2), 025019 (2008).

[21] V. A. Tolmachev, T. S. Perova, E. V. Astrova *et al.*, "Vertically etched silicon as 1D photonic crystal," physica status solidi (a), 197(2), 544-548 (2003).

[22] M. KGaA, [Data Sheet Licristal® E7], Germany(2001).

[23] I. C. Khoo, "The Infrared Optical Nonlinearities of Nematic Liquid Crystals and Novel Two-wave Mixing Processes," Journal of Modern Optics, 37(11), 1801-1813 (1990).

[24] S.-T. Wu, U. Efron, and L. D. Hess, "Infrared birefringence of liquid crystals," Applied Physics Letters, 44(11), 1033-1035 (1984).

[25] V. A. Tolmachev, S. A. Grudinkin, J. A. Zharova *et al.*, "Electro-tuning of the photonic band gap in SOI-based structures infiltrated with liquid crystal," Proccedings of SPIE, 6996, 69961Z-9 (2008).

[26] T. S. Perova, V. A. Tolmachev, and E. V. Astrova, "Tunable photonic structures based on silicon and liquid crystals," Proccedings of SPIE, 6801, 68010W-15 (2007).

[27] D. A. G. Bruggeman, "Berechnung verschiedener physikalischer Konstanten von heterogenen Substanzen. I. Dielektrizitätskonstanten und Leitfähigkeiten der Mischkörper aus isotropen Substanzen," Annalen der Physik, 416(7), 636-664 (1935).

[28] S. P. Anderson, M. Haurylau, J. Zhang *et al.*, "Hybrid photonic crystal microcavity switches on SOI," Proceedings of SPIE, 6477, 647712-647712-8 (2007).

[29] A. Lipson, and E. M. Yeatman, "A 1-D Photonic Band Gap Tunable Optical Filter in (110) Silicon," Journal of Microelectromechanical Systems, 16(3), 521-527 (2007).

[30] V. A. Tolmachev, V. A. Melnikov, A. V. Baldycheva *et al.*, "Electrically tunable Fabry-Perot resonator based on microstructured Si containing liquid crystal," Progress In Electromagnetics Research, 122, 293-309 (2012).

[31] S. Weiss, H. Ouyang, J. Zhang *et al.*, "Electrical and thermal modulation of silicon photonic bandgap microcavities containing liquid crystals," Opt. Express, 13(4), 1090-1097 (2005).

[32] J. Cos, J. Ferré-Borrull, J. Pallarès *et al.*, "Double-cavity Fabry–Pérot tunable equalizer based on 1D photonic crystals," International Journal of Numerical Modelling: Electronic Networks, Devices and Fields, 23(4-5), 400-410 (2010).

[33] G. Pucker, A. Mezzetti, M. Crivellari *et al.*, "Silicon-based near-infrared tunable filters filled with positive or negative dielectric anisotropic liquid crystals," Journal of Applied Physics, 95(2), 767-769 (2004).

[34] J. D. Joannopoulos, [Photonic Crystals: Molding The Flow Of Light] Princeton University Press, (2008).

[35] V. A. Tolmachev, T. S. Perova, and A. V. Baldycheva, "Transformation of one-dimensional silicon photonic crystal into Fabry-Perot resonator," Proceedings of SPIE, 7943, 79430E-10 (2011).

[36] Y.-G. Han, X. Dong, J. H. Lee *et al.*, "Wavelength-spacing-tunable multichannel filter incorporating a sampled chirped fiber Bragg grating based on a symmetrical chirp-tuning technique without center wavelength shift," Opt. Lett., 31(24), 3571-3573 (2006).

Chapter 5.

Photonic Crystals with Structural Fluctuations

5.1 Introduction

Although Si fabrication technology has significantly developed over the last 20 years, one of the main problems for optical, micro- and nano-scale, periodic structures, such as photonic crystals, remains defining the maximum structural deviations precisely in the system [1-3]. In general, structural deviations and non-uniformities, presented in the patterned features on the wafer, occur for three principal reasons. First of all, there is the fundamental diffraction limit of the projection optics. Secondly, the mask pattern differs from the original design due to limitations in the mask fabrication process. Finally, random and systematic variations inevitably occur in a multitude of lithographic process parameters, such as focus and exposure [4]. Fabrication tolerances for modern e-beam lithography are usually assumed to be a minimum of about 5-10% of the nominal target dimensions. The question arises as to how imperfections in the fabricated 1D PhC structure might influence their optical properties? Answering this question requires the development of a mathematical model of the multilayer structure. Once this model is validated, the response of the optical properties of the system to fluctuations in the structural parameters is estimated. When modelling a 1D PhC, four main structural parameters are involved. These are, the thicknesses, d_H and d_L, and the

refractive indices, n_H and n_L, of the high and low refractive index components, respectively (Figure 5-1). The sum of d_H and d_L is a, the lattice constant of the PhC.

Another structural imperfection that can occur at certain level in practical 1D PhC structure fabricated by a microstructuring process [5], is a roughness of the side-walls of etched air channels. Depending on the aspect ratio and particular method used, the surface roughness can be varied from 0.4% to 20% of the Si wll thickness during reactive ion etching, from 10% to 15% during photo-electrochemical etching and <1% during anisotropic chemical etching (see Chapter 2). Technological deficiencies resulting in side-wall roughness in 1D PhCs were investigated in Refs. [6-10], whereas in Refs. [6, 8, 11-12], non-uniformities in wall thickness were analysed. The investigation of the influence of fluctuations in the geometrical parameters, or PhC disorder, on the optical properties of PhCs is a crucial aspect of material engineering, since this allows an estimation of the maximum level of disorder, beyond which the optical properties of the crystal are unacceptably degraded. For example, in Ref. [13], the threshold level of disorder below which the probability of formation of an eigenstate at the center of a PBG is negligible was established. Introduction of disorder into a 2D PhC as a result of the variation in the size of the air cylinders leads to increasing transmission within the PBG and to a distortion of the PBG's shape [13]. The PBG width is used as a metric to describe this distortion. The width can be determined as the distance between the boundaries of areas on dispersion curve where the Bloch wave vector K has imaginary values [14].

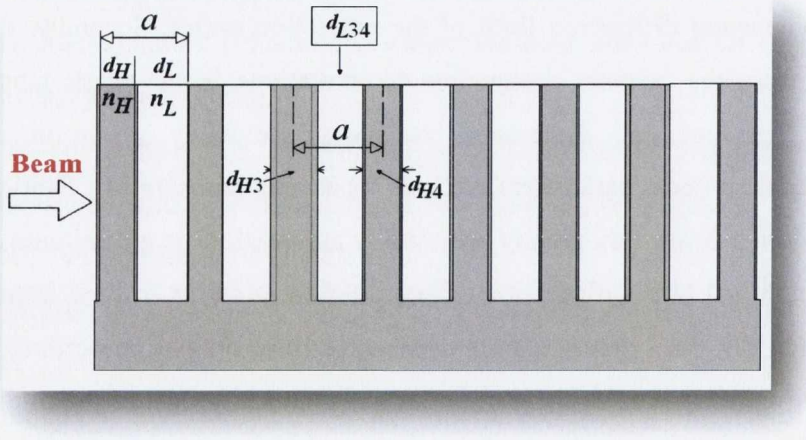

Figure 5-1: *Schematic diagram of a seven-period, 1D PhC with a lattice constant* $a=d_H+d_L$ *and an optical contrast of* n_H/n_L. *A wall thickness with fluctuation* $(d_H)_i$ *in the*

H-component appears in each lattice period, causing a variation $(d_L)_i$ in the L-component of the structure.

Typically, 1D PhCs are designed as Bragg reflectors with the optical thickness of both layers, $d_H n_H$ and $d_L n_L$, corresponding to the quarter wavelength for which this PhC is going to be utilized. In addition to the first PBG, one-dimensional PhCs have numerous secondary and higher orders, PBGs. These have been investigated in Refs. [10, 15], for example. Utilisation of secondary and higher order PBGs allows number of applications of 1D PhCs, including Fabry-Pérot optical filters with tunable resonance peaks of high-order (Chapter 4), or the formation of wide-band windows of transparency in Si (Chapter 3). For these structures [16, 17], a large variation of filling fractions, $f_H = d_H/a$ or $f_L = d_L/a$, was used, unlike conventional structures based on quarter wavelength optical thicknesses.

In this Chapter, the influence of disorder on 1D PhCs of high optical contrast for use in Si photonics is investigated. Using a combination of calculations and gap map analysis, the influence of random thickness fluctuations in PhC parameters on the transmission spectra and PBGs is explored. The advantage of using PBGs map approach is that it enables the analysis of the optical properties of the PhCs over a range of possible filling fractions and photonic band gaps of any order, including the most common quarter wavelength structures.

5.2 Calculations of spectra and PBG map

A two-component 1D PhC with thicknesses of d_H and d_L for the high (n_H) and low (n_L) refractive index components, respectively, and a total of seven periods is shown in Figure 5-1. During microstructuring processes such as lithography and wet or dry etching, the optical constants of the constituent materials generally remain unchanged. We use an n_H value for Si in the mid-IR range of 3.42 and a value of $n_L = 1$ for the air component of the grooved Si structure. Figure 5-2(a) shows the reflection spectrum R at normal incidence of light, calculated for a filling fraction $f_H = d_H/a = 0.23$, corresponding to a quarter wavelength optical thickness for both components. Wavelength values, λ, are shown in units of normalized frequency, a/λ, on the x-axis. Reflection spectra calculated for $f_H = 0.5$ and $f_H = 0.08$, are shown in Figure 5-2(b) and Figure 5-2(c), respectively. Wide reflection bands with a characteristic Π-shape, corresponding to the first and higher order PBGs, are seen in all of the R spectra.

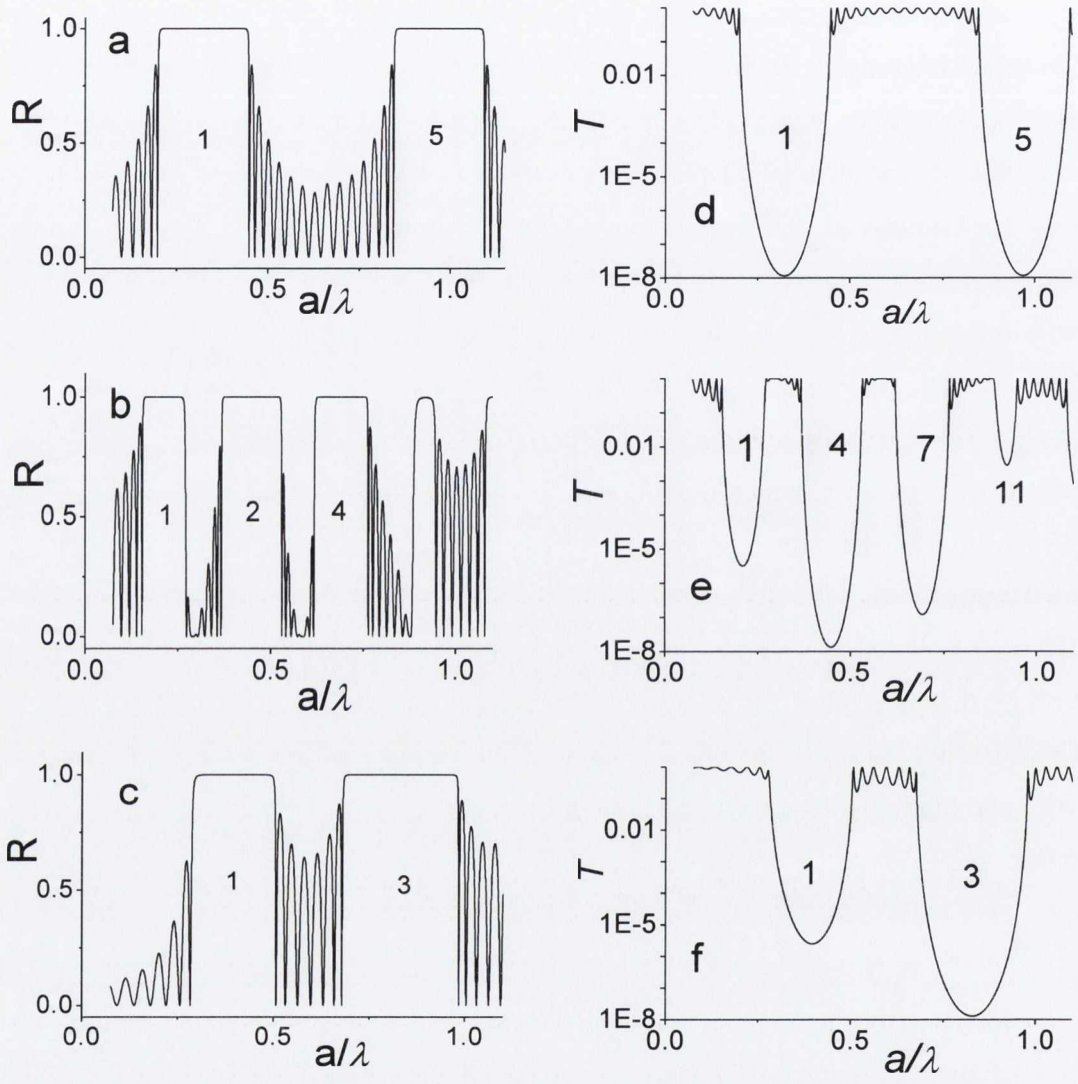

Figure 5-2: *(a), (b), (c) R and (d), (e), (f) T spectra of an ordered PhC based on a "Si-air" structure for (a),(d) f_H=0.23; (b, e) f_H=0.5 and (c, f) f_H=0.08. The number of lattice periods, N=7, the incoming and outgoing medium is air and a normal incidence of light is used for these calculations. The numbers correspond to the order number of the PBGs from Figure 5-3.*

From Figure 5-2(d,e,f) it is clear that within the PBG's frequencies, the very pronounced dips in transmission indicate that amplitude modulation of up to ~80 dB in the T spectra are possible. (Note the log scale on the y-axis). For comparison, the amplitude modulation of T outside the PBG regions is around 10 dB. These dips can be

explained by the appearance of the imaginary part of the wave vector, K, in the range of PBGs frequencies [14]. The imaginary part of the wave vector K affects the spectrum in a way which is equivalent to strong absorption of the light. The light is not absorbed via the usual electronic route within the atoms of the material. Rather, it is due to a strong interaction of the incident light with the periodic structure. Clearly, the boundaries of the strong dips are the boundaries of PBGs. The transmission spectra and PBG map will be further used for the evaluation of the impact of thickness fluctuations on the optical properties of PhCs.

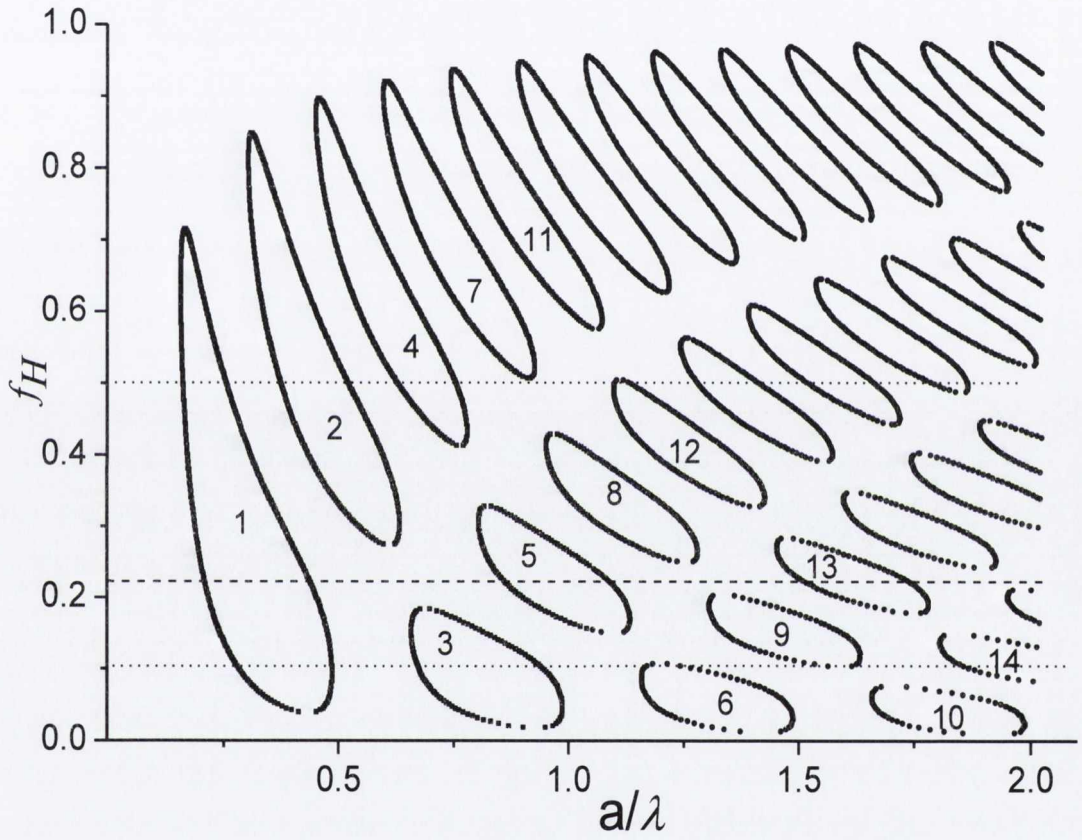

Figure 5-3: *Gap Map for ordered PhC, based on "Si-air" structure, with N=7. The lines, intersecting the PBG regions labelled with the numbers shown, are demonstrated for f_H =0.23 (dashed line), f_H =0.08 (dotted line) and 0.5 (short dotted line).*

The main (or 1st) PBG and a number of PBGs of high order, labelled 1 to 14, are observed on the gap map in a wide range of filling fractions in Figure 5-3. It can be seen that for the number of periods here (N=7), the 1st PBG with R>0.99 can be obtained in the range f_H = 0.04-0.7. The PBGs of higher order number occupy smaller areas on the map. The filling factor f_{Si} =0.23 corresponds to $\lambda/4$ optical thicknesses for

each PhC component. Note that the maximum width of the 1st PBG is at this value of f_{Si}, marked with a dashed line on the map. We are also interested in the high-order PBGs, for example, the regions numbered 2-9. The widest part of the second PBG corresponds to f_{Si} =0.5, the associated R spectrum is presented in Figure 5-2(b). The widest part of the third PBG corresponds to f_{Si} =0.08, the associated R spectrum is presented in Figure 5-2(c).

The width of the 3rd PBG is larger than the width of the 1st PBG. Therefore, this PBG can be used as a wide-band reflector, with the width of the R band being larger by a factor of 1.3 than the R-band of the reflector with an optical thickness of the components equal to $\lambda/4$.

5.3 *Modelling of thickness fluctuation*

`During the fabrication of PhCs, the tolerance in the lattice period of the ordered structure $a = d_H + d_L$ is determined by the lithographic accuracy, which is typically high. However, if an inaccuracy, for example, in the thickness of one of the components, d_H, occurs as a result of process variations, this will lead to an inaccuracy in the thickness of the second PhC component, d_L (Figure 5-1). Note that technologically all layers in these periodic structures are fabricated simultaneously and, therefore, it is impossible to make any alterations to the final structure. This is not the case for thin film coatings, where the periodic structure is formed by sequential deposition.

Let the number of walls in a PhC be i=8 as shown in Figure 5-1. In order to draw the PBG map, it is necessary to first calculate the spectra R (or T) in a range of values of d_H from 0 to a. Next, let us introduce the standard deviation, δ, as a parameter which is related to the wall thickness, d_H, in the ordered PhC and leads to the inaccuracy, or relative fluctuation, δ_i, induced in the i^{th} wall of the ordered structure in accordance with the random distribution law.

We will use two approaches to account for the thickness fluctuation δd_{Hi}. The first approach consists of the introduction of fluctuations proportional to the thickness of the i^{th} wall. Thus, the value of the fluctuation increases with an increase in the wall thickness. In this case, the thickness of the i^{th} wall, $(d_H)_i$, in the presence of a thickness fluctuation $\delta d_{Hi} = \delta_i \cdot d_H$, is determined from the following Equation (5.1):

$$(d_H)_i = d_H + d_H \cdot \delta_i = d_H (1 + \delta_i) \qquad (5.1)$$

In the second approach, the thickness fluctuation is determined by equation $\delta d_{Hi} = (d_H)_{min} \cdot \delta_i$, where $(d_H)_{min}$ is some minimal value of the wall thickness. In this case the value $(d_H)_i$ changes in accordance with equation (5.2):

$$(d_H)_i = d_H + (d_H)_{min} \cdot \delta_i \qquad (5.2)$$

Let us select the value of $(d_H)_{min}$, corresponding to the filling fraction $f_H = 0.08$. Eqn. (5.2) transforms to Eqn. (5.3):

$$(d_H)_i = d_H + 0.08 \cdot a \cdot \delta_i \qquad (5.3)$$

For example, using the first approach and standard deviation, δ=0.05, if the value of the relative fluctuation δ_i=0.11 (for i =1 in Table 5-0-1) then the thickness fluctuation will correspond to $0.11 d_H$. For a=3 μm at a lower value of f_H = 0.1, the thickness d_H will be equal to 0.3 μm, while at a higher value of f_H=0.7, the value of d_H = 2.1 μm. The calculated thickness fluctuations δd_H, determined from Eqn. (5.1), are $0.3 \cdot 0.11 = 0.033$ μm =33 nm and $2.1 \cdot 0.11 = 0.231$ μm =231 nm, respectively, i.e. δd_H will be proportional to the thickness of the walls. Using the second approach, if δ = 0.1, for the selected lower value of $(f_H)_{min} = 0.08$, the value of the thickness fluctuation δd_H = 24 nm at a=3 μm, and therefore, all other walls thicknesses in the range of the filling fraction from 0 to 1 will have fluctuations of 24 nm. Therefore, the difference between the approaches 1 and 2 is that in the first case we are dealing with more radical changes in thickness fluctuation $(d_H)_i$, while in case 2 the thickness fluctuation is less pronounced.

For both approaches, we use a random-number generator, which, based on a standard deviation of δ, generates for each i^{th} wall, a value of δ_i in accordance with the normal random distribution law. Using Equations (5.1-3), we obtain the variation of thickness in each i^{th} wall as $(d_H)_i$. Since actual values of δ_i can be either positive or negative, the thicknesses $(d_H)_i$ can be either smaller or larger than d_H in an ordered PhC. As an example, histograms for 12 types of thickness fluctuation distribution for a structure with eight walls (Figure 5-1) with δ=0.05 are presented in Figure 5-4.

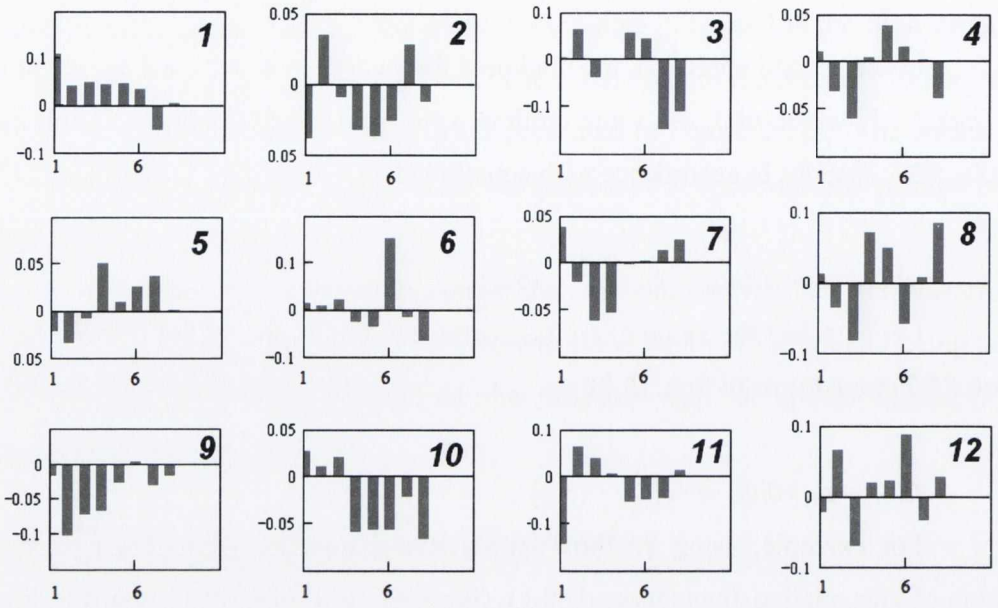

Figure 5-4: *Histograms for 12 types of thickness fluctuation distribution values δ_i for an eight wall PhC with standard fluctuation δ=0.05.*

5.4 PhC with thickness dependent variations in the wall thickness

Let us consider in detail the first approach using, as a model, a PhC with eight walls (i.e. i=8) as shown in Figure 5-1. For the first type of distribution (type 1) the dependence of the values of δ_i on the wall number is presented in Figure 5-4. The thickness fluctuation δ_i and the thickness d_H=0.66 μm (corresponding to f_H =0.23 for a PhC with a=3 μm) are presented in Table 5-0-1 along with the altered values of wall thickness $(d_H)_i$, taking into account the relative fluctuation δ_i .

Now that the new values of $(d_H)_i$ are known, a calculation of layer thickness d_L, the distance between the walls in Figure 5-1, can be performed. Since in our model, a has a constant value, i.e. the distance between the centres of the walls remains unchanged, the new value of the distance between the two walls (for example walls 3 and 4) will correspond to the difference $(d_L)_{34}$, determined by Equation (5.4):

$$(d_L)_{34}=a-[(d_H)_3/2+(d_H)_4/2] \qquad (5.4)$$

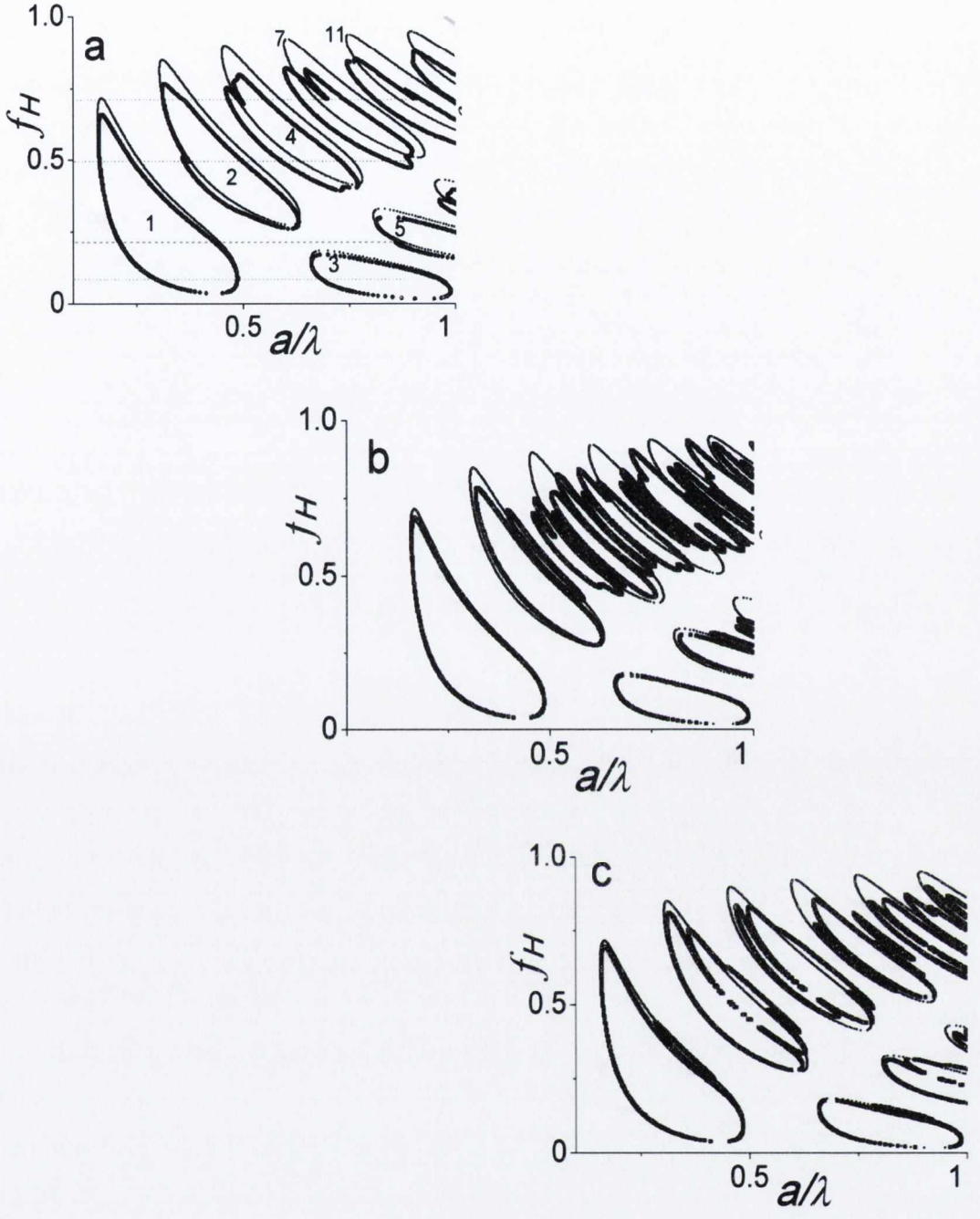

Figure 5-5: *Gap maps of an a) ordered (thin line) PhC (from Figure 5-3) and a disordered (thick line) PhC with standard random thickness deviation of the walls of δ=0.05. The fluctuation distribution used is type 1 from Figure 5-4(a), (b) Gap maps under identical conditions to those in figure (a) but with fluctuation distribution of type 8 (Figure 5-4(h)) and (c) type 6 (Figure 5-4(f)). Wall fluctuations are proportional to wall thickness. The dashed line corresponds to f_H=0.23 and the dotted lines correspond to f_H = 0.08, 0.5 and 0.71.*

Table 5-0-1: *Dependence of the relative fluctuations δ_i (for distribution of type 1) on the wall number and wall thickness values $(d_H)_i$ for a standard deviation of δ=0.05. Values are given for an eight-wall structure in a PhC with d_H=0.66 μm (f_H =0.23, a=3 μm).*

i	Values of fluctuation δ_i	Values of thickness for i^{th} wall $(d_H)_i$, μm
1	0.110	0.732
2	0.040	0.687
3	0.049	0.693
4	0.043	0.688
5	0.046	0.690
6	0.023	0.682
7	-0.052	0.626
8	0.003	0.662

Next, taking into account the changes in all of the thicknesses, d_H and d_L, we perform a calculation of the gap map taking into account the thickness fluctuations. Using the approach suggested earlier for an ordered PhC (Figure 5-3), we use the criterion R>0.99 and draw the gap map for the disordered PhC with a thickness fluctuation of type 1 and a value for δ = 0.05. In Figure 5-5(a) we present both maps on the same graph. From Figure 5-5(a), the position of the PBGs regions for ordered and disordered PhCs with δ=0.05 for lower values of f_H are practically the same, while at higher f_H values the PBGs are shifted to smaller a/λ values, that is, a red shift.

Let us analyse in detail what happens with the T spectra for a few values of f_H (Figure 5-6). From Figure 5-6(a), for f_H =0.08 there are no changes visible in the dips in the T-spectra within the same frequency range. For f_H=0.23, a red shift of the PBGs begins to become apparent, which increases when f_H is increased to f_H =0.5 and 0.71 (Figure 5-6 (b, c, d)). In parallel with this shift, a distortion in the shape of the high-order PBGs also occurs.

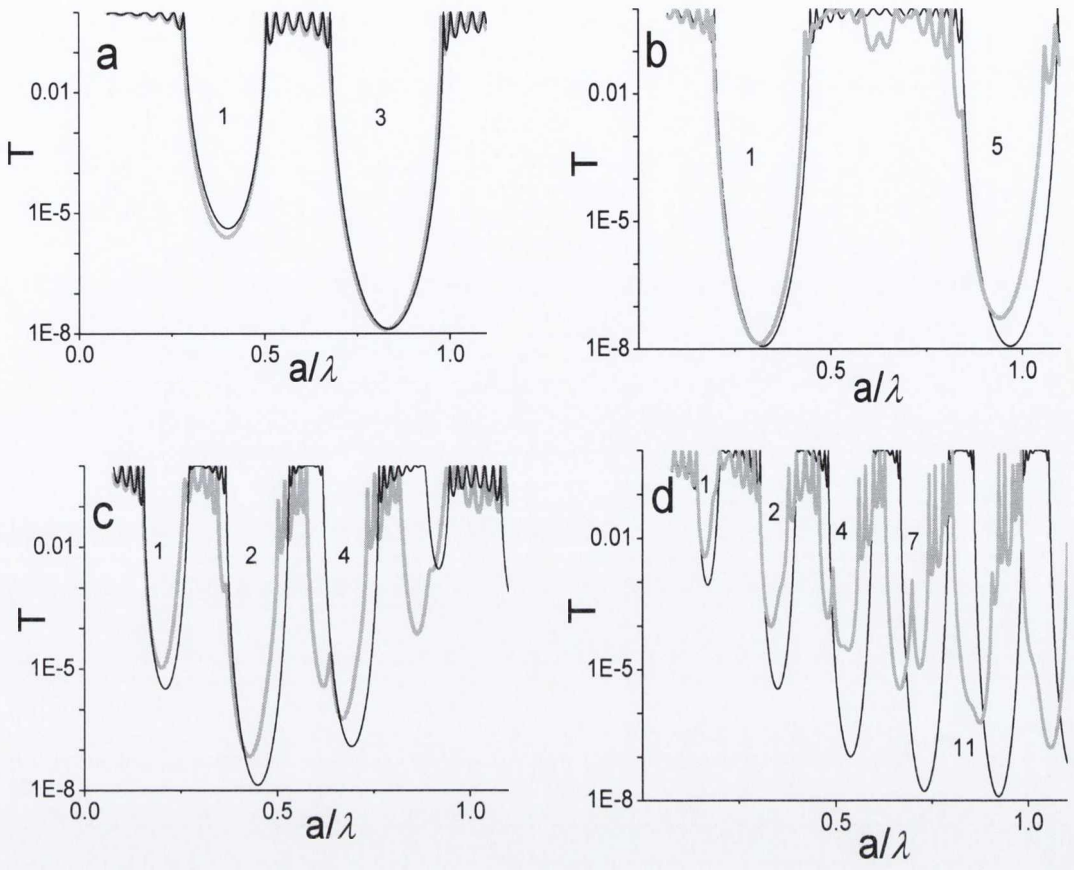

Figure 5-6: *Transmission spectra T for ordered (black line) and disordered (grey line) PhCs with filling fractions a) f_H =0.08, b) 0.23, c) 0.5, d) 0.71, with corresponding thickness fluctuations δd_H=0.004a, 0.0115a, 0.025a and 0.036a and fluctuation distributions of type 1 from Figure 5-4(a) and Table 5-1. Numbers inside the dips (PBGs) correspond to the number of the PBG shown on the gap map in Figure 5-5(a).*

A shift in the PBG regions, and a change in the T spectra, typically occurs for a small change in filling fraction, f_H. Analysing the distribution of thickness fluctuations in Figure 5-4 and Table 5-0-1, it is apparent that nearly all H-layers increase their thickness $(d_H)_i$ when compared with the ideal case of d_H=0.66 μm. Evidently, the filling factor has changed. The increase of $(d_H)_i$ here generates a red shift in the PBG on the map and in the T spectra. A proportionate dependence of the increase in PBG edges with an increase of f_H is observed, which can be explained by the increase in the optical thickness of the altered H-layers and their bands in the T spectra (Figure 5-6(c)) and its increasing influence with an increase in filling fraction f_H.

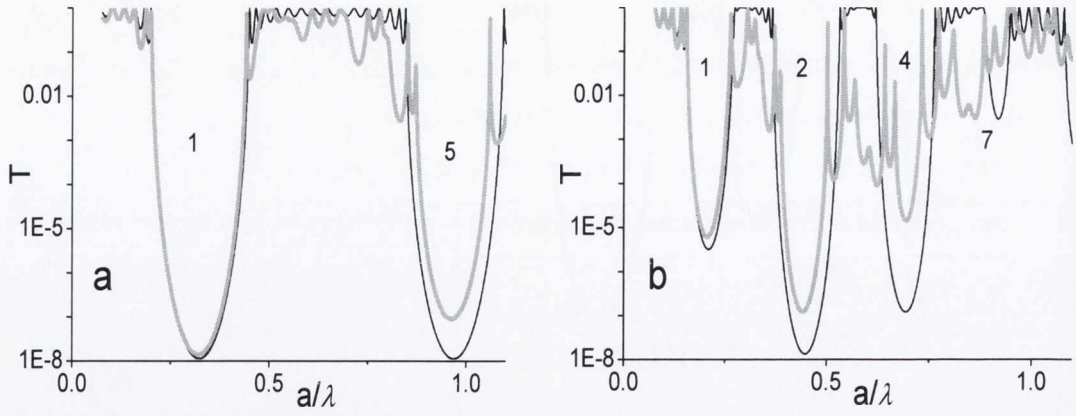

Figure 5-7: *T spectra for ordered (black line) and disordered (grey line) PhC with fluctuation distribution of type 8 for a) f_H=0.23 and b) f_H=0.5 with thickness fluctuations δd_H =0.0115a and 0.025a, respectively.*

From the fluctuation distributions, shown in Figure 5-4, the fluctuation type 8 was selected and used to calculate the *T* spectra for two values of f_H, a low f_H =0.23 and a high f_H=0.71 (see Figure 5-7). It is apparent that the distortion of the PBG occurs without a frequency shift outside the PBG band in ordered PhCs. If the fluctuation type 8 is used, it does not lead to a shift in the PBG as a function of filling fraction. This conclusion is supported by calculations using fluctuation type 8, presented in Figure 5-5(b), which demonstrates that distortion of PBGs occurs with increasing order without an associated shift in the PBG regions.

Figure 5-4 also shows fluctuation type 6, which demonstrates an approximately even distribution of δ on *i* around the middle line (at y=0), but with a pronounced single fluctuation within one of the internal walls, namely the 6th wall. The gap map calculated for this distribution type, is shown in Figure 5-5(c). Analysing this gap map, it is apparent that disorder does not result in a shift of PBGs, however characteristic narrow-band regions within the PBG regions have appeared, either in the centre or at the edges.

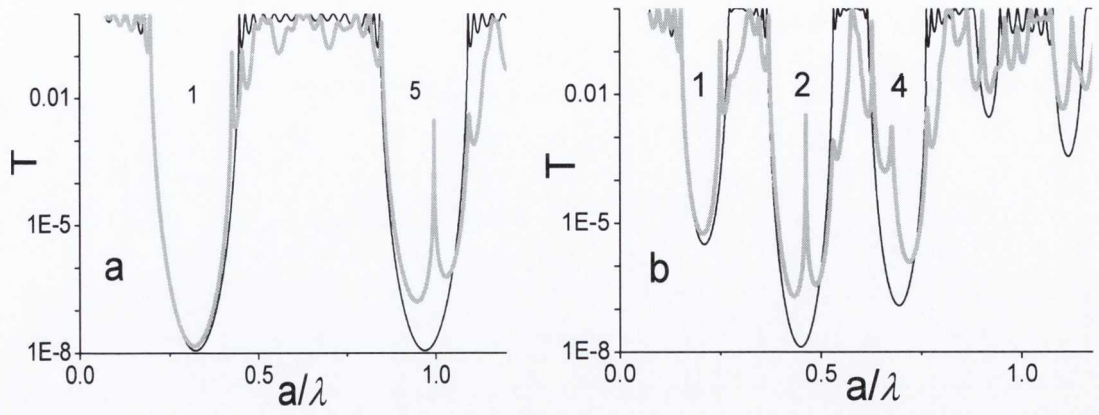

***Figure 5-8**: T spectra for ordered (black line) and disordered (grey line) PhCs with filling fractions of a) f_H=0.23, b) f_H=0.5 with corresponding thickness fluctuations δd_H =0.0115a and 0.025a. The fluctuation distribution of type 6 from Figure 5-4(f) was used.*

Let us select a PBG where the influence of thickness fluctuations is easily observed, for example, in the case of f_H=0.23 and f_H=0.5. For these values of f_H, the well-modulated transmission dips in the T spectra correspond to the 1st and the 5th PBGs in Figure 5-8(a) and the 1st, 2nd and 4th PBGs in Figure 5-8(b). The narrow peaks within the dips in the T-spectra are related to the defect modes. When these peaks are close to the PBG edges, they deform the edges of PBGs and a decrease in the modulation of the amplitude of T within the PBG region occurs simultaneously. The distortion of the PBG in the T spectrum caused by thickness fluctuations is more pronounced for the higher band orders.

From Figure 5-6, 7, 8 it can be seen how the interference fringes between PBGs change. They increase in the T spectra with an increase in the PBG order. This is also a result of the introduction of thickness non-uniformities into the PhC. If a simultaneous degradation of the edges also occurs, then determining the position of the PBG boundaries becomes problematic. As the band number increases, these effects intensify, increasing the difficulties in determining the PBG's width.

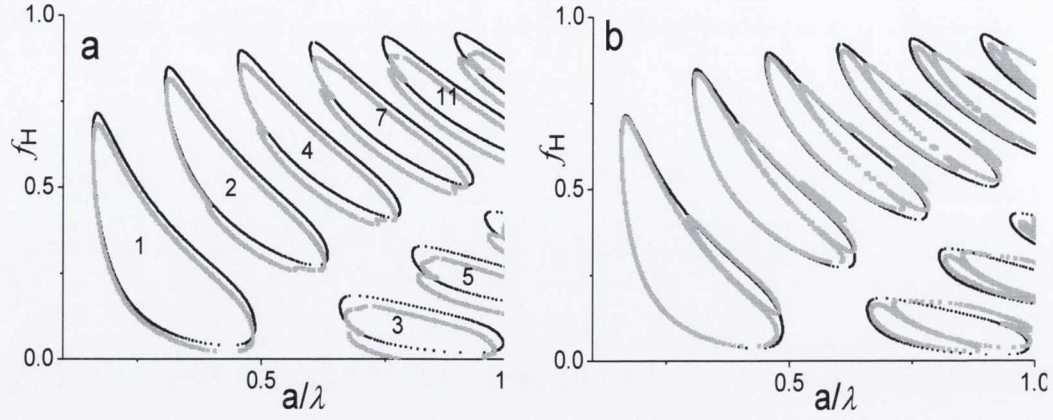

Figure 5-9: *Gap map of ordered (black line) and disordered (grey line) PhC with a standard deviation in thickness δ=0.2 and fluctuation distribution of type a) 1 and b) 6. The value of the fluctuation δd_H=0.016a is constant for different wall thicknesses.*

5.5 PhC with a constant value of fluctuation for all wall thicknesses

Let us consider a second approach for the introduction of thickness fluctuation values, using a minimal thickness deviation for all filling fractions f_H. Absolute fluctuation values from Eqn. (5-2) will correspond to $\delta(d_H)_i$ =12, 24 and 48 nm for a = 3 μm and f_{Hmin} =0.08 for the corresponding three values of δ = 0.05, 0.1 and 0.2 for two types of fluctuation distribution, viz. type 1 and type 6. Differences in the position of the PBG regions on the maps for ordered and disordered PhC with fluctuations of type 1 are negligible up to δ=0.05 (δd_H =0.004a). For δ=0.2 (δd_H=0.016a) these become apparent (Figure 5-9(a)) as a shift of the PBG region edge, this shift is more pronounced for PBGs of high order. We can explore this further by analyzing the dips in the T spectra for various values of f_H (Figure 5-10). In this model, the same red shift will be observed in all spectra with different values of f_H. This red shift was discussed earlier in relation to Figure 5-5(a) and Figure 5-6. These shifts are explained by the nature of the fluctuation distribution, which increases the filling fraction at the expense of wall thickness.

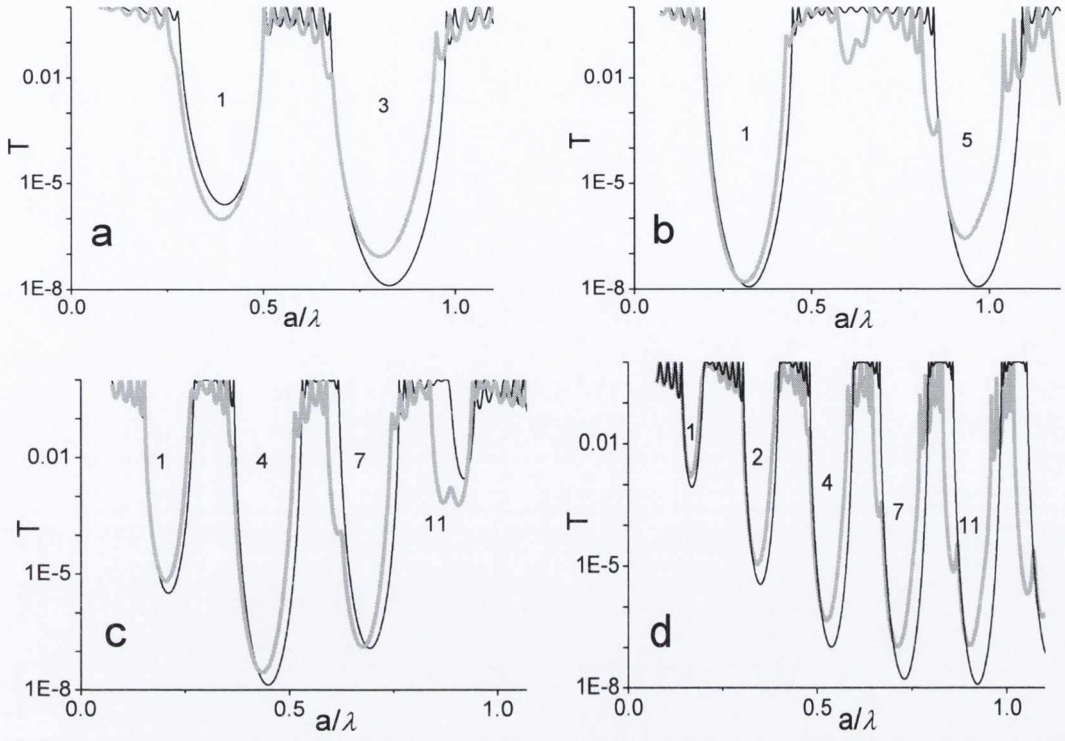

***Figure 5-10**: T spectra of ordered (black line) and disordered (grey line) PhC with fluctuations of type 1 for a) f_H =0.08, b) f_H=0.23, c) f_H=0.5 and d) f_H=0.71. The value of the thickness fluctuation δd_H=0.016a is constant for different wall thicknesses.*

For the fluctuation type 6, it can be seen from Figure 5-9(b) that changes in the PBG regions are observed as a result of the introduced fluctuation with δ=0.2. The boundaries of the regions are not shifted, but defect peaks have appeared within the PBG's frequencies. The same effect is observed in the *T* spectra (Figure 5-11). For example, in Figure 5-11(b) for f_H=0.23, the shape of the 1st PBG is partially distorted due to the appearance of a defect peak near it's edge. The presence of the defect peaks, as discussed earlier, can be explained by the type of fluctuation 6, in which the dominant thickness deviation is present near the centre of the PhC.

During our investigations of the influence of other types of thickness fluctuation shown in Figure 5-4 (i.e. types 2-5, 7-8 and 10-12) we observed that the boundaries of the PBG regions in the disordered structures are not shifted. Their behaviour is generally similar to that of type 8 (see the analysis of Figure 5-5(b) and Figure 5-7), because this type of thickness fluctuation demonstrates broadly similar positive and negative thickness fluctuations.

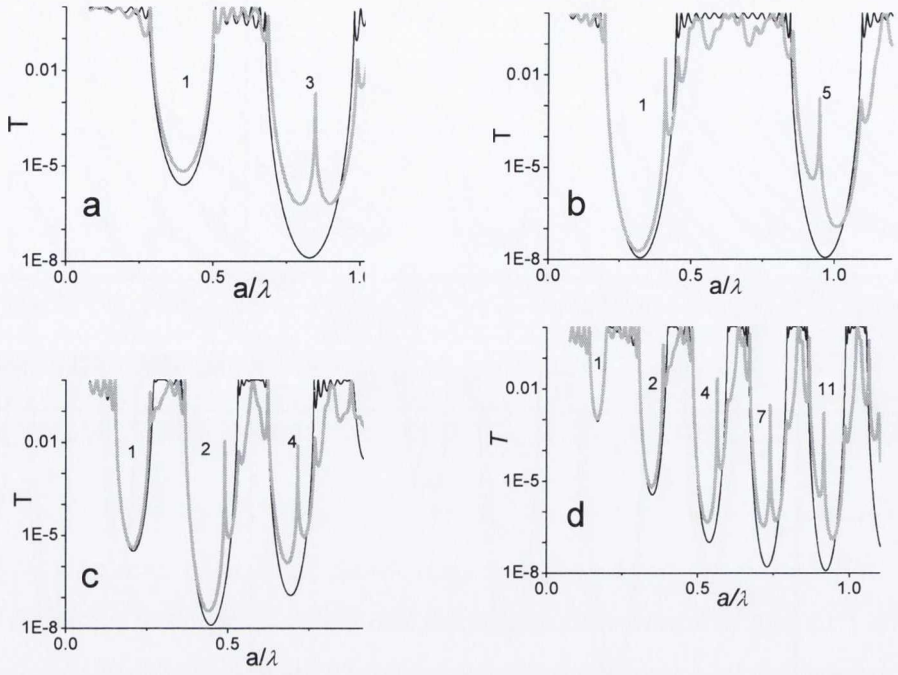

Figure 5-11: *T spectra of ordered (black line) and disordered (grey line) PhC with fluctuation distribution of type 6 for a) f_H=0.08, b) f_H=0.23, c) f_H=0.5 and d) f_H=0.71. The value of the thickness fluctuation δd_H=0.016a is constant for different wall thicknesses.*

Analysing the shift of PBGs regions from Figure 5-9(a, b), it is clear that the shift does not depend on filling fraction, i.e. on thickness of d_H. Therefore, only the amount of thickness fluctuation introduced into the PhC influences the bands shift. This conclusion is confirmed by the increase in the PBG shift noted above, together with an associated shift in the spectra, as a consequence of increasing thickness fluctuation from δd_H =0.004a to 0.036a (Figure 5-6).

5.6 Summary

A combination of mathematical modelling and gap map analysis allows the influence of randomly induced thickness fluctuations in photonic crystal components on the distortion of photonic band gaps in one-dimensional PhCs to be investigated. The investigation of band gaps in the transmission spectra provides further, detailed information on the influence of thickness fluctuations. In this study, 1D PhCs based on microstructured semiconductors "*Si-air*", with a range of filling fractions and PBGs of

different order was studied. Three characteristic types of fluctuation distribution and two ratios of the fluctuation parameters to the wall thicknesses were considered. By introducing thickness disorder into the PhC, and depending on the type of fluctuation distribution, a shift of the PBGs, the appearance of defect modes, a decrease in the amplitude modulation of transmission within the PBG and an increase in interference fringe modulation between PBGs were observed.

We established that the change in the PBGs depends on the magnitude of the fluctuations and increases with an increase in the order of the PBG. Introducing thickness non-uniformity into the PhC of up to 0.004 from value of lattice constant *a* for different types of fluctuation distribution has almost negligible effect on either the position or the shape of the 1st and nearest PBGs. However, depending on the type of fabrication, whether the optical or e-beam lithography is used, the effect can be larger or smaller. For example, the e-beam lithography provides small fabrication error (Chapter 4; Section 4.4.5), while the classical optical lithography, used for the fabrication of structures with a.>1 μm, gives significantly higher fabrication errors. The approach presented here enables the determination of the fabrication tolerances required for the geometrical parameters of the PhC structure and allows optimisation of the design of these structures for the utilisation of high order PBGs, including structures with PhC components with quarter wavelength optical thicknesses. This approach is also useful for the solution of the complementary task, the determination of the parameters of the PhC structure from it's reflection/transmission spectra.

5.7 References

[1] G. T. Reed, [Silicon Photonics: The State of the Art]' John Wiley & Sons; (2008).

[2] R. B. Wehrspohn, H. S. Kitzerow, K. Busch, [Nanophotonic Materials: Photonic Crystals, Plasmonics, and Metamaterials], John Wiley & Sons (2008).

[3] L. Pavesi, D. J. Lockwood, [Silicon Photonics], Springer (2004).

[4] S. Postnikov, S. Hector, C. Garza, R. Peters, and V. Ivin, "Critical dimension control in optical lithography", Microelectronic Engineering, 69:452-458 (2003).

[5] K. Busch, S. Lölkes, R. Wehrspohn, H. Föll, [Photonic Crystals. Advances in Design, Fabrication, and Characterization], Weinheim: Wiley-VCH, Ch.1 (2004).

[6] S. Fan, P. R. Villeneuve, and J. D. Joannopoulos, "Theoretical investigation of fabrication-related disorder on the properties of photonic crystals", J. Appl. Phys., Vol. 78, No. 3, 1415-1418 (1995).

[7] K.R. Maskaly, G.R. Maskaly, W.C. Carter, and J.L. Maxwell, "Diminished normal reflectivity of one-dimensional photonic crystals due to dielectric interfacial roughness", Opt. Lett., Vol. 29, No. 23, 2791-2793 (2004).

[8] Z. Jaksic, M. Maksimovic, O. Jaksic, D. Vasiljevic-Radovic, Z. Djuric, and A. Vujanic, "Fabrication-induced disorder in structures for nanophotonics", Microelectronic Engineering, Vol. 83, No. 4-9, 1792-1797 (2006).

[9] O. Glushko, R Meisels, F Kuchar, and R. Danzer, "Numerical and experimental investigations of surface roughness in 1D photonic Crystals", J. Phys.: Condens. Matter, Vol. 20, No. 45, 454220/1-7 (2008).

[10] G. Barillaro, L. M. Strambini, V. Annovazzi-Lodi, and S. Merlo, "Optical Characterization of High-Order 1-D Silicon Photonic Crystals", IEEE Journal of Selected Topics in Quantum Electronics, Vol. 15, No. 5, 1359-1367 (2009).

[11] A. R. McGurn, K. T. Christensen, F. M. Mueller, and A. A. Maradudin, "Anderson localization in one-dimensional randomly disordered systems that are periodic on average", Phys. Rev. B, Vol. 47, No.20, 13120-13125 (1993).

[12] M. A. Kaliteevski, J. Manzanares Martinez, D. Cassagne, and J. P. Albert, "Disorder-induced modification of the attenuation of light in a two-dimensional photonic crystal with complete band gap", Phys. Stat. Sol. *A*, Vol.195, No. 3, 612-617 (2003).

[13] M. A. Kaliteevskii, V. V. Nikolaev, and R. A. Abram, "Eigenstate Statistics and Optical Properties of One-Dimensional Disordered Photonic Crystals", Phys. Solid State, Vol. 47, No. 10, 1948–1957 (2005).

[14] P. Yeh, [Optical Waves in Layered Media], New York: Wiley, Ch.6, p.118 (1988).

[15] Lu Xiaodong, Han Peide, Quan Yujun, Ran Qijiang, Gao Lipeng, Zeng Fanping, Zhao Chunhua, and Yu Jinzhong, "Optical response of high-order band gap in one-dimensional photonic crystal applying in-plane integration", Opt. Commun., Vol. 277, 315–321 (2007).

[16] V. A. Tolmachev, V. A. Melnikov, A. V. Baldycheva, K. Berwick, and T. S. Perova, "Electrically tunable Fabry-Perot resonator based on microstructured Si containing liquid crystal", Progress in Electromagnetic Research, Vol.122, 293-309 (2012).

[17] A. Baldycheva, V.A. Tolmachev, T.S. Perova, Yu.A. Zharova, E.V. Astrova, and K. Berwick, "Silicon photonic crystal filter with ultra-wide pass-band characteristics", Opt. Lett., Vol. 36, No.10, 1854-1856 (2011).

[18] V.A. Tolmachev, T.S. Perova, J. Ruttle, and E. Khokhlova, "Design of One-dimensional Photonic Crystals Using Combination of Band Diagrams and Photonic Gap Map Approaches", J. Appl. Phys., Vol.104, No. 3, 033536/1-6 (2008).

[19] V.A. Tolmachev, A.V. Baldycheva, S.A. Dyakov, K. Berwick, and T.S. Perova, "Optical contrast tuning in three-component 1D Photonic Crystals", IEEE Journal of Lightwave Technology, Vol. 28, No. 10, 1521-1529 (2010).

[20] V. A. Tolmachev, T. Perova, A. Baldycheva. Transformation of one-dimensional Silicon photonic crystal into Fabry-Pérot resonator. Proceedings of SPIE 7943, 79430E/1-12 (2011).

[21] R. M. A. Azzam, Bashara, N. M., [Ellipsometry and polarized light], Amsterdam, North-Holland, P.334, Ch.4, p.269 (1977).

[22] V. Tolmachev, T. Perova, E. Krutkova, and E. Khokhlova, "Elaboration of the gap map method for the design and analysis of one-dimensional photonic crystal structures", Physica E: Low-dimensional Systems and Nanostructures, Vol. 41, No. 6, 1122-1126 (2009).

[23] J. Manzanares-Martinez, R. Archuleta-Garcia, P. Castro-Garay, D. Moctezuma-Enriquez, and E. Urrutia-Banuelos, "One-dimensional photonic heterostructure with

broadband omnidirectional reflection," Progress In Electromagnetics Research, Vol. 111, 105–117 (2011).

[24] C.-J. Wu, Y.-C. Hsieh, and H.-T. Hsu, "Tunable photonic band gap in a doped semiconductor photonic crystal in near infrared region," Progress In Electromagnetics Research, Vol. 114, 271–283 (2011).

[25] A. Banerjee, "Enhanced Temperature Sensing by Using One-Dimensional Ternary Photonic Band Gap Structures", Progress In Electromagnetics Research Letters, Vol. 11, 129-137 (2009).

[26] J. Ni, B. Chen, S. L. Zheng, X.-M. Zhang, X.-F. Jin, and N. Chi, "Ultra-wideband on electrooptic phase modulator and phase- shift fiber Bragg grating," Journal of Electromagnetic Waves and Applications, Vol. 24, No. 5–6, 795–802 (2010).

[27] C.-J.Wu, Y.-N. Rau, and W.-H. Han, "Enhancement of Photonic Band Gap in a Disordered Quarter-Wave Dielectric Photonic Crystal", Progress In Electromagnetics Research, PIER, Vol. 100, 27-36 (2010).

[28] M. Khalaj-Amirhosseini, and S. M. J. Razavi, "Wide-angle reflection wave polarizers using inhomogeneous planar layers", Progress In Electromagnetics Research M, Vol. 9, 9–20 (2009).

[29] S. K. Awasthi, U. Malaviya, S. P. Ojha, N. K. Mishra, and B. Singh, "Design of a Tunable Polarizer Using a One–Dimensional Nano Sized Photonic Bandgap Structure", Progress In Electromagnetics Research B, Vol. 5, 133-152 (2008).

[30] H.-T. Hsu, M.-H. Lee, T.-J. Yang, Y.-C. Wang, and C.-J. Wu, "A multichanneled filter in a photonic crystal containing coupled defects," Progress In Electromagnetics Research, Vol. 117, 379–392 (2011).

Chapter 6.

Conclusion

This thesis has been concerned with the design, fabrication and optical investigation of novel photonic crystal structures for application in integrated Silicon microphotonics. The studies undertaken yield information on the new unique optical properties of the developed *multi-component* as well as *single-* and *multi-cavity photonic crystals* based on grooved Silicon for in-plane light modulation.

The basic concepts underlying the photonic crystal optical properties and their modifications have been demonstrated in Introduction Chapter. A classical transfer matrix method and gap map approach have been elaborated and applied to mathematically describe and design the one-dimensional photonic crystals structures based on Silicon. The viability of the results achieved in this thesis is confirmed by experimental results as well as by comparison with previous results reported by other authors. For experimental technological realization of the proposed free-space photonic crystal structures the classic optical and e-beam lithography as well as wet and dry etchings of (100) and (110) Silicon were utilized. The optical characterization was performed in a wide infrared spectral range using the Fourier Transform Infrared microspectroscopy (1-15 μm) and optical fiber-coupling set-up based on optical spectrum analyzer (1.2-1.7 μm).

The effects demonstrated have practical applications in integrated Silicon microphotonics. The suggested photonic crystal models can be applied to the design of any micro- and nanostructured semiconductor or dielectric material for application across the entire electromagnetic range.

Multi-component Photonic Crystal structures

Utilisation of a multi-component photonic crystal by the introduction of an additional regular material into a grooved Silicon structure, while leaving the lattice constant unchanged, provides a suitable model for designing a new type of photonic crystal. Use of a gap map allows visualization of the transformation of the photonics band gap areas caused by converting an ordinary two-component PhC to a three-component PhC by the addition of the new regular layer. The introduction of the third component to the 1D PhC enables variation of the PBGs areas of the three-component PhC and, therefore, engineering of the optical contrast of the original two-component PhC. This is achieved, not by filling its air channels, but by selecting either the thickness or the refractive index of the third layer. Using the approach suggested for decreasing the optical contrast in photonic crystal, the omni-directional bands can be obtained in a high-contrast "*Si-air*" periodic structure. A number of simulated models of three-component 1D photonic crystals are described, some of which may have practical applications.

For the first time the principle of suppression of the PBGs and replacing them with transmission bands (TBs) is demonstrated for a high contrast 1D PhC with the introduction of an additional layer. By varying the thickness of this layer, the width and the number of the TBs can be altered. The TBs obtained numerically show a high transmission value (>99 %) and a substantial band width in the infrared spectral range. The GM approach was used to generate the map of transmission bands in order to observe the effect in the entire range of Si filling fraction and in a wide wavelength range. The generated maps of TBs have demonstrated the formation of the ultra-wide transmission bands over the suppressed PBGs in a whole range of possible filling factors. The TBs obtained demonstrate a substantial bandwidth (>200 nm) and a negligible number of ripples within the bands. For the certain angles of incidence of light the multi-component PhC devices demonstrate the polarization effect: the remaining PBGs for one-polarization may overlap with the obtained wide TBs for another polarization, therefore transforming the PhC into a broadband polarizer. In order to fine tune the wavelength position, number and width of the output transmitting or reflecting bands, thermal oxidation of the grooved Si structures was exploited. Based on the generated map of TBs the PhC filter with ultra-wide TB characteristics has been successfully fabricated and characterized. The TB obtained exhibit a high transmission

of 92-96 % and a substantional bandwidth of 1800 nm with negligible number of ripples on the top.

Microcavity Photonic Crystal Structures:

The model of transformation of one-dimensional, high-contrast Silicon photonic crystal into an efficient tunable Fabry-Perot resonator in which a wide Stop Band is used for frequency resonance separation has been proposed and investigated. This transformation is achieved by introduction of the optical defects in the ordinary photonic crystal by infiltration of certain periods with refractive index matching filler.

The FP-resonator based on PhC with optical defects has a number of significant advantages from the practical point of view. These are, for example, the possibility to avoid the specific procedure for the defects fabrication but rather use the possibility of introducing the filler in the centre of PhC and tuning capability of the resonance peaks within the SBs by variation of the refractive index of the defect filler.

The utilisation of common gap maps of PBGs (or stop-bands) and TBs allows to predict the resonance appearance or disappearance in the optical spectra and to determine the optimal design parameters, namely the wavelength position, the quality factor and the free spectral range depending on the order of PBG and the value of filling fraction.

By using nematic liquid crystal E7 as a filler, the precise continuous tuning of the obtained resonances was experimentally achieved by either varying the temperature from 10° to 65°C or by application of electric field from 0 to 15 V. The obtained result has demonstrated the largest experimental shift, achieved up to date for the microstructured resonators based on Si and Liquid Crystal (LC), and utilized for molding of light propagated parallel to the substrate. It was also shown theoretically and experimentally, that for the high optical contrast structure on Silicon the reflection from Si wall is reached the value of ~0.95, that provide a high quality resonance peaks in a wide range of spectra, measured from 1.5 to 15 μm. Most importantly it was established that a significant shift of peak position is achieved by using the resonance peaks of high order. In particular, a superposition of the transmission peaks with reflection maxima, predicted from calculations, was confirmed experimentally.

For the first time, an electro-optical technique for precise position control of individual transmission channels/resonances in a triple-cavity resonator device has been

proposed. By controllable tuning of the refractive index in all coupled cavities, a continuous individual tuning of the central channel (or edge channels) up to 25% of the total channel spacing has been demonstrated. Additionally, an approach for precise controllable improvement of transmission up to 100 % is demonstrated for the edge channels with decrease of the channel spacing on ~1 %. Based on the proposed design, a prototype triple-channel filter was fabricated on Silicon-On-Insulator platform and optimized to the desired operational mode. The suggested approach has been utilized for compensation of the fabrication tolerances in multi-channel Silicon devices in a wide infrared range.

Influence of the thickness fluctuations on PBG properties:

The influence of randomly induced thickness fluctuations in photonic crystal components on the distortion of photonic band gaps in one-dimensional PhCs has been investigated in detail. Three characteristic types of fluctuation distribution and two ratios of the fluctuation parameters to the wall thicknesses have been considered in this study. By introducing thickness disorder into the PhC, and depending on the type of fluctuation distribution, a shift of the PBGs, the appearance of defect modes, a decrease in the amplitude modulation of transmission within the PBG and an increase in interference fringe modulation between PBGs have been obtained. The change in the PBGs depends on the magnitude of the fluctuations and increases with an increase in the order of the PBG. Introducing thickness non-uniformity into the PhC of up to 0.004 from value of lattice constant for different types of fluctuation distribution has a negligible effect on either the position or the shape of the first and nearest PBGs. The developed mathematical approach presented here allows the determination of the tolerances required in the geometrical parameters of the PhC structures during fabrication. It also allows the optimization of PhC structures using high order PBGs.

The scientific novelty of the work:

- The full and systematic analyses of the optical characteristics of the in-plane one-dimensional multi-component photonic crystal structures and micro-cavity photonic crystals filters have been developed and proposed using the gap map approach.

- The model of a three-component PhC was developed and the approach for engineering of the optical contrast by variation of the additional component thickness was suggested and experimentally demonstrated.
- For the first time, the regions of transparency in multi-component PhC have been discovered and experimentally demonstrated for the three-component PhC based on "*Si-SiO_2-air*" structure with bandwidth of the flat-top pas-bands of 1800 nm.
- The utilization of common maps of stop-bands and pass-bands allows extensive analyse of the discovered effect of total transparency in Silicon based photonic crystals. The full suppression of the certain order stop-bands and their replacement with wide-band pass-bands have been demonstrated.
- The reverse continuous electro-tuning of the LC director orientation from spontaneous planar to homeotropic has been achieved and demonstrated for the defect-free PhC FP-resonators based on SOI platform. An outstanding experimental wide shift of 10 % of the resonance peaks has been successfully demonstrated. This is the largest resonance shift achieved to date in Si photonic crystals.
- For the first time, the compact and integratable solution for multi-channel photonic crystal filter with fine-tuning capability of individual channels up to 25 % is demonstrated.

Summary of the potential applications of the methods used in this work:

- For the first time, the Gap Map approach proposed as a core engineering tool for photonic crystal based devices, such as resonators and ultra-wide band-pass filters. From the theoretical point of view, the determination of the optimal design parameters using the GM approach in the entire range of wavelength and filling fraction provides deeper understanding of the physical processes in photonic optical devices. From the fabrication point of view the developed gap maps here allow highly accurate determination of the fabrication tolerances of the photonic crystal structures.
- The transfer matrix method source code developed for multi-component and micro-cavity PhC structures in MathCad and Matlab Software during the doctoral work can be used to simulate various optical devices and investigate their basic characteristics.

- The experimental result obtained for multi-component PhC structures based on grooved Silicon and thermally grown oxide proves that fabrication of interference filters with almost 100 % transmission and flat-top characteristic over a selected wide range of the infrared spectrum is practical.
- For tunable LC photonic crystal filters the new design of a whole system of micro-fluidic channels and infiltration reservoirs has been developed.
- The new technique for manual infiltration of the micro-scale structures with liquid crystal has been experimentally developed.
- The fiber-optic test set-up based on end-fire technique for NIR characterization of planar integrated photonic devices has been designed and assembled.
- The mathematical approach based on transfer matrix method and random number generator in MathCad Software has been developed for simulations of the photonic band gap deviations caused by various structural deviations after fabrication process and can be used for determination of the fabrication tolerances and their compensation.

Future work:

From the results obtained on the relationship between TBs and angle of incidence of light for multi-component PhC structure it has become clear that even one-dimensional photonic crystal structure can be used as a broadband polarizing beam splitter in a wide-angular range. However, there is still a lot to be learnt about polarized regions of transparency:

- How the angular field of polarization splitting can be extended using the multi-component model.
- Why only the TM(H)-polarized regions of transparency possess the omni-directional properties, while the TE(E)-polarized regions of transparency are almost totally suppressed at oblique incidence of light.

Demonstrated in this work model of fine-tunable individual channels in coupled-cavity photonic crystals have resulted in the development of the design and fabrication technology of the integrated triple channel photonic crystal filters on SOI platform. The preliminary results obtained for the first prototype structures have been included in the Chapter 4, demonstrating the modern technological capability of fabrication of this type of device. The final, improved design of the filters is currently going through the final

fabrication step at Tyndall National Institute. Similar experimental methodology to the one developed for single-cavity photonic crystals will be used for optical characterization of the device during the operation.

Appendix I

A MathCad program code for simulation of the gap map of transmission regions in 1D multi-component photonic crystal:

$rad := \frac{\pi}{180}$ $SiO2 := READPRN("SiO2nk2000.csv")$

$\lambda := SiO2^{\langle 0 \rangle}$ $\phi r := \phi \cdot rad$ $i := \sqrt{-1}$

$\upsilon := \frac{10000}{\lambda}$

$Nt := SiO2^{\langle 1 \rangle}$

$kt := SiO2^{\langle 2 \rangle}$

$m := 2 .. length(\lambda) - 1$

$Nkt_m := Nt_m - kt_m \cdot i$

$A := 4$

$per := 3$ $No := 1$

$Ns := 1$ $NH := 3.42$

$NL := 1$ $Dt := 0$

$Nt := 1.5$ $DH0 := 0$

$dDH := 0.01$ $maxn := 160$

$n := 1 .. max$

$DH1(n) := [DH0 + dDH \cdot (n - 1)]$ $DH2(n) := [DH0 + dDH \cdot (n - 1)] + 2D$

$DL(n) := A - DH2(n)$ $DA(n) := \frac{DH1(n)}{A}$

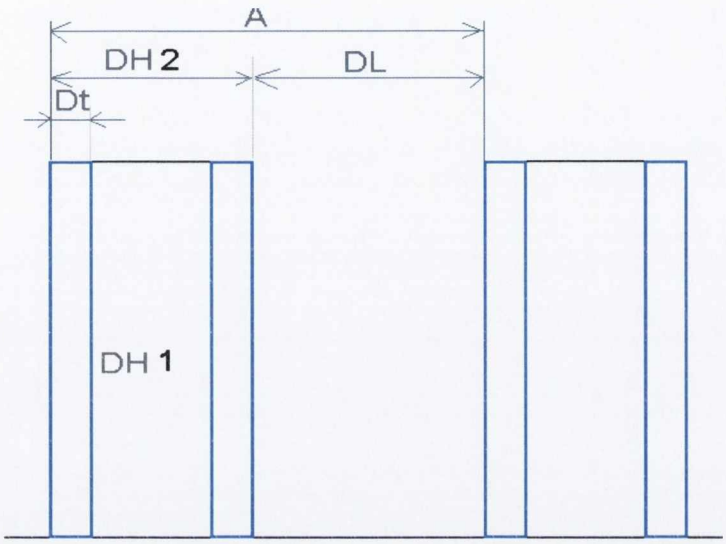

2x2matrix method:

$q0 := \cos(\phi r)$

$$q0t_m := \sqrt{1 - \frac{(No)^2}{(Nkt_m)^2} \cdot (1 - q0^2)}$$

$$r0tp_m := \frac{Nkt_m \cdot q0 - No \cdot q0t_m}{Nkt_m \cdot q0 + No \cdot q0t_m}$$

$$r0ts_m := \frac{No \cdot q0 - Nkt_m \cdot q0t_m}{No \cdot q0 + Nkt_m \cdot q0t_m}$$

$ZOtp_m := Nkt_m \cdot q0 + No \cdot q0t_m$

$ZOts_m := No \cdot q0 + Nkt_m \cdot q0t_m$

$t0tp_m := \frac{2 \cdot No \cdot q0}{ZOtp_m}$ $C0t := 2 \cdot No \cdot qC$ $t0ts_m := \frac{C0t}{ZOts_m}$

$$I0tp(m) := \begin{pmatrix} 1 & r0tp_m \\ r0tp_m & 1 \end{pmatrix} \cdot \begin{pmatrix} 1 \\ \overline{t0tp_m} \end{pmatrix}$$

$$I0ts(m) := \begin{pmatrix} 1 & r0ts_m \\ r0ts_m & 1 \end{pmatrix} \cdot \begin{pmatrix} 1 \\ \overline{t0ts_m} \end{pmatrix}$$

$$a\beta t(m) := 2 \cdot \frac{\pi}{\lambda_m} \cdot Dt \cdot Nkt_m \cdot i$$

$$\beta t(m) := 2 \cdot \frac{\pi}{\lambda_m} \cdot Dt \cdot q0t_m \cdot Nkt_m \cdot i$$

$$Mt(m) := \begin{pmatrix} e^{\beta t(m)} & 0 \\ 0 & e^{-\beta t(m)} \end{pmatrix}$$

$$qtH_m := \sqrt{1 - \frac{(Nkt_m)^2}{(NH)^2} \cdot \left[1 - (q0t_m)^2\right]}$$

$$rtHp_m := \frac{NH \cdot q0t_m - Nkt_m \cdot qtH_m}{NH \cdot q0t_m + Nkt_m \cdot qtH_m} \qquad rtHs_m := \frac{Nkt_m \cdot q0t_m - NH \cdot qtH_m}{Nkt_m \cdot q0t_m + NH \cdot qtH_m}$$

$$ZtHs_m := Nkt_m \cdot q0t_m + NH \cdot qtH_m \qquad ZtHp_m := NH \cdot q0t_m + Nkt_m \cdot qtH_m$$

$$ttHp_m := \frac{2 \cdot Nkt_m \cdot q0t_m}{ZtHp_m} \qquad CtH_m := 2 \cdot Nkt_m \cdot q0t_m$$

$$ttHs_m := \frac{CtH_m}{ZtHs_m}$$

$$ItHp(m) := \begin{pmatrix} 1 & rtHp_m \\ rtHp_m & 1 \end{pmatrix} \cdot \begin{pmatrix} 1 \\ \overline{ttHp_m} \end{pmatrix} \qquad ItHs(m) := \begin{pmatrix} 1 & rtHs_m \\ rtHs_m & 1 \end{pmatrix} \cdot \begin{pmatrix} 1 \\ \overline{ttHs_m} \end{pmatrix}$$

$$\beta H(n,m) := 2 \cdot \frac{\pi}{\lambda_m} \cdot DHl(n) \cdot qtH_m \cdot NH \cdot i$$

$$MH(n,m) := \begin{pmatrix} e^{\beta H(n,m)} & 0 \\ 0 & e^{-\beta H(n,m)} \end{pmatrix}$$

$$qHt_m := \sqrt{1 - \frac{(NH)^2}{(Nkt_m)^2}\cdot\left[1 - (qtH_m)^2\right]}$$

$$rHtp_m := \frac{Nkt_m \cdot qtH_m - NH \cdot qHt_m}{Nkt_m \cdot qtH_m + NH \cdot qHt_m}$$

$$rHts_m := \frac{NH \cdot qtH_m - Nkt_m \cdot qHt_m}{NH \cdot qtH_m + Nkt_m \cdot qHt_m}$$

$$ZHts_m := NH \cdot qtH_m + Nkt_m \cdot qHt_m \qquad ZHtp_m := Nkt_m \cdot qtH_m + NH \cdot qHt_m$$

$$tHtp_m := \frac{2 \cdot NH \cdot qtH_m}{ZtHp_m}$$

$$CHt_m := 2 \cdot NH \cdot qtH_m$$

$$tHts_m := \frac{CHt_m}{ZtHs_m}$$

$$IHtp(m) := \begin{pmatrix} 1 & rHtp_m \\ rHtp_m & 1 \end{pmatrix} \cdot \left(\frac{1}{tHtp_m}\right) \qquad IHts(m) := \begin{pmatrix} 1 & rHts_m \\ rHts_m & 1 \end{pmatrix} \cdot \left(\frac{1}{tHts_m}\right)$$

$$qtL_m := \sqrt{1 - \frac{(Nkt_m)^2}{(NL)^2}\cdot\left[1 - (qtH_m)^2\right]}$$

$$rtLp_m := \frac{NL \cdot qHt_m - Nkt_m \cdot qtL_m}{NL \cdot qHt_m + Nkt_m \cdot qtL_m} \qquad rtLs_m := \frac{Nkt_m \cdot qHt_m - NL \cdot qtL_m}{Nkt_m \cdot qHt_m + NL \cdot qtL_m}$$

$$ZtLp_m := NL \cdot qHt_m + Nkt_m \cdot qtL_m \qquad ZtLs_m := Nkt_m \cdot qHt_m + NL \cdot qtL_m$$

$$tLp_m := \frac{2 \cdot Nkt_m \cdot qHt_m}{ZtLp_m} \qquad CtL_m := 2 \cdot Nkt_m \cdot qHt_m$$

$$ttLs_m := \frac{CtL_m}{ZtLs_m}$$

$$ItLp(m) := \begin{pmatrix} 1 & rtLp_m \\ rtLp_m & 1 \end{pmatrix} \cdot \begin{pmatrix} 1 \\ ttLp_m \end{pmatrix}$$

$$ItLs(m) := \begin{pmatrix} 1 & rtLs_m \\ rtLs_m & 1 \end{pmatrix} \cdot \begin{pmatrix} 1 \\ ttLs_m \end{pmatrix}$$

$$\beta L(n,m) := 2\frac{\pi}{\lambda_m} \cdot DL(n) \cdot qtL_m \cdot NL \cdot i$$

$$ML(n,m) := \begin{pmatrix} e^{\beta L(n,m)} & 0 \\ 0 & e^{-\beta L(n,m)} \end{pmatrix}$$

$$qLt_m := \sqrt{1 - \frac{(NL)^2}{(Nkt_m)^2} \cdot \left[1 - (qtL_m)^2\right]}$$

$$rLtp_m := \frac{Nkt_m \cdot qtL_m - NL \cdot qLt_m}{Nkt_m \cdot qtL_m + NL \cdot qLt_m}$$

$$rLts_m := \frac{NL \cdot qtL_m - Nkt_m \cdot qLt_m}{NL \cdot qtL_m + Nkt_m \cdot qLt_m}$$

$$ZLtp_m := Nkt_m \cdot qtL_m + NL \cdot qLt_m$$

$$ZLts_m := NL \cdot qtL_m + Nkt_m \cdot qLt_m$$

$$tLtp_m := \frac{2 \cdot NL \cdot qtL_m}{ZLtp_m} \quad tLts_m := \frac{CLt_m}{ZLts_m}$$

$$CLt_m := 2 \cdot NL \cdot qtL_m$$

$$ILtp(m) := \begin{pmatrix} 1 & rLtp_m \\ rLtp_m & 1 \end{pmatrix} \cdot \begin{pmatrix} 1 \\ tLtp_m \end{pmatrix} \qquad ILts(m) := \begin{pmatrix} 1 & rLts_m \\ rLts_m & 1 \end{pmatrix} \cdot \begin{pmatrix} 1 \\ tLts_m \end{pmatrix}$$

$$qtLast_m := \sqrt{1 - \frac{(Nkt_m)^2}{(Ns)^2} \cdot \left[1 - (qHt_m)^2\right]}$$

$$rtLastp_m := \frac{Ns \cdot qHt_m - Nkt_m \cdot qtLast_m}{Ns \cdot qHt_m + Nkt_m \cdot qtLast_m}$$

$$rtLasts_m := \frac{Nkt_m \cdot qHt_m - Ns \cdot qtLast_m}{Nkt_m \cdot qHt_m + Ns \cdot qtLast_m}$$

$$ZtLastp_m := Ns \cdot qHt_m + Nkt_m \cdot qtLast_m$$

$$ZtLasts_m := Nkt_m \cdot qHt_m + Ns \cdot qtLast_m$$

$$ttLastp_m := \frac{2 \cdot Nkt_m \cdot qHt_m}{ZtLastp_m}$$

$$CtLast_m := 2 \cdot NL \cdot qLt_m$$

$$ttLasts_m := \frac{CtL_m}{ZtLs_m}$$

$$ItLastp(m) := \begin{pmatrix} 1 & rtLastp_m \\ rtLastp_m & 1 \end{pmatrix} \cdot \begin{pmatrix} 1 \\ ttLastp_m \end{pmatrix}$$

$$ItLasts(m) := \begin{pmatrix} 1 & rtLasts_m \\ rtLasts_m & 1 \end{pmatrix} \cdot \begin{pmatrix} 1 \\ ttLasts_m \end{pmatrix}$$

$$sp(n,m) := (IHtp(m) \cdot Mt(m) \cdot ItLp(m) \cdot ML(n,m) \cdot ILtp(m) \cdot Mt(m) \cdot ItHp(m) \cdot MH(n,m))^{I}$$

$$ss(n,m) := (IHts(m) \cdot Mt(m) \cdot ItLs(m) \cdot ML(n,m) \cdot ILts(m) \cdot Mt(m) \cdot ItHs(m) \cdot MH(n,m))^{pe}$$

$$Sp(n,m) := I0tp(m) \cdot Mt(m) \cdot ItHp(m) \cdot MH(n,m) \cdot sp(n,m) \cdot IHtp(m) \cdot Mt(m) \cdot ItLastp(m)$$

$$Ss(n,m) := I0ts(m) \cdot Mt(m) \cdot ItHs(m) \cdot MH(n,m) \cdot ss(n,m) \cdot IHts(m) \cdot Mt(m) \cdot ItLasts(m)$$

$$rs(n,m) := \left| \left[\frac{(Ss(n,m))_{1,0}}{(Ss(n,m))_{0,0}} \right]^2 \right| \qquad rp(n,m) := \left| \left[\frac{(Sp(n,m))_{1,0}}{(Sp(n,m))_{0,0}} \right]^2 \right|$$

$$tp(n,m) := \frac{Ns}{No} \cdot \left| \left[\frac{1}{(Sp(n,m))_{0,0}} \right] \right|^2 \qquad ts(n,m) := \frac{Ns}{No} \cdot \left| \left[\frac{1}{(Ss(n,m))_{0,0}} \right] \right|^2$$

cutoff level - Tpbg

$$M^{\langle 0 \rangle} := \lambda \qquad M^{\langle 1 \rangle} := \gamma \qquad M^{\langle 2 \rangle} := tp$$

$Tpbg := 0.99$

$tpl_{n,m} := tp(n,m)$

$tsl_{n,m} := ts(n,m)$

$qpl(n,m) := if(tpl_{n,m} > Tpbg, tpl_{n,m}, 0)$

$qpl_{n,m} := qpl(n,m)$

$qsl(n,m) := if(tsl_{n,m} > Tpbg, tsl_{n,m}, 0)$

$qsl_{n,m} := qsl(n,m)$ $\quad wpl(n,m) := if(qpl_{n,m} > Tpbg, \lambda_m, 0.000000001)$

$wpl_{n,m} := wpl(n,m)$

$$dqpl(n,m) := \begin{cases} tpl_{n,m} & \text{if } tpl_{n,m-2} \geq Tpbg \wedge tpl_{n,m-1} \geq Tpbg \wedge tpl_{n,m} \geq Tpbg \\ 0 & \text{otherwise} \end{cases}$$

$dqpl_{n,m} := dqpl(n,m)$

BEFORE CUTOFF PROCESS:

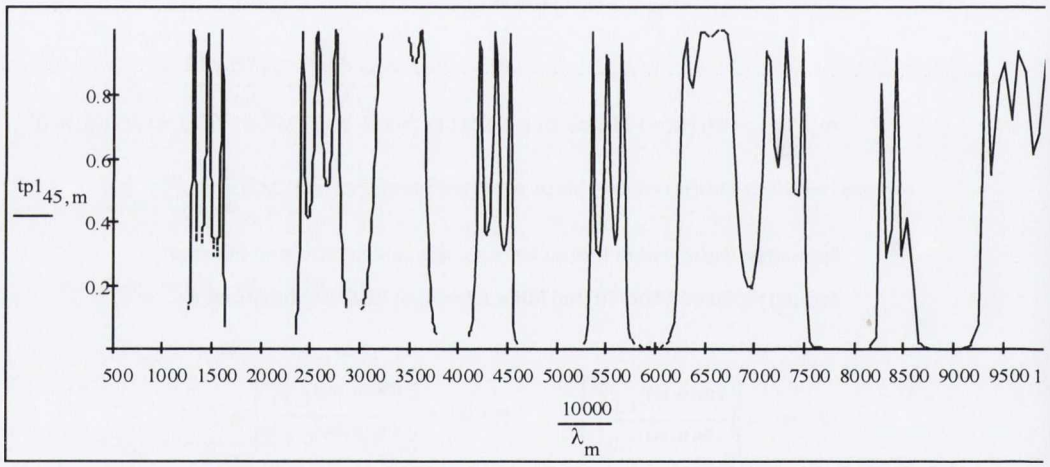

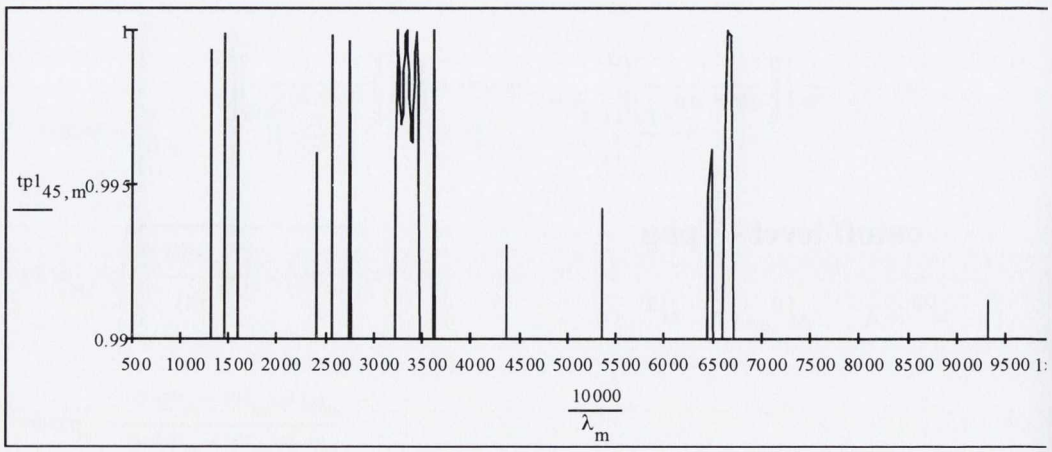

After CUTOFF Process:

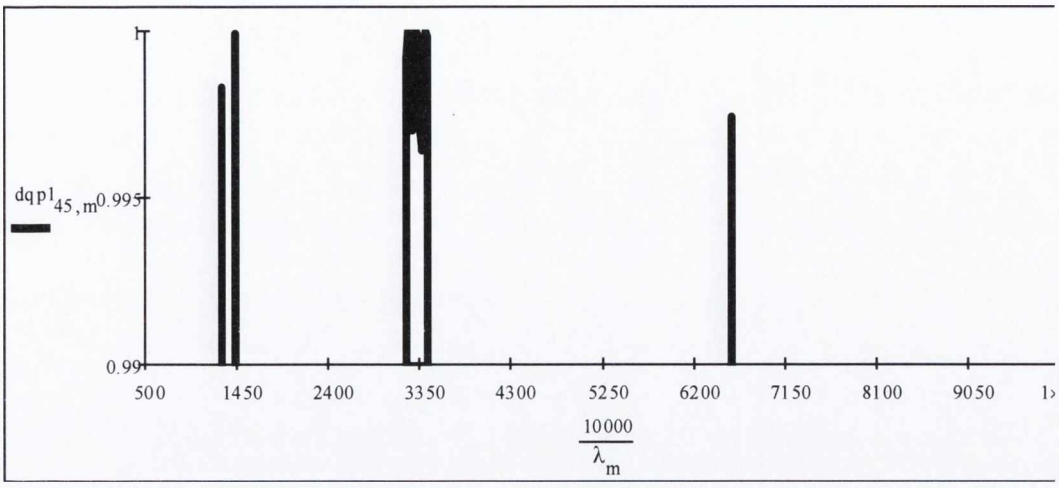

FILLING FRACTION,

as a function of DH and Wavelength

$$DAf(n,m) := \frac{dqpl_{n,m} \cdot DA(n)}{tpl_{n,m}}$$

DAf(n,m) =

0
0
0
0
0
0
0
0
0
0
0
0
0
0
...

WAVENUMBER, CM^{-1}

$\frac{10000}{wpl_{n,m}}$ =

$1.1 \cdot 10^4$
$1 \cdot 10^{13}$
$1 \cdot 10^{13}$
$1 \cdot 10^{13}$
$1 \cdot 10^{13}$
$1 \cdot 10^{13}$
$1 \cdot 10^{13}$
$1 \cdot 10^{13}$
$1 \cdot 10^{13}$
$1 \cdot 10^{13}$
$1 \cdot 10^{13}$
$1 \cdot 10^{13}$
$1 \cdot 10^{13}$
$1.1 \cdot 10^4$
$1 \cdot 10^{13}$
...

NORMALIZED

FREQUENCY

$\frac{A}{wpl_{n,m}}$ =

4.4
$4 \cdot 10^9$
$4 \cdot 10^9$
$4 \cdot 10^9$
$4 \cdot 10^9$
$4 \cdot 10^9$
$4 \cdot 10^9$
$4 \cdot 10^9$
$4 \cdot 10^9$
$4 \cdot 10^9$
$4 \cdot 10^9$
$4 \cdot 10^9$
$4 \cdot 10^9$
4.4
$4 \cdot 10^9$
...

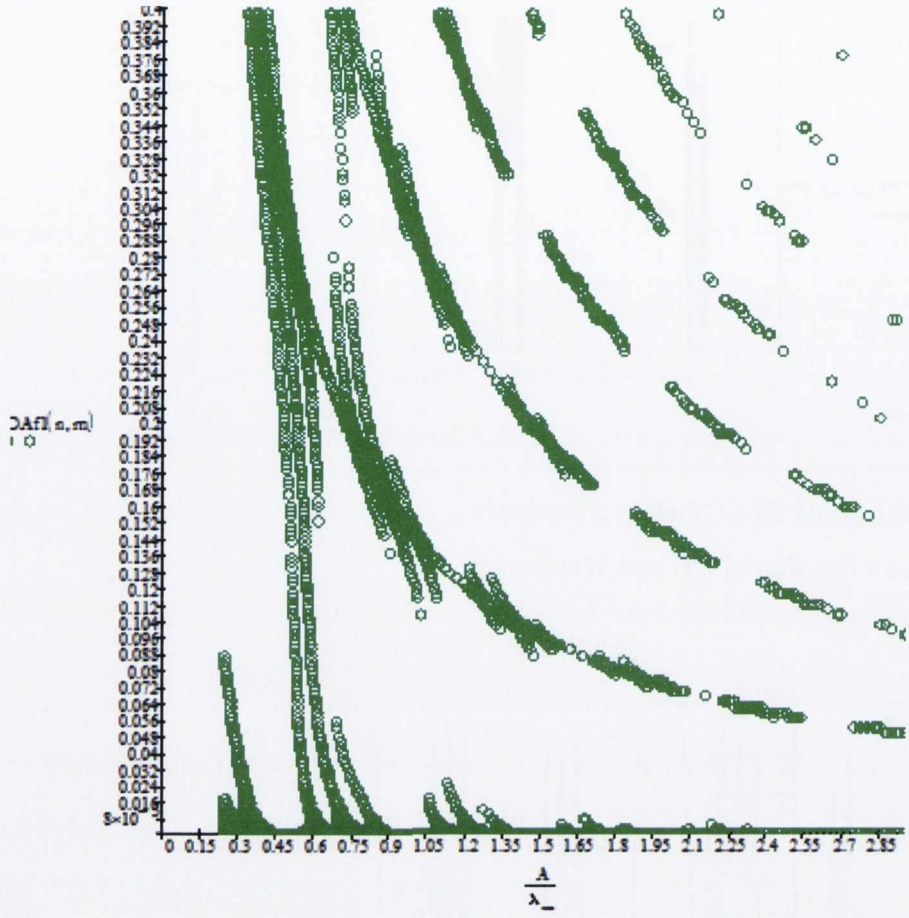
0.4
0.392
0.384
0.376
0.368
0.36
0.352
0.344
0.336
0.328
0.32
0.312
0.304
0.296
0.288
0.28
0.272
0.264
0.256
0.248
0.24
0.232
0.224
0.216
0.208
0.2
0.192
0.184
0.176
0.168
0.16
0.152
0.144
0.136
0.128
0.12
0.112
0.104
0.096
0.088
0.08
0.072
0.064
0.056
0.048
0.04
0.032
0.024
0.016
8×10⁻³
0 0.15 0.3 0.45 0.6 0.75 0.9 1.05 1.2 1.35 1.5 1.65 1.8 1.95 2.1 2.25 2.4 2.55 2.7 2.85
A
λ

Appendix II

A MathCad program code for simulation of the reflection spectra and gap maps of 1D photonic crystal with triple-cavity.

$i := \sqrt{-1}$

$\phi := 0$

$d\lambda := 0.0001$

$m := 1 .. 6000$

$\lambda 0 := 1.2$

$\lambda_m := \lambda 0 + d\lambda \cdot (m - 1)$ $\quad \nu_m := \frac{10000}{\lambda_m}$

$A1 := 0.8$

$per1 := 2$

$per2 := 2$

$No := 1.0$

$Ns := 1$

$NH := 3.42$

$NL := 1$

$maxn := 10$

$n := 1 .. maxn$

$dDH := 0.001$

$DH0 := 0.368$

$DH1(n) := DH0 + dDH \cdot (n - 1)$

$DL1(n) := A1 - DH1(n)$

$DA1(n) := \frac{DH1(n)}{A1}$

$Ddef(n) := DL1(n)$

Defect refractive index

$k := 1..100$

$Ndef1(k) := 1.54 + (k - 1)0.00$

$Ndef3(k) := 1.54 - (k - 1)0.002$

$Ndef2(k) := 1.54 - (k - 1)\cdot 0.00$

2x2matrix method:

$rad := \frac{\pi}{180}$

$\phi r := \phi \cdot rad$

$q0 := \cos(\phi r)$

$$q0H := \sqrt{1 - \frac{(No)^2}{(NH)^2}\cdot\left(1 - q0^2\right)}$$

$$r01p := \frac{NH\cdot q0 - No\cdot q0H}{NH\cdot q0 + No\cdot q0H} \qquad r01s := \frac{No\cdot q0 - NH\cdot q0H}{No\cdot q0 + NH\cdot q0H}$$

$$t01p := 2\cdot No\cdot\frac{q0}{NH\cdot q0 + No\cdot q0H} \qquad t01s := 2\cdot No\cdot\frac{q0}{No\cdot q0 + NH\cdot q0H}$$

$$I01s := \begin{pmatrix} 1 & r01s \\ r01s & 1 \end{pmatrix}\cdot\begin{pmatrix} \frac{1}{t01s} \end{pmatrix}$$

$$I01p := \begin{pmatrix} 1 & r01p \\ r01p & 1 \end{pmatrix}\cdot\begin{pmatrix} \frac{1}{t01p} \end{pmatrix}$$

$$\beta H1(n,m) := 2\cdot\frac{\pi}{\lambda_m}\cdot DH1(n)\cdot q0H\cdot NH\cdot i$$

$$LH1(n,m) := \begin{pmatrix} e^{\beta H1(n,m)} & 0 \\ 0 & e^{-\beta H1(n,m)} \end{pmatrix}$$

$$qHL := \sqrt{1-\frac{(NH)^2}{(NL)^2}\cdot\left[1-(q0H)^2\right]}$$

$$rHLp := \frac{NL\cdot q0H - NH\cdot qHL}{NL\cdot q0H + NH\cdot qHL} \qquad rHLs := \frac{NH\cdot q0H - NL\cdot qHL}{NH\cdot q0H + NL\cdot qHL}$$

$$tHLp := 2\cdot NH\cdot\frac{q0H}{NL\cdot q0H + NH\cdot qHL} \qquad tHLs := 2\cdot NH\cdot\frac{q0H}{NH\cdot q0H + NL\cdot qHL}$$

$$IHLp := \begin{pmatrix} 1 & rHLp \\ rHLp & 1 \end{pmatrix}\cdot\begin{pmatrix} 1 \\ tHLp \end{pmatrix} \qquad IHLs := \begin{pmatrix} 1 & rHLs \\ rHLs & 1 \end{pmatrix}\cdot\begin{pmatrix} 1 \\ tHLs \end{pmatrix}$$

$$\beta L1(n,m) := 2\cdot\frac{\pi}{\lambda_m}\cdot DL1(n)\cdot qHL\cdot NL\cdot i$$

$$LL1(n,m) := \begin{pmatrix} e^{\beta L1(n,m)} & 0 \\ 0 & e^{-\beta L1(n,m)} \end{pmatrix}$$

$$qLH := \sqrt{1-\frac{(NL)^2}{(NH)^2}\cdot\left[1-(qHL)^2\right]}$$

$$rLHp := \frac{NH\cdot qHL - NL\cdot qLH}{NH\cdot qHL + NL\cdot qLH} \qquad rLHs := \frac{NL\cdot qHL - NH\cdot qLH}{NL\cdot qHL + NH\cdot qLH}$$

$$tLHp := 2\cdot NL\cdot\frac{qHL}{NL\cdot qHL + NH\cdot qLH} \qquad tLHs := 2\cdot NL\cdot\frac{qHL}{NL\cdot qHL + NH\cdot qLH}$$

$$ILHp := \begin{pmatrix} 1 & rLHp \\ rLHp & 1 \end{pmatrix}\cdot\begin{pmatrix} 1 \\ tLHp \end{pmatrix} \qquad ILHs := \begin{pmatrix} 1 & rLHs \\ rLHs & 1 \end{pmatrix}\cdot\begin{pmatrix} 1 \\ tLHs \end{pmatrix}$$

$$\beta H(n,m) := 2\cdot\frac{\pi}{\lambda_m}\cdot DH1(n)\cdot qLH\cdot NH\cdot i \qquad LH(n,m) := \begin{pmatrix} e^{\beta H(n,m)} & 0 \\ 0 & e^{-\beta H(n,m)} \end{pmatrix}$$

$$qdoDefl(k) := \sqrt{1 - \frac{(NH)^2}{(Ndefl(k))^2} \cdot \left[1 - (qLH)^2\right]}$$

$$rHdoDefsl(k) := \frac{NH \cdot qLH - Ndefl(k) \cdot qdoDefl(k)}{NH \cdot qLH + Ndefl(k) \cdot qdoDefl(k)}$$

$$rHdoDefpl(k) := \frac{Ndefl(k) \cdot qLH - NH \cdot qdoDefl(k)}{Ndefl(k) \cdot qLH + NH \cdot qdoDefl(k)}$$

$$tHdoDefsl(k) := 2 \cdot NH \cdot \frac{qLH}{NH \cdot qLH + Ndefl(k) \cdot qdoDefl(k)}$$

$$tHdoDefpl(k) := 2 \cdot NH \cdot \frac{qLH}{Ndefl(k) \cdot qLH + NH \cdot qdoDefl(k)}$$

$$IHdoDefpl(k) := \begin{pmatrix} 1 & rHdoDefpl(k) \\ rHdoDefpl(k) & 1 \end{pmatrix} \cdot \begin{pmatrix} \frac{1}{tHdoDefpl(k)} \end{pmatrix}$$

$$\beta defl(n, m, k) := 2 \cdot \frac{\pi}{\lambda_m} \cdot Ddef(n) \cdot qdoDefl(k) \cdot Ndefl(k) \cdot i$$

$$IHdoDefsl(k) := \begin{pmatrix} 1 & rHdoDefsl(k) \\ rHdoDefsl(k) & 1 \end{pmatrix} \cdot \begin{pmatrix} \frac{1}{tHdoDefsl(k)} \end{pmatrix}$$

$$Ldefl(n, m, k) := \begin{pmatrix} e^{\beta defl(n, m, k)} & 0 \\ 0 & e^{-\beta defl(n, m, k)} \end{pmatrix}$$

$$qposleDefl(k) := \sqrt{1 - \frac{(Ndefl(k))^2}{(NH)^2} \cdot \left[1 - (qdoDefl(k))^2\right]}$$

$$rDefHpl(k) := \frac{NH \cdot qdoDefl(k) - Ndefl(k) \cdot qposleDefl(k)}{NH \cdot qdoDefl(k) + Ndefl(k) \cdot qposleDefl(k)}$$

$$tDefHp1(k) := 2 \cdot Ndef1(k) \cdot \frac{qdoDef1(k)}{Ndef1(k) \cdot qdoDef1(k) + NH \cdot qposleDef1(k)}$$

$$IDefHp1(k) := \begin{pmatrix} 1 & rDefHp1(k) \\ rDefHp1(k) & 1 \end{pmatrix} \cdot \begin{pmatrix} 1 \\ \hline tDefHp1(k) \end{pmatrix}$$

$$rDefHs1(k) := \frac{Ndef1(k) \cdot qdoDef1(k) - NH \cdot qposleDef1(k)}{Ndef1(k) \cdot qdoDef1(k) + NH \cdot qposleDef1(k)}$$

$$tDefHs1(k) := 2 \cdot Ndef1(k) \cdot \frac{qdoDef1(k)}{Ndef1(k) \cdot qdoDef1(k) + NH \cdot qposleDef1(k)}$$

$$IDefHs1(k) := \begin{pmatrix} 1 & rDefHs1(k) \\ rDefHs1(k) & 1 \end{pmatrix} \cdot \begin{pmatrix} 1 \\ \hline tDefHs1(k) \end{pmatrix}$$

$$qdoDef2(k) := \sqrt{1 - \frac{(NH)^2}{(Ndef2(k))^2} \cdot \left[1 - (qLH)^2\right]}$$

$$rHdoDefp2(k) := \frac{Ndef2(k) \cdot qLH - NH \cdot qdoDef2(k)}{Ndef2(k) \cdot qLH + NH \cdot qdoDef2(k)}$$

$$rHdoDefs2(k) := \frac{NH \cdot qLH - Ndef2(k) \cdot qdoDef2(k)}{NH \cdot qLH + Ndef2(k) \cdot qdoDef2(k)}$$

$$tHdoDefs2(k) := 2 \cdot NH \cdot \frac{qLH}{NH \cdot qLH + Ndef2(k) \cdot qdoDef2(k)}$$

$$tHdoDefp2(k) := 2 \cdot NH \cdot \frac{qLH}{Ndef2(k) \cdot qLH + NH \cdot qdoDef2(k)}$$

$$IHdoDefp2(k) := \begin{pmatrix} 1 & rHdoDefp2(k) \\ rHdoDefp2(k) & 1 \end{pmatrix} \cdot \begin{pmatrix} 1 \\ \hline tHdoDefp2(k) \end{pmatrix}$$

$$IHdoDefs2(k) := \begin{pmatrix} 1 & rHdoDefs2(k) \\ rHdoDefs2(k) & 1 \end{pmatrix} \cdot \begin{pmatrix} 1 \\ \hline tHdoDefs2(k) \end{pmatrix}$$

$$\beta def2(n,m,k) := 2\cdot\frac{\pi}{\lambda_m}\cdot Ddef(n)\cdot qdoDef2(k)\cdot Ndef2(k)\cdot i$$

$$Ldef2(n,m,k) := \begin{pmatrix} e^{\beta def2(n,m,k)} & 0 \\ 0 & e^{-\beta def2(n,m,k)} \end{pmatrix}$$

$$qposleDef2(k) := \sqrt{1 - \frac{(Ndef2(k))^2}{(NH)^2}\cdot\left[1 - (qdoDef2(k))^2\right]}$$

$$rDefHp2(k) := \frac{NH\cdot qdoDef2(k) - Ndef2(k)\cdot qposleDef2(k)}{NH\cdot qdoDef2(k) + Ndef2(k)\cdot qposleDef2(k)}$$

$$rDefHs2(k) := \frac{Ndef2(k)\cdot qdoDef2(k) - NH\cdot qposleDef2(k)}{Ndef2(k)\cdot qdoDef2(k) + NH\cdot qposleDef2(k)}$$

$$tDefHp2(k) := 2\cdot Ndef2(k)\cdot\frac{qdoDef2(k)}{Ndef2(k)\cdot qdoDef2(k) + NH\cdot qposleDef2(k)}$$

$$IDefHp2(k) := \begin{pmatrix} 1 & rDefHp2(k) \\ rDefHp2(k) & 1 \end{pmatrix}\cdot\begin{pmatrix} \frac{1}{tDefHp2(k)} \end{pmatrix}$$

$$tDefHs2(k) := 2\cdot Ndef2(k)\cdot\frac{qdoDef2(k)}{Ndef2(k)\cdot qdoDef2(k) + NH\cdot qposleDef2(k)}$$

$$IDefHs2(k) := \begin{pmatrix} 1 & rDefHs2(k) \\ rDefHs2(k) & 1 \end{pmatrix}\cdot\begin{pmatrix} \frac{1}{tDefHs2(k)} \end{pmatrix}$$

$$qdoDef3(k) := \sqrt{1 - \frac{(NH)^2}{(Ndef3(k))^2}\cdot\left[1 - (qLH)^2\right]}$$

$$rHdoDefs3(k) := \frac{NH\cdot qLH - Ndef3(k)\cdot qdoDef3(k)}{NH\cdot qLH + Ndef3(k)\cdot qdoDef3(k)}$$

$$rHdoDefp3(k) := \frac{Ndef3(k)\cdot qLH - NH\cdot qdoDef3(k)}{Ndef3(k)\cdot qLH + NH\cdot qdoDef3(k)}$$

$$tHdoDefs3(k) := 2\cdot NH\cdot\frac{qLH}{NH\cdot qLH + Ndef3(k)\cdot qdoDef3(k)}$$

$$\beta def3(n,m,k) := 2\cdot\frac{\pi}{\lambda_m}\cdot Ddef(n)\cdot qdoDef3(k)\cdot Ndef3(k)\cdot i$$

$$IHdoDefs3(k) := \begin{pmatrix} 1 & rHdoDefs3(k) \\ rHdoDefs3(k) & 1 \end{pmatrix}\cdot\begin{pmatrix} 1 \\ \overline{tHdoDefs3(k)} \end{pmatrix}$$

$$tHdoDefp3(k) := 2\cdot NH\cdot\frac{qLH}{Ndef3(k)\cdot qLH + NH\cdot qdoDef3(k)}$$

$$IHdoDefp3(k) := \begin{pmatrix} 1 & rHdoDefp3(k) \\ rHdoDefp3(k) & 1 \end{pmatrix}\cdot\begin{pmatrix} 1 \\ \overline{tHdoDefp3(k)} \end{pmatrix}$$

$$Ldef3(n,m,k) := \begin{pmatrix} e^{\beta def3(n,m,k)} & 0 \\ 0 & e^{-\beta def3(n,m,k)} \end{pmatrix}$$

$$qposleDef3(k) := \sqrt{1 - \frac{(Ndef3(k))^2}{(NH)^2}\cdot\left[1 - (qdoDef3(k))^2\right]}$$

$$rDefHp3(k) := \frac{NH\cdot qdoDef3(k) - Ndef3(k)\cdot qposleDef3(k)}{NH\cdot qdoDef3(k) + Ndef3(k)\cdot qposleDef3(k)}$$

$$rDefHs3(k) := \frac{Ndef3(k)\cdot qdoDef3(k) - NH\cdot qposleDef3(k)}{Ndef3(k)\cdot qdoDef3(k) + NH\cdot qposleDef3(k)}$$

$$tDefHp3(k) := 2\cdot Ndef3(k)\cdot\frac{qdoDef3(k)}{Ndef3(k)\cdot qdoDef3(k) + NH\cdot qposleDef3(k)}$$

$$IDefHp3(k) := \begin{pmatrix} 1 & rDefHp3(k) \\ rDefHp3(k) & 1 \end{pmatrix}\cdot\begin{pmatrix} 1 \\ \overline{tDefHp3(k)} \end{pmatrix}$$

$$tDefHs3(k) := 2 \cdot Ndef3(k) \cdot \frac{qdoDef3(k)}{Ndef3(k) \cdot qdoDef3(k) + NH \cdot qposleDef3(k)}$$

$$IDefHs3(k) := \begin{pmatrix} 1 & rDefHs3(k) \\ rDefHs3(k) & 1 \end{pmatrix} \cdot \begin{pmatrix} 1 \\ \overline{tDefHs3(k)} \end{pmatrix}$$

$$qLast := \sqrt{1 - \frac{(NH)^2}{(Ns)^2} \cdot \left[1 - (qLH)^2\right]}$$

$$rLasts := \frac{NH \cdot qLH - Ns \cdot qLast}{NH \cdot qLH + Ns \cdot qLast} \qquad rLastp := \frac{Ns \cdot qLH - NH \cdot qLast}{Ns \cdot qLH + NH \cdot qLast}$$

$$tLasts := 2 \cdot NH \cdot \frac{qLH}{NH \cdot qLH + Ns \cdot qLast}$$

$$tLastp := 2 \cdot NH \cdot \frac{qLH}{Ns \cdot qLH + NH \cdot qLast}$$

$$ILastp := \begin{pmatrix} 1 & rLastp \\ rLastp & 1 \end{pmatrix} \cdot \begin{pmatrix} 1 \\ \overline{tLastp} \end{pmatrix}$$

$$ILasts := \begin{pmatrix} 1 & rLasts \\ rLasts & 1 \end{pmatrix} \cdot \begin{pmatrix} 1 \\ \overline{tLasts} \end{pmatrix}$$

$$Inp(n,m,k) := I01p \cdot LH1(n,m) \cdot (IHLp \cdot LL1(n,m) \cdot ILHp \cdot LH(n,m))^1$$

$$Ins(n,m,k) := I01s \cdot LH1(n,m) \cdot (IHLs \cdot LL1(n,m) \cdot ILHs \cdot LH(n,m))^1$$

$$def1p(n,m,k) := (IHdoDefp1(k) \cdot Ldef1(n,m,k) \cdot IDefHp1(k) \cdot LH(n,m))^1$$

$$Def1p(n,m,k) := def1p(n,m,k) \cdot (IHLp \cdot LL1(n,m) \cdot ILHp \cdot LH(n,m))^1$$

$$def1s(n,m,k) := (IHdoDefs1(k)\cdot Ldef1(n,m,k)\cdot IDefHs1(k)\cdot LH(n,m))^{1}$$

$$Def1s(n,m,k) := def1s(n,m,k)\cdot(IHLp\cdot LL1(n,m)\cdot ILHp\cdot LH(n,m))^{1}$$

$$def2p(n,m,k) := (IHdoDefp2(k)\cdot Ldef2(n,m,k)\cdot IDefHp2(k)\cdot LH(n,m))^{1}$$

$$def2s(n,m,k) := (IHdoDefs2(k)\cdot Ldef2(n,m,k)\cdot IDefHs2(k)\cdot LH(n,m))^{1}$$

$$Def2p(n,m,k) := def2p(n,m,k)\cdot(IHLp\cdot LL1(n,m)\cdot ILHp\cdot LH(n,m))^{1}$$

$$Def2s(n,m,k) := def2s(n,m,k)\cdot(IHLp\cdot LL1(n,m)\cdot ILHp\cdot LH(n,m))^{1}$$

$$def3p(n,m,k) := (IHdoDefp3(k)\cdot Ldef3(n,m,k)\cdot IDefHp3(k)\cdot LH(n,m))^{1}$$

$$def3s(n,m,k) := (IHdoDefs3(k)\cdot Ldef3(n,m,k)\cdot IDefHs3(k)\cdot LH(n,m))^{1}$$

$$Def3p(n,m,k) := def3p(n,m,k)\cdot(IHLp\cdot LL1(n,m)\cdot ILHp\cdot LH(n,m))^{1}$$

$$Def3s(n,m,k) := def3s(n,m,k)\cdot(IHLp\cdot LL1(n,m)\cdot ILHp\cdot LH(n,m))^{1}$$

$$sp(n,m,k) := Inp(n,m,k)\cdot Def1p(n,m,k)\cdot Def2p(n,m,k)\cdot Def3p(n,m,k)\cdot ILastp$$

$$ss(n,m,k) := Ins(n,m,k)\cdot Def1s(n,m,k)\cdot Def2s(n,m,k)\cdot Def3s(n,m,k)\cdot ILasts$$

$$rp(n,m,k) := \left\lfloor \frac{(sp(n,m,k))_{1,0}}{(sp(n,m,k))_{0,0}} \right\rfloor \qquad tp(n,m,k) := \frac{Ns}{No}\cdot\left[\left[\left[\frac{1}{(sp(n,m,k))_{0,0}}\right]\right]\right]^{2}$$

$$rs(n,m,k) := \left\lfloor \frac{(ss(n,m,k))_{1,0}}{(ss(n,m,k))_{0,0}} \right\rfloor \qquad \gamma_m := \frac{10000}{\lambda_m}$$

$$ts(n,m,k) := \frac{Ns}{No}\cdot\left[\left[\left[\frac{1}{(ss(n,m,k))_{0,0}}\right]\right]\right] \qquad NF_m := \frac{A1}{\lambda_m}$$

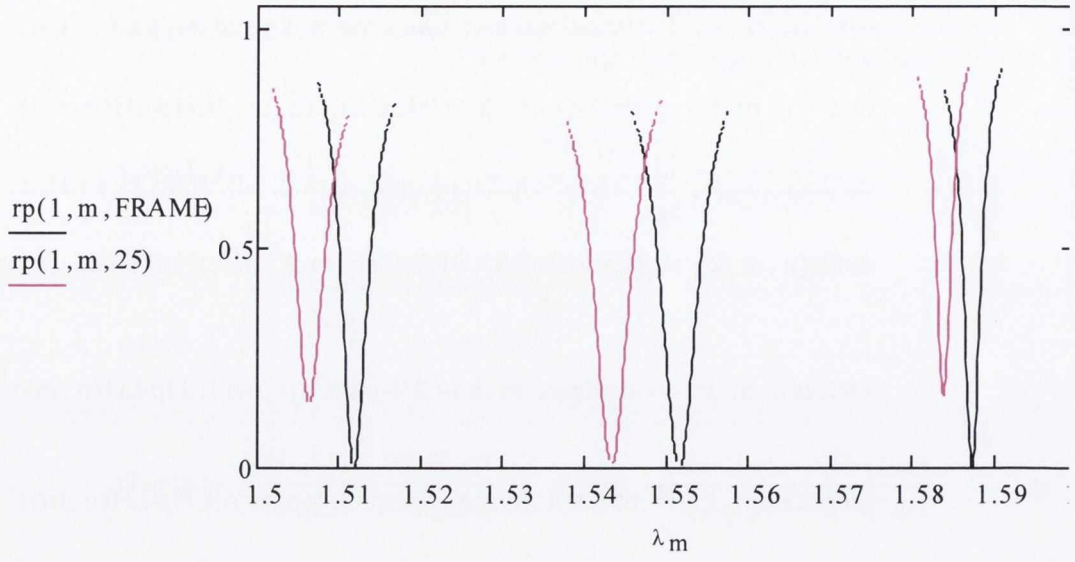

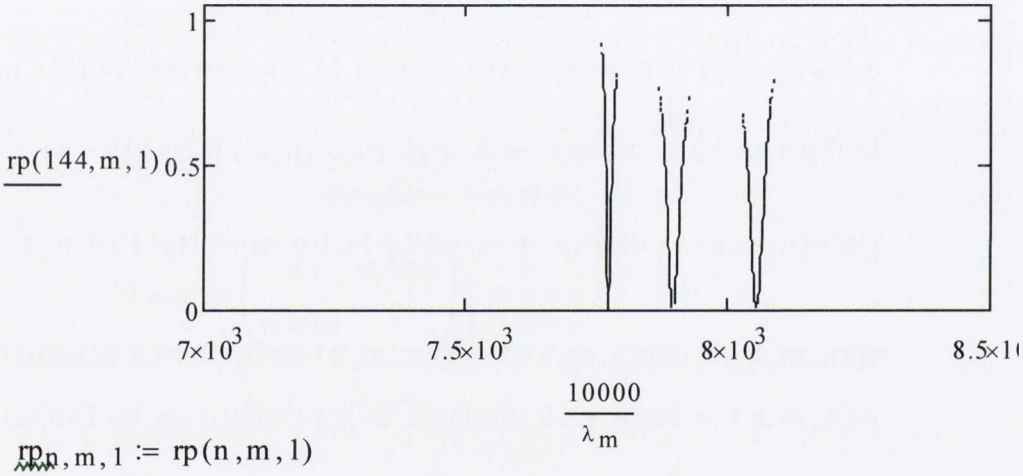

$rp_{n,m,1} := rp(n,m,1)$

$rp =$

	0	1	2	3	4	5	6	7	8	9
0	0	0	0	0	0	0	0	0	0	0
1	0	929335	929022	928706	928386	928062	927735	927404	927069	992673
2	0	941936	941711	941483	941253	941019	940783	940545	940303	940059
3	0	951814	951653	995149	951324	951157	950987	950816	950642	950466
4	0	959631	959517	959401	959283	959164	959043	958921	958797	958672
5	0	965872	965793	965712	965629	965546	965461	965376	965288	.99652
6	0	970898	970844	970789	970733	970676	970618	997056	.99705	970439
7	0	974976	974941	974906	997487	974833	974795	974757	974718	974678
8	0	997831	997829	997827	978248	978227	978204	978181	978157	978133
9	0	981055	981046	981037	981027	981016	981006	980994	980982	980969
10	0	983329	983329	983328	983327	983325	983323	998332	983317	...

Appendix III

A MathCad program code for simulation of the reflection spectra and gap maps of 1D photonic crystal with structural deviations.

$\lambda 0 := 1$

$m := 1 .. 2000$ $d\lambda := 0.01$ $i := \sqrt{-1}$

$Ns := 1$

$No := 1$ $period := 8$

$\lambda_m := \lambda 0 + d\lambda \cdot (m - 1)$

$NH := 3.42$

$NL := 1$ $LatCon := 3$

$Ndef := 1$

$maxn := 100$ $n := 1 .. maxn$

$$dDH := \frac{LatCon}{maxn}$$

$DH0 := 0$

$DH(n) := DH0 + dDH \cdot (n - 1)$

$DL1(n) := LatCon - DH(n)$

$$DA(n) := \frac{DH(n)}{LatCon}$$

$s1 := 8$

$\mu 1 := 0.1$

$\sigma 1 := 0.1$

$bin := 50$

$N := rnorm(s1, \mu 1, \sigma 1)$

upper := ceil(max(N))

lower := floor(min(N))

$j := 0..bin$

$$h := \frac{upper - lower}{bin}$$

$int_j := lower + h \cdot j$

$int := int + 0.5 \cdot h$

$f := hist(int, N)$

$F(x) := s \cdot h \cdot dnorm(x, \mu 1, \sigma 1)$

Normal fitting function:

$h := 0..8 - 1$

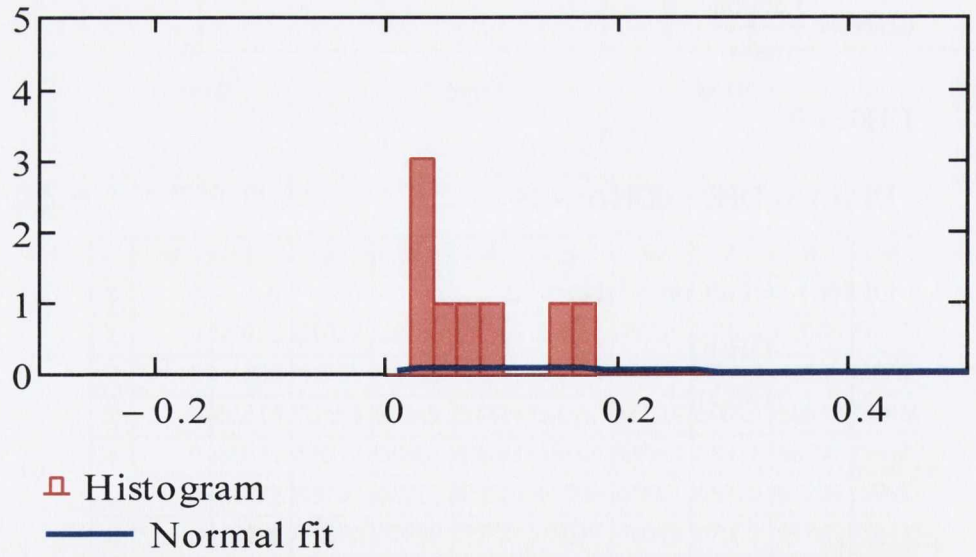

$s := 8$

$\mu := 0$

$dDH := rnorm(s, \mu, \sigma H)$

$\sigma H := 0.05$

$$DisOrd := \frac{\sigma H}{LatCon}$$

$DisOrd \cdot 100 = 1.667$

$ddH_{h,n} := DH(n) \cdot dDH_h$

h=

0
1
2
3
4
5
6
7

$DH1(n) := DH(n) + ddH_{0,n}$

$DH2(n) := DH(n) + ddH_{1,n}$

$DH3(n) := DH(n) + ddH_{2,n}$

$DH4(n) := DH(n) + ddH_{3,n}$

$DH5(n) := DH(n) + ddH_{4,n}$

$DH6(n) := DH(n) + ddH_{5,n}$

$DH7(n) := DH(n) + ddH_{6,n}$

$DH8(n) := DH(n) + ddH_{7,n}$

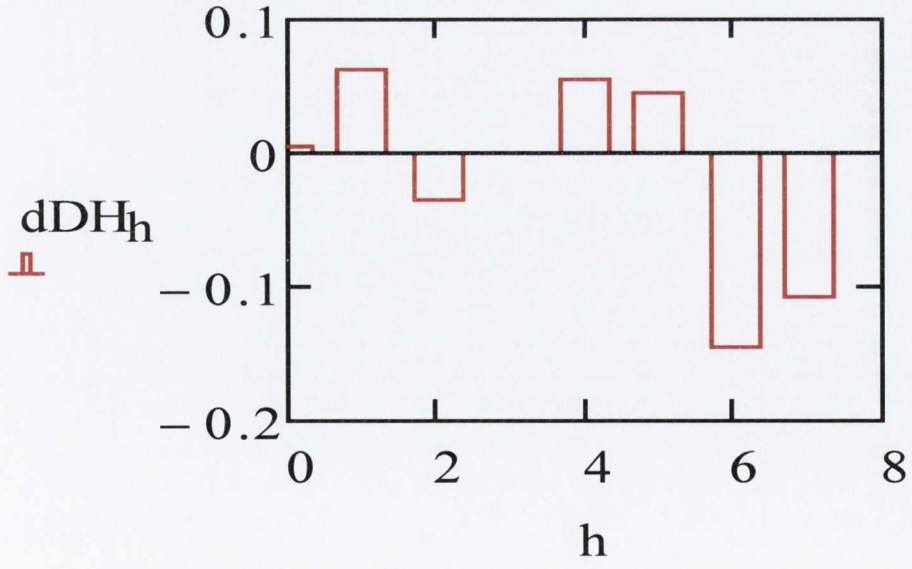

$$DL12(n) := LatCon - \frac{DH1(n) + DH2(n)}{2}$$

$$DL34(n) := LatCon - \frac{DH3(n) + DH4(n)}{2}$$

$$DL56(n) := LatCon - \frac{DH5(n) + DH6(n)}{2}$$

$$DL78(n) := LatCon - \frac{DH7(n) + DH8(n)}{2}$$

$$DL23(n) := LatCon - \frac{DH2(n) + DH3(n)}{2}$$

$$DL45(n) := LatCon - \frac{DH4(n) + DH5(n)}{2}$$

$$DL67(n) := LatCon - \frac{DH6(n) + DH7(n)}{2}$$

$$I01 := \begin{pmatrix} 1 & r01 \\ r01 & 1 \end{pmatrix} \cdot \begin{pmatrix} \frac{1}{t01} \end{pmatrix}$$

$$r01 := \frac{NH - No}{NH + No} \qquad t01 := 2 \cdot No \cdot \frac{1}{NH + No}$$

$$\beta H1(n,m) := 2 \cdot \frac{\pi}{\lambda_m} \cdot DH1(n) \cdot NH \cdot i$$

$$LH1(n,m) := \begin{pmatrix} e^{\beta H1(n,m)} & 0 \\ 0 & e^{-\beta H1(n,m)} \end{pmatrix}$$

$$tHL := 2 \cdot NH \cdot \frac{1}{NL + NH} \qquad IHL := \begin{pmatrix} 1 & rHL \\ rHL & 1 \end{pmatrix} \cdot \begin{pmatrix} \frac{1}{tHL} \end{pmatrix}$$

$$\beta L12(n,m) := 2 \cdot \frac{\pi}{\lambda_m} \cdot DL12(n) \cdot NL \cdot i$$

$$L12(n,m) := \begin{pmatrix} e^{\beta L12(n,m)} & 0 \\ 0 & e^{-\beta L12(n,m)} \end{pmatrix}$$

$$rLH := \frac{(NH - NL)}{(NH + NL)}$$

$$tLH := 2 \cdot NL \cdot \frac{1}{NH + NL}$$

$$ILH := \begin{pmatrix} 1 & rLH \\ rLH & 1 \end{pmatrix} \cdot \begin{pmatrix} \frac{1}{tLH} \end{pmatrix}$$

$$\beta H2(n,m) := 2 \cdot \frac{\pi}{\lambda_m} \cdot DH2(n) \cdot NH \cdot i$$

$$\beta L23(n,m) := 2 \cdot \frac{\pi}{\lambda_m} \cdot DL23(n) \cdot NL \cdot i$$

$$\beta H3(n,m) := 2 \cdot \frac{\pi}{\lambda_m} \cdot DH3(n) \cdot NH \cdot i$$

$$\beta L34(n,m) := 2 \cdot \frac{\pi}{\lambda_m} \cdot DL34(n) \cdot NL \cdot i$$

$$LH2(n,m) := \begin{pmatrix} e^{\beta H2(n,m)} & 0 \\ 0 & e^{-\beta H2(n,m)} \end{pmatrix}$$

$$L23(n,m) := \begin{pmatrix} e^{\beta L23(n,m)} & 0 \\ 0 & e^{-\beta L23(n,m)} \end{pmatrix}$$

$$LH3(n,m) := \begin{pmatrix} e^{\beta H3(n,m)} & 0 \\ 0 & e^{-\beta H3(n,m)} \end{pmatrix}$$

$$L34(n,m) := \begin{pmatrix} e^{\beta L34(n,m)} & 0 \\ 0 & e^{-\beta L34(n,m)} \end{pmatrix}$$

$$\beta H4(n,m) := 2 \cdot \frac{\pi}{\lambda_m} \cdot DH4(n) \cdot NH \cdot i$$

$$\beta L45(n,m) := 2 \cdot \frac{\pi}{\lambda_m} \cdot DL45(n) \cdot NL \cdot i$$

$$\beta H5(n,m) := 2 \cdot \frac{\pi}{\lambda_m} \cdot DH5(n) \cdot NH \cdot i$$

$$\beta L56(n,m) := 2 \cdot \frac{\pi}{\lambda_m} \cdot DL56(n) \cdot NL \cdot i$$

$$LH4(n,m) := \begin{pmatrix} e^{\beta H4(n,m)} & 0 \\ 0 & e^{-\beta H4(n,m)} \end{pmatrix}$$

$$L45(n,m) := \begin{pmatrix} e^{\beta L45(n,m)} & 0 \\ 0 & e^{-\beta L45(n,m)} \end{pmatrix}$$

$$LH5(n,m) := \begin{pmatrix} e^{\beta H5(n,m)} & 0 \\ 0 & e^{-\beta H5(n,m)} \end{pmatrix}$$

$$L56(n,m) := \begin{pmatrix} e^{\beta L56(n,m)} & 0 \\ 0 & e^{-\beta L56(n,m)} \end{pmatrix}$$

$$\beta H6(n,m) := 2\cdot\frac{\pi}{\lambda_m}\cdot DH6(n)\cdot NH\cdot i$$

$$\beta L67(n,m) := 2\cdot\frac{\pi}{\lambda_m}\cdot DL67(n)\cdot NL\cdot i$$

$$\beta H7(n,m) := 2\cdot\frac{\pi}{\lambda_m}\cdot DH7(n)\cdot NH\cdot i$$

$$\beta L78(n,m) := 2\cdot\frac{\pi}{\lambda_m}\cdot DL78(n)\cdot NL\cdot i$$

$$\beta H8(n,m) := 2\cdot\frac{\pi}{\lambda_m}\cdot DH8(n)\cdot NH\cdot i$$

$$LH6(n,m) := \begin{pmatrix} e^{\beta H6(n,m)} & 0 \\ 0 & e^{-\beta H6(n,m)} \end{pmatrix}$$

$$L67(n,m) := \begin{pmatrix} e^{\beta L67(n,m)} & 0 \\ 0 & e^{-\beta L67(n,m)} \end{pmatrix}$$

$$LH7(n,m) := \begin{pmatrix} e^{\beta H7(n,m)} & 0 \\ 0 & e^{-\beta H7(n,m)} \end{pmatrix}$$

$$L78(n,m) := \begin{pmatrix} e^{\beta L78(n,m)} & 0 \\ 0 & e^{-\beta L78(n,m)} \end{pmatrix}$$

$$LH8(n,m) := \begin{pmatrix} e^{\beta H8(n,m)} & 0 \\ 0 & e^{-\beta H8(n,m)} \end{pmatrix}$$

$$rlast := \frac{Ns - NH}{Ns + NH} \qquad tlast := 2 \cdot NH \cdot \frac{1}{NH + Ns}$$

$$Ilast := \begin{pmatrix} 1 & rlast \\ rlast & 1 \end{pmatrix} \cdot \begin{pmatrix} \frac{1}{tlast} \end{pmatrix}$$

$$P1(n,m) := LH1(n,m) \cdot IHL \cdot L12(n,m) \cdot ILH$$

$$P2(n,m) := LH2(n,m) \cdot IHL \cdot L23(n,m) \cdot ILH$$

$$P3(n,m) := LH3(n,m) \cdot IHL \cdot L34(n,m) \cdot ILH$$

$$P4(n,m) := LH4(n,m) \cdot IHL \cdot L45(n,m) \cdot ILH$$

$$P5(n,m) := LH5(n,m) \cdot IHL \cdot L56(n,m) \cdot IL$$

$$P6(n,m) := LH6(n,m) \cdot IHL \cdot L67(n,m) \cdot ILH$$

$$P7(n,m) := LH7(n,m) \cdot IHL \cdot L78(n,m) \cdot ILH$$

$$P123(n,m) := P1(n,m) \cdot P2(n,m) \cdot P3(n,m)$$

$$P45(n,m) := P4(n,m) \cdot P5(n,m)$$

$$sFluct(n,m) := I01 \cdot P123(n,m) \cdot P45(n,m) \cdot P6(n,m) \cdot P7(n,m) \cdot LH8(n,m) \cdot Ilast$$

$$rFluct(n,m) := \left| \left[\frac{(sFluct(n,m))_{1,0}}{(sFluct(n,m))_{0,0}} \right]^2 \right|$$

$$rFluct_{n,m} := rFluct(n,m)$$

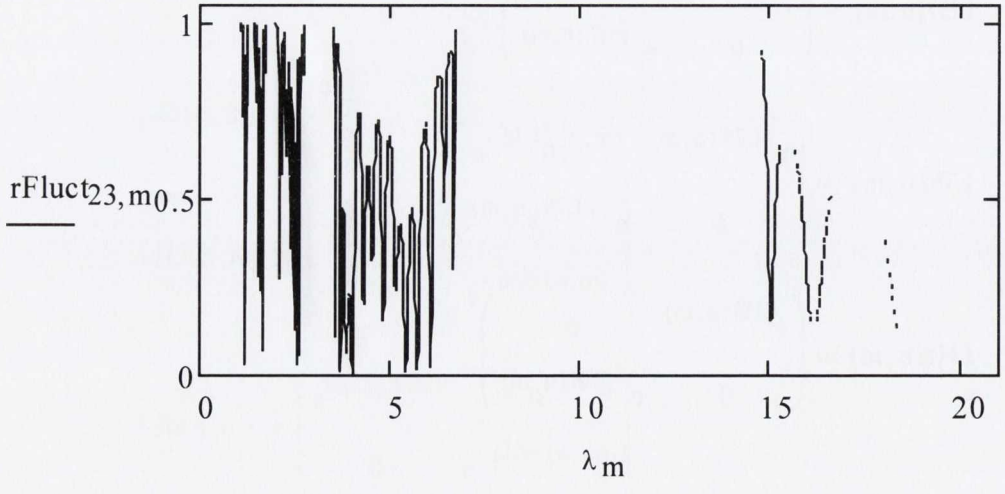

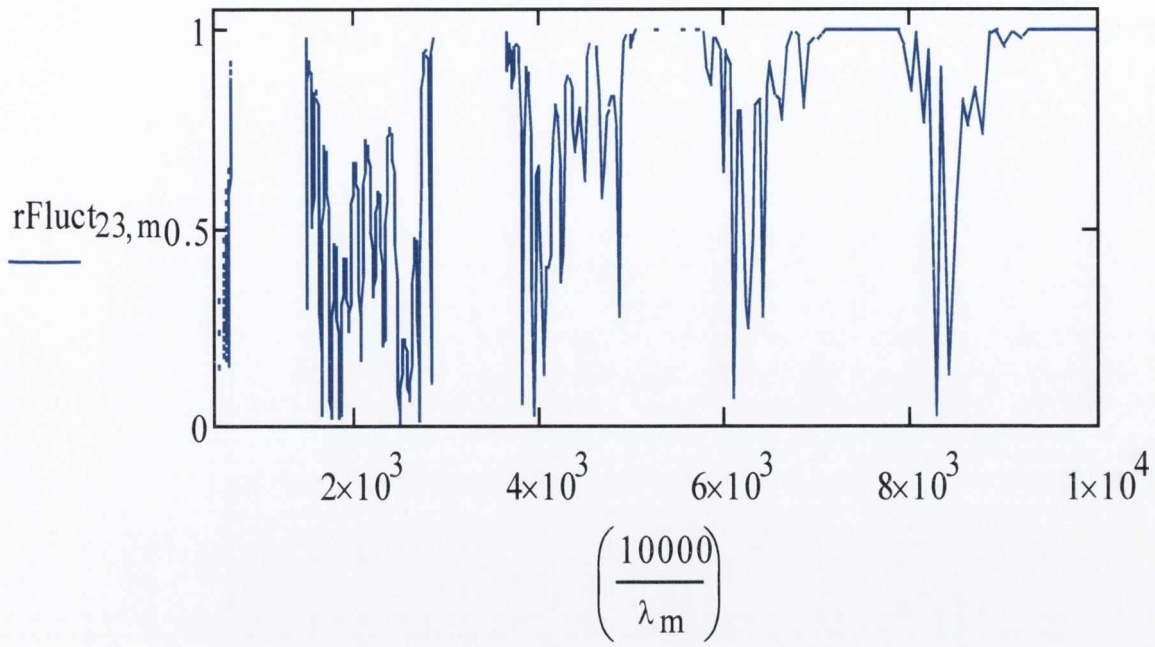

cutoff level - Rpbg

$$qp(n,m) := if(rFluct_{n,m} > 0.999, \lambda_m, 0)$$

$$qs(n,m) := if(rFluct_{n,m} > 0.999, \lambda_m, 0)$$

$$qp_{n,m} := qp(n,m)$$

$$qs_{n,m} := qs(n,m)$$

$$bp(n,m) := \begin{cases} qp_{n,m} & \text{if } qp_{n,m} > 0 \wedge qp_{n,m-1} = \\ qp_{n,m-1} & \text{if } qp_{n,m-1} > 0 \wedge qp_{n,m} \\ 0 & \text{if } qp_{n,m-1} = 0 \wedge qp_{n,m} = 0 \\ 0 & \text{if } qp_{n,m-1} > 0 \wedge qp_{n,m} > 0 \end{cases}$$

$$bs(n,m) := \begin{cases} qs_{n,m} & \text{if } qs_{n,m} > 0 \wedge qs_{n,m-1} = \\ qs_{n,m-1} & \text{if } qs_{n,m-1} > 0 \wedge qs_{n,m} \\ 0 & \text{if } qs_{n,m-1} = 0 \wedge qs_{n,m} = 0 \\ 0 & \text{if } qs_{n,m-1} > 0 \wedge qs_{n,m} > 0 \end{cases}$$

$bp_{n,m} := bp(n,m)$ $bs_{n,m} := bs(n,m)$

$qs_{2,2} = 1.01$

$bp_{1,1} = 0$

$bs_{1,1} = 0$

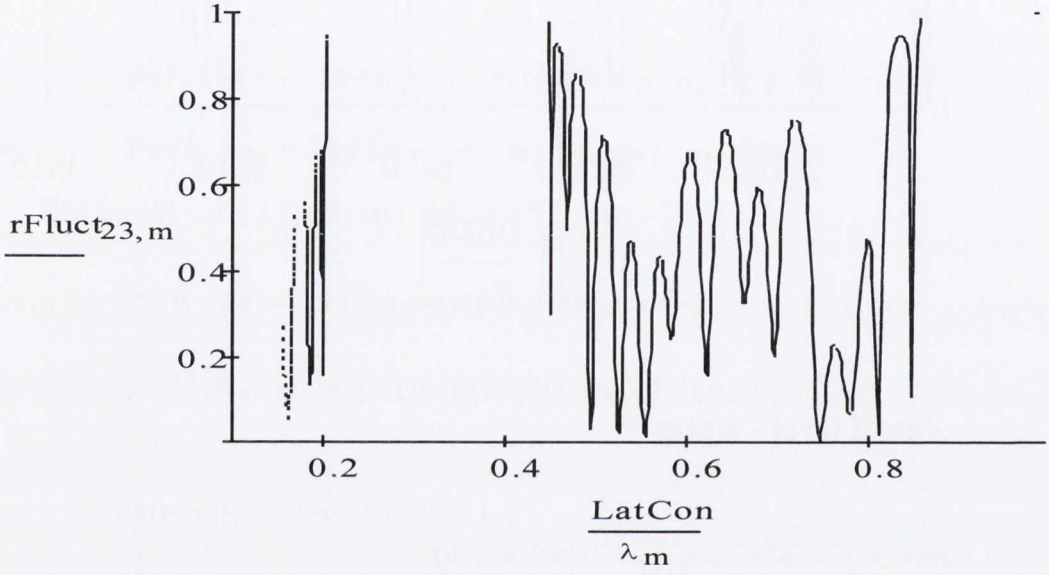

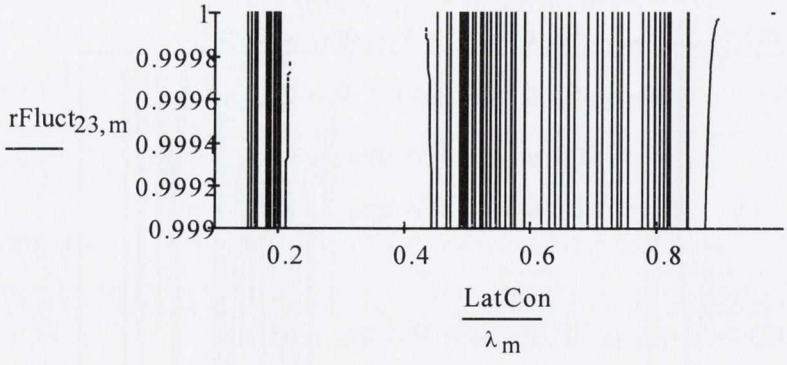

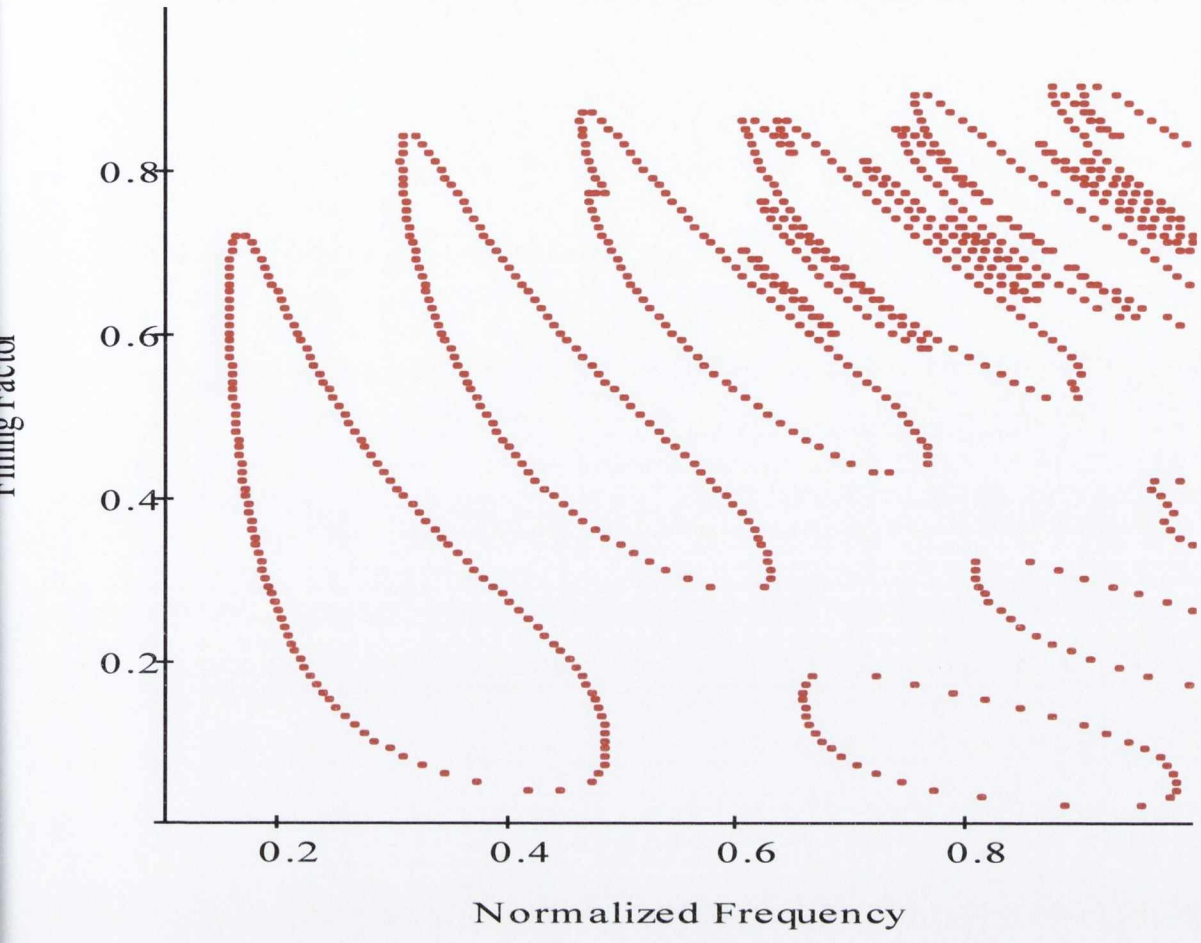
Filling Factor
0.8
0.6
0.4
0.2
0.2
0.4
0.6
0.8
Normalized Frequency

Appendix IV

The parameters of the photonic crystal structure used in the simulations

Chapter 3 Multicomponent Photonic Crystals

Section 3.4.1 Engineering of the optical contrast: Normal incidence of light.

Number of periods, N	10								
Lattice constant, a (μm)	3								
Refractive index of Si, $n_H=n_{Si}$	3.42								
Refractive index of air, n_{air}	1								
Thickness of t-layer, d_t (μm)	0.1	0.2	0.3	0.4	0.6	0.8	1.0	1.2	1.4
Refractive index of t-layer, n_t	1.5 2.21								
Angle of incident light, θ	Normal incidence, $\theta=0°$								

Section 3.4.2 Oblique incidence of light: Omni-directional properties

Number of periods, N	10								
Lattice constant, a (μm)	3								
Filling fraction of Si, f_{Si}					0.3	0.3			
Thickness of Si wall, d_{Si} (μm)					0.9				
Refractive index of Si, $n_H=n_{Si}$	3.42								
Refractive index of air, n_{air}	1								
Thickness of t-layer, d_t (μm)	0.1	0.2	0.3	0.4	0.6	0.8	1.0	1.2	1.4
Refractive index of t-layer, n_t	1.5 2.21								
Angle of incident light, θ	0°; 5°; 10°; 15°; 20°; 25°; 30°; 35°; 40°; 45°; 50°; 55°; 60°; 65°; 70°; 75°; 80°; 85°								

Section 3.5.1 *Suppression of Photonic Band Gaps*

Number of periods, N	5
Lattice constant, a (μm)	3
Filling fraction of Si, f_{Si}	0.08…0.1
Thickness of Si wall, d_{Si} (μm)	0.24…0.3
Refractive index of Si, $n_H=n_{Si}$	3.42
Refractive index of air, n_{air}	1
Thickness of t-layer, d_t (μm)	0.3
Refractive index of t-layer, n_t	1.5
Angle of incident light, θ	0°

Section 3.5.2 *Influence of the additional component thickness*

Number of periods, N	5		
Lattice constant, a (μm)	3		
Filling fraction of Si, f_{Si}	0.117		
Thickness of Si wall, d_{Si} (μm)	0.351		
Refractive index of Si, $n_H=n_{Si}$	3.42		
Refractive index of air, n_{air}	1		
Thickness of t-layer, d_t (μm)	0.4	0.6	0.8
Refractive index of t-layer, n_t	1.5		
Angle of incident light, θ	0°		

Section 3.5.3 *Influence of the oblique incidence of light*

Number of periods, N	5
Lattice constant, a (μm)	3
Filling fraction of Si, f_{Si}	0.18
Thickness of Si wall, d_{Si} (μm)	0.54
Refractive index of Si, $n_H=n_{Si}$	3.42
Refractive index of air, n_{air}	1
Thickness of t-layer, d_t (μm)	0.6
Refractive index of t-layer, n_t	1.5
Angle of incident light, θ	60°

Section 3.6 *Photonic Crystal ultra-wide pass-band filter*

Number of periods, N	3
Lattice constant, a (μm)	4
Filling fraction of Si, f_{Si}	0.25…0.33 0.10…0.17
Refractive index of Si, $n_H=n_{Si}$	3.42
Refractive index of air, n_{air}	1
Thickness of t-layer, d_t (μm)	0.72
Refractive index of t-layer, n_t	Refractive index of SiO2 in MIR from 1 to 8 μm.
Angle of incident light, θ	0°

Chapter 4 Microcavity Photonic Crystals

Section 4.2 *Basic Concept: Modelling of 1D micro-cavity PhC*

Number of periods, N	7.5
Lattice constant, a (μm)	3
Filling fraction of Si, f_{Si}	0.243
Refractive index of Si, $n_H=n_{Si}$	3.42
Refractive index of air, n_{air}	1
Refractive index of cavity, $n_{cav}^{1,2,3}$	1.5 2.0
Angle of incident light, θ	0°

Section 4.3.1.1 *"Si-air-Si" Fabry-Perot resonator*

Number of periods, N	1.5
Lattice constant, a (μm)	3
Filling fraction of Si, f_{Si}	0…1
Refractive index of Si, $n_H=n_{Si}$	3.42
Refractive index of air, n_{air}	1
Refractive index of cavity, $n_{cav}^{1,2,3}$	1
Angle of incident light, θ	0°

Section 4.3.1.2 *"Si-LC-Si" Fabry-Perot resonator*

Number of periods, N	1.5
Lattice constant, a (μm)	3
Filling fraction of Si, f_{Si}	0…1
Refractive index of Si, $n_H=n_{Si}$	3.42
Refractive index of air, n_{air}	1
Refractive index of cavity, $n_{cav}^{1,2,3}$	1.49 1.69
Angle of incident light, θ	0°

Section 4.3.1.3 *Photonic Crystal with "optical defect"*

Number of periods, N	3
Lattice constant, a (μm)	3
Filling fraction of Si, f_{Si}	0…1
Refractive index of Si, $n_H=n_{Si}$	3.42
Refractive index of air, n_{air}	1
Refractive index of cavity, $n_{cav}^{1,2,3}$	1.49…1.69
Angle of incident light, θ	0°

Section 4.3.2.1 *Fabry-Perot resonator fabricated by anisotropic etching of (110) Si*

Number of periods, N	1.5
Lattice constant, a (μm)	4.6
Thickness of Si wall, d_{Si} (μm)	1.2
Thickness of cavity, d_L (μm)	3.4
Refractive index of Si, $n_H=n_{Si}$	3.42
Refractive index of air, n_{air}	1
Refractive index of cavity, $n_{cav}^{1,2,3}$	1 1.72 1.53
Angle of incident light, θ	0°

Section 4.3.2.2 *Fabry-Perot resonator fabricated on (100) Si by Deep Reactive Ion Etching*

Number of periods, N	1.5
Lattice constant, a (μm)	8
Thickness of Si wall, d_{Si} (μm)	2.6
Thickness of cavity, d_L (μm)	5.4
Refractive index of Si, n_H=n_{Si}	3.42
Refractive index of air, n_{air}	1
Refractive index of cavity, $n_{cav}^{1,2,3}$	1 1.53
Angle of incident light, θ	0°

Section 4.3.3.1 *Thermo-tunable single channel devices*

Number of periods, N	1.5
Lattice constant, a (μm)	4.8
Thickness of Si wall, d_{Si} (μm)	1.2
Thickness of cavity, d_L (μm)	3.6
Refractive index of Si, n_H=n_{Si}	3.42
Refractive index of air, n_{air}	1
Refractive index of cavity, $n_{cav}^{1,2,3}$	1 1.54 1.67
Angle of incident light, θ	0°

Section 4.3.3.2 *Electrically tunable Fabry-Perot resonator*

Number of periods, N	1.5	
Lattice constant, a (μm)	5	8
Thickness of Si wall, d_{Si} (μm)	1	0.6
Thickness of cavity, d_L (μm)	4	7,4
Refractive index of Si, n_H=n_{Si}	3.42	
Refractive index of air, n_{air}	1	
Refractive index of cavity, $n_{cav}^{1,2,3}$	1 1.45 1.67	1.51 1.34
Angle of incident light, θ	0°	

Section 4.4 *Coupled multi-cavity Photonic Crystal resonators*

Number of periods, N	7.5		
Lattice constant, a (μm)	0.573		
Thickness of Si wall, d_{Si} (μm)	0…0.573		
Thickness of cavity, d_L (μm)	0.573…0		
Refractive index of Si, n_H=n_{Si}	3.42		
Refractive index of air, n_{air}	1		
Refractive index of cavity, n_{cav}^1	1.74…1.52	1.643…1.617	1.63
Refractive index of cavity, n_{cav}^2	1.63	1.617…1.643	1.678…1.682
Refractive index of cavity, n_{cav}^3	1.52…1.74	1.643…1.617	1.63
Angle of incident light, θ	0°		

Section 4.4.5 *Optimization: Compensation of the fabrication tolerances*

Number of periods, N	7.5		
Lattice constant, a (μm)	0.9		
Filling fraction of Si f_{Si}	0.4		
Refractive index of Si, n_H=n_{Si}	3.42		
Refractive index of air, n_{air}	1		
Refractive index of cavity, n_{cav}^1	1.63	1.60	1.61
Refractive index of cavity, n_{cav}^2	1.63	1.60	1.59
Refractive index of cavity, n_{cav}^3	1.63	1.60	1.61
Angle of incident light, θ	0°		

Section 5.3 *Modelling of thickness fluctuation*

Number of periods, N	7.5
Lattice constant, a (μm)	3
Filling fraction of Si, f_{Si}	0…1
Refractive index of Si, $n_H=n_{Si}$	3.42
Refractive index of air, n_{air}	1
Standard deviation	$0.004a$ $0.0115a$ $0.025a$ $0.036a$
Angle of incident light, θ	0°

Section 5.5 *Photonic crystals with a constant value of fluctuation of all wall thickneses*

Number of periods, N	7.5
Lattice constant, a (μm)	3
Filling fraction of Si f_{Si}	0.08 0.23 0.5 0.71
Refractive index of Si, $n_H=n_{Si}$	3.42
Refractive index of air, n_{air}	1
Standard deviation	$0.004a$ $0.0115a$ $0.025a$ $0.036a$
Angle of incident light,θ	0°